THE CHEMICAL BEHAVIOR OF HEAVY METAL SALT SOLUTIONS WITHIN POROUS SOL-GEL SILICA

By

JAMES MICHAEL KUNETZ

A DISSERTATION PRESENTED TO THE GRADUATE SCHOOL
OF THE UNIVERSITY OF FLORIDA IN PARTIAL FULFILLMENT
OF THE REQUIREMENTS FOR THE DEGREE OF
DOCTOR OF PHILOSOPHY

UNIVERSITY OF FLORIDA

1995

TABLE OF CONTENTS

ABSTRACT v

CHAPTER 1 INTRODUCTION 1

CHAPTER 2 LITERATURE REVIEW OF RESTRICTED GEOMETRIES 5
2.1 Definition of a Restricted Geometry 5
2.2 Forces and Properties 6
2.3 Properties of Liquids Within Restricted Geometries 9
2.3.1 Historically Early Evidence 9
2.3.2 Molecular Motion 10
2.3.3 Water at Silica Surfaces 12
2.3.4 Partitioning within Restricted Environments 16
2.4 Restricted Transport or Diffusion 20
2.4.1 Hydrodynamic Literature 22
2.5 Conclusions 27

CHAPTER 3 THE CREATION AND CHARACTERIZATION OF POROUS SOL-GEL SILICA 30

3.1 Introduction 30
3.2 Factors Influencing Pore Morphology 33
3.2.1 Pre-gelation 34
3.2.2 Aging 40
3.2.3 Drying 42
3.2.4 Densification 44
3.3 Experimental Production of Monoliths 48
3.3.1 Processing Methodology 49
3.4 Characterization of Pore Monoliths 55
3.4.1 Mercury Pyncnometry 55
3.4.2 Archimedes Density 56
3.4.3 Nitrogen Adsorption 58
3.5 Water Percolation into Porous Monoliths 58
3.5.1 Introduction 58
3.5.2 Experimental Results 66
3.5.2.1 Methods 66
3.5.2.2 Cracking versus bulk density 67
3.5.2.3 Penetration kinetics into porous sol-gel monoliths 72
3.6 Conclusions 83

CHAPTER 4 ANALYSIS OF POROUS GEL SILICA MONOLITHS WITH CALORIMETRY AND ELECTROPHORESIS 85

4.1 Introduction 85
4.2 Heats of Immersion 87
4.2.1 Theory 87
4.2.2 Related Studies 88
4.2.3 Experimental Procedure 92
4.2.3.1 Sample preparation 92
4.2.3.2 Calorimeter operating conditions and principles . 93
4.2.3.3 Calorimeter procedure 94
4.3 Zeta Potential 97
4.3.1 Theory 97
4.3.2 Related Studies 104
4.3.3 Experimental Procedure 106
4.3.3.1 Sample preparation 106
4.3.3.2 ZetaPlus® operating conditions and principles . . 109
4.3.3.3 Zeta potential measurement 113
4.4 Results and Discussion 115
4.4.1 Results 115
4.4.1.1 Heats of immersion 115
4.4.1.2 Zeta potential 115
4.4.2 Discussion and Results 131
4.4.2.1 Wetting 139
4.4.2.2 Rehydration 142
4.4.2.3 Microporosity and surface roughness 143
4.4.2.4 Impurities 147
4.4.2.5 Zeta potential 147
4.5 Conclusions 164

CHAPTER 5 THE DIFFUSION OF HEAVY METAL SALT SOLUTIONS INTO POROUS SILICA MONOLITHS 166

5.1 Introduction 166
5.2 Theory and Related Studies 167
5.3 Experimental Methods 175
5.3.1 Materials 175
5.3.2 Procedures 176
5.3.3 Analysis 180

5.4 Results and Discussion 183
5.4.1 Presentation and Results 183
5.4.1.1 Diffusion coefficients 183
5.4.1.2 Partition coefficients 186
5.4.2 Discussion of the Results 200
5.5 Conclusion 213

CHAPTER 6 INVESTIGATION OF THE BINDING OF Cr^{3+} TO POLYSILOXANE STRUCTURES WITH A SEMI-EMPIRICAL MOLECULAR ORBITAL MODEL 216

6.1 Introduction 216
6.2 Molecular Orbital Modeling 216
6.2.1 ZINDO 221
6.3 Experimental 222
6.3.1 Peak Shifting Phenomena 222
6.3.2 Experimental Discussion 222
6.4 Theoretical Modeling 224
6.4.1 Theoretical Method 224
6.4.2 Parameterization 224
6.4.3 Structures 225
6.4.4 Theoretical Results 225
6.5 Discussion 230
6.6 Conclusions 233

CHAPTER 7 CONCLUSIONS AND SUGGESTIONS FOR FUTURE WORK . 235

REFERENCE LIST 240

BIOGRAPHICAL SKETCH 253

Abstract of Dissertation Presented to the Graduate School of the University of Florida in Partial Fulfillment of the Requirements for the Degree of Doctor of Philosophy

THE CHEMICAL BEHAVIOR OF HEAVY METAL SALT SOLUTIONS WITHIN POROUS SOL-GEL SILICA

By

James Michael Kunetz

August 1995

Chairman: Dr. Larry L. Hench
Major Department: Materials Science and Engineering

The purpose of this research was to study the evolution of the porous network during the processing of silica gel monoliths and to provide new knowledge about the relationships between the chemical behavior of heavy metal salt solutions and the pore structure of the porous monoliths.

The evaluation of the porous structure of sol-gel silica monoliths, based mostly upon N_2 gas adsorption experiments, indicated that the different processing steps substantially modified the pore morphology of these materials.

The stability of these different porous structures to aging in water were determined by electrophoresis measurements in the 2.5 to 5.5 pH range. The isoelectric point of the porous silica was found to vary with the processing method. The isoelectric points correlated linearly with the heats of immersion

generated in water. Zeta potential experiments on these porous powders indicated that porosity decreased the electrophoretic mobility of the porous particle.

The effective diffusion coefficients and equilibrium partition coefficients within silica gel monoliths were determined for various heavy metal salt solutions using visible absorption spectroscopy. The cations were found to have a partition coefficient less than one within the porous monoliths. The partition coefficient decreased with the pore size and increased towards one as the pH of the solution was increased. The effective diffusion coefficients of the salt solutions varied over an order of magnitude for the pore sizes and solution variables investigated. The effective diffusion coefficients for the different pore sizes and volume fractions of porosity within the gels predict tortuosity values of 5.5 to 0.7.

Semi-empirical molecular orbital calculations were performed to investigate the interaction of the hydrated chromium ion with the gel surface. Various models were proposed to account for peak shifting which occurred as a function of the solution pH. The peak shifting phenomena is explained by the change in the Cr-O distance in the $Cr[(H_2O)_6]^{3+}$ complex. This distance changes for different degrees of interaction of the hydrated species with the surface charge of the gel.

CHAPTER 1

INTRODUCTION

Technology is defined by the New Encyclopedia Britannica to be "the application of science to the practical aims of human life or, as it is sometimes phrased, to the change and manipulation of the human environment." The late 20th century is a time in which the population's demand upon technology is forcing the development of faster, smaller, more efficient, more practical, and more economically produced machines. The fabrication of these machines requires reliably produced materials at levels of preciseness in the nanoscale dimension.

One synthesis route for the fabrication of an advanced material with a controlled nanoscale structure is sol-gel processing. The sol-gel process is a method in which chemical precursors are mixed on a molecular level to form an oxide gel which can be subsequently converted into a ceramic or glass. The molecular scale processing of these materials offer advantages such as higher purity, higher homogeneity, and lower processing temperatures over traditionally produced glass making or powder methods.[1]

Sol-gel science has grown markedly in the last two decades due to potentially unique applications for this new class of materials.[2-11] Sol-gel processing uses both organic and inorganic metalloid precursors, water, organic solvents, and catalysts to create an array of materials ranging from thin films to

fibers which include porous ceramics obtained by heat treating the gel to remove the pore liquid.[12]

One area of research and development has been in the development of optical composites.[13] These composites combine the high homogeneity and purity required for optical transmission with an optically active second phase. Sol-gel silica matrices are usually the material of choice because of silica's excellent optical properties. Optical composites can be created by adding the optical dopant to the sol or to the nanosize pores which are uniformly distributed throughout the bulk.

Sometimes as a consequence of the "advancement of technology or the manipulation of the environment" unwanted substances are released which threaten the quality of this environment. Substantial efforts to "clean up" the environment initiated the research and commercialization of environmental sensing.[14,15] The current state of sensing uses materials in which the pore features of the matrix are difficult to characterize.[16-19] The combined optical and porous properties of sol-gel silica based materials make them ideal candidates for sensing applications.[20]

The movement of molecules through the pores of the silica matrix are influenced by the restricted geometry.[21] Understanding this molecular movement through the pores is important for sensing applications and for the doping of these sol-gel silica matrices with optically active second phases. It may be argued that an ion's molecular movement is the simplest. The ion is the smallest species in solution and carries a net charge. The UV/visible transitions characteristic of

transition metal ions provide a convenient method to examine the diffusion of these ions into porous sol-gel glasses. Therefore, in this work the diffusion of heavy metal salt solutions into porous gel-silica monoliths is studied, with an emphasis upon chromium, in order to understand more fully the connection between the pore characteristics and the ion movement.

Understanding the relationship between the stability of the porous silica monoliths in water and the sol-gel processing variables is a prerequisite to the development of an environmental sensor. Aging studies on the gels prepared in this study provide information to the changes occurring to the gels in water for different sol-gel processing conditions. The objectives of the study are outlined in the following section.

In order to construct improved composite materials, one should understand the transport properties of solutions and the degree of interaction between the surface and these solutions. The extremely small physical size (12-90 Å pore radii) and active chemical state (surface silanols) of the porous network itself suggests that solute-surface interactions will play a major role in governing the motion of diffusing species. Chapter 2 is a review of the literature on confined geometries. Restricted diffusion, concentration partitioning, and the modification of solvent properties within porous materials are reviewed as an introduction to understanding finite size effects within small pores.

The first step of the study is to create porous materials capable of being used as restricted geometry hosts. Chapter 3 investigates the interrelationship of

the sol-gel processing variables and the pore morphology of the stabilized monoliths. The pore structure is characterized with N_2 adsorption/desorption isotherms and pycnometry techniques. Additionally, the pore structure of these materials is further characterized by immersion in water. This also provides information about the stability of these porous monoliths.

Chapter 4 combines heats of immersion and electrophoresis experiments to determine the surface charge properties which may affect the movement of charged species through the porous network. Aging electrophoresis studies provide a first indication as to the relative stability of the differently processed sol-gel porous monoliths.

The main emphasis of chapter 5 is the measurement of the diffusion of chromium ions and the concentration partitioning effects within differently prepared sol-gel monoliths for assorted solution conditions. Other ions are investigated to understand more fully the chemical behavior of salt solutions within these optical materials with restricted geometries. Possible interactions of the chromium ion with the silica surface is explored further with the aid of semi-empirical molecular orbital calculations. The results of these calculations are presented in chapter 6. The final chapter, 7, summarizes the conclusions from this study and offers suggestions for future work.

CHAPTER 2
LITERATURE REVIEW OF RESTRICTED GEOMETRIES

2.1 Definition of a Restricted Geometry

Materials characterized by spatial confinement or small dimensions such as polymers, zeolites, clays, porous glasses, and porous coatings are often used in applications where the movement of molecules within the pore structure is a key or important component of the underlying process. The diversity of disciplines utilizing confined properties are wide, ranging from petroleum engineering to medicine. However, central questions arise which are fundamental to understanding these systems such as: To what extent are the properties of fluids affected within these confined systems? Which properties of the porous matrices such as pore size, the pore size distribution, surface area, or the chemical nature of the surface affect molecular transport or selective separation? A definition for restricted geometries is required before reviewing the literature and attempting to understand the answers to these questions.

A restricted geometry is defined by the relationship of the size of the molecule to the size of the pore. If the confinement of the molecular system alters the dynamic and/or thermodynamic properties of the confined molecules the system is defined as a restricted geometry. The confinement forces can be both

physical and chemical in nature. The most easily visualized restricted geometry is one containing microporosity, pores less than 20 Å in diameter. The tiny size of a micropore is within an order of magnitude of the size of even the simplest molecules. However, if the molecule is complex, such as a high molecular weight protein, a porous system with pore sizes ranging in the 100's of angstroms would be considered a restricted environment. The ratio of the molecule size to the pore size is a common measure of how restrictive an environment will be. To make explicit or unambiguous connections between molecular behavior and the geometry of the confining space is difficult and frequently controversial. In spite of this, studies have shown that within similarly prepared materials, one effect of finite size on the behavior of confined liquids and gases scales with geometric size. As a background to understanding the restricted diffusion of heavy metal salts into porous monolithic sol-gel glasses the following literature is reviewed.

2.2 Forces and Properties

The forces acting upon solutes and solvents within confined systems are intimately related to the geometrical structure of the pores and the chemical properties of the surface and solution. This is because most restricted geometries have large surface area-to-volume ratios which provide large interfacial areas between the substrate and solution. Interfacial regions are transitional regions from one phase to another and are in themselves another phase or "interphase" which usually has graded properties from the well defined boundary of one phase

to the other. In the interphase region electric and molecular forces decrease with distance into each of the contiguous phases. Four types of surface forces are generally acting at the interface of a solid and solution. These surface forces have been divided into two kinds by Derjaguin[22] in which he refers to as surface forces of the first and second kind.

The first kind of surface forces are those treated by Gibbs capillarity theory, "in which the mass components of the system and extensive thermodynamic functions of the system equal the sum of terms proportional to the volume between the phases and terms proportional to the areas of interfaces between the phases" (page 2).[22] This presupposes that the interfacial zones do not overlap or that the thin interlayer has a region in which it retains the intensive properties of the bulk.

A special case of interest, excluded from Gibbs theory, is when the forces of the first kind overlap as a result of the thinning of the interlayer sandwiched between the other two. These forces are referred to as surface forces of the second kind. Derjaguin[22] clearly illustrates the additional complexity induced by overlapping forces both mathematically and physically. The resulting force is the disjoining force which has an adsorption component, electrostatic component, and a structural component which are similar in nature to the forces of the first kind. The adsorption component is due to an unequal molecular interaction energy of the solute and solvent with the surfaces of a thin interlayer or film. This leads to a nonuniform distribution of concentration across the film. The

electrostatic component of the disjoining pressure is still a result of the spontaneous charging of the interface in an electrolyte but now includes the effect of surface potentials overlapping as a result of two such interfaces being brought close together. Certainly this must affect the behavior of ions contained within small size sol-gel pores. The last component of the disjoining pressure is the structural component which is particularly evident for polar solvents. Solvation implies the formation of boundary layers of different molecular structure and hydration is the same concept specific to water as the solvent. The boundary layers apply to macroscopic surfaces or interfaces of solutes of a solution. The modification of the structure in the boundary layer is thought to result from oriented intermolecular hydrogen bonds(see below).

In porous silica filled with an electrolyte solution, both kinds of surface forces to different degrees act upon both the solvent and the solute(ions). These forces are expected to alter the equilibrium concentration of the solution within the pores and the solvent properties such as density and viscosity. Also, it is highly likely that radial gradients in the solution properties exist, even at equilibrium. The smaller the constriction of the pore space, the larger the fraction of total radial distance over which these gradients act and, therefore, the larger the average deviation from bulk properties.

There are three types of surface forces or effects which influence molecular behavior at an electrolyte-silica interface. Dispersion type forces(molecular or van der Waal), electrostatic forces generated by a nonuniform distribution of

ions(formation of an electrical double layer), and structural or ion-dipole forces(associated with the modification of solvent structure at the boundary layer).

Thus, the remaining portion of this literature review first examines the deviation of solution properties in restricted environments and then examines how the altering of properties combined with geometrical confinement affects the motion of solutes within restricted environments.

2.3 Properties of Liquids Within Restricted Geometries

2.3.1 Historically Early Evidence

Following the concept of Hardy[23] in 1912 which was popularized by Reychler[24] and Langmuir, interfacial layers of liquids consist of at least a monolayer of oriented molecules. The experimental evidence collected before 1950, both direct and circumstantial, of the orientation of liquids at interfaces is reviewed by Henniker[25] in a fascinating manner. He presents dozens of experiments for many different liquids measuring a wide range of physical properties, such as refractive index, multilayer adsorption, X-ray and electron diffraction, surface viscosity, adhesion, compressive strength, electrical conductance, dielectric constant, electrokinetic potential, density, and thixotropy viscosity. The anomalies witnessed in all of these experiments he claimed was evidence of the existence of a "surface zone of a liquid."

The measurement of repulsive forces between two surfaces was an extremely difficult experiment to perform in the 1950s because both surfaces had

to be smooth, flat, parallel, and less than a micron apart. Nonetheless, in 1956 Derjaguin, Overbeek, and Abricosova[26] succeeded in measuring long-range van der Waal forces in vacuum between mica sheets. Their results were later confirmed by Kitchener[27] and Black.[28]

The viscosity of liquids is very sensitive to their structure. In the 1960's much experimental work was done by the Russian scientific community attempting to gain information about surface forces based upon kinetic effects in dispersed systems and capillaries.[29] In particular, the pressure rise during the filtration of water through filters and powders having pores less than 0.05 microns was interpreted by assuming that the viscosity of thin layers is higher than the bulk.[30] It was also noted that this pressure rise decreased as the electrolyte concentration increased. This was attributed to a contraction of the boundary layer under an osmotic pressure drop, assuming that the concentration of ions in the bulk of solution is higher than at the interface. A series of experiments utilizing the blow-off method[31] indicates that the viscosity of surface layers for polar solvents increases at the interface and also increases with increasing length of the molecule. Nonpolar molecules showed no increase in viscosity down to 10-100 Å in thickness.

2.3.2 Molecular Motion

A specific anisotropic structure in the boundary layers of liquids is possible only if the freedom of rotation of the molecules is more limited than in the bulk.

A consequence of this restricted motion would be a lowering of the dielectric permeability of dipolar molecules. This was confirmed in adsorbed water layers.[32]

A more direct measurement of the rotational motion of molecules confined within sol-gel glasses has been made by Warnock and coworkers.[33] Warnock uses a subpicosecond optical birefringence technique to measure a rotation correlation time, τ_r, for carbon disulfide and nitrobenzene. The relationship of τ_r to the viscosity is described through the following two equations. The Stokes-Einstein relation,

$$D_o = \frac{k_b T}{\eta 6 \pi r_s} \qquad (2.1)$$

describes the hydrodynamic behavior of spherical objects of radius, r_s, in a liquid of viscosity, η, as related to the diffusion coefficient at infinite dilution, D_o. The rotation correlation time, τ_r, is related to the viscosity through the Stokes-Einstein-Debye equation,

$$\tau_r = \frac{\eta v_m f}{k_b T} \qquad (2.2)$$

where v_m and f are the hydrodynamic volume and shape of the molecules, respectively. The correlation time for the linear carbon disulfide molecule did not change within pores varying from 44 to 375 Å in radius. However, the polar nitrobenzene exhibited biexponential behavior in τ_r indicating hindered rotation adjacent to the glass. Further calculations indicated that this hindered region was 12 Å thick with a viscosity three times that of the bulk.

Nikiel, Zerda, and Hench[34] studied the rotational behavior of various polar and nonpolar molecules within small pore size sol-gel glasses using polarized Raman bands transformed into rotational correlation times. The reorientational times for acetonitrile and chloroform in the bulk liquid phase were quite different than inside the pores. However, SF_6, CS_2, and nitromethane showed no differences. It was suggested that hydrogen bonding played the major role in the slowing of the correlation time for the polar molecules. However, molecular dynamic studies[35] of SF_6 indicate that although surface interactions do participate in altering translational and rotational movements, this only occurs over two molecular diameters.

In a different Raman spectroscopy study, Zerda[36] presented diffusion and preferential adsorption data for a variety of organic solvent mixtures. He attributed a reduced diffusion coefficient for various components based on increased resistance to movement due to preferentially adsorbed molecular layers. His less convincing explanations for preferential adsorption due to proton-donating and proton-accepting solvents can probably be related to the relative strengths of the dielectric constants of the individual components of the solution and silica.

2.3.3 Water at Silica Surfaces

Peschel and Adlfinger[37] measured the apparent viscosity in thin layers adjacent to hydroxylated fused silica surfaces by means of a special device in which a spherical silica surface approaches a planar silica surface. The device enabled both the strength of the shearing force and the distance of separation to

be varied independently. It was found that an increase in the shearing force above 700 dynes or an increase in separation above 160 nm resulted in a measured value for the viscosity close to that of bulk water. At very small separation distances(30 nm) and low shearing force(300 dynes) the viscosity was twenty times higher than in the bulk. This is the same phenomenon seen in flow through porous ceramic filters.[38] At high pressure differences the flow was Poiseuille type and at low pressure differences the flow exhibited non-Newtonian behavior.

Two types of silica, manufactured by Mallinckrodt, were studied by Morariu and Mills[39] in terms of the self-diffusion of water by high-resolution nuclear-magnetic-resonance(NMR). The study explored two different pH's(4 and 7) for various statistical monolayers from 0.7 to 5. At one statistical monolayer the diffusion coefficient was an order of magnitude smaller than the bulk. An extrapolation of the effective diffusion coefficient versus the number of water monolayers predicted 15 monolayers before the diffusion coefficient of the bulk water value is reached.

The freezing of water in porous materials is associated with many engrossing phenomena. A simple demonstration is the transformation of water into a cubic crystal structure in small pores instated of the usual hexagonal structure as studied by Dunn et al.[40] A Small-Angle Neutron Scattering(SANS) study[41] of the conversion of water inside of porous Vycor® to ice revealed a smaller density change in the transition from water to ice than in the bulk. It was estimated that the water inside the pores is already 10.8% denser than bulk water.

Wallace[42] combined results from the adsorption of water vapor into sol-gel silica pores, as analyzed by dielectric relaxation spectroscopy, with measurements of the latent heat of fusion of water within the pores, as determined by differential scanning calorimetry, to calculate a statistical bound water thickness as a function of pore size. The results indicated a different structure of water adjacent to the pore walls which increased in thickness with increasing temperature and/or average pore radius.

Another exciting piece of work is the NMR relaxation of water in unsaturated porous Vycor® silica glasses.[43] The longitudinal and transverse relaxations as well as the self-diffusion coefficient of deionized water were measured. The self-diffusion coefficient increased above one monolayer similar to Morariu and Mills[39] results, while both relaxation rates increased below one monolayer. D' Orazio et al. concluded that the two relaxations are strongly interrelated and that one of the O-H bonds rotates in the plane of the surface.[43] This may indicate that in their system the loose hydrogen of the water molecule is hydrogen bonded to a deprotonated oxygen. Others[42] have modeled adsorbed water to have the oxygen of the water molecule hydrogen-bonded to the proton of the silanol. Discussions of this nature must consider the silica surface dependency upon the pH of water.

Braun and Drost-Hansen[44] have measured the heat capacity of water adsorbed onto an assortment of surfaces and have found the heat capacity to be 25% greater than in the bulk. The unique aspect of their study is finding that the heat capacity was independent of the type of surface. In agreement with this,

Watts-Tobin[45] have also shown that there is a weak tendency for water to orient itself at the interface between two media of different permittivity even in the absence of an external field.

Two general classes of theories are used to explain the features of water at interfaces: mixture models[46-47] and continuum models.[48-49] The mixture models suggest that water is in two different states with an enrichment of the low energy state at interfaces. This model has the advantage of being able to explain the maximum in density, the minimum in the isothermal compressibility, and heat capacity data. The continuum models postulate that water is essentially entirely hydrogen bonded and the general effect of heating is to bend hydrogen bonds and not break them. This model implies that the surface imposes orientational constraints on the water molecules at an interface.

Israelachvili,[50-51] in his studies of surface forces, finds contradicting evidence with regards to development of repulsive and attractive forces, and very little viscosity changes at the interface. In dilute solutions of NaCl, an increase in force was detected until approximately 10 Å separation at which point the surfaces jump into adhesive contact indicating an attractive force. The viscosity was measured from separations of 1600 Å down to 50 Å, with less than a ten percent increase in viscosity. In more concentrated solutions of NaCl a short-range repulsive hydration force was seen below 40 Å with no force maximum as in the dilute electrolyte case. This hydration(as called when water is the solvent), solvation(includes all solvents), or structural(Derjaguin terminology) force is due to

the adsorbed Na^+ ions on the mica surface. Again, no apparent increase in viscosity was noted down to 20 Å separation. These results are contradicting in that forces arising due to structural orientation at an interface should lead to an increase in viscosity. This may be as result of the method applied. Israelchvilis' apparatus used curved surfaces which might cause a weaker effect than two flat parallel surfaces at the same separation distance.

In general, it is agreed that solvation forces monotonically decrease from the surface up to 40 Å and can be repulsive or attractive, depending upon the chemical nature and dynamic state of the surface. An oscillatory component is usually superimposed upon the monotonic component but only out to 15 Å or 6-7 water molecules. The oscillatory component corresponds to the short-range, one-dimensional order of the arrangement of molecules at the surface of an adjacent phase.

2.3.4 Partitioning Within Restricted Environments

It is suggested that two contributions to the restricted diffusion of particles and/or solutes within confined systems are a result of the exclusion of solute from a fraction of the pore volume within the pores and the increase in hydrodynamic resistance due to the close proximity of the pore walls. This section reviews the roles of solution concentration, solute adsorption, and solute-to-pore diameter ratio on the equilibrium partitioning of solutes in a micropore relative to the bulk phase. The partition coefficient is defined as the ratio of the concentration in the pore to

the bulk. The final section of this chapter reviews restricted diffusion of particles and molecules.

One of the simplest potential interaction models for a molecule inside a pore is a hard-spherical molecule inside a pore with non-attracting hard walls. This has been studied by Giddings et al.[52] for molecules of different shapes. It was found that as the number of molecules begins to increase within the pore, molecular interactions become important and high density regions form at the pore wall. The study conducted by Glandt[53-54] investigated applying a simple theoretical model which described the number density or molecular concentration variation across pores of different geometries. The geometrical shape which increased molecular exclusion from the walls within the pores was slit-shaped > cylindrical > spherical. The difference became larger as the ratio of solute diameter to pore diameter increased. It is also assumed that these differences would increase if the walls exerted an attractive potential.[55]

An expected result from experimental work on the partitioning of macromolecules within porous Vycor® glass shows a reduced concentration within the pore for all the polymers[56] and proteins[57] studied, compared to the bulk, as the molecular size of the molecules increased relative to the pore dimensions. A surprising result, however, was the constant effective diffusivity of different molecular weight polystyrenes whereas effective diffusivity decreased for the proteins. This was attributed to polystyrene behaving similar to a free-draining macromolecule. A Monte Carlo simulation[58] was used to investigate the effects of

overall chain length and individual segment lengths upon the partitioning of freely jointed chains in the bulk and in cylindrical pores. The results indicate that the partition coefficient was substantially higher for a chain with finite segment length than a chain with an infinite number of infinitesimally short segments (both with the same radius of gyration). This could indicate the possible chromatographic separation of molecules with differing flexibility but the same radius of gyration or size.

The next level of complexity, including the electrical double layer or electrostatic force, was modeled by Smith and Deen[59-60] to include electrostatic interactions between a colloid particle and a long cylindrical pore. The first model[59] only allowed for centerline axisymmetric positions of the particle which was later refined to allow for all radial positions[60] to be occupied by the particle. The Gouy-Champman diffuse double-layer model, with an analytical solution to the linearized Poisson-Boltzmann equation, was employed to obtain the electric potential distribution within the pores(this model is discussed more in chapter 5 with regard to diffusion). The potential energy of interaction is then calculated from the system free energy after Verwey and Overbeek.[61] The electrostatic contributions to the interaction energy reflect distortions in the electric potential near the particle and the pore wall. The charge on the sphere was the same as the pore and therefore a repulsive electrostatic interaction is observed, decreasing the partition coefficient. Without electrostatic effects, the model predicted partitioning based solely upon hard-wall, hard-sphere interactions. This limit was approached as the

concentration of electrolyte was increased because an increase in concentration decreases the Debye-Huckel length of the double layer.

Wiggins[62] investigated the ionic partitioning of a number of different light metal aqueous salt solutions in a silica gel with 0.4 cc/gm of porosity. All the cations exhibited partitioning upon extrapolation of her data to infinite dilution. She attributed the changes in the partitioning to the different ions ability to "break" or "make" the water structure. Those with structure-breaking ability were assumed to have an enhanced solubility in the vicinal water adjacent to the pore walls and thus have an increased partition coefficient. Another way of saying this is that highly hydrated ions were excluded to a larger extent. Wiggins did not include electrostatic effects in her analysis. However, it is evident from her results that as the electrolyte concentration increased(i.e. decreasing double-layer thickness), the partition coefficient increased.

It is apparent that the distribution of charged particles within a charged pore is extremely complicated. Even more so, the distribution of ions of different types varies by nearly an order of magnitude under similar conditions. The combination of finite volume effects of ions being radially excluded within the pores, the alteration of the solvent viscosity by its propinquity to the surface as well as by the ion concentration, and the effects of an electrostatic potential developed by the silica surface, predict a very complex and extremely difficult system in which to separate the various contributions. This description was made simpler with reference to the partitioning discussions in that the systems studied were at

equilibrium. The last section reviews the diffusive or transport behavior of both macromolecules and small molecules within restricted geometries with respect to some of the same variables mentioned for the partitioning.

2.4 Restricted Transport or Diffusion

As mentioned in the introduction, transport in liquid-filled pores of molecular dimensions plays an important role in chromatography separations, drug delivery, and catalysis, as examples. Two key distinguishing features of hindered transport theories involve the decrease in the diffusion coefficient due to radial force gradients or static interactions and alterations of the particle motion due to liquid flow being perturbed by the wall and reacting back onto the particle.

Einstein[63] showed that the driving force for diffusion, the gradient in chemical potential, may be treated as a body force on the solute molecule. This body force, under steady motion in an isothermal fluid, and neglecting other body forces, is exactly balanced by the hydrodynamic force,

$$-kT\frac{\partial \ln C}{\partial z} - 6\pi r_s K(V_s - GV) = 0 \qquad (2.3)$$

where k = Boltzmann constant, T = absolute temperature, C = concentration, z = direction of diffusion, η = the solution viscosity, r_s = radius of a sphere, K and G = coefficients for enhanced drag and velocity lag, respectively, V_s = sphere velocity, and V = solution velocity. The flux of the sphere is a product of its velocity

and concentration, $J_s = V_s * C$. Therefore equations 2.1 and 2.3 can be rewritten in the form,

$$J_s = -K^{-1} D_o \frac{\partial C}{\partial z} + GVC \qquad (2.4)$$

For a stagnant, unbounded solution(V=0, K=1), this reduces to equation 3.1, the Stokes-Einstein equation. The convective flow of a solution through porous media is more relevant to chemical or petroleum engineering operations and in this study the solution velocity is zero. Also, the lower limit of the size of molecules in which hindered hydrodynamic factors contribute is approximately a radius of 10 Å.[64] One of the assumptions of hydrodynamic theory is that the molecule is a rigid sphere larger than the molecules of the solvent, and therefore the solvent can be treated as a continuum. It is well known that the sizes of ionic spheres(the solvated ion), which vary for the hydrated ion from 2-4 Å in radius, are not predicted by the diffusion coefficient when calculated by the Stokes-Einstein equation.[65] However, the concept of a more restricted diffusion as the pore size becomes commensurate with the molecule's size provides a useful framework for analyzing the phenomena. In addition, the current advancement of hydrodynamic theories to include quantification of electrostatic interactions and effects of solute concentration on partitioning suggests some effect on ionic movement in the small pores of sol-gel monoliths. This literature with respect to ionic diffusion is presented in chapter 5 along with the diffusion data from this investigation. The literature review in this section discusses the language and historical development of concepts for

restricted diffusion. Most of the restricted transport literature involves concurrent transport by both convection and diffusion.

2.4.1 Hydrodynamic Literature

The first hydrodynamic models of restricted transport were developed to understand transport through biological membranes.[66] Using frog mesentery, resting mammalian muscle, and the glomerular capillaries in the kidneys of mammals, Pappenheimer et al. determined the diffusion rates of various lipoid insoluble molecules which enabled them to evaluate the areas and the effective pore dimensions of these biological structures. This work was the impetus for the application of many restricted transport theories in the biological sciences, as reviewed by Solomon.[67]

Most of the literature consists of empirical relationships between the effective diffusivity in the pore, D_p and the bulk diffusion coefficient, D_o. This ratio can be defined as D_f, the effective diffusivities fractional value of the bulk diffusion coefficient, which varies from 0 to 1. The ratio of the molecule size, r_s, to the pore size, r_p, is defined as λ, which also varies from 0 to 1. A typical plot of D_f versus λ displays a decrease in D_f as λ decreases. Additional factors such as pore shape, electrical charges(either or both wall and solute), porosity, concentration, non-spherical solutes, to name a few, are varied in order to determine their contribution to the system being studied.

Complexities arise as a result of different types of interconnected media and specific interactions with solutes. Unlike sol-gel matrices, some porous materials

(rock, concrete, carbonaceous, etc.) may contain dead-ended or isolated pores in which this closed porosity must be treated differently.[68] Also, stationary traps within the media such as fixed reaction or adsorption sites are governed by a different mechanism which must be handled separately.[69,70] If the diffusional flux is faster than expected for diffusion in the pore volume alone, then one might conclude that an additional contribution from surface diffusion exists.[71,72] This is usually witnessed at the solid-gas interface but can occur in liquid systems.[73] The additional complication in separating the relative contributions arises from evaluating the change in concentration with distance in both the pore volume, dc/dx, and the surface, dc_s/dx.

Confirmation of hindered hydrodynamic theories was made possible by the development of the track-etch process.[74] This process is usually performed upon mica or polycarbonate sheets, and enables the production of straight, extremely small pores of constant cross-sectional area. Deen[75] believes the major contributions to the confirmation of the existing models were made by Bean et al.,[76] Anderson and Quinn,[77] and Beck and Schultz.[78]

As discussed by Deen[75] in an excellent review, radial variations within the pore in the solute concentration are of great importance. Malone and Anderson[79] realized that the partition coefficient was important to transport processes even though it is an equilibrium parameter. They stabilized mono-disperse latex particles with ionic surfactants and measured the diffusion rate as a function of pore radius and ionic strength. Greater restriction than predicted by current models was

found, and it was concluded that not only did the particle to pore size ratio affect hindered diffusion, but so did the solution and membrane properties.

The most versatile model with regard to radial variations in concentration was derived by Brenner and Gaydos,[80] who modeled the constrained Brownian movement of a spherical particle in cylindrical pores of comparable radius. The model accounted for both diffusive and convective transport, as well as non-hydrodynamic particle/wall interactions arising from London, van der Waal, and Debye double layer wall potentials. Two of the most striking predictions of their theory, at least for sufficiently small λ, are that (1) on average the Brownian particle moves faster than the fluid in which it is suspended and (2) the larger the particle, the more rapidly it moves. Qualitatively these predictions indicate that the particle is not able to sample the slowest moving streamlines at the wall due to its finite size, and that the larger the particle the larger is the inaccessible region of the cross-sectional area near to the walls. These two predictions were later confirmed by the results of Garnier and Ostrowsky[81] using an evanescent quasielastic light scattering technique to study an aqueous suspension of latex particles 450 Å in radius.

Particles are ideal for hindered hydrodynamic studies because their shape is usually spherical, and if the particle is non-spherical the shape can easily be determined. However, many investigations have addressed macromolecular diffusion[82-86] mostly due to the science of chromagraphic separation. The macromolecules can be defined in terms of a hydrodynamic radius if they are

globular proteins or compact solutes, or in terms of a radius of gyration, if they are more linear and flexible. One significant conclusion with respect to molecular configuration[82] and hindered transport is that the predicted hydrodynamic resistance to solute motion in pores is lower for flexible molecules than for spheres, for the same Stokes-Einstein radius and driving force. However, the less favorable partitioning of random coils between the pores and the bulk leads to an overall lower diffusion of coils than spheres. Independently, the same conclusion was found by Anderson et al.[83] with regard to diffusion of long and short-chain polystyrene and planar disk-shaped porphyrins. The freely-jointed long-chains behaved significantly differently from hard spheres, whereas the shorter chain polystyrene approached the transport behavior of the porphyrins, which in turn diffused very much like hard spheres of equivalent Stokes-Einstein radius. A final point with respect to macromolecules, which may be applicable to the zeta potential measurements of porous sol-gel silica particles, is a reference to Deen and Smith.[84] They measured the electrophoretic mobility and D_o in bulk solution and D_p within polycarbonate etched-membranes for the polyelectrolytes ficoll sulfate and dextran sulfate as a function of ionic strength. Good quantitative agreement with theory was found for electrostatic double layer interactions in hindered diffusion. Still more interesting is the modeling of the electrostatic partitioning calculations to more closely fit a porous sphere with charge distributed throughout as opposed to a solid sphere with the charge confined to the surface.

The porosity of the porous silica particles was also found to alter the electrophoretic mobility (see chapter 4).

As mentioned in the beginning of this section, as the molecule size approaches the size of the solvent molecules, hydrodynamic interactions decrease. However, surface forces must still dominate the behavior of these small molecules within micropores due to size constraints.

The self-diffusion of the dye Azobenzene (C_{14}) was studied by a forced Rayleigh scattering technique within porous Vycor® glass with an average pore radius of 30 Å.[87] The diffusion coefficient was measured to decrease by two orders of magnitude from the bulk value. It was thought that hydroxyls could act as local chemical traps to restrict the movement of the dye. However, after an esterification of the surface with 1-propanol, the diffusion coefficient was redetermined to be essentially the same value, within experimental error. It is also worth noting that the tortuosity of the sample, as calculated from the reduction in the diffusion coefficient and the volume fraction was 18, higher than the values found from hydrogen diffusion, 5.6.

A somewhat larger molecule, fullerene C_{60}, was diffused through sol-gel glasses of average pore radius 14 Å, in solutions of cyclohexane.[88] A diaphragm cell technique was used in the measurement of both the solvent and the C_{60}. The solvent diffusion was decreased by a factor of three from the bulk value and the diffusion of C_{60} was 12 times slower than the solvent. The diffusion value of the C_{60} molecule compared to the Vycor® diffusion experiment with the C_{14} molecule

seems somewhat high. That is, why does a molecule with one-fourth the number of carbons diffusing in a pore twice the size results in a diffusion coefficient one order of magnitude less? This could demonstrate the shape effects mentioned earlier for macromolecules in which the C_{60} is acting more like a sphere and the dye acts more like a freely-jointed molecule. Otherwise, it may indicate discrepancies or unaccounted differences in experimental methods.

Finally, a study by Koh and Anderson[89] investigated the possible affects of the electrostatic double layer upon the diffusion of neutral or uncharged solutes in an aqueous medium through porous membranes. The effective diffusion coefficient for five different organic species with dipoles varying from 1.6 to 20 Debye (1 D = 10^{-18} esu.cm) was determined at a range of ionic strengths. It was found that the diffusion coefficient was unaffected by the presence of the double layer.

2.5 Conclusions

In conclusion, a summary is presented of the important categories or variables which affect the motion of molecules and the solute partioning within these restricted geometries.

In general, a restricted geometry is a geometry in which a solution is confined within a region where the force-fields, which originate from the surface of the confining media, alter a significant portion of the solution properties from the bulk solution properties. The forces involved are in general, the dispersion forces

(London and van der Waal), the electrostatic forces from a charged surface (electrical double layer), and structural or ion-dipole forces.

The size of a restricted geometry is relative to the molecular size of interest. Large spaces or pores which do not alter the physical properties of the solvent except at the interface can still affect the motion and concentration of macromolecules with similar dimensions. On the other hand, extremely small size pores affect not only the movement of solute molecules but the rotational and translational movement of the solvent molecules. This leads to a change in the physical properties of the solution such as density and viscosity.

The force-fields decrease with distance from the surface of pores and therefore create gradients in the solution properties and the concentration of solutes and solvents. In addition, if the object under study is a molecule or particle which can be treated as a hard sphere, larger than the solvent molecule, hydrodynamic factors become important.

The diffusion of a particle or molecule, through a porous material with a restrictive environment, decreases as the size of the pores approach the size of the molecule. The effective diffusion coefficient may be modified by several orders of magnitude from the bulk value. Also, the concentration of a species within this environment might be substantially different from the bulk concentration. This is especially the case for charged species within a charged environment. The concentrations can be both larger and smaller within the restricted environment than the bulk concentration.

In general, the restricted environments and the solution interactions cannot be examined directly because of the size scale. Inhomogeneities in the restricted material, such as dead-end pores, reaction sites, size distributions, etc. create variables which can only be in some instances averaged. However, if multiple characterization techniques to are used to investigate the structure and the surface of the porous material in combination with transport or molecular motion studies, useful engineering parameters may be deduced for use in creating new materials.

CHAPTER 3
THE CREATION AND CHARACTERIZATION OF POROUS SOL-GEL SILICA

3.1 Introduction

The intent of this chapter is to introduce the fundamental physics and chemistry of sol-gel processing with an emphasis on how the sol-to-densification processing steps can be varied to alter the pore morphology in the final glass piece. Morphologically different pore structures, as characterized by nitrogen adsorption and bulk density measurements, are discussed in relation to the different sol recipes and processing procedures used to create porous sol-gel silica monoliths. The different pore structures in these porous glasses are studied further in this work in terms of heats of immersion, zeta potential, and effective ionic diffusion and partitioning. Data for the percolation of water into dehydrated porous monoliths is presented as the concluding segment to this chapter. Theoretical and empirical relationships between the water imbibing rate and the pore morphology are correlated to a topological parameter, B_v, which represents the number of branches, in the gels pore network.

The earliest recorded history of the processing of sol-gel ceramics is the work of Ebelmen[90] in 1846 which resulted in the conversion of an organic precursor to an inorganic silica, by hydrolysis and polycondensation of tetraethyl

orthosilicate under acidic conditions. The first technological interest occured in the 1950's with the work of Roy[91] and Iler.[92] Roy synthesized oxide compositions which could not be made using traditional ceramic processing techniques. Iler devoted his efforts to the chemistry of silica which led to the development of commercial colloidal silica powders.

Successful low temperature synthesis of monolithic glass pieces from a metal alkoxide did not occur until 1978. Yamane[93,94] hydrolyzed tetramethoxysilane (TMOS) under neutral and basic conditions and then proceeded to heat treat the gel up to 1000°C. The properties of these approximately 15-20 mm in diameter synthetic monolithic glass disks are similar to those of commercial vitreous silica with the exception that a highly interconnected porosity exists in the sol-gel derived glass. The conference proceedings[2-8] from the 1980's along with other journal publications produced approximately 15-20 thousand papers on the basic science of sol-gel and novel processing techniques to create or improve, on the nanostructure level, new or existing materials.

Even though very few fully developed products have evolved from the studies of sol-gel processing, the amount of fundamental information archived is phenomenal. Research and development continues into the 1990's with materials such as coatings, fibers, and porous matrices or hosts. Various optical components which take advantage of the near net shape casting process intrinsic in the sol-gel system are also finding a small niche in the market. Most of the process variables of the sol-to-gel conversion and subsequent heat treatments

used to produce the final material have been investigated to some extent. However, exact reproduction of work cited in the literature, is difficult due to the extremely sensitive nature of the sol-gel process to procedural variables and material precursors. The supplier and the purity of precursors, which sometimes vary from batch to batch, mixing sequences, type of casting container, and laboratory atmosphere are a few of the major obstructions to achieving reproducability. However, the general effect of the processing variables upon the final properties of gel derived silica are fairly well known. In this work, one variable is varied systematically, which makes direct comparisons within the porous sol-gel silica monoliths possible.

Types of sol-gel systems range from single to multi-component compositions with a large list of both organic and inorganic additives mixed in at all steps in between. For a list of systems and other references see Sol-Gel Science[12] or The Chemistry of Silica.[92] The system employed in this study is pure silicon dioxide or silica. The glass variables are the number, size, and distribution of pores. The salt solution variables are the pH, type, and concentration of the ionic solution. The first step in this work was to create morphologically different porous monoliths as restricted geometry hosts. The pore structure is created in the sol by hydrolysis of the silicon alkoxide to silicic acid, followed by polymerization into discrete particles, which eventually link together to form a three dimensional network. This structure can then be modified in subsequent aging, drying, and densification steps. The next section is a summary of the theory and

literature with respect to the influence of these processing variables upon the pore structure followed by the characterization of the glasses produced in this study.

3.2 Factors Influencing Pore Morphology

A stabilized gel is a gel which has been strengthened by heat treatment so as to withstand the capillary stresses generated upon immersing in a liquid. The final pore characteristics of the stabilized gel are determined by the chemical and physical conditions at all steps in the process. These are:

1. The size and concentration of the primary particles in solution at gelation.
2. The time, type and pH of aging liquid, and temperature of the aging step.
3. The type and pH of drying liquid, applied pressure, and temperature during drying.
4. The temperature, time, and atmosphere of the ensuing heat treatments.

The above variables may be changed to create drastically different porous silicas with pore diameters and surface areas ranging from 12-150 Å and 5-1200 m^2/gm, respectively. The four numbered steps above represent pre-gelation, aging, drying, and densification, respectively. A summary of the relationships between the pore structure and these factors follows.

3.2.1 Pre-gelation

The components of the sol include a metal alkoxide, sometimes an organic solvent, water, and a catalyst. There are a number of different precursors capable of creating silica gels. The two most commonly studied precursor systems are tetramethyl orthosilicate (TMOS) and tetraethyl orthosilicate (TEOS). For reviews of other precursors see refs. 3 or 12. All of the gels used in this study were made using TMOS.

Alcohols were initially added to prevent liquid-liquid phase separation,(p.109)[12] but it was later discovered[95] that large R ratios(moles of water/moles of TMOS) in acid-catalyzed systems promote rapid hydrolysis of $Si(OCH_3)_4$ to $Si(OH)_4$ which produces methanol. Both effects decrease immiscibility and eliminate the need to include alcohol in the sol. However, catalytic species such as OH^- or H_3O^+ are attracted to or repelled from potential reactions sites based on electrostatic effects. Solvents with different dipole moments can be added to alter the kinetics of hydrolysis and condensation. Aprotic solvents (solvents not capable of losing a proton) effectively make hydroxyl ions more nucleophilic and protic solvents (containing a labile proton) make hydronium ions more electrophilic.[96] Artaki et al.[97] used Raman spectroscopy and molybdic acid reagent to investigate the effect of polar protic, and non-polar aprotic solvents on the formation of polysilicate species. There was some contradiction in the results, thought to be due to steric effects, but in general aprotic solvents at pH > 2.5 increase the polycondensation rate. A final and

counter-effect of solvents is their ability to cause alcoholysis (the reverse of alcohol condensation) and therefore promote depolymerisation of the particles leading to a more highly condensed species or particle. All of the sols in this study had R > 12. Therefore, no alcohol or other organic solvents were added to the sol.

As indicated in the chapter introduction, the pore characteristics which develop first are a result of the size and concentration of primary particles prior to gelation in the sol. The concentration of particles is controlled by the R ratio. The size of the primary particles is indirectly influenced by the R ratio. Higher R ratios decrease the silicate concentration, which decreases the hydrolysis and polymerization reactions and affects the structural evolution. The most important variables in determining the size of the primary particles are the temperature and pH of the sol, and the type of catalyst used. This is because these factors influence the solubility and the rates of hydrolysis and condensation. The solubility, S, of a particle is related to its radius, r, by the Ostwald-Freundlich equation[3]:

$$S=S_o\exp\left(\frac{2\gamma_{sl}V_m}{R_gTr}\right) \qquad (3.1)$$

where S_o is the solubility of a flat plate, γ_{sl} is the solid-liquid interfacial energy, V_m is the molar volume of the solid phase, R_g is the ideal gas constant, and T is the absolute temperature. The consequence of this equation to the primary particle size in the sol, with all of the other variables being constant, is two fold. First, the

radius of the particle is exponentially related to the solubility with positive values of r increasing the solubility of the particle while negative values of r (negative radii of curvature) decrease the solubility. Secondly, the exponential relationship forces the solubility to approach asymmtoically infinite solubility at particle radii less than 30Å. This solubility phenomena based on particle size is known as Ostwald ripening. Particles with small positive radii of curvature dissolve and precipitate on larger particles or surfaces and regions with negative radii of curvature (particle necks) fill in. As the silicic acid molecules polycondense they start to form particles which will reach different sizes depending partly upon the solubility. Equation 3.1 shows that an increase in temperature will also increase solubility. However, all the gels in this study were gelled at room temperature. Therefore, the solubility in this system is controlled by the solution pH.

Plank and Drake[97] studied the effect of pH on particle size and pore size. For an increase in pH from 2.7-8.7, they saw an increase in particle diameter from 42-77 Å and an increase in pore diameter from 64-138 Å. Iler[92](p.517) states that colloidal silica suspensions with particles ranging from 50-600 Å form gels with surface areas affected very little by pH. This is because the solubility does not begin to increase significantly until the particle diameter is below 30 Å. The particle diameter at gelation in an acid-catalyzed TMOS system was shown by Orcel[99] to be approximately 20 Å. This small primary particle size indicates that the solubility of silica will play a role in the structural evolution of the gel. Not only is the solubility a function of pH but so are the hydrolysis, k_h, and condensation, k_c, rate

reaction constants. These factors, k_h and k_c, are discussed in the final part of this pre-gelation section with an emphasis on the effects of the type of catalyst and pH.

Hydrolysis and polycondensation reactions in the sol can proceed thermally in the absence of catalysts but are fastest and more complete when catalysts are utilized.[100] Also, the size and shape of the polymeric structural units, and ultimately the gel structure, are determined by the relative values of the rate constants for hydrolysis and condensation.[101] Again, the major variables affecting the rate constants are temperature, the nature of the electrolyte(acid or base), the solvent and the alkoxide. An increase in the R ratio of the sol generally promotes hydrolysis, although an increase in R while maintaining a constant solvent:silicate ratio reduces the silicate concentration and thus reduces the rate constants. Schmidt[3](p.87) showed a reduction in the hydrolysis rate constant as the R value increased in a HCl catalyzed system with R values less than one and constant ethanol:TEOS ratio. More importantly, Schmidt discussed the many problems associated with the computation of reaction rate constants. Generally, it is necessary to verify which species are present, as Pouxviel[101] and co-workers did in an investigation of an acid-catalyzed TEOS using ^{29}Si NMR. They performed the experiment for short times at which the overall order of the reaction remained constant[3](p.173). Monolithic sol-gel components require large R ratios, much larger than one($R > 10\text{-}25$), which cause the hydrolysis of $Si(OCH_3)_4$ to $Si(OH)_4$ under acidic conditions to take place in a few minutes. An increase in R at these large R ratios always increases hydrolysis.

The rate and extent of the hydrolysis is most influenced by the type and concentration of the catalyst. All strong acids(HNO_3, HCl, H_2SO_4) behave the same, whereas a weaker acid like acetic (CH_3OOH) requires longer times to produce a similar reaction extent. Unlike the acid catalyzed systems, basic conditions are influenced more by the nature of the solvent.[102] Individual rate constants were not calculated in this study. However, studies have shown that the overall time to gelation correlates with acid concentration. Pope and Mackenzie[103] report gel times from 10 to 1000 hours depending upon the strength, type and concentration of acid. The most notable result is the anomalous behavior of HF acid in which the fluoride ion behaves similarly to the hydroxyl ion producing gels similar to those made by base catalysis. Similar results on HF catalyzed gels are presented later in this chapter.

The overall effect of pH on gel time is shown schematically in figure 3.1. Even though small shifts for different catalysts take place, the trend is the same for different acid catalysts. The maximum gel time is around pH 2, where the surface charge on the silica particles is at a minimum[92] so that not only is the rate of aggregation a minimum but so is the rate of growth of the particles (because of a minimum in the solubility and condensation reaction). A minimum gel time occurs somewhere around pH 5-6 where monomeric silicic acid is converted rapidly to particles which gel quickly. At higher pH's only particles can be obtained because the particles are highly negatively charged which prevent collisions and particles

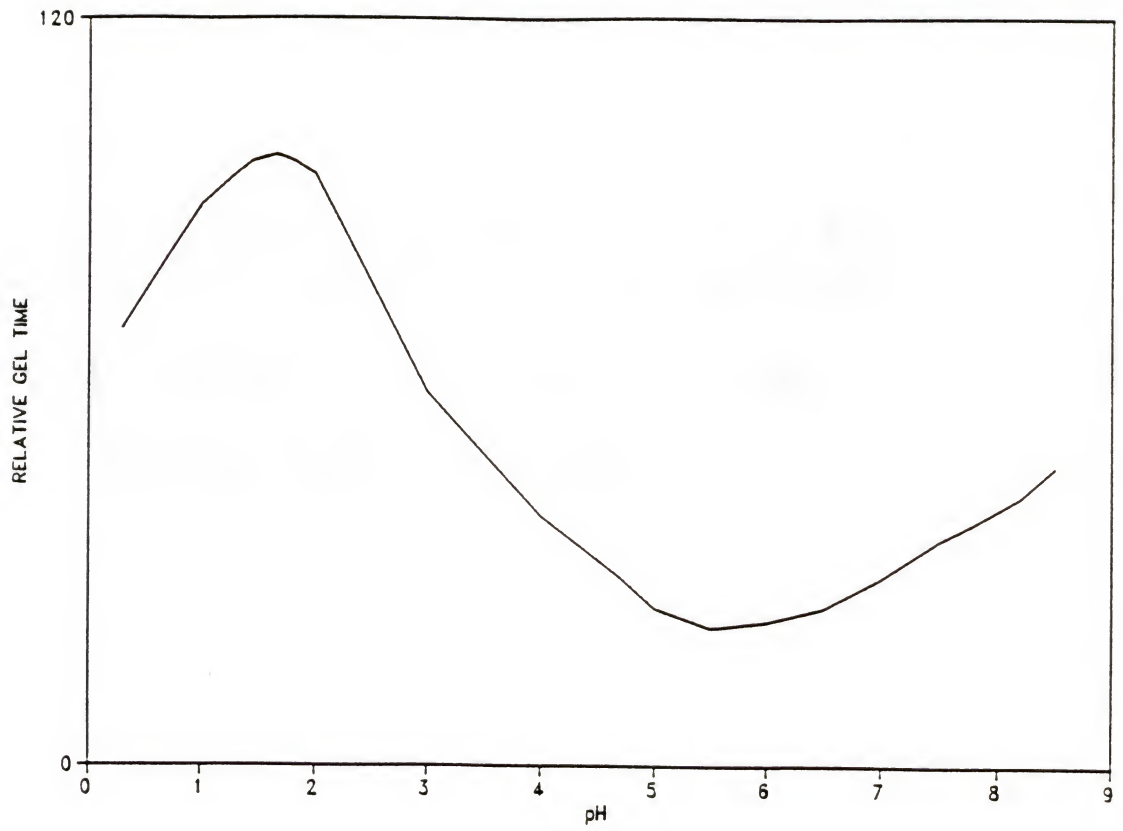

Figure 3.1 This is a figure of the relative time for a silica sol to gel as a function of sol pH. Source: Iler [92].

continue to grow without aggregation or gelling. The pH effects on the polymerization of silica are fully explained in Iler.[92]

A summary of the above effects with regard to the production of porous sol-gel silica monoliths follows. Porous monoliths can be prepared under acidic conditions in the sol (pH < 4). Gel times are adjusted mostly by the concentration of acid and not the type of acid, except for HF which causes rapid gelling and behaves like a base. The gel time is inversely proportional to the condensation reaction rate. The minima in solubility and polymerization rates are at low pH levels which create small primary clusters which grow to different sizes as the pH is increased. The evolution of the structure in this region takes place by polymerization or connection of these primary particles. Larger particles imply larger pore radii and larger pore volumes.

These are general trends for a simple system of alkoxide, water and acid-catalyst, which is the system used in this work to create gel-silica monoliths. The next three sections, aging, drying, and sintering, are the subsequent steps in the sol-gel process which enable one to modify the resultant pore structure created at gelation. The gel structure with its interconnected porosity is already established at this step in the process and can only be modified.

3.2.2 Aging

This section reviews changes in the structure of the gels occurring after gelation and before drying. Three major processes operate during aging: 1. condensation reactions occur between adjacent silanols, 2. syneresis, a process

which involves polycondensation, shrinkage and expulsion of pore liquor, and 3. coarsening or ripening. The first two contribute to the shrinkage of the gel while ripening induces micro-rearrangement and little shrinkage. Because some of the same processes are functioning during aging as in the sol, time, pH and temperature of the aging solution is very important. Small pore gels, 12 Å in average pore radius, were shown to increase in pore size to 100 Å after aging in a 0.25 N basic solution of ammonium hydroxide for one day[104] demonstrating the catalytic dissolution of silica by OH^- ions. This process must significantly reduce the surfaces of positive radii of curvature to much larger radii of negative curvature, according to equation 3.1 above. Also, Liu[104] shows the affect of aging at higher temperatures for 3-64 days. Very small decreases in surface area and increases in pore volume are seen in short times (less than a week) at 80°C compared to aging at room temperature for nitric acid-catalyzed gels. However, at longer times, significant changes occurred in the porosity measurements producing a doubling of the average pore size. These results indicate pH has more of an effect on the aging of gels than temperature at this step of the process. Klimentova[105] showed that the gel time and syneresis shrinkage are a maximum at pH 1.7, eg. very close to the isoelectric point. This indicates the same condensation reaction is responsible for both.

Two explanations usually given for shrinkage are the continuation of the polycondensation, (ie. two silanols take up less room than a bridging oxygen), and the drive by the gel to reduce the interfacial solid-liquid area.[106] Both could occur

simultaneously, but does the formation of a bridging bond cause the structure to bend or does the reduction of interfacial area move the skeletal walls in order for the reaction between two silanols to take place? Scherer[107] measured the shrinkage of two different sized gels and found that the smaller the gel's physical size, the more it shrinks. He assumed the gel shrinkage rate was inversely proportional to the viscosity of the solid phase(more bridging bonds, higher viscosity). His model suggests that the rate of shrinkage decreases because of stiffening of the structure and not a depletion of reactive sites.

From this short review several points are evident. First, aging in aqueous solutions of high pH has the greatest effect upon modifying the pore structure. Second, this aging is accompanied by an increase in pore volume and a decrease in surface area. Third, the number of positive radii of curvature features formed from the gelling of small primary particles, if present on the gel surface, are reduced during base aging and larger negative radii of curvature are formed.

3.2.3 Drying

In this dissertation, the drying step was not used as a variable to modify the pore structure. All of the samples were dried in a similar fashion. Drying is briefly discussed here for completion.

The drying step in the sol-gel process consists of three stages: Stage one, involves free water evaporation from the surfaces creating capillary stresses which draw together the solid network, decreasing the pore volume. Classically, this was viewed as a constant evaporation rate period on systems with large pores.

Dwivedi[108] and Kawaguchi[109] who studied large pore alumina gels observed a constant evaporation rate in this stage. Wilson[110] carefully and accurately measured the weight, and dimensional changes occurring for small pore silica gels (pore radius < 20 Å) and found the evaporation rate to decrease during the first stage. This decrease in evaporation rate is attributed to a vapor pressure reduction within the pores as described by the Gibbs-Kelvin equation and to the presence of bound water at the gels surfaces.[110] The pore liquid meniscus remains at the surface during the first stage of drying and thus some of the variables from the aging stage; eg. type of pore liquor, pH of aging solution and temperature are still altering the pore morphology.

Stage two drying starts at the critical point where shrinkage no longer takes place. The compressive and tensile forces on the gel and pore liquor, respectively, are at maxima. It is at this point the gels turn opaque and might crack. After this point the gels expand slightly as the liquid is released. The pore liquid evaporates at a constant rate.

The third stage or drying is characterized by water vapor transport by diffusion to the surface at an evaporation rate that is a fraction of the rate of the second stage. No changes to the pore morphology occur during stages two and three. It is obvious that the interfacial liquid-vapor energy exerts the forces collapsing the structure and any change in this interfacial energy alters the pore volume of the dried gel. In fact, aerogels, gels dried above the critical point of the solvent, eliminate this interfacial energy and the resultant gel can be as much as

95% volume fraction pores. The reader is referred to Brinker and Scherer[12] for a more detailed discussion of surfactants added to lower the liquid-vapor interfacial energy during drying as well as hypercritical drying of aerogels.

At this step in the process the gel is a highly interconnected porous phase surrounded by a skeletal glass phase which resembles the structure of vitreous silica only in its tetrahedral building blocks. The size of the pores and gel walls depend entirely upon the structure frozen in at gelation and the extent to which the structure was modified and deformed during aging and drying. The surfaces of the gel are covered with hydroxyls(SiOH) and in cases where lower R values are used, unreacted alkoxide groups(SiOR). However, the gel is extremely weak and depending upon the previous processing steps the bulk density of the gel is approximately 20-60% of its theoretical density of 2.2 gm/cc. This structure cannot withstand the enormous capillary pressure predicted by the Laplace equation upon immersing in a liquid.[12] Thus, further heat treatment is required to increase the strength of the gel.

3.2.4 Densification

The densification of dried gels involves the removal of water and residual organics, polymerization, structural relaxation, and surface dehydroxylation. The densification of silica gels and the subsequent surface changes have been thoroughly investigated. Iler[92] and more recently Brinker[12] have published books with hundreds of references with regard to heat treatments and the corresponding changes observed for not only silica gels but multicomponent systems as well.

More specifically to the gels used in this study, the reader is directed towards Hench[1] and Wallace.[42] With respect to diffusion of ionic solutions, it is more important to understand how the surface and structure evolve than why. Accordingly, the structural evolution during densification is first reviewed followed by the surface changes occurring during thermal treatments.

Brinker[12] divides the structural changes into three regions: 25°-180°C, 180°-500°C, and 500°-1100°C. At 25°-180°C, the gel loses physically adsorbed water and shrinks very little. The shrinkage is associated with a strain resulting from an increase in the surface energy following the desorption of water.[111] A dilation is observed for weakly branched xerogels, with a reported thermal expansion value 100x that of vitreous silica in this temperature range[3](pp.37-51). This reiterates the openness, on a molecular level, of the structure at this point in the process.

At 180-500°C, the gel continues to lose weight and shrinks further. The weight loss is due primarily to organics although continuing condensation removes water. The shrinkage results from both polymerization and structural relaxation. TGA results[6](pp.25-31) indicate weight loss and shrinkage still occurs even after the organics have been burned off. This suggests condensation reactions are still occurring. Also, the skeletal density increases from 1.8 gm/cc to 2.2 gm/cc from 350-500°C[11] indicating internal silanols are also polymerizing. Structural relaxation, a process by which the excess free volume is removed by diffusive movements of the network, can also contribute to the shrinkage that occurs in this region.[112]

Structural relaxation can be detected by an observed increase in skeletal density without weight loss.

At 500-1100°C, shrinkage occurs with very little weight loss. As the temperature increases the viscosity decreases and the gel continues to consolidate. This viscous sintering process is driven by the energy gained by the reduction in surface area. As will be seen in the next section, both surface area and pore volume decrease as the densification temperature is raised. Several methods are available to minimize the inclusion of water in the fully consolidated gel.[12] Various theories have been developed to describe the viscous sintering of gels.[12] These are not mentioned further because this work involves the development and use of unconsolidated porous silica monoliths. The last part of this section discusses the modification of the surface over these same three thermal regions.

The thermal stabilization required to increase the strength of the structure also modifies the surface. After drying there remains a large concentration of hydroxyl groups on the surface. These include hydroxyls on different silicons that are hydrogen bonded (vicinal), two hydroxyls on the same silicon (geminal), and isolated hydroxyls. The extent of the hydrogen bonding of the hydroxyls is related to the curvature of the surface. The extent of hydrogen bonding increases from small radii of positive curvature to flat surfaces to small radii of negative curvature or necks assuming the same surface coverage of hydroxyls. Thus, in general, the distribution and percentage of hydrogen bonded hydroxyls depend largely on

curvature. There are three different regions with regard to dehydration. The first region is 180 to 400°C, where physisorbed water which is hydrogen bonded to hydroxyls is removed first, while surface silanol groups condense forming in some cases rings on the surface. Within, the second region, 400 to ≈800°C, irreversible elimination of adjacent hydroxyls results from shrinkage and sintering across pores. From 800°C to full density, viscous flow begins which enables isolated hydroxyls to meet and react to eliminate voids. These are approximate temperature ranges which can be altered depending upon the sintering atmosphere. Halogens have been used extensively for chemical dehydroxylation of the surface and have been combined or alternated with ambient air, desiccated air, oxygen, and helium[113] to produce different modifications of both the structure and surface during heat treatment.

The surface of SiO_2 is not easily rehydrated by simple exposure to the atmosphere or even water vapor, particularly if it has been dehydrated previously at temperatures above 400°C.[92,114-115] This is attributed to the poor affinity for water by the siloxane bridges and to the relatively high stability of the silicon-oxygen bond. However, the form of the silica affects the generality of these broad statements. Silica formed from the sol-gel process has a much larger percentage of two-, three-, and four- membered rings than melt-derived vitreous silica.[116] Studies have shown that the extent of ring strain dictates the kinetics of phyisorption of water and ring opening.[42,117-118] Highly strained two- and three-membered rings rehydroxylate 5 million and 100 times faster respectively, than

does fused silica.[12] However, these rings go through a maximum in concentration between 650°C and 850°C with the final concentration of two- and three-membered rings at higher temperatures being similar to fused silica.[42]

It is evident that the stabilization of the gels is a complicated yet predictable process which enables one to create substantially different morphological structures and surface states. The experimental methods for creating the porous monolith structures used in this research and the subsequent characterization of the pore morphology is presented in the following section.

3.3 Experimental Production of Monoliths

The production of monolithic porous sol-gel silica is a time consuming process. The average number of days involved in producing a batch of approximately 200 cc of sol and converting the 12 samples to porous stabilized monoliths is 9-11 days. This time assumes continuous operations, and the sample number, 12, assumes 100% success through the drying and stabilization steps. Realistically, this process takes two weeks with about an 80% drying success and a 90% stabilization success. More than 50 batches of sols varying in size from 180 cc to 500 cc were prepared to make samples for this investigation. The processing methodology, recipes, and characterization of gels presented in this chapter are for gels which were used in experiments presented in later chapters. Some data is also included to illustrate, the effects of the assorted processing variables.

3.3.1 Processing Methodology

The most important aspects in producing porous sol-gel monoliths are cleanliness, respect for the chemical precursors, and patience. All of the laboratory equipment to be used in mixing the sol should be thoroughly cleaned, and rinsed in deionized water. All casting containers should be new and briefly gassed with dry compressed air to remove any residual particles from manufacturing. Failure to ensure these conditions often results in the loss of part or an entire sol batch. The precursor alkoxides are a health threat and proper precautions must be taken in handling. Also, dry nitrogen should be used to backfill the alkoxide after use if mixing took place under ambient conditions. Figure 3.2 is a flow chart of the processing methods used and can be referred to for clarity through the following description.

A vessel large enough to contain the entire sol was cleaned and placed on a stir plate and filled with deionized water. The acid catalyst was pipetted into the water while being stirred at approximately 200 rpm. If nitric acid and hydrofluoric are both used, the nitric acid was added first followed by the hydrofluoric acid. The solution was allowed to mix for 10 minutes. The amount of TMOS to be used was weighed into a clean graduated cylinder and then slowly added to the stirring acid water solution. A 100 cc of TMOS should be added over approximately 30 seconds. Phase separation was first noted as the TMOS was added. Within seconds of completion of adding the TMOS, the solution becomes homogeneous and the temperature begins to rise to a maximum of 48-53°C. Stirring was

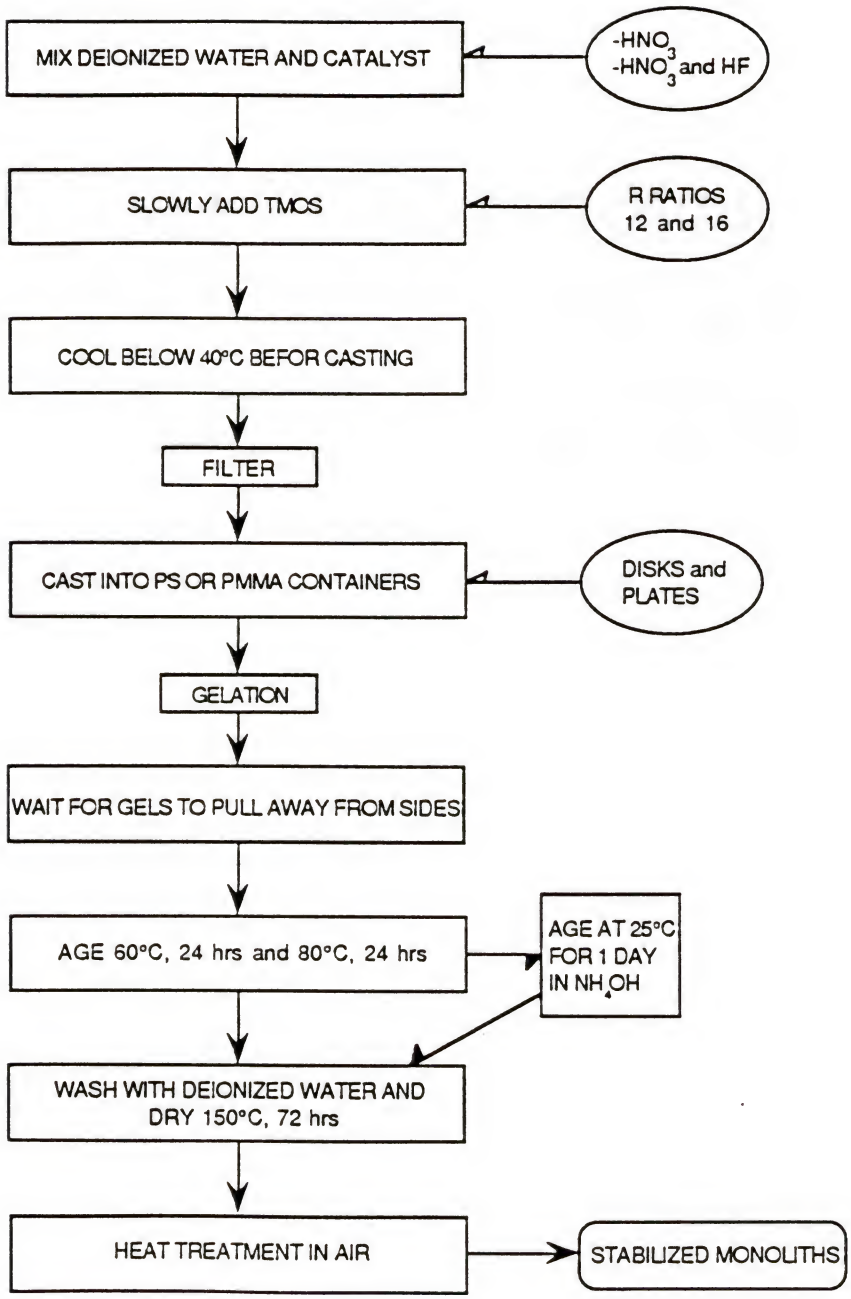

Figure 3.2 This is a process flow chart for creating porous sol-gel silica monoliths with various pore structures.

continued until the sol cools below 40 °C at which time the sol is filtered through a 0.2 micron nylon filter and transferred to a sterile graduated cylinder. A glass pipet is used to transfer approximately 12-15 cc of sol to the plastic airtight molds. One of the samples is monitored by tipping sideways to determine the gel time. Some of the recipes used and their respective gel times are listed in table 3.1.

The gels were kept at room temperature for 2-4 days to allow enough syneresis to take place so that the gels could be more easily removed without damage from the casting containers. Some of the gels were removed at this time and aged in 0.025 N solution of ammonium hydroxide before drying in order to increase their average pore radius.[104] The majority of the gels were first aged at higher temperatures in the original casting containers before transferring to the drying chambers so as to increase their modulus and thus their chances of surviving the large stresses generated at the critical point during drying. The high temperature aging schedule is shown in figure 3.3.

After completion of the aging step the samples were washed with deionized water, carefully transferred to Teflon® drying chambers, and just covered with deionized water. The drying chambers enabled moisture to slowly escape while maintaining the atmosphere close to 100% humidity during drying. The drying schedule is shown in figure 3.3. After drying the gels were stored in an oven at 150 °C.

The samples were stabilized at temperatures between 600 and 1050°C in air in a box furnace. The stabilization schedules are shown in figure 3.4. The gels

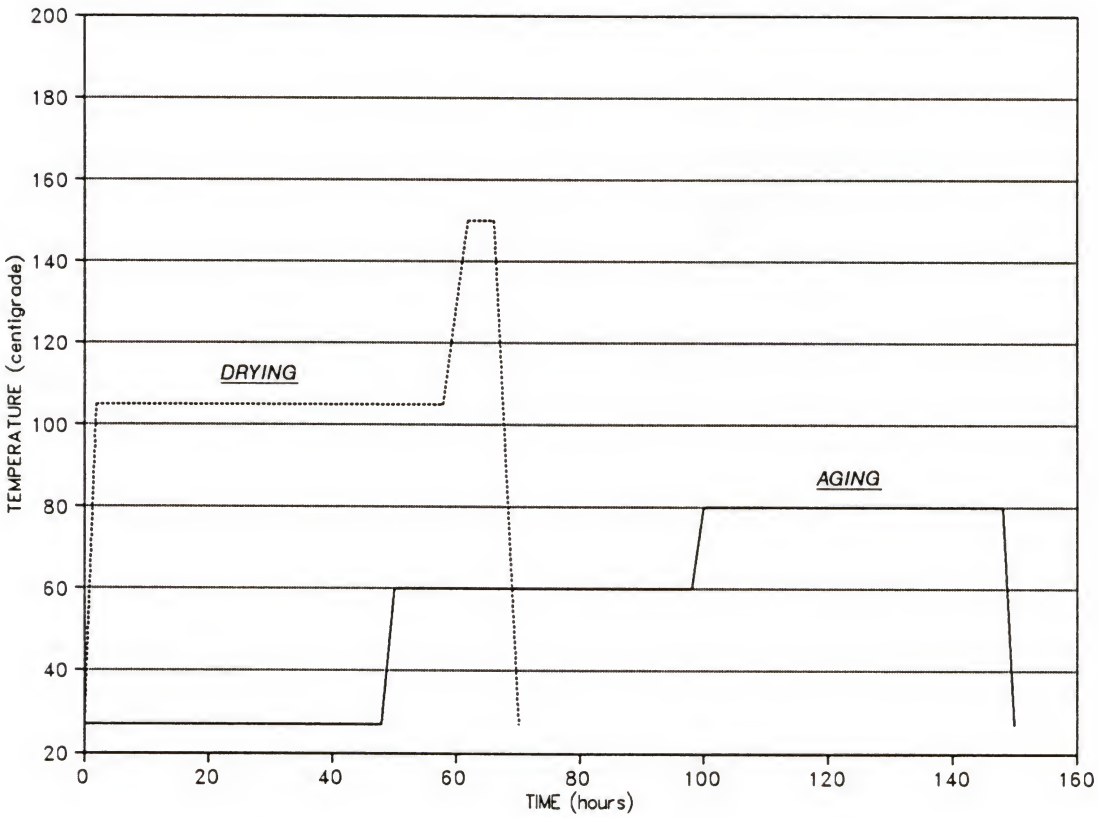

Figure 3.3 Drying and aging schedules for the production of sol-gel silica porous monoliths.

Table 3.1 Recipes for making porous monoliths.

BATCH ID	DI H_2O (m/o)	TMOS (m/o)	12.6 N HNO_3 (m/o)	1.5v/o HF (m/o)	R ratio	Pore Radius (Å)	Gel Time (hours)
46	94.3	5.63	0.036	--	16.8	16	≈120
48	94.2	5.67	0.100	--	16.6	17	≈120
52	93.9	5.84	0.246	--	16.1	16	76
53	94.2	7.68	0.144	--	12.0	14	≈72
10	93.7	5.8	0.490	--	16.2	12	48
40	93.7	5.81	0.490	--	16.1	15	--
50	93.6	6.05	0.338	0.0023	15.5	24	20
49	93.6	5.93	0.505	0.0052	15.8	26	<8
45	93.5	5.96	0.508	0.0159	15.7	27	--
38	93.2	6.30	0.500	0.0275	14.8	29	<6
39	93.2	6.26	0.505	0.0280	14.9	31	<6
37	93.4	6.03	0.510	0.0320	14.9	33	<4
47	93.9	6.04	0.034	0.0161	15.5	36	<1
41	93.5	6.00	0.505	0.0500	15.6	40	0.76
15	93.2	6.19	0.522	0.0551	15.1	61	0.43
21	93.2	6.19	0.522	0.1095	15.1	80	0.21

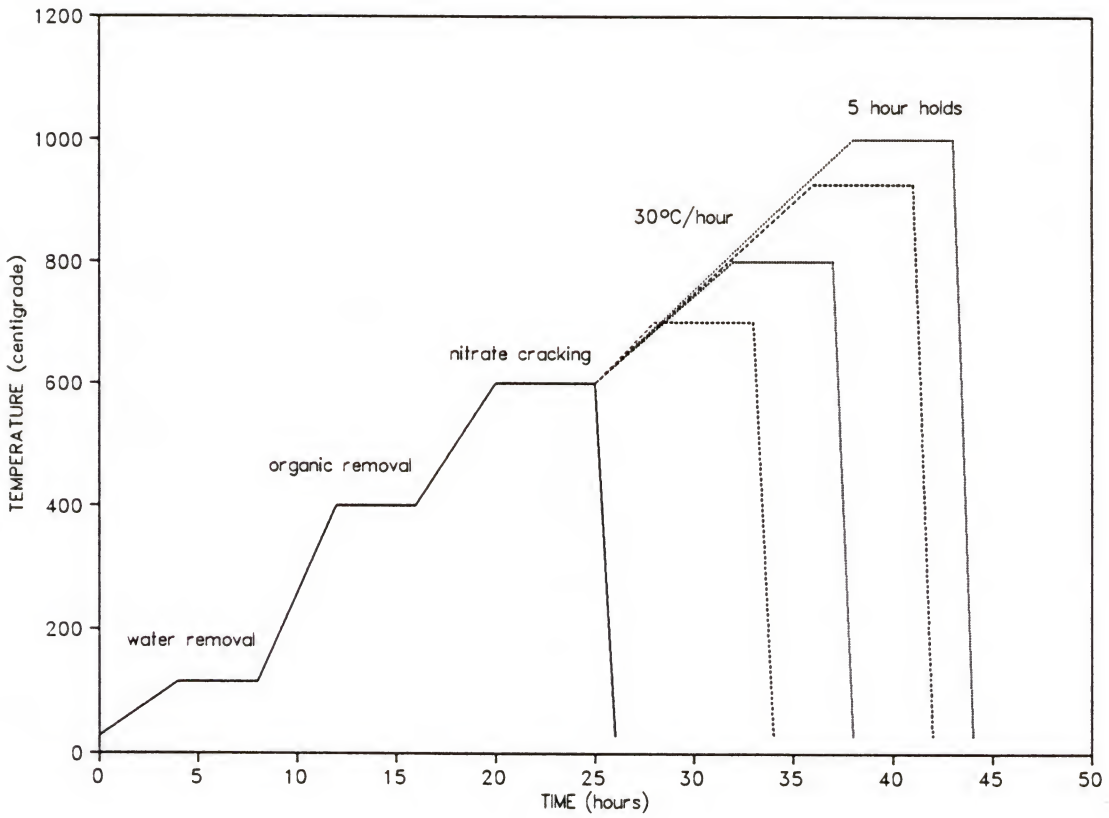

Figure 3.4 Densification schedules for producing different pore characteristics within sol-gel silica monoliths.

were held at 400 °C and 600 °C to ensure the removal of residual organics and nitrates. The heating rate used was typically 30 °C/min. The samples were held at the maximum temperature for 5 hours. After stabilization the furnace cooled to a 150 °C hold so as to minimize moisture exposure. The gels were then transferred to an oven at 150 °C.

3.4 Characterization of Porous Monoliths

The gels pore characteristics were analysed by a nitrogen adsorption method, and the bulk density measured by mercury pycnometry and Archimedes density. Prior to characterization the gels were cut on a diamond saw to remove approximately 20 weight percent of the gel which could be ground into a powder for the nitrogen adsorption analysis. The samples sometimes were slightly warped(as a result of drying stresses) so both sides of the gels were polished at 600 grit with SiC sandpaper to create two flat faces.

3.4.1 Mercury Pycnometry

A 25 cc glass pycnometer was used to measure the bulk volume of the porous monoliths. The pycnometer is a glass container with a ground glass fitting lid which has a small hole to allow the excess fluid inside to escape and therefore the fluid always occupies the same volume. Mercury is used because it will not penetrate into pores of this size at atmospheric pressures. The following procedure was used to measure the geometrical volume and calculate the bulk density of the gels. First, the pycnometer was filled with mercury and weighed.

The lid was removed, the gel placed on top of the mercury, and the lid reinserted forcing out the mercury displaced by the volume of the gel. The pycnometer was then reweighed and the temperature of the mercury was measured. The volume of mercury displaced is equivalent to the bulk volume of the gel. Because the mass of the gel was known, the bulk density of the gel was calculated. This procedure was repeated three times per gel in order to obtain an average density and standard deviation. Table 3.2 summarizes the bulk densities obtained from this procedure.

3.4.2 Archimedes Density

The gravitational force of an object in a fluid balances the buoyant force. That is to say, a body that is submerged in a fluid is buoyed up by a force equal in magnitude to the weight of the displaced fluid. Utilizing this principle, one can determine the bulk volume and thus the bulk density of the gels. The following procedure was used to measure the bulk density of the gels. The dry mass of the gels were noted before the gels were allowed to fill and equilibrate with water. After two days the saturated mass of the gels was measured by removing the gels from the water, wiping off any excess liquid, and weighing. A tiny wire(less than 1% the mass of the gel) was weighed and wrapped around the gel. The gel was then suspended in water from the scale. This enabled the measurement of the suspended weight. The bulk volume, bulk density, and volume fraction of pores were calculated from the dry, saturated, and suspended weights. These values are reported in table 3.2.

Table 3.2 Gel characteristics as determined from mercury pyncnometry and Archimedes density measurements.

SAMPLE ID	Pore Radius (Å)	ρ_b Hg (gm/cc)	vol_b Hg (cc)	ρ_b H_2O (gm/cc)	vol_b H_2O (cc)
df1	12.3	1.45	0.95	1.53	0.94
df2	14.6	1.49	0.98	1.48	0.98
df3	13.8	1.49	0.96	1.54	0.95
df4	15.1	1.45	0.83	1.75	0.71
df13	18.0	1.38	0.97	1.40	0.87
df14	16.5	1.45	0.83	1.45	0.73
df15	16.9	1.43	0.83	1.47	0.73
df27	12.0	1.57	0.58	1.64	0.56
df32	13.8	1.55	0.94	1.58	0.93
df41	90.0	0.68	1.14	0.69	1.13
df45	38.4	0.89	1.21	0.89	1.19
df47	38.0	0.91	0.71	0.93	0.69
df57	46.8	0.87	0.94	0.90	0.92
df62	34.8	1.0	0.88	1.05	0.84
df73	11.9	1.42	0.57	1.46	0.55
df74	12.0	1.46	0.8	1.47	0.80
df80	95.0	0.77	1.4	0.77	1.39
df81	94.2	0.75	1.23	0.76	1.21
df82	95.3	0.74	1.8	0.75	1.79

3.4.3 Nitrogen Adsorption

The piece of glass which was cut from the monolith was ground in a mortar with a pestle. The glass powder was then loaded into a glass cell and outgassed at 150 °C under vacuum overnight. The nitrogen adsorption/desorption measurements were performed by an Autosorb-6 manufactured by Quantachrome. The total number of points taken varied from sample to sample but was always more than 40. Average pore radii, pore volumes, surface areas, and pore size distributions are all calculated by the software using the Brunauer, Emmett, and Teller(BET) theory. The reader is referred to an excellent reference by Sing and Gregg[119] for the theory of BET. Typical pore characteristics which include the pore-size distributions, isotherms, pore radii, surface area, and pore volume are presented in figures 3.5-3.10.

3.5 Water Percolation Into Porous Monoliths

3.5.1 Introduction

Prior to the diffusing of salt solutions into the porous monoliths the pores were filled with deionized water which had been adjusted in pH with nitric acid. All of the salts in the study were nitrate salts, and hence adjusting the water with nitric acid did not introduce other anions into the system. This step of filling the gels with water enabled the measurement of the rate at which the water spontaneously imbibed into the gels. The goal was that a comparison between the rate in which

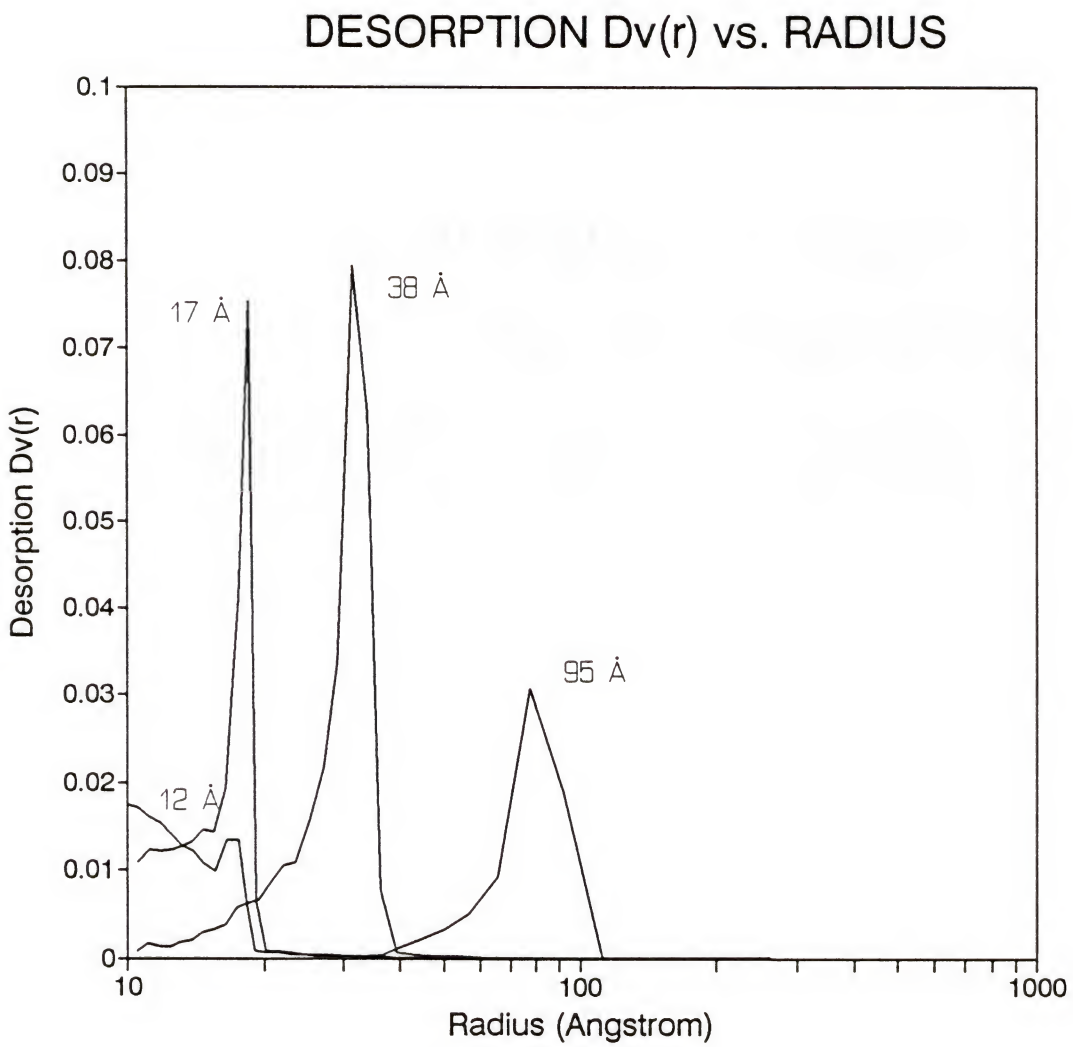

Figure 3.5 Pore size distribution for various sol-gel silica monoliths.

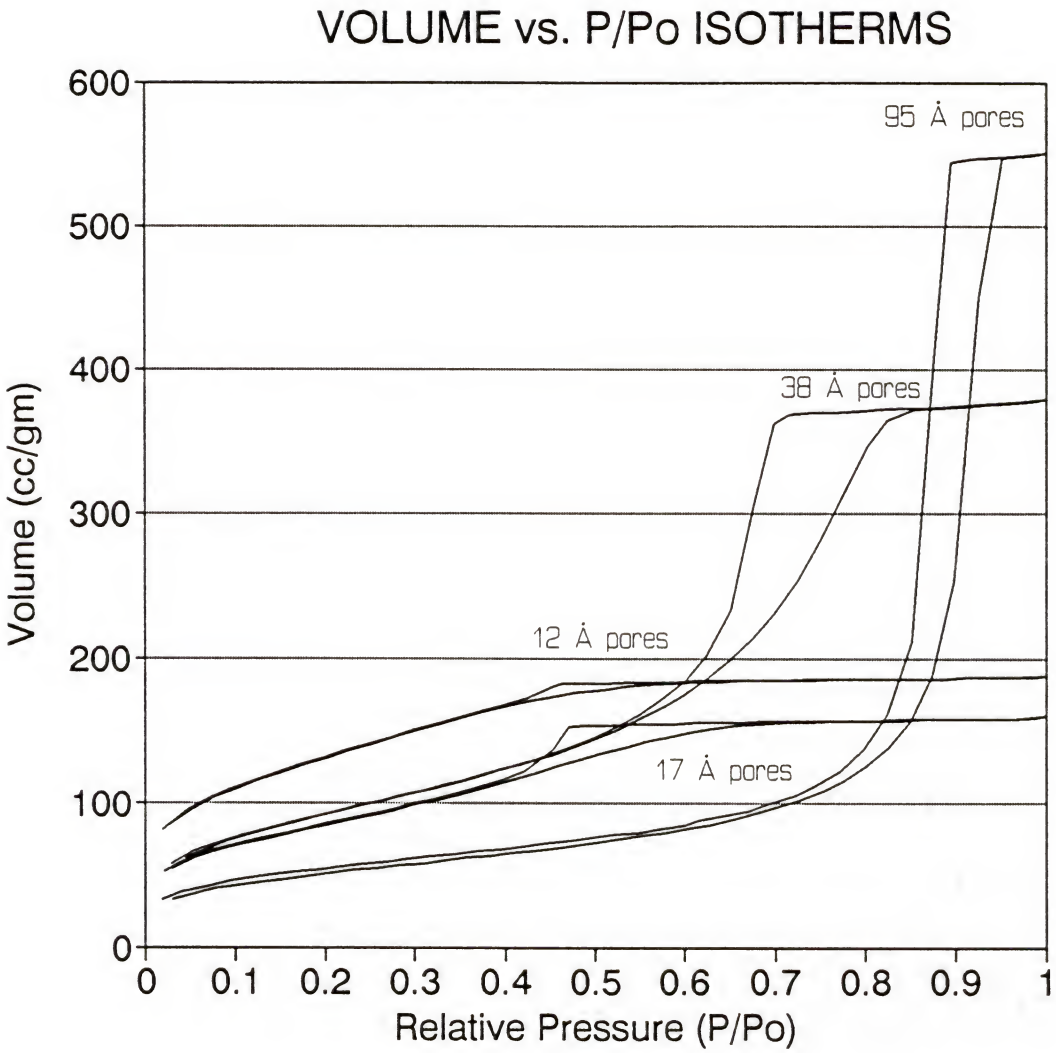

Figure 3.6 Nitrogen adsorption/desorption isotherms for gel silica matrices with different average pore radii.

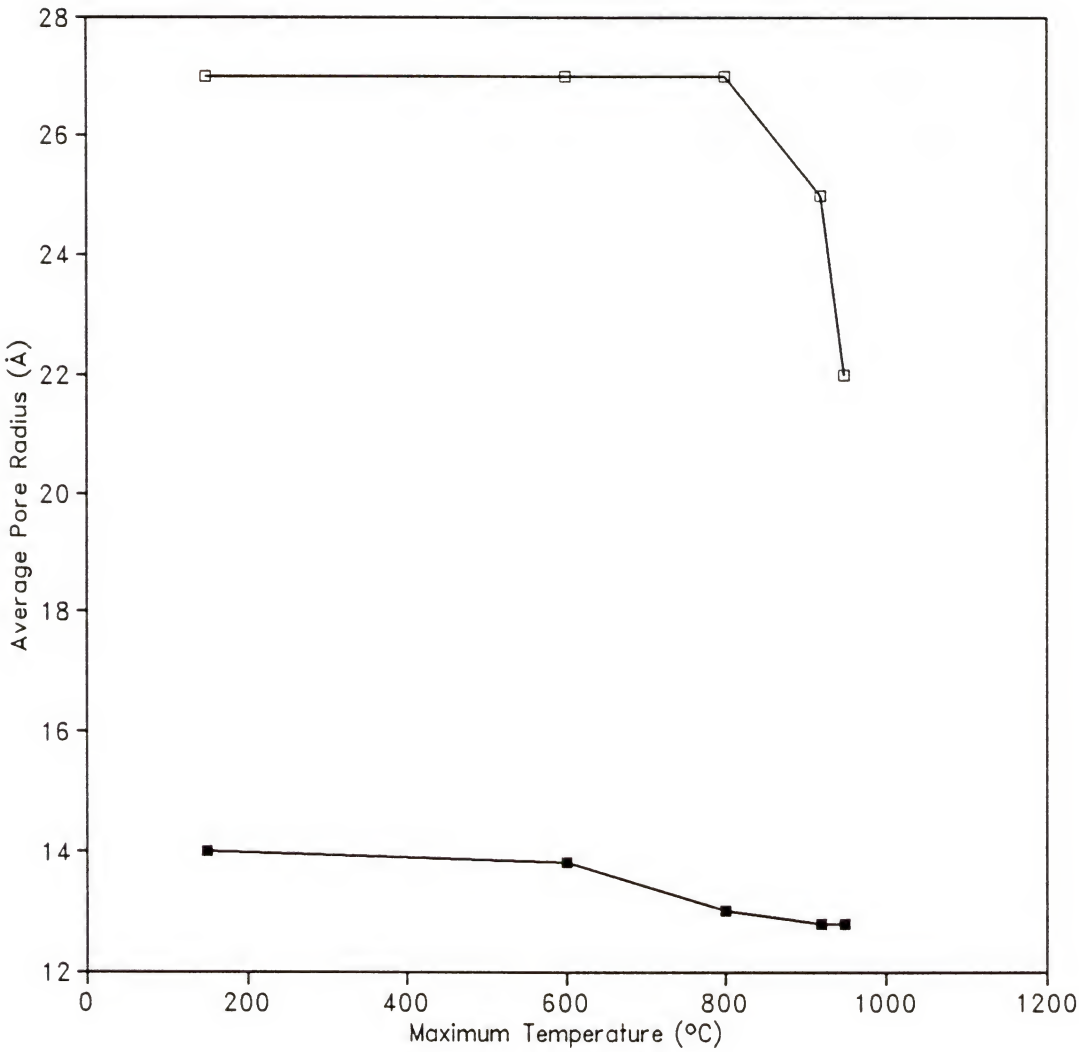

Figure 3.7 The change in average pore radius for the 27 Å and 14 Å gels as a function of heat treatment temperature.

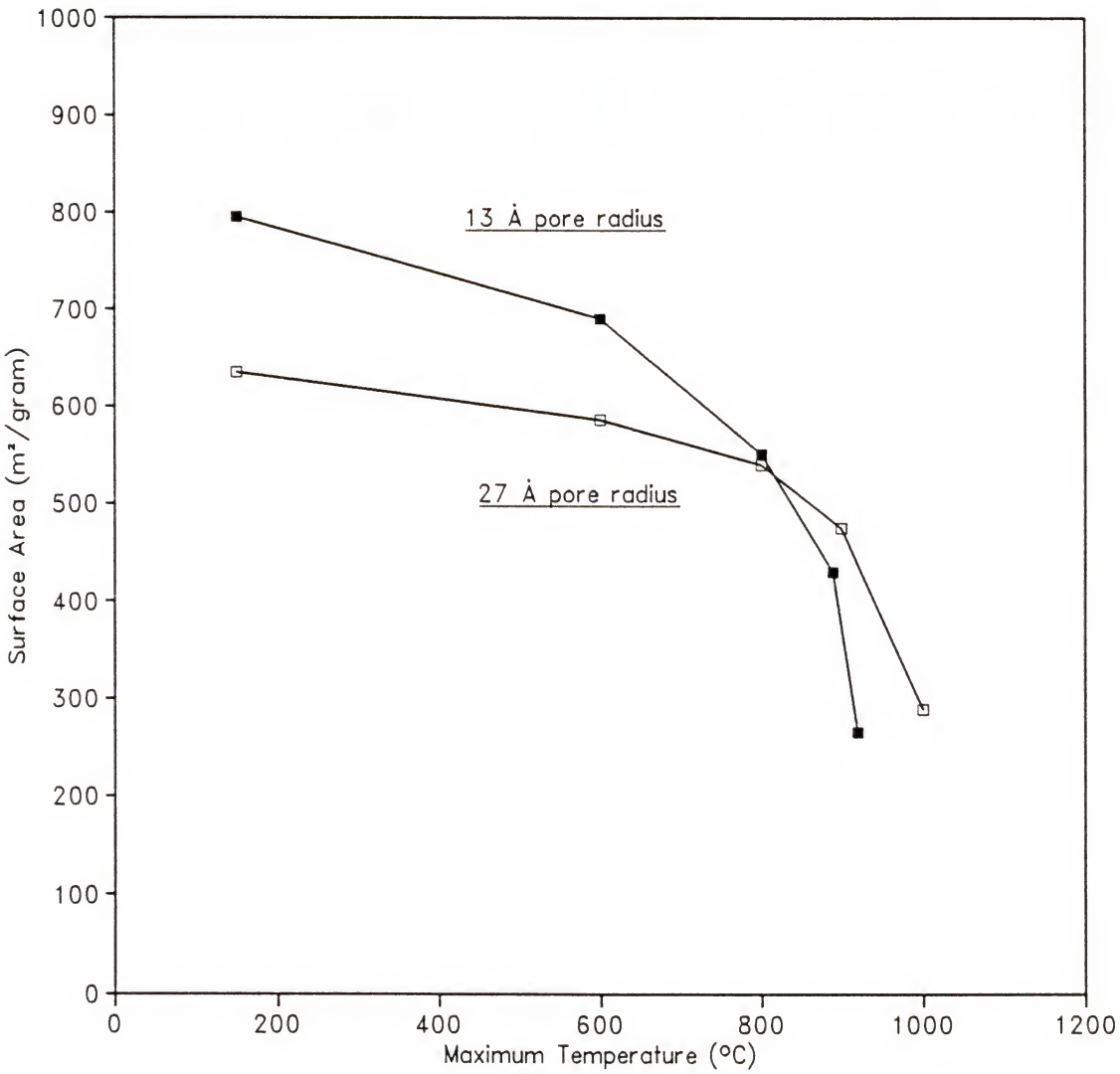

Figure 3.8 The change in surface area as a function of heat treatment temperature for 14 Å and 27 Å average pore radius gels.

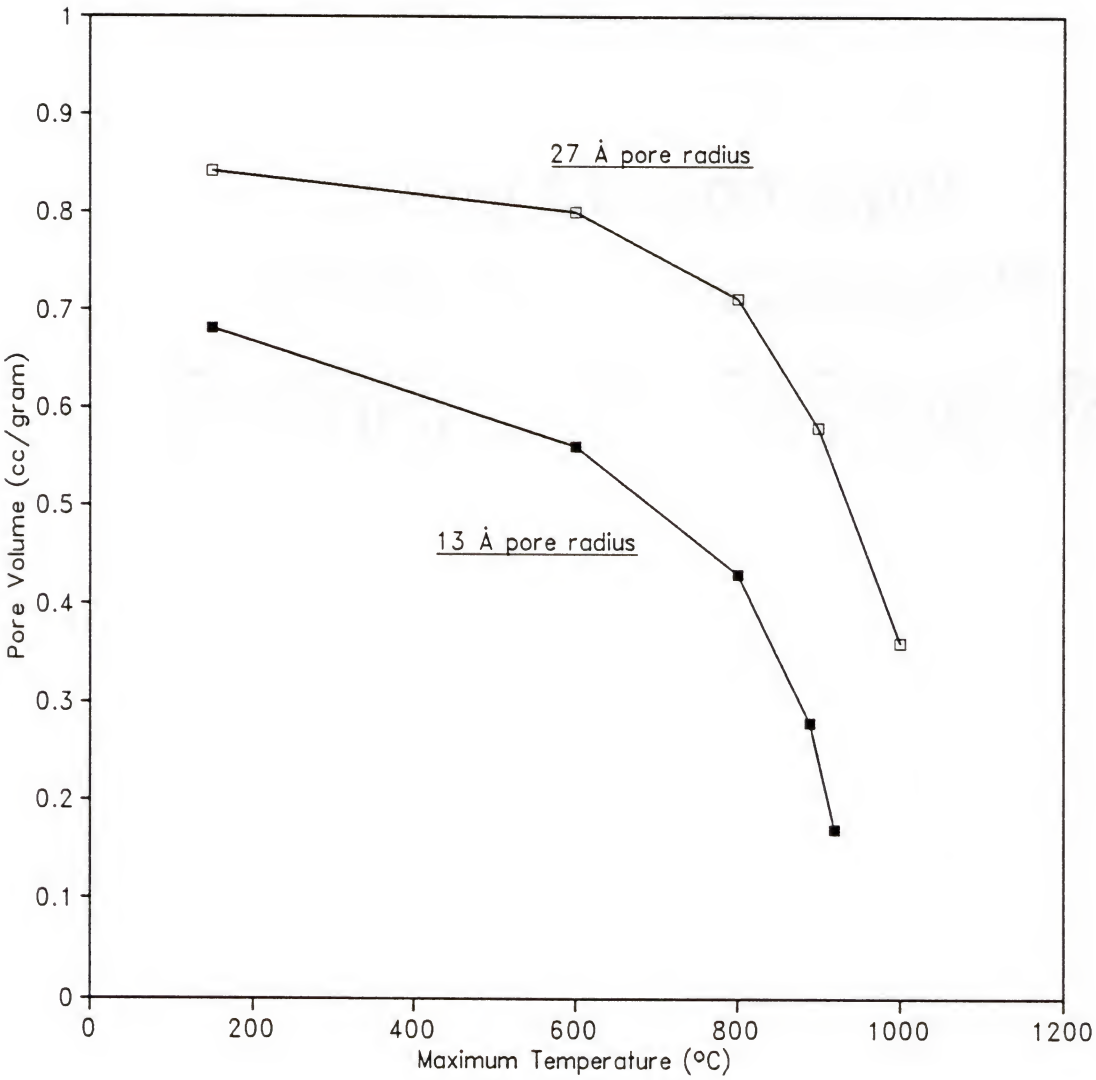

Figure 3.9 The change in pore volume as a function of heat treatment temperature in air for 14 Å and 27 Å average pore radius gels.

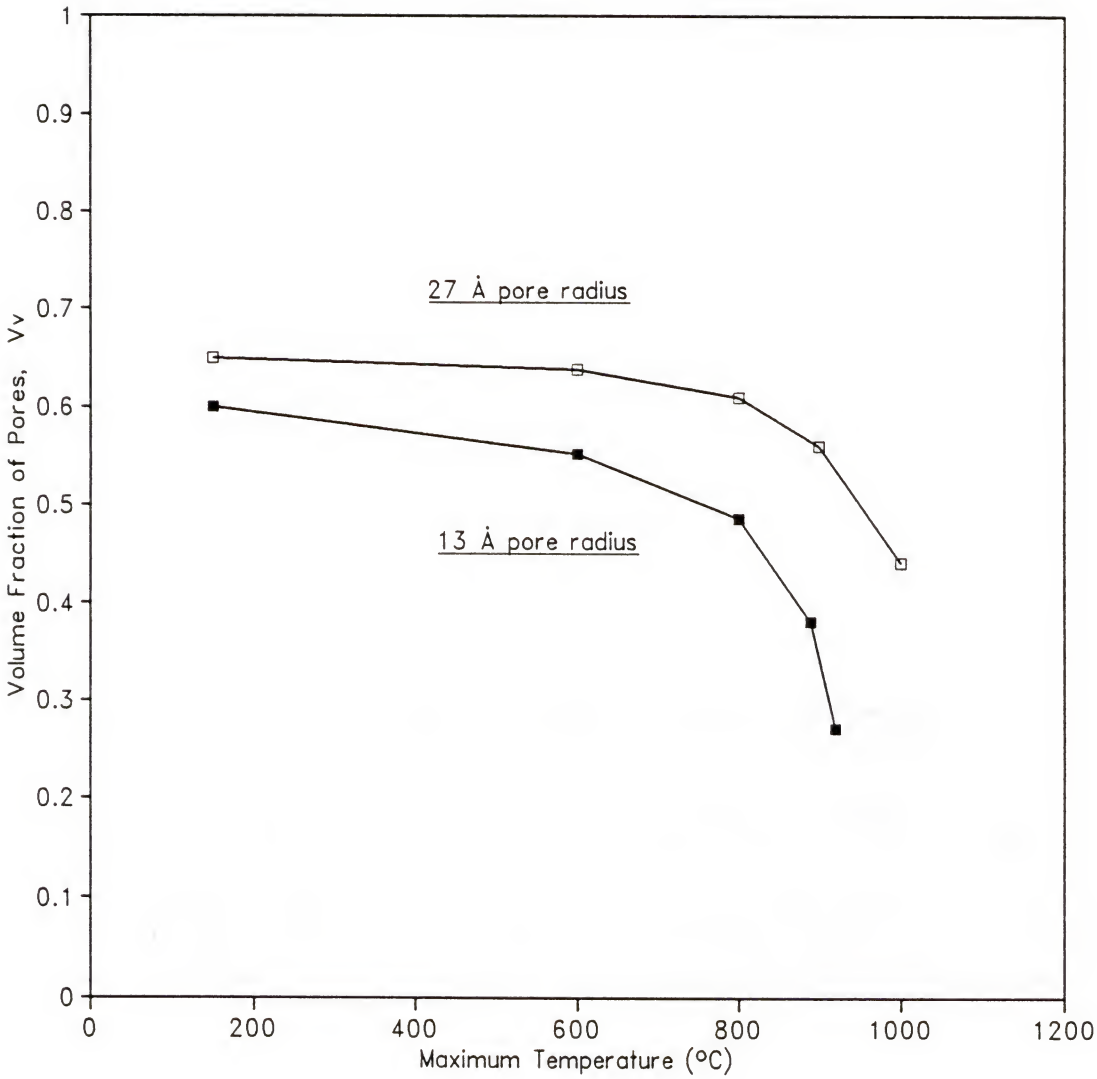

Figure 3.10 The change in volume fraction of porosity in two different pore radius gels as a function of heat treatment temperature in air.

the gels filled could be correlated with the diffusion coefficent. Theoretically the rate of filling should be a function of the pore size and pore structure.

The transport of fluids through porous rock,[120-122] powder compacts,[123] porous Vycor®,[124,125] and sol-gel silica[126] has been studied by many authors. Also, computer models[127-128] of percolation processes for different geometrical representations of porous media has been extensively calculated. These studies confirm the compliance of flow in small pore structures to a Poiseuille type flow and D'Arcy's law[129,130] is obeyed for a wide range of fluid viscosities. Most of this literature relates the flow characteristics of a wide range of fluids to a specific permeability which is a function of the volume fraction of porosity and surface area of material.

It is the aim of this work to determine an empirical characteristic constant which can be used to compare the rate of filling of the gel to a topological model[131] predicting the connectivity of the gel. The interconnectivity as predicted by the topological models should be related to not only the imbibing rate of water but to the diffusion coefficients measured in chapter 5 as well. The penetration of water into these porous sol-gel monoliths was fit both theoretically and empirically. In addition, a minimum bulk density was determined as a function of pore size which serves as the lower limit for gels to be rehydrated and remain monolithic.

3.5.2 Experimental Results

3.5.2.1 Methods

The monolithic plates as prepared above were outgassed in an oven at 150 °C overnight. Each sample was removed one at a time from the oven and its dry mass was recorded. The monolith was then put in a specially designed airtight container which was capable of being purged with different gases. All samples were purged in extra pure helium for 15 minutes to allow the sample to cool to room temperature and then reweighed. The weight on average changed less than one percent so it was assumed that very little water was adsorbed during the mass measurements and purging.

The gel sample was then removed from the purge container and dropped into approximately 25 cc of water. The pH of the water was altered using very small amounts of concentrated nitric acid. There was no detectable density change due to the small additions of acid and it was assumed that all the water solutions ranging in pH from 0.9 to 5.5 have essentially the same viscosity and wetting behavior. The sample was removed from the water at various time intervals, the surface wiped dry, the weight recorded in less than 20 secs, and then returned to the water. Several experiments were done in which the time intervals were varied to inspect the possible influence of removing the gel from the water upon the penetration rate. No change was noted in the penetration rate even when the intervals between weight measurements varied from 0.5 to 5 minutes.

The temperature of the water was recorded in order to determine a density for the water. This density was then used to convert the change in gel mass with time, to a volumetric flow rate. The geometrical size(height, width and thickness) of the gel was measured with digital calipers accurate to 0.01 mm. The geometrical surface area of each gel could then be calculated. The gels length and width were approximately 5 to 7 times longer than the gel was thick. It was assumed that a majority of the flow occurred on the two faces.

3.5.2.2 Cracking versus bulk density

It was seen that some of the gels would crack within a minute of being immersed in the water. The bulk density versus pore radius of the gels that cracked is plotted in figure 3.11. Also plotted on the secondary y-axis is the inverse of the average pore radius. As discussed in the introduction of this chapter, the pressure generated within the pores is governed by the Gibbs-Kelvin equation which predicts the pressure in the pores to be inversely related to the pore size. The pressure in atmospheres across the curved interface can be calculated if we assume the interfacial tension for water is 72 dynes/cm and the curvature is $2/r_p$ for cylindrical pores. The pressure generated within the pores and the bulk density are plotted in figure 3.12 versus the pore radius. The pressure generated within the pore and the inverse of the volume fraction of the is plotted versus the pore radius in figure 3.13. These plots indicate that the fracturing of the porous monoliths is a function of both volume fraction of pores

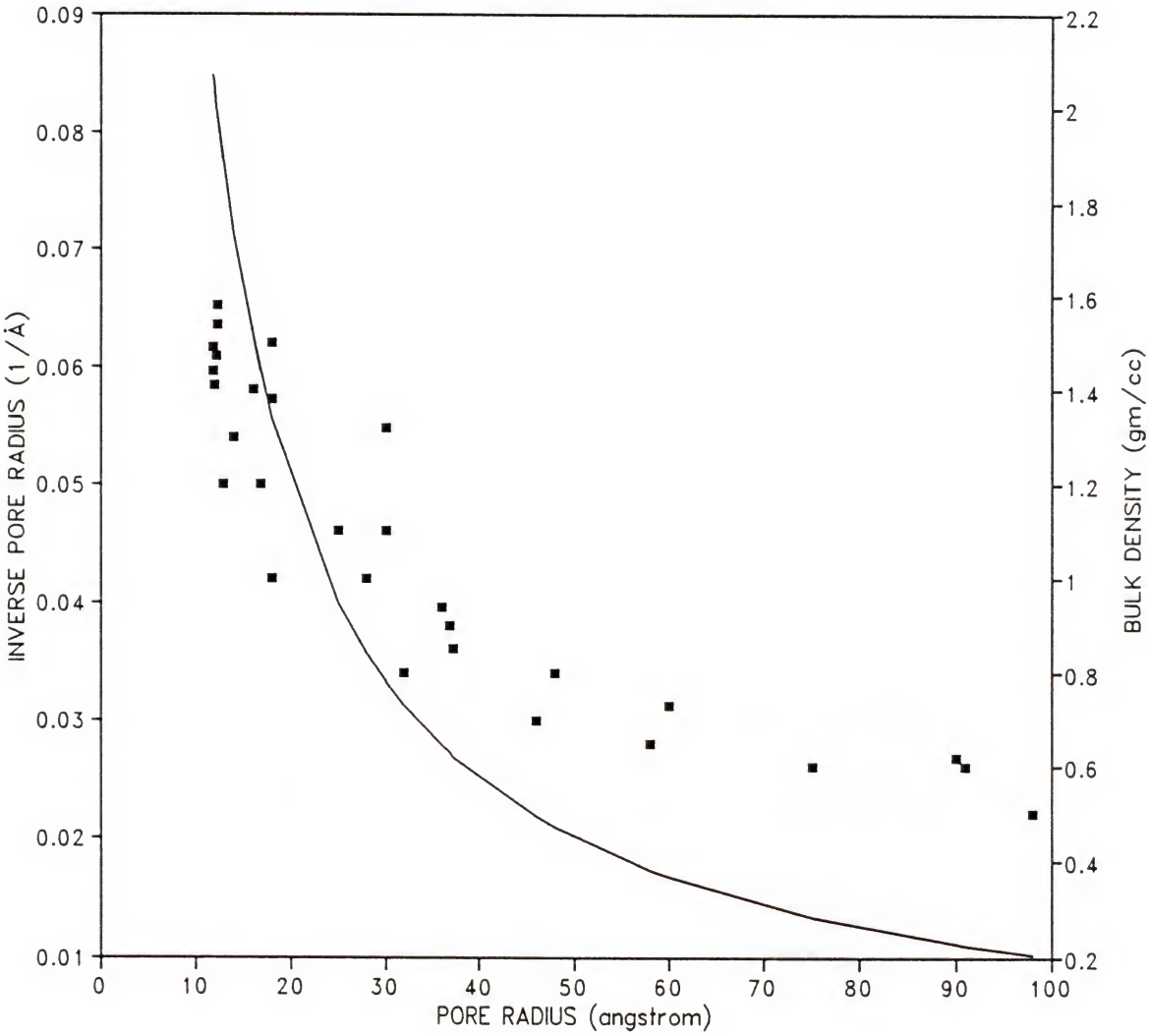

Figure 3.11 The points are monolithic gels which broke for each bulk density and pore radius. The solid line is a plot of the inverse pore radius versus pore radius.

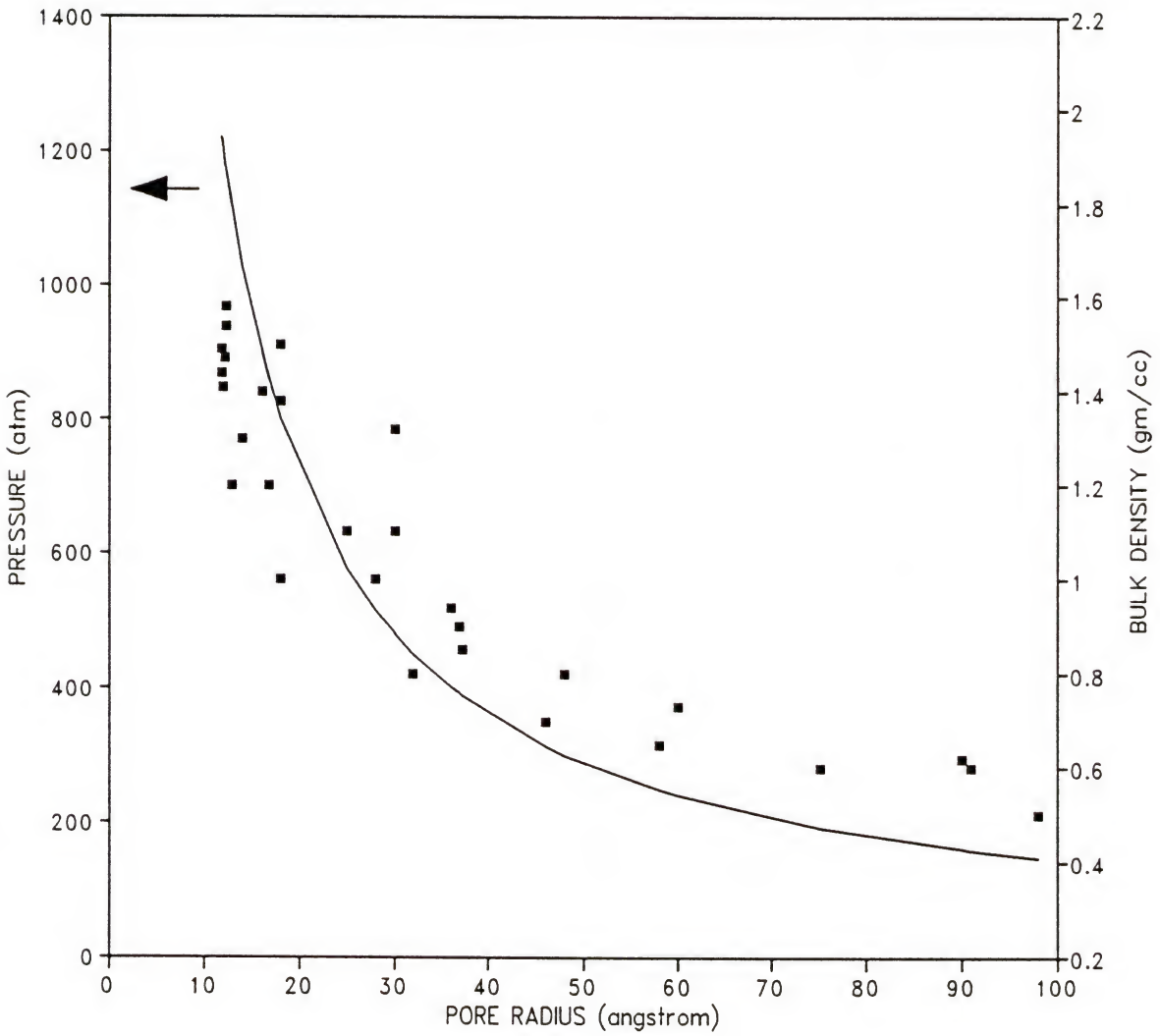

Figure 3.12 The points are monolithic gels which broke for each bulk density and pore radius. The solid line is a plot of the pressure generated within the pores assuming a surface tension of 72 dynes per cm for water versus the average pore radius.

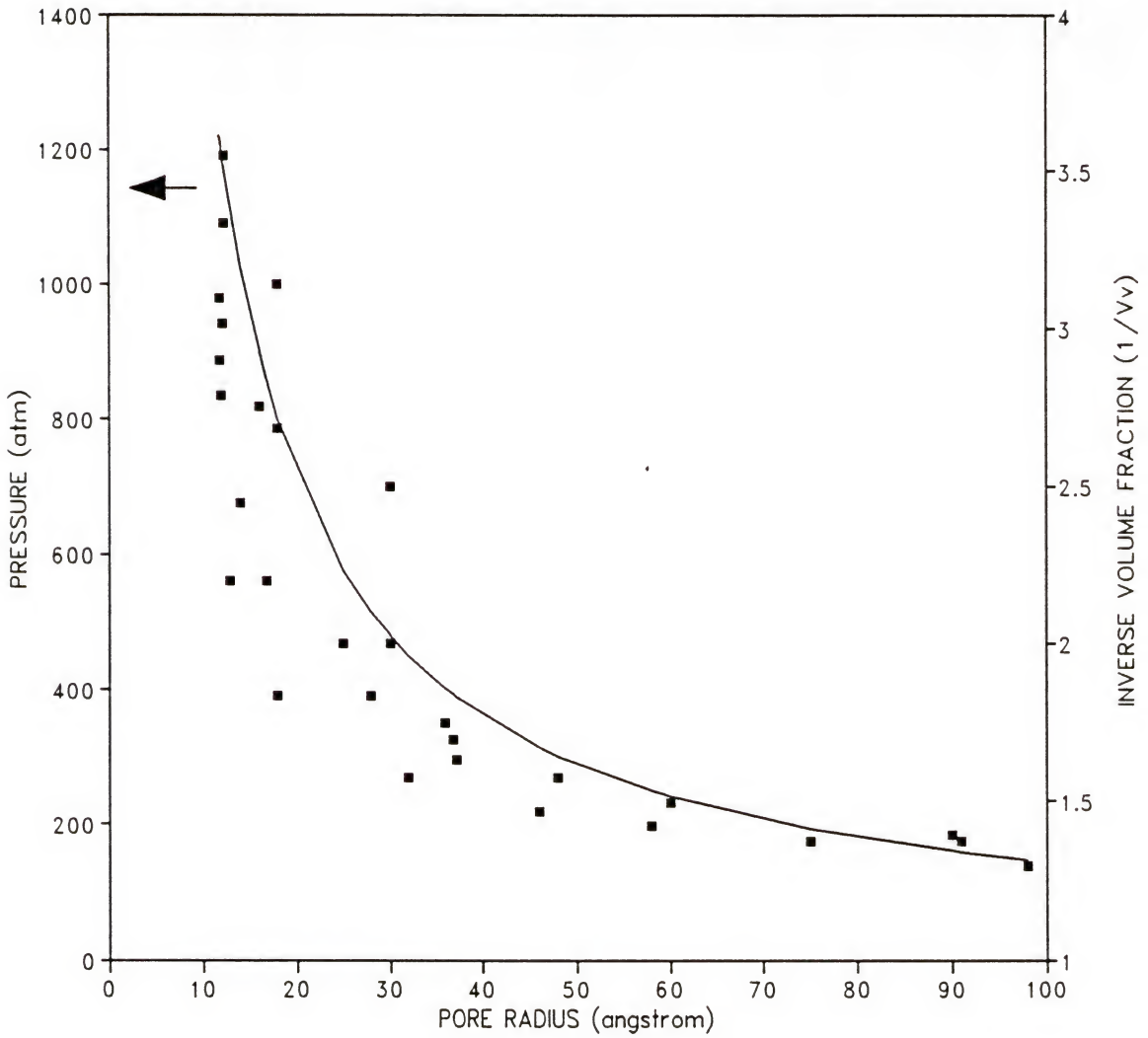

Figure 3.13 The points on the plot are monoliths which cracked upon being immersed in water. The solid line is a plot of the pressure generated within the pores assuming a surface tension of 72 dynes per cm for water versus the average pore radius.

and the pore size. At a constant average pore radius of 12.5 Å cracking occured for pores with a volume fraction of pores from 0.28 to 0.45. At a constant volume fraction of pores, 0.32 and 0.65, the average pore radius of the cracked samples varied from 12Å to 18Å and 32Å to 60Å, respectively. The pressure across the capillaries varies from 1200-800 atm and 450-250 atm for this range of pore sizes.

Kendall[130] attempted to determine whether the dominant factor describing the strength of porous Vycor® was the volume of pores or the longest pore (viewed as a crack length). The results of his three-point bending tests indicated that at a given volume fraction strength fits the Griffith behavior, meaning the longer the induced notch, the lower the strength for a given volume fraction. He concluded that the volume fraction of fine pores provides the porosity to reduce the elastic modulus whereas the induced notch initiated fracture.

The results from the current study can not distinguish between the effects of the pore size and the volume fraction of pores on the cracking of the gels because the stress is generated by the pore size. Although it appears that for a constant pore radius(constant stress) the samples cracked for a range of volume fraction of pores, the samples probably crack because they are all too weak to withstand the large pressures. It also appears that the larger pore gels break at higher relative bulk densities than the smaller pore gels as indicated by the larger deviation from the pressure versus pore radius curve in figure 3.12 at large pore radii. The microhardness of the gels increases as the pore size and the volume fraction decreases.[1] This could indicate a larger flaw size was created during the

mechanical cutting or polishing for these larger pore gels since all of the samples were cut and polished under the same conditions. The surface of the gels as viewed through a light microscope indeed indicates, qualitatively, that there is some evidence of an increase in pitting of the surface with increasing pore size.

In conclusion, the general trend for the stability of the gels to immersion in a fluid is shown in figure 3.12 but might also be shifted along the y-axis depending upon the surface preparation and the surface tension of the fluid penetrating into the gel. The trend is useful for determining a minimum bulk density that must be achieved for a specific impregnation under the sample preparation conditions of this study. Also, if the polishing of the samples can be eliminated from the processing higher volume fractions of porosity may be used. These conclusions are helpful in designing environmental sensors. The response time for the sensing of a contaminante may be reduced by directly submerging the initially void sensor into the groundwater. The contaminated groundwater penetration rate would be similar to the times found in this study.

3.5.2.3 Penetration kinetics into porous sol-gel monoliths

The measurement of the volumetric flow rate into gels of various average pore radii was described in the methods section above. This volumetric flow rate can be converted to a penetration distance with time if one assumes that the majority of the water enters through the faces of the plates and divides the volumetric flow rate by the surface area of these two faces. The area of the sides of the plates averaged less than 15% of the total area so the approximation

provides a reasonable penetration thickness. The first data point taken includes water which has come in on all faces of the plate and thus over estimates the penetration distance. Also, at long times the gel filling rate levels off as the water continues to compress the trapped volume of air. The analysis of the plots is done for short times after the first point. Figure 3.14 is a plot of the normalized penetration thickness versus time for a range of pore sizes. The Rideal[131]-Washburn[132] equation (3.2) describes the rate of liquid penetration into pore channels.

$$\frac{dL}{dt} = \frac{r\gamma_{lv}\cos\theta}{4\eta L} \qquad (3.2)$$

After integration,

$$L = \sqrt{\frac{r\gamma_{lv}\cos\theta\, t}{2\eta}} \qquad (3.3)$$

where, L (cm) is the distance penetrated in time, t (sec), r (cm) is the pore radius, γ_{lv} is the liquid-vapor interfacial energy, Θ is wetting angle, and η is the liquid viscosity. This equation indicates that the distance of penetration is proportional to the square root of time and the pore radius. The data for penetration into the porous monoliths of this work is plotted versus the square root of time in figure 3.15. The graph displays a linear region over which the slope is proportional to the pore radius. The data can also be plotted versus the square root of time and

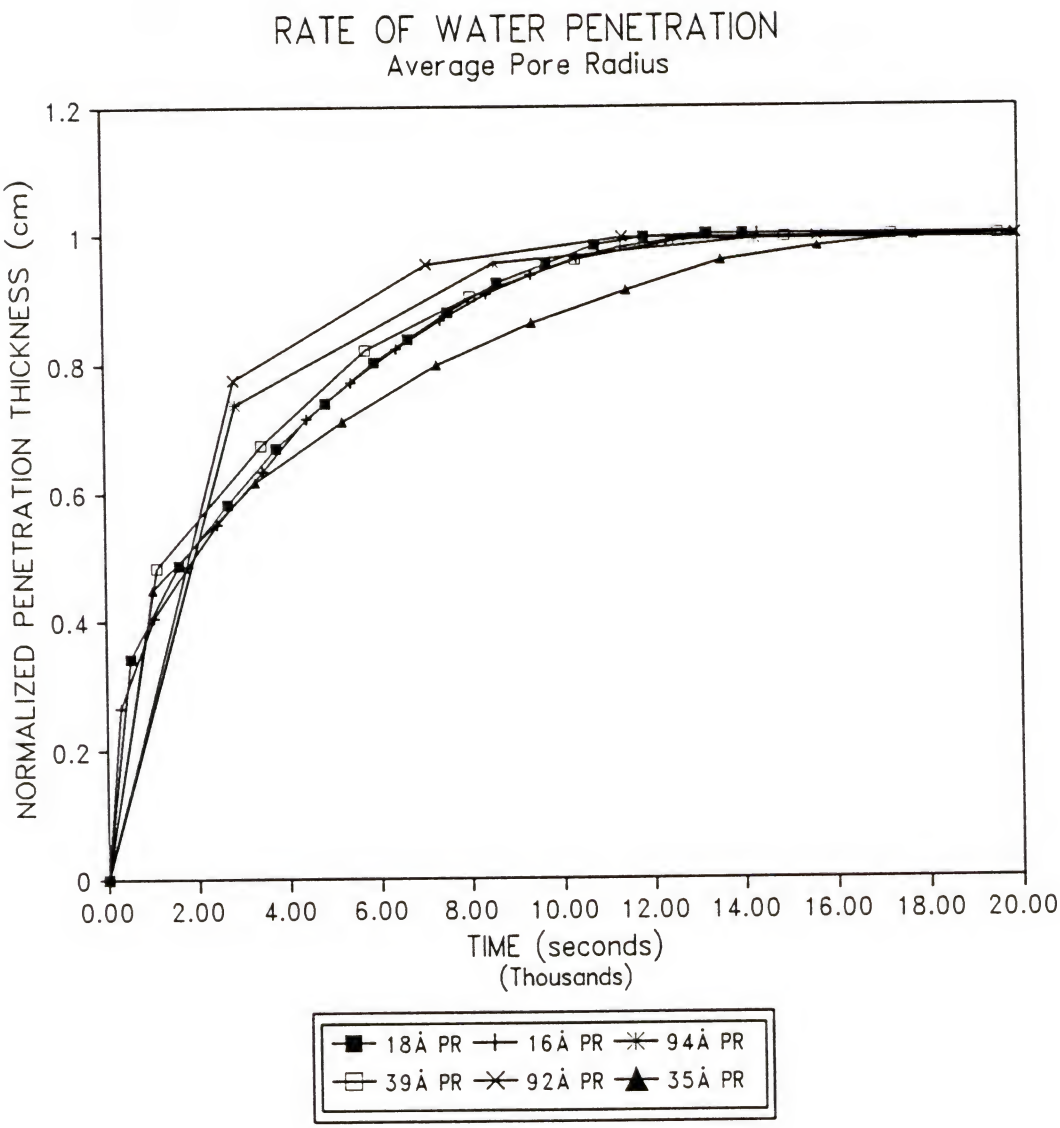

Figure 3.14 A plot of normalized penetration thickness versus time for different average pore radii sol-gel silica monoliths.

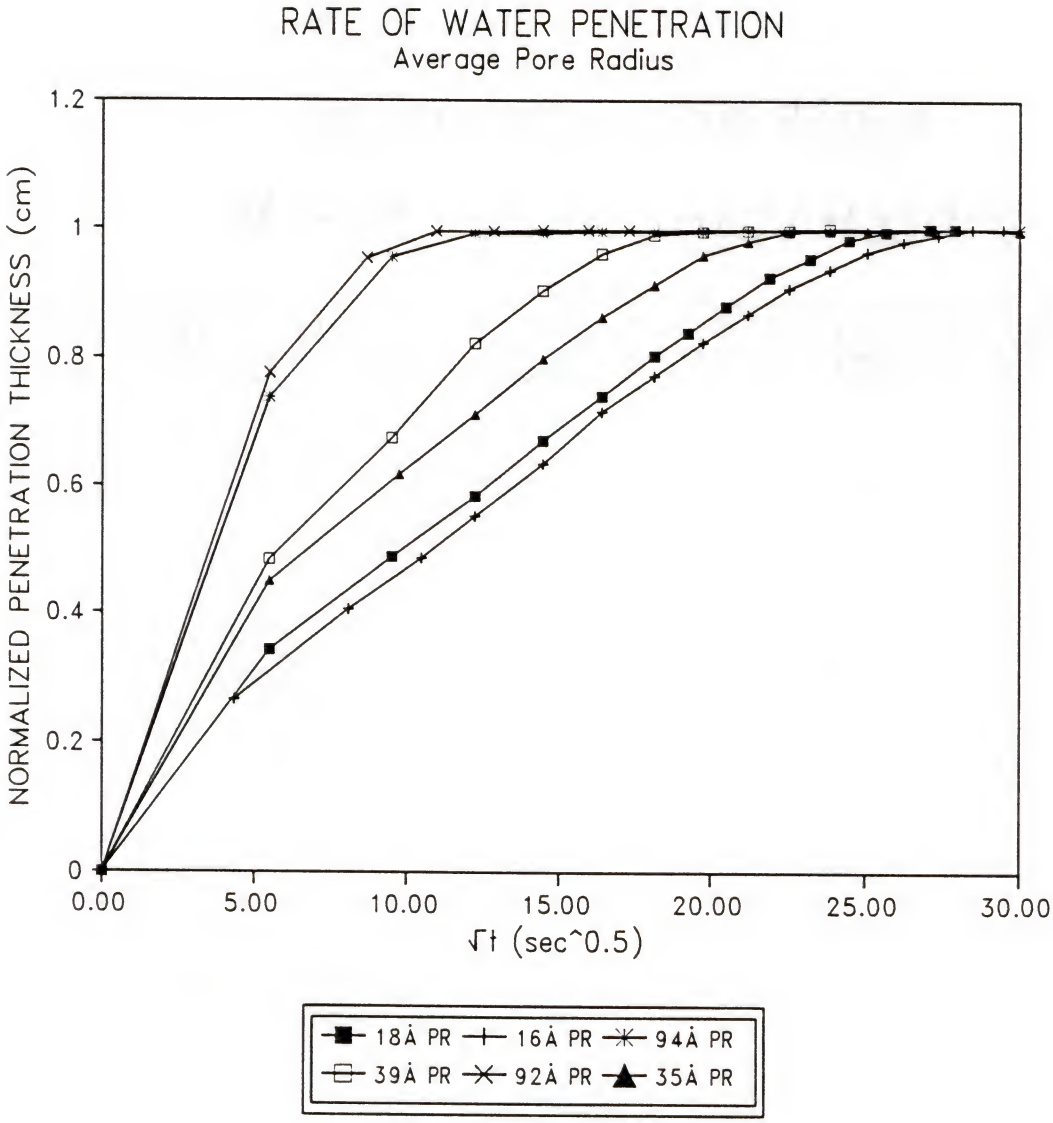

Figure 3.15 A plot of normalized penetration thickness versus the square root of time for different average pore radii sol-gel silica monoliths.

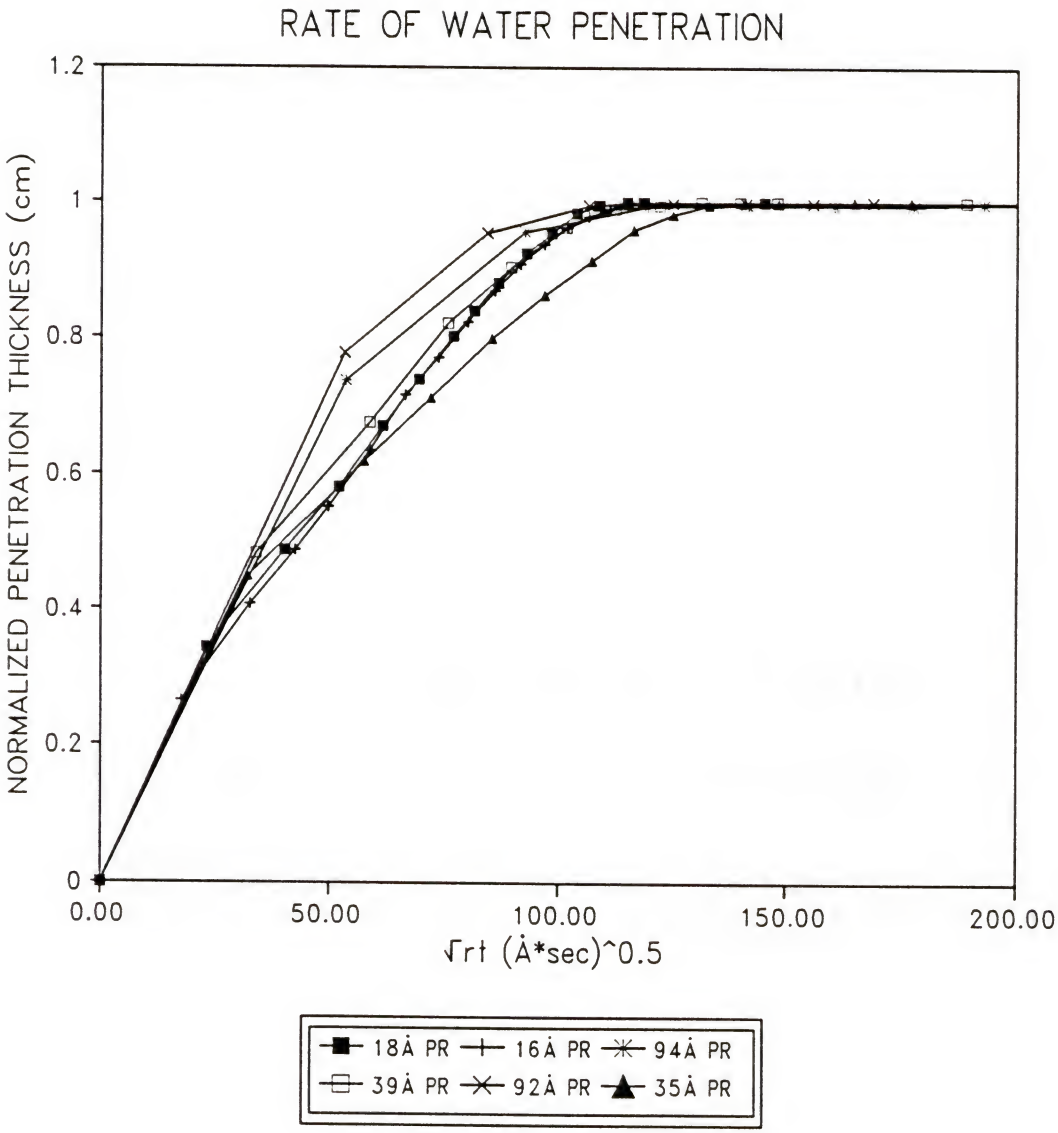

Figure 3.16 A plot of normalized penetration thickness versus the square root of time and the square root of the radius for different average pore radii sol-gel silica monoliths.

pore radius, as in figure 3.16. This indicates that for short times equation 3 is a good fit for the data within experimental error. The data was also fit empirically to,

$$\frac{L}{L_o} = 1 - e^{-kt} \tag{3.4}$$

where L (cm) is the distance penetrated at time t (sec), L_o (cm) is the saturation value, and k (1/sec) is a characteristic constant. This can be rewritten as,

$$-\ln\left[1 - \frac{L}{L_o}\right] = kt \tag{3.5}$$

The left hand side of equation 3.5 plotted versus t should display linearity with a slope of k which is proportional to the rate of filling. A table of the regression analysis for short times is shown in table 3.3 and the graph is shown in figure 3.17. The purpose of plotting an empirical equation independent of r is to determine a constant, k, which can be used independently to compare the rate of filling. The value of k is plotted versus pore radius and volume fraction of pores in figure 3.18. The plot indicates a linear relationship between r and k as already predicted from equation 3.2, and a nonlinear relationship for volume fractionof porosity. The pore size dominates over the volume fraction of porosity as a controlling factor in the filling kinetics of these porous materials. Another way of illustrating the same point is by applying a topological model, which uses porosity and surface area

Table 3.3 Regression analysis of the linear portion of the plots in figure 3.17.

Pore Radius (Å)	x coeff or k	error in x coeff	R^2
16	0.00369	7.11E-5	0.998
18	0.00333	4.26E-5	0.999
35	0.00950	4.48E-4	0.995
38	0.01406	1.11E-3	0.993
92	0.04193	3.71E-3	0.992
94	0.03559	3.24E-3	0.992

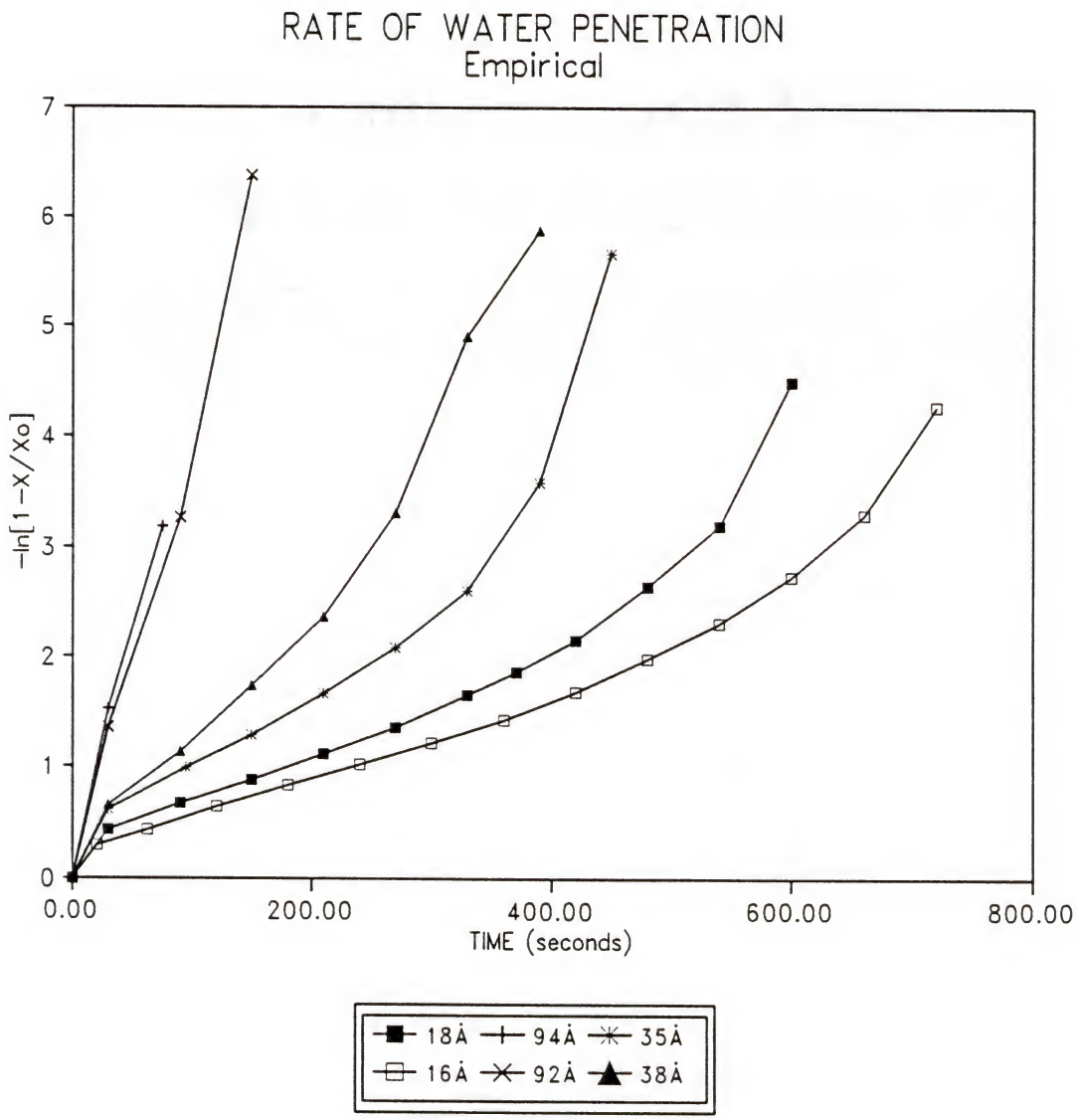

Figure 3.17 A plot of equation 3.5 such that the slope at small times is equal to the characteristic constant, k.

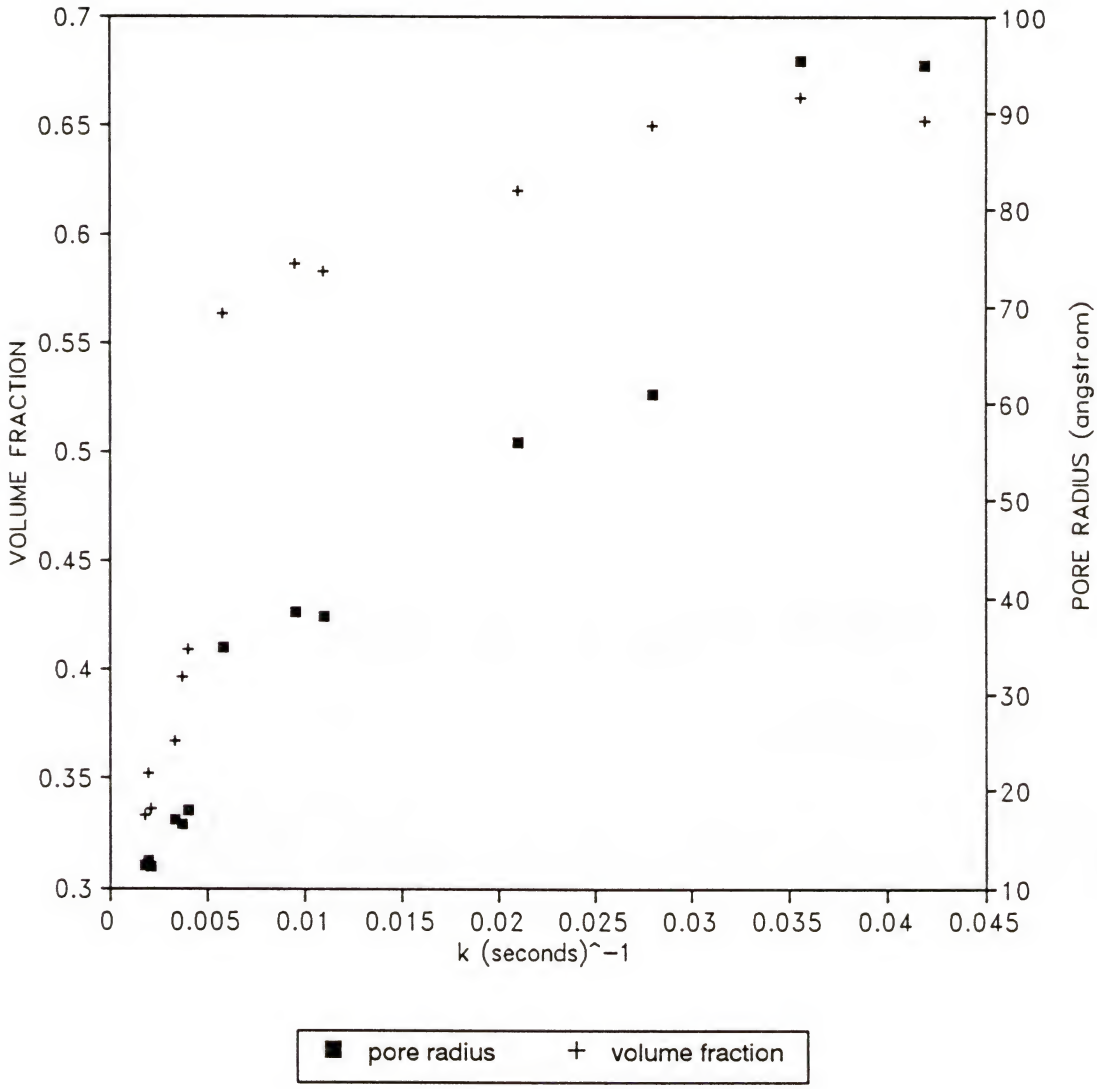

Figure 3.18 A plot of the relationships between the characteristic constant, k, from equation 3.5, and the volume fraction and average pore radius of the monoliths.

measurements as determined by nitrogen adsorption (BET), to determine the connectivity of the gel and to compare this to the rate of filling or k. Vasconceloas[133] applied 12 topological models to porous sol-gel monoliths in order to characterize the relationship between mechanical properties of the gels and the topological parameters, genus and number of branches. Model 12, based upon a cylindrical pore model, showed the best fit to his data and was used to calculate the number of branches for the gels in this study. In general, model 12 predicts the number of nodes to be half the number of branches and therefore the number of branches in his model can be used as a measure of the interconnectivity of the gel pore network. A plot of the number of branches per unit volume is plotted versus the characteristic constant, k in figure 3.19. It is not surprising that the relationship is linear because the number of branches decreases as the average pore size increases. However, the graph illustrates that even though the smaller pore size gels have an order of magnitude more branches(ie. connections) the pore size still dominates the penetration rate of water into these gels. It would be interesting to determine the filling rate at a constant pore size for different numbers of branches to see if k increased with the number of branches.

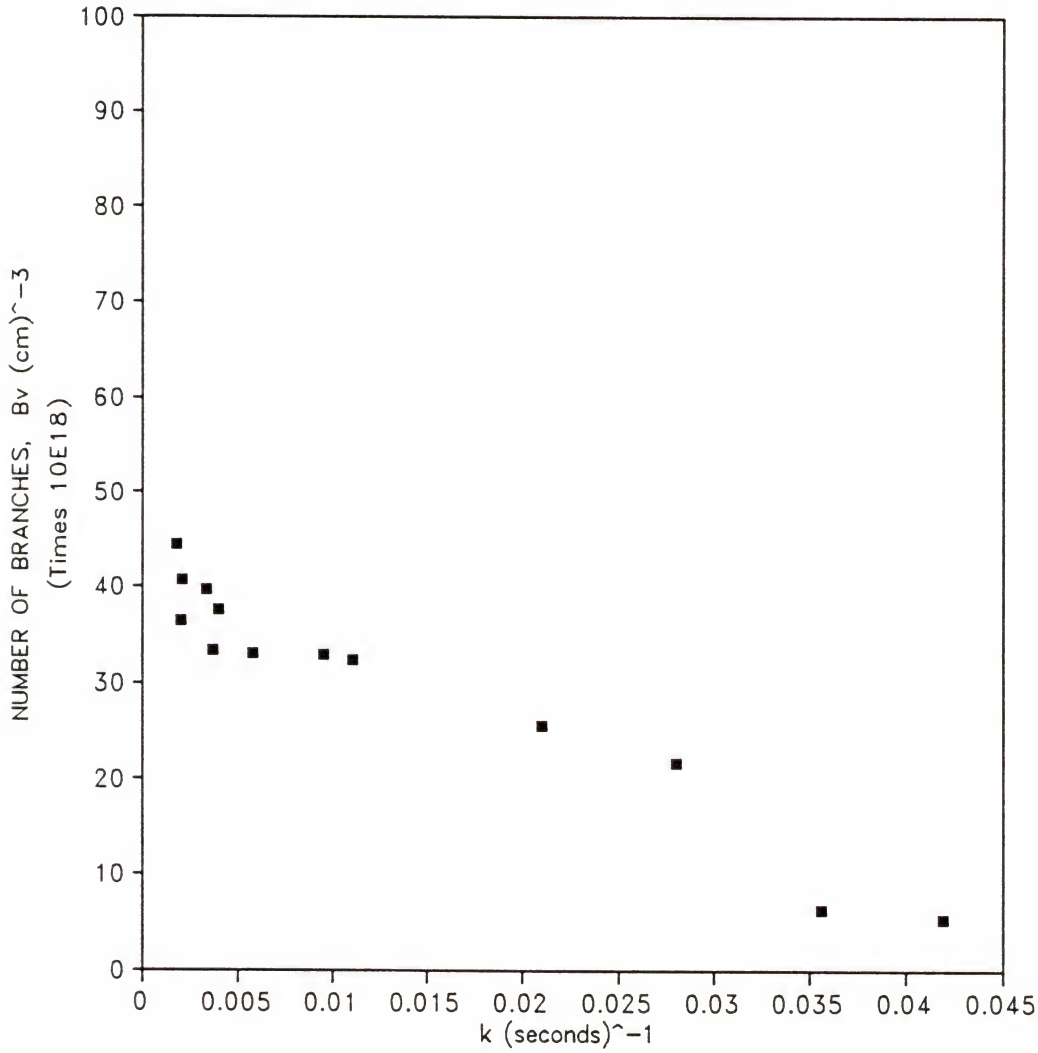

Figure 3.19 The number of branches as calculated from a topological model versus the characteristic constant, k.

3.6 Conclusions

Characterization of the gels by different methods indicates that the pore morphologies of the gels can be successfully altered at various steps in the process. Small pore gels were created by using nitric acid as a catalyst in concentrations which maximize the gel time. These gels can also be subsequently aged at higher pH's to produce gel pores nearly ten times larger. HF used as a catalyst dramatically increases the average pore size by increasing the average particle size and decreasing the gel time. Heat treatment of the gels up to temperatures before pore closure begins is an effective method for creating constant pore size gels with varying amounts of volume fraction and surface areas.

Immersion of the gels in water revealed a trend indicating the minimum bulk density required for the gels to withstand rehydration pressures. The minimum bulk density is a function of the pore size and the volume fraction of porosity. The gels, due to cutting and polishing, contained surface defects which ultimately control the fracture. The minimum bulk density would be an upper limit for gels which were not polished. This is a useful indicator for preparing porous monoliths for use in environmental sensing. However, the trend was immediately useful for preparing samples for this study.

The penetration rate of water was theoretically as well as empirically fit to two different equations. The correlation to the theoretical, Rideal-Washburn equation, was excellent for short times. The rate of filling was shown to be

proportional to the square root of both the time and the pore radius. The data also fit empirically an equation of a different form which enabled a characteristic constant to be calculated. This constant was calculated to be strongly dependent on the average pore radius.

A topological model was used to calculate the number of branches for the different pore size gels. The number of branches was an order of magnitude larger for the smaller pore size gels than the largest pore size gel. When the characteristic constant is plotted versus the number of branches it was seen that the penetration rate was controlled by the average pore size and not the number of branches.

CHAPTER 4
ANALYSIS OF POROUS GEL SILICA MONOLITHS WITH CALORIMETRY AND ELECTROPHORESIS

4.1 Introduction

Porous sol-gel materials are shown in chapter 3 to posses large surface area-to-volume ratios (100,000 to 10 million cm^{-1}) with surface areas varying from 10 to 1000 m^2/gm. In chapter 2, the influence of the surface and the finite-size upon the behavior of a wide range of types of solutions was shown to substantially affect the transport and equilibrium properties of the solutions. It is difficult to separate effects of restricted geometry from surface effects because surface effects introduce spatial inhomogeneities such as chemical reaction or adsorption sites. This is especially true for porous materials comprised of micropores that have overlapping potentials from adjacent pore walls. The large surface area-to-volume ratios also indicate that the network structure of the surface has a notable contribution to the bulk structure of the glass. Therefore, experimentally measured values related to the surface structure may be able related to bulk structure as well.

This chapter reports on three phases of related studies. The first examines the relationships between the processing variables discussed in chapter 3 and experimentally measured heats of immersion. Since the emphasis of the

dissertation is upon understanding the diffusion behavior of chromium salt solutions within the restricted geometries of porous sol-gel monoliths, the heats of immersion investigation was performed with deionized water.

Second, the presence of electrolytes indicate that the electrical-double layer and surface charge will have an influence upon charged species within these confined systems. Therefore, additional experimentation in the form of electrophoresis measurements were performed to characterize these electrical surface properties. In addition, for environmental sensing applications the stability of the monoliths with respect to the different pore characteristics is unknown. This is explored by examining the changes of the electrophoresis measurements with aging of the gel powder solutions.

Lastly, an electrokinetic study of porous sol-gel particles represents one of the first attempts to understand how porosity produces deviations from the electrokinetic behavior of similar dense particles. Very few studies have been performed previously to understand the electrokinetic behavior of porous particles.

The chapter is organized in the following manner. A brief theory and literature review is provided as an introduction to the experimental procedures for measuring heats of immersion. A presentation and discussion of these results does not ensue until the same format has been administered for the electrophoresis experiments. As will be seen, both results are interrelated and thus will be examined together in the results and discussion section. All of the conclusions will then be summarized at the end of the chapter.

4.2 Heats of Immersion

4.2.1 Theory

The theory for the calculation or determination of the surface energy or free energy changes which occur upon immersing a clean solid surface in a liquid is straightforward.[134,135] The analysis is made simpler because both phases involved are condensed and no distinction need be made between enthalpy and energy since the difference is small.

When a liquid spreads over an area, S_1, a solid-gas interface is destroyed and an energy, $S_1\gamma_{sg}$, is gained, where γ_{sg} is the solid-gas interfacial tension. At the same time, an energy is expended, $S_1\gamma_{sl}$, in forming the new solid-liquid interface. Also, a liquid-gas interface is created, S_2, which requires an additional energy, $S_2\gamma_{lg}$. The total energy of the system can then defined as,

$$\Delta H_i = S_1\gamma_{sl} - S_1\gamma_{sg} - S_2\gamma_{sg} \qquad (4.1)$$

The contact angle of a liquid drop upon a solid can be defined as,

$$\gamma_{lg}\cos\theta = \gamma_{sg} - \gamma_{sl} \qquad (4.2)$$

Since we are determining the heats of immersion of a porous medium $S_1 >> S_2$. Substitution of equation 4.2 into 4.1 and rewriting leads to,

$$\Delta H_i = -\gamma_{lg} S_1 \cos\theta \qquad (4.3)$$

where S_1 is equivalent to the internal surface area of the porous medium. The heat of immersion is a negative quantity if the wetting is exothermic. This is usually the case since the solid-gas interface is a higher energy then the solid-liquid. Heats of wetting are reported in ergs/cm² or dynes/cm. Both units represent equivalent quantities of heat.

4.2.2 Related Studies

When immersing in water, the hydrophilic nature of a solid surface is revealed as a large exothermic heat which indicates a strong interaction with water molecules. Numerous studies reporting heats of immersion for a wide range of materials in water report a range of values from a low of 6 ergs/cm² for Teflon®, and as high as 900 ergs/cm²for Al_2O_3.[136-142] A polar solid will produce a large heat of immersion in a polar liquid and a much smaller heat in a non-polar liquid. Zettlemoyer[140] notes that for a given solid the heat of immersion is linearly related to the dipole moment of the wetting liquid.

It is possible to pre-adsorb a thin film upon the surface before immersion in that liquid. The energy of the adsorption of the film can then be determined. If three or more water layers already exist on a polar solid before immersion, the heat value falls to a constant, 120 ergs/cm² which is the surface enthalpy of liquid water.[138]

Griffiths[139] studied the effect of outgassing temperature on the heat of immersion of Al_2O_3 in water and concluded that approximately half of the heat was from physically adsorbing water and the other half was from rehydroxylating the surface. An additional experimental variable in his study was the temperature of immersion which showed little variation in the heat differences. Griffths believed this indicated the water structure at the surface consisted of a tightly bound layer which ended discontinuously or abruptly into bulk water structure and properties.

As described in chapter 3[42,92] the surface of sol-gel silica contain a large percentage of 3- and 4-membered rings on the surface at intermediate sintering temperatures. Another study[143] investigated the rehydroxylation of the surface of amorphous silicas. This study included Vycor® porous glasses, silica gels, and aerogels. The surface of silica gels in water at room temperature for 100 days and after heat treatment in air at 850 °C was about 60% rehydroxylated. A more prolonged treatment of 5 years in water at room temperature produced a 95% rehydroxylation. However, complete rehydroxylation of the surface for the same 850 °C sintered gels occurred after boiling in water for 5-10 hours. Similar results were found for the other amorphous silicas. It appears as if the reversible sites for rehydroxylation will rehydrate at room temperature but the activation energy is appreciable if 3-membered rings are not present.

In an early study, Wade et al.[144] investigated the relationship of the substrate structure upon the heat of wetting in the water-silica system. Both β-quartz and an amorphous silica (the origin of the amorphous silica was not reported) were

investigated as a function of outgassing temperature. Extremely high values of the heat of wetting for β-quartz, 850 ergs/cm² were reported. Undoubtedly these samples contained significant ionic impurities. Values reported for the heats of wetting for a silica gel with a surface area of 188 m²/gm varied from 162-182 ergs/cm² for heat treatments from 110-450 °C, respectively. A second silica gel sample with 162 m²/gm surface area had a measured value of 88 ergs/cm² which remained constant over the same temperature range, 110-450 °C. Wade concluded that amorphous structures produce significantly lower heats of wetting than crystalline phases of the same oxide. However, impurities in naturally occurring crystals cannot be ignored.

Egorov and coworkers[145] found a decrease in the heat of wetting of silica gels with water as the surface area increased. Three gels with surface areas of 275, 400, and 695 m²/gm produced heats of wetting of 200, 175, 150 ergs/cm². The first gel was made from the flame hydrolysis of $SiCl_4$ and the others were "purified" commercial silica gels. It appears from their study that water is more effective in wetting lower surface area gels. The absolute values are similar to the heats found in this study.[145]

A careful study involving the adsorption of water vapor on the surface of flame hydrolyzed $SiCl_4$ as a function of heat treatment was conducted by Young[146]. By correlating the water vapor adsorption with infrared spectroscopy it was found that water adsorbs onto the silanols and not on the remainder of the surface

structure. Wade[144] suggests that the Si-O bonds are nearly homopolar or more hydrophobic than the silanols which helps explain Young's results.

Taylor and Hockey[147] heat treated a commercially available "Aerosil" between temperatures of 700 and 1040 °C for 4 to 16 hours. The samples were then immersed in water at 95 °C for 5 hours and dried in air at 115 °C to constant weight. All samples had a measured heat of wetting with water of 160 ±3 ergs/cm². This series of samples varied in surface area from 147 to 8 m²/gm. The study also suggested that N_2 isotherm analysis underestimates the surface area of samples containing pores less than 7 Å in diameter. This smaller area produces artificially high heats of immersion when normalized to surface area.

A precise gravimetric data set was obtained by Whalen[148] for nitrogen and benzene adsorption onto high purity precipitated silica gels. It was determined that nitrogen interaction energies changed from 1.9-2.3 kcal/mole to 2.9-3.2 kcal/mole as the surface was rehydrated. Benzene adsorption produced larger interaction energies of 10-11 kcal/mole. Whalen concluded that benzene was strongly dependent upon the chemical nature of the surface although no simple relationship existed. Also, surface area measurements determined from BET appear to be slightly dependent upon the surface structure of the silica.

Whalen measured heats of immersion by differential calorimetry[149] using water at two different temperatures, 27 °C and 45 °C, for two well characterized aerosil gels prepared in air and vacuum and annealed at 700 °C. It was suggested that a different structure is created by the presence of water vapor. It

is known that the densification behavior (faster densification kinetics in the presence of moisture) of sol-gel silica is different depending upon the atmosphere.[12]

A study which investigated the surfaces of amorphous and crystalline silica, before and after grinding, and after etching in 3% HF solution, showed that the grinding products and particle size affected the results.[150] The free energy of adsorption, which is determined from the difference between the surface tension of a vacuum-baked surface and the surface tension after adsorption of a water vapor, increased for both the ground amorphous and crystalline samples. The free energy and the heat of adsorption decreased for the etched samples as the surface area increased. The heat of adsorption remained constant for the amorphous silica with grinding. One explanation suggests a correlation between particle size and crystalline surface order. An increase in crystalline surface order increases the electrostatic field potential causing a greater polarization of the surface hydroxyls and increase water-silica interactions.

4.2.3 Experimental Procedure

4.2.3.1 Sample preparation

The preparation and processing of the gels for this study is identical to the procedure outlined in figure 3.2. In addition, after the heat treatments (600-1000 °C) the gels were ground in a mortar with a pestle, passed through a 400 mesh stainless steel screen, passage was enhanced by a vibratory mechanism, and then reheated to 400 °C within quartz crucibles in a box furnace

in air overnight. The furnace was cooled to 150 °C to minimize exposure to moisture. The crucibles were removed as needed for each experiment. Immediately before the measurement was taken, a precise amount of powder was weighed and within minutes was placed within the calorimeter. The following section describes the operating principle of the calorimeter.

4.2.3.2 Calorimeter operating conditions and principles

The calorimeter, model number C 80, was manufactured in France by the Societe d'Etudes d'Automatisation de Regulation et d'Appareils de Mesures (SETARAM). Two highly conductive stainless steel experimental vessels are placed in a calorimetric block which is capable of imposing the temperature of the experiment as fixed or variable. Two symmetrical fluxmeters, composed of thermocouples connected in series, surround the experimental vessels and thermally connect them to the calorimetric block. These fluxmeters produce an electrical signal which represents the thermal changes between the vessels and the calorimetric block. These fluxmeters are differentially connected to cancel any signal other than that due to the system being studied. When a heat flow is detected the signal from the reference cell is subtracted from the sample vessel to reflect the net heat change to the sample only.

Each of the vessels (reference and sample) are identical. The vessels contain Teflon® O-rings or seals to prevent leaking of the wetting fluid, an aluminum foil membrane separating the top portion of the cell (where the liquid is held) from

the bottom (where the sample is contained), and a stainless steel plunger to break the membrane to allow the wetting liquid and sample to mix.

4.2.3.3 Calorimeter procedure

3 cm^3 ±0.05 cm^3 of water, which was measured with a pipette, was used to wet each sample. The sample weight was varied from 58 mg to 191 mg ±0.03 mg. More sample was used to generate similar signals for samples with smaller surface areas. The powder sample was weighed, placed in the sample vessel bottom and sealed, 3 cc of water was added and sealed in the top of each vessel and then both vessels were placed in the calorimeter.

The operating temperature for this series of experiments was chosen to be an isothermal 29.20 ±0.03 °C. This temperature was chosen because the ambient laboratory temperature fluctuated between 20 and 25 °C. The system was allowed to equilibrate before the immersion of the sample. This equilibration time was generally 45 minutes and was monitored by the power change in milliwatts. Power was added during equilibration to heat the vessels from room temperature to 29.20 °C.

At time equal to zero, both plungers were pushed through their respective membranes and twisted once clock-wise, then once counter-clockwise, and finally withdrawn. The plungers had small paddle shaped ends to aid in the thorough mixing of the water and glass powder. Identical movements were made to both the reference and the sample to decrease the possibility of introducing a differential amount of heat and thus affecting accuracy of the results.

An immediate rise in heat was noted by monitoring the power versus time plot. The onset of the peak maximum always occurred in less than 2 minutes from the start. Data points were collected every 2 seconds over a 45-60 minute period which was the extent and variation of the run time. All of the samples exhibited exothermic wetting.

At the completion of the run the software assigned a baseline and integrated the area under the power versus time curve. An enthalpy was then computed from this area and the sample weight. As discussed later the enthalpy was then normalized further by the internal surface area of the powder.

Prior to the investigation of the sol-gel powders a KCl standard powder from the National Bureau of Standards (now National Institute for Standards and Technology) was tested. The enthalpies from the three trial runs of the KCl were 222.1, 214.4, and 220.3 J/gm for a computed average of 218.9 $\pm$4.0 J/gm. This is compared to the standard enthalpy of 211.0 J/gm. The absolute difference in error from the standard and the average value is (218.9-211.0)/218.9=3.6% and the average measurement error of the three measurements is 4/218.9=1.8%. Two runs were conducted per sample unless these two values differed by more than 5% in which case an additional run was performed. The reported values represent an average value of all the runs conducted per sample.

The errors in the heat of immersion experiments are from weighing the powder and from the amount of time the powder was exposed to the air. The weighing error is small since a scale accurate to $\pm$0.3 mg was used(i.e. a change

of 0.5 mg in the weight of the powder for a typical heat value of 30 J/gm changes the enthalpy by less than 0.5%). The amount of time the powder was exposed to the atmosphere was variable due to the sharing of the balance and the time to load the sample. The weighing error could be both positive and negative and therefore the enthalpy could be higher or lower than the actual value. Also, the water adsorbing from the atmosphere onto the powders prior to an immersion trial would have an effect of increasing the heat of a sample for a surface lower in energy or enthalpy than that of water (the surface enthalpy of water is 120 ergs/cm^2) and to decrease the enthalpy of wetting for a substance which has a enthalpy higher than the surface enthalpy of water. In general it is impossible to know the extent of moisture adsorbed per sample. Therefore since differences larger than 5% were reanalyzed, $\pm$5% is a good approximation of the error in the measurement of the heat of immersion of the powders.

An additional error is introduced in normalizing the surface area measurements. The surface areas are calculated from the N_2 desorption isotherm applying the BET theory, as discussed in chapter 3. It is assumed that the instrument operates under the same tolerances from sample to sample and that the most error is introduced in weighing the sample. All samples were outgassed for four hours or more under 10^{-3} torr vacuum at 150 °C even though it was determined that two hours was sufficient to remove adsorbed water from the gels under these outgassing conditions. This was based upon no weight changes to the sample after two hours of outgassing. The weight of the sample and analysis

cell was measured four times from which an average value was determined. The variation of the weight was typically as much as ± 0.002 grams from the largest measured value to the smallest. The sample weights were typically 0.1 grams; therefore this is approximately a 2% weighing error. Figure 4.1 displays the linear change in the pore volume and surface area for a weight percent change of the sample. A 2% change in weight changes the surface area and pore volume by 2% also. Therefore, the total error associated with the heats of immersion, as reported in ergs/cm², is 7%.

4.3 Zeta Potential

4.3.1 Theory

When two phases are brought into contact a migration of charge takes place from one phase to another across the boundary creating a potential difference. This migration or distribution of charge is governed by the laws of thermodynamics. For an electrolyte solution the charge carriers are the ions of a particular species that can reside in both phases. These common constituents or common charges are the potential determining ions. In silica-water suspensions the surface groups(silanols) are capable of dissociating and producing the potential determining ions OH^- and H^+.

In general, this two phase contact creates an escaping tendency of the ions from the phases or environment in which they reside. The ions will migrate from the phase in which the escaping tendency is the largest. This will produce an

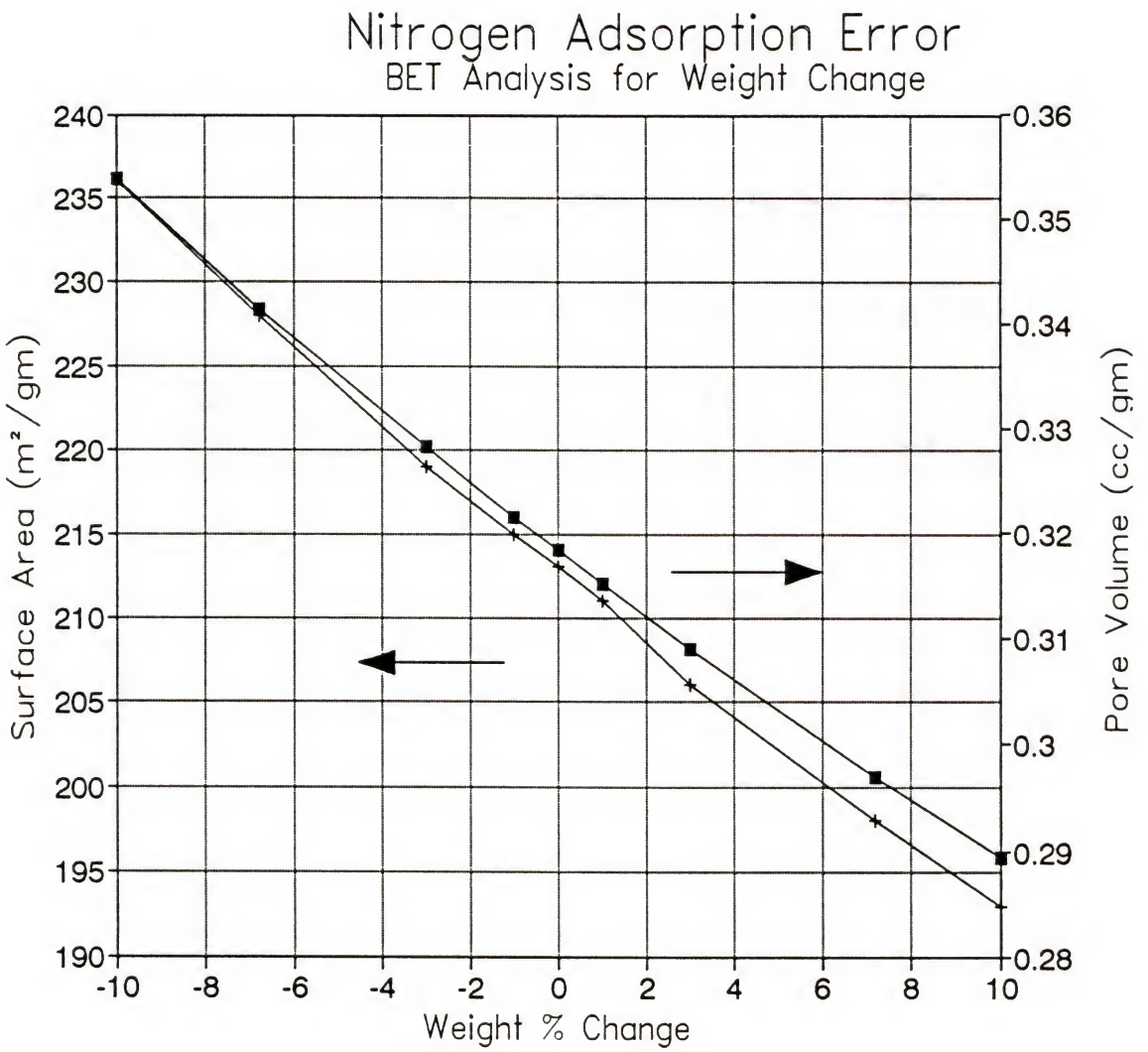

Figure 4.1 A plot of the change in the calculated surface area and pore volume of sol-gel silica powders as a function of percent weight change.

electric field which will hinder further migration of the ions until equilibrium is reached. At equilibrium a difference in electric potential is established between the two phases.

The thermodynamic concept of escaping tendency is the chemical potential. The chemical potential is determined by the concentration difference or more accurately the activity of the ions. This chemical potential for charged species in the presence of an electric potential becomes the electrochemical potential, which accounts for the influence of the field. These oppositely charged species concentrate at the phase boundary generating a gradient of the electric potential which is gradually reduced with distance from the interface.

Gouy[151] and Chapman[152] proposed the first diffuse double-layer model which accounted for the thermal motion of the counterions in the solution phase. Counterions are attracted to the surface charges by Coulombic forces and at the same time thermal motion moves them back to the bulk phase. Their model consists of Poissons equation, which utilizes the dielectric displacement in terms of the permittivity of the substance (this permittivity accounts for the polarization of the molecules in response to the field), which defines the charge distribution or volume density of charge at given distance from a point charge and Boltzmanns equation which defines the number of ions at a given distance from a charged surface, in terms of the concentration of ions in solution, the potential gradient, and thermal motion. The Poisson-Boltzmann (PB) equation(equation 4.4) is one of the

most important equations to understanding electrolyte solutions and colloid interaction.

$$\nabla \psi = -\frac{1}{\varepsilon_o \varepsilon_r} \sum n_i^o z_i e \exp\left(\frac{-z_i e \psi}{kT}\right) \qquad (4.4)$$

ψ is the potential, ε_o and ε_r are the permittivities of vacuum and the solution, n^o_i is the bulk concentration of ions i, z_i is the valence, e is the elementary charge of an electron, k is Boltzmanns constant and T is the absolute temperature.

If the electrical energy is small compared to the thermal energy, ($|z_i e\psi| < kT$), the Debye-Hückel approximation enables simplification of the PB equation,

$$\nabla \psi = \left(\frac{\sum z_i^o e^2 n_i^o}{\varepsilon_r \varepsilon_o kT}\right) \psi \qquad (4.5)$$

or

$$\nabla \psi = \kappa^2 \psi \qquad (4.6)$$

where κ, is the Debye-Hückel parameter (length^{-1}). The extent of the double-layer is measured by the size of $1/\kappa$. If one substitutes for the values of the fundamental constants, κ is given by equation 4.6 for water at 25 °C to be:

$$\kappa = 0.3288\ I^{1/2} \quad (\text{Å}^{-1}) \qquad (4.7)$$

where I is the ionic strength of the solution and is defined as,

$$I = \frac{1}{2}\sum c_i z_i^2 \qquad (4.8)$$

with c_i the concentration of species i in moles/liter. For a 1:1 electrolyte typical values of $1/\kappa$ are, 96 Å for 0.001 M and 9.6 Å for a 0.1 M solution. The above values of the double-layer thickness are as a rule approximations because for most systems the electrical energy is not much, much, smaller than the thermal energy, (i.e. large surface charges can be generated at an metal-oxide interface).

The complete PB equation must then be solved. This is only possible analytically for the case of a planar surface.[153] Other geometries require numerical solutions and/or the use of the Debye-Hückel approximation.

The Derjaguin-Landau-Verwey-Overbeek(DLVO) theory,[154,155] which discusses the interaction of the electrical-double layers just described and London-van der Waal forces between colloid particles, is the foundation of colloid science today. The stability of an aqueous suspension is determined by the total potential energy of interaction of the particles, both the repulsive forces of the double-layer and the short-range London attractive forces.

The form of the potential energy which determines the repulsive and attractive force varies for different geometries. In general the repulsive force depends upon the size of the double-layer, $1/\kappa$, and varies with the exponential of the distance of separation. The attractive potential of van der Waal is expressed as the inverse sixth power of the separation distance. The additivity of this force allows it to become long-range for macroscopic bodies. Hamaker[155] calculated the

potential energy of two parallel plates as a function of distance in his derivation or creation of the Hamaker coefficient. The potential energy for the plates varies as an inverse function of the square of the separation. Therefore, the total force is repulsive at large distances but as the separation decreases the attractive potential increase faster then the repulsive potential which produces an attraction between the particles.

For increasing ionic strengths or concentrations of ions κ increases and the potential decays more rapidly with distance. An increasing double-layer thickness or decreasing κ extends the potential further out into solution and the suspension is more stable to coagulation.

The above principles are incorporated into theories which enable the calculation of surface potentials by electrokinetic phenomena. All electrokinetic phenomena are caused by the flow of charge and liquid in an electrical double-layer relative to the surface. The plane immediately adjacent to the surface is a concentration of charges which are immobile and is referred to as the Helmholtz plane or Stern layer.[156] This plane is subsequently divided into two regions, the inner Helmholtz plane (IHP) which is the locus of the centers of adsorbed ions and the outer Helmholtz plane (OHP) which is the locus of hydrated ions. The outer edge of this layer is the slipping plane at which it is assumed the liquid movement relative to the particle surface begins. It is at this layer that the zeta-potential is calculated. It is necessary to keep in mind that not only the particle moves under the applied field but the fluid does as well.

An excellent description of electrophoresis phenomena is available in Hunter.[157,158] In an electrophoresis measurement the charged particle moves under the potential of an applied external field, E (V/cm). The electrophoretic mobility can be calculated by first approximations from Stokes law (see chapter 2). However, as mentioned above the counter-ions in the diffuse double-layer are forced to move in the other direction under the applied field transferring their movement to the liquid around them causing liquid flow in the opposite direction. The exact calculation of this effect results in Hückels equation,

$$\mu_e = \frac{\varepsilon \zeta E}{6 \pi \eta a} \qquad (4.9)$$

where ζ is the measured zeta potential. Smoluchowski independently derived the electrophoretic velocity from electroosmosis theory, the flow of a liquid under an applied potential through a stationary solid. His derivation is in the form,

$$\mu_e = \frac{\varepsilon \zeta E}{4 \pi \eta a} \qquad (4.10)$$

The discrepancy between the two methods is because Smoluchowski in his derivation, accounted for the deformation of the electric field in the liquid due to the presence of the insulating particle. Hückel's derivation is still applicable when the conductivity of the particle and fluid are similar or if the particle is small and therefore deformation of the field is localized to the inner portion of the double-layer. Smoluchowskis' equation is used in the calculation of the zeta potential in this work.

An important point of the zeta potential curve with solution pH is the isoelectric point of solids (IEPS) as distinguished from IEP which is the isoelectric point of dissolved species.[159] The isoelectric point represents the pH at which a surface has a zero net charge. The point of zero charge (PZC) is the pH were a surface has equivalent concentrations of positive and negative complexes. Since the IEP is measured electrokinetically at the slipping plane and not the surface, PZC and IEP are not the same. PZC is measured by acid-base titrations or additions. However, the PZC and IEP are nearly equivalent for most systems.

The following section discusses other related work for zeta potential measurements of silica systems, a porous aggregate system, a system involving the aging of oxides, and the effect of variables on the PZC.

4.3.2 Related Studies

It is appropriate to begin the discussion of this section with an excellent review by Parks[159] of the isoelectric points of solid oxides, solid hydroxides, and aqueous hydroxo complex systems. It also introduces the concept of charge neutrality on the surfaces of oxides, discusses the variables affecting the isoelectric point, and presents an electrostatic model for the variation of IEP with cationic size and charge. The number in parenthesis is the reference associated with the remark from Parks review.

It is shown that heat treated α-aluminum oxide produces an IEP near pH 6.7 which increases to 9.2 after aging in water for one week[159](103). An investigation by Horn [160] of the aging of several aluminum oxides revealed the dependency of

the PZC upon both the amount of impurities and the extent of hydration due to grinding. The IEP's of various forms of silica vary from pH 3.7 for Brazilian quartz to pH 0.5 for silica sols. Parks suggests that the average value of IEP for the quartz species is pH 2.2 and for silica gels and sols the IEP is pH 1.8. Certainly multiple factors must affect measurement of the IEP.

In general the IEP becomes more acidic for metal oxides as the ratio of oxygen to metal increases. Several groups[159](55, 80,110-113) reported relationships between the IEP and sample history and agree that treatments which lead to dehydration produce a more acidic IEP than is observed for materials that are likely to be hydrated.

Purposeful studies of the effects of impurities upon the IEP of oxides are few. It is assumed that perchlorate, nitrate and chloride ions[159](45) do not interact with oxides in any specific sense. It was determined[159](83c) that specific adsorption of anions or structural anionic impurities shift the IEP to more acidic values. The opposite shift is found for cationic specific adsorption.

An electrokinetic streaming potential study of various types of crystalline and vitreous silica suggest no difference in their behavior.[161] This was based upon the similarity of the shapes of the curves representing the electrokinetic potential and pH. A study with three controlled pore size glasses indicated a decrease in the measured electrokinetic potential for a decrease in the pore size. However, the surface area and pore volumes of the porous glasses were not kept constant.

More discussion of the measurement of zeta potential with porous materials is presented in the discussion of results.

Silica, TiO_2, and Fe_2O_3 exhibit odd behavior in that titration experiments indicate that surface charges in excess of 20 $\mu C/cm^2$ exist on the surface yet silica has a relatively low diffuse double-layer potential. Different models, including a porous gel layer[162] and site binding,[163] have been proposed as an explanation of this behavior.

A recent study[164] proposed the existence of a hydration force not considered in the DLVO theory to explain the stability of silica suspensions at reduced zeta potentials due to either adjustment of the pH or concentration of electrolyte. Measuring the forces between atomically smooth surfaces at very small separations with a surface force apparatus has become an exciting area of research as mentioned in chapter 2. It is clear from the literature that current models cannot explain all aspects of the silica-solution interface. Undoubtedly, measurements of the components of charge in the double layer will have to be made on multiple systems before one can confidently and completely assert an adequate model of the structure of the oxide-solution interface.

4.3.3 Experimental Procedure

4.3.3.1 Sample preparation

The identical powders used in determining the heats of immersion from section 4.2.3 were used in this study (see table 4.1). Dilute solutions ranging from 253 mg/L to 330 mg/L were mixed by adding each powder to 240 cc of deionized

Table 4.1 Pore characteristics of gels used in heats of immersion and zeta potential studies.

Temperature (° C)	Pore Radius (Å)	Surface Area (m^2/gm)	Pore Volume (cc/gm)	BET constant
		Series #1		
700	32	509	0.802	72
800	31	455	0.704	66
850	31	430	0.672	63
950	29	415	0.596	60
		Series #2		
600	29	581	0.828	82
675	28	567	0.792	71
750	29	526	0.757	63
850	30	390	0.540	61
925	28	286	0.394	69
1000	28	68	0.092	58
		Series #3		
600	39	438	0.857	102
775	38	401	0.758	76
900	35	312	0.540	73
950	31	215	0.325	83
		Series #4		
600	16	643	0.501	48
700	15	579	0.436	54
800	15	487	0.360	65
860	16	388	0.305	57
890	15	344	0.250	72
920	14	332	0.236	82

Table 4.1 is continued on the following page

Table 4.1 continued — Pore characteristics of gels used in heats of immersion and zeta potential studies.

		Series #5		
600	102	232	1.182	245
750	99	224	1.062	160
950	98	205	1	133
1050	72	150	0.39	128
		Series #6		
800	14	541	0.362	65
920	14	441	0.302	78
950	14	313	0.222	89

water which had a measured conductivity of 0.2 μS/cm or Mhos/cm. The solutions were acidified by drop-wise addition of 1.4 N HNO_3 solution using a micropipette. Less than 2 cc total of acid had to be added in order to obtain the lowest solution pH measured which was 2.7 pH. All solutions were made in Nalgene® bottles which had been washed with a 1.4 N HNO_3 solution and then rinsed several times with deionized water. A Fisher® model 710 pH meter was calibrated each day over the pH range 7.00 to 2.00 with appropriate standards to insure accuracy of the pH readings. Tables 4.2-4.4 tabulate the concentration and the pH of each of the solutions measured for the 14 Å, 30 Å, and 95 Å pore radius gels, respectively. Although silica remains well dispersed over the pH ranges investigated, all solutions were sonicated for at least 5 minutes prior to any measurement. Longer sonication times were avoided to prevent increasing the temperature of the solutions.

4.3.3.2 ZetaPlus® operating conditions and principles

The instrument used in measuring the zeta potential was the ZetaPlus® manufactured by Brookhaven Instruments Corporation (New York). The system consists of a main enclosure, a DOS-based computer, and software for collecting, analyzing, and storing the data.

In the main chamber is a laser beam operating at λ_o=670nm focused upon a cell containing the dilute suspension of charged particles. The charged particles move perpendicularly between two differently charged electrodes being modulated at 250 Hz. Due to the motion of the charged particles a frequency shift, called the

Table 4.2. Solutions created with 14 Å pore radius gels.

Temperature (°C)	600	700	800	920
Concentration (mg/L)	304	296	327	326
Initial pH	5.71	5.69	5.96	6.01
Days in Solution	1	1	2	2
pH	5.30	5.73	5.91	5.51
	3.77	3.75	3.79	3.78
	3.31	3.31	3.30	3.31
	3.10	3.13	3.09	3.09
	2.77	2.75	2.78	2.79
Days in Solution	11	14	14	15
pH	5.68	6.00	6.07	5.54
	3.84	3.84	3.85	3.80
	3.38	3.37	3.38	3.29
	3.18	3.20	3.18	3.12
	2.85	2.82	2.95	2.80
Days in Solution	37	38	38	39
pH	5.61	6.02	6.09	5.73
	3.80	3.81	3.88	3.73
	3.40	3.35	3.36	3.32
	3.19	3.19	3.13	3.14
	2.84	2.85	2.85	2.82

Table 4.3. Solutions created with 30 Å pore radius gels.

Temperature (°C)	600	750	850	1000
Concentration (mg/L)	294	262	253	328
Initial pH	5.76	5.56	5.82	5.57
Days in Solution	2	1	1	2
pH	4.76	5.12	5.03	5.25
	3.72	3.63	3.51	3.59
	3.26	3.09	3.11	3.12
	3.00	2.73	2.74	2.82
	2.70	2.56	2.55	2.54
Days in Solution	13	8	12	12
pH	4.90	5.07	5.02	5.31
	3.77	3.62	3.58	3.62
	3.28	3.04	3.08	3.14
	3.01	2.65	2.72	2.78
	2.67	2.54	2.55	2.51
Days in Solution	38	36	40	38
pH	4.90	5.13	5.01	5.32
	3.76	3.63	3.57	3.58
	3.27	3.06	3.10	3.11
	3.02	2.70	2.70	2.78
	2.67	2.54	2.52	2.52

Table 4.4. Solutions created with 100 Å pore radius gels.

Temperature (°C)	600	750	950	1050
Concentration (mg/L)	313	296	323	312
Initial pH	5.61	5.61	5.83	5.77
Days in Solution	1	1	2	3
pH	5.35	5.58	5.62	5.58
	3.80	3.82	3.92	3.91
	3.34	3.29	3.46	3.47
	3.13	3.13	3.24	3.24
	2.87	2.94	2.96	2.99
Days in Solution	14	15	15	16
pH	5.56	5.83	5.88	5.60
	3.81	3.94	3.88	3.87
	3.36	3.41	3.34	3.42
	3.14	3.20	3.14	3.17
	2.93	2.93	2.85	2.88
Days in Solution	37	42	42	42
pH	5.56	5.71	5.77	5.64
	3.89	3.83	3.90	3.90
	3.40	3.32	3.45	3.50
	3.20	3.15	3.22	3.26
	2.93	2.95	2.94	2.97

Doppler shift, occurs in light scattered by the particles. The frequency of the Doppler shift, ω_s, is equal to the dot product of the scattering wave vector, $q=(4\pi n/\lambda_o)\cdot\sin(\theta/2)$ (the condition for the laser beam being perpendicular to the applied field), and the velocity of the particles, v_p. The refractive index of water (1.332) is represented by n and θ is 15°. The velocity of the particles, as mentioned in the theory section, is the product of the electrophoretic mobility, μ_e, and the electric field vector, E. Thus, by measuring the Doppler shift and knowing the applied field, μ_e can be calculated from, $3.22\cdot E/\omega_s$. For good measurements a high field strength is required for a low mobility and vice versa. During a cycle the field is reversed causing the frequency spectrum to be reversed about the modulated frequency of 250 Hz from which the sign of the mobility can be determined. The zeta potential is then calculated from the electrophoretic mobility according to Smoluchowski's equation(see equation 4.10).

4.3.3.3 Zeta potential measurement

The instrument was always allowed to warm up for at least half of an hour prior to the start of the measurements. The pH meter was calibrated in the interim. The sample solutions to be tested were always sonicated for several minutes prior to measuring the electrophoretic mobility. After sonication of the solution, the electrode was immersed in a small volume of the sample for a 30 sec equilibration period. A fresh sample ($\approx$2ml) was then poured into a polystyrene cuvette designed to fit in the laser chamber. The electrode was then inserted into the cuvette and the whole assembly placed in the main chamber.

With the electric field off, the 250 Hz modulator frequency was measured. Thermal gradients and dust particles generated additional frequencies. Three repeats of ±6 Hz of 250 Hz are required before the electric field is turned on. If this criteria was not met within a few minutes the sample and disposable cell were discarded and a new cell and sample was inserted into the chamber.

Several adjustments were made to the default settings in order to increase the quality of the results. It was noticed that at longer sampling times the electrode contained bubbles at its surfaces. This was especially so for samples below 3.0 pH. This was a result of the high conductance of the sample allowing a current to be passed through the solution. The bubbles along with turbulent motion associated with the eddy currents generate a noisy and unreliable spectrum. The sampling time was decreased from 256 μsecs to the minimum value of 128 μsecs. The manual indicates this reduced the resolution by a factor of two. In addition the current was manually limited to 5 mA.

The manual indicated a sample could be used for up to three measurements. It was decided that the extra time to replace the sample for each measurement was worth the more reliable result and this was the practice followed. For each solution a total of 6-15 runs were made, the high and low value discarded, and the remaining values averaged. Six measurements were sufficient above pH 4 but below pH 4 the number of measurements required to obtain a reproducible value increased proportionally to the decrease in pH. The plotted values represent the average value of all of the measurements.

4.4 Results and Discussion

4.4.1 Results

4.4.1.1 Heats of immersion

The heats of immersion for five different silica gels are displayed in figure 4.2 as a function of the heat treatment temperature. The heat treatment schedules are given in chapter 3 figure 3.4. The 5 different pore radii investigated are 14, 29, 32, 39, and 100 Å. The 14 Å pore radius gel was made using nitric acid as a catalyst. The three medium sized pores were made with nitric acid and different concentrations of hydrofluoric acid. The largest pore size gel was gelled under the same conditions as the 14 Å gel and then was exposed to 1 day aging treatment in 0.025 N NH_4OH. The differences in the preparation are explained in more detail in chapter 3.

All of the gels initially show a decrease in the heat of immersion as the temperature is increased from 600 °C to 800 °C. The 100 Å pore radius gel continues this trend to the highest temperature investigated. The other four gels and most notably the smallest pore size show an increase in the heat of immersion in the temperature range 800 to 1000 °C.

4.4.1.2 Zeta potential

The measured zeta potential versus solution pH are plotted in figures 4.3-4.11. Figures 4.3-4.5 are for solutions composed of the 14 Å pore radius gels, figures 4.6-4.8 are for the solutions composed of 30 Å pore radius gels, and figures

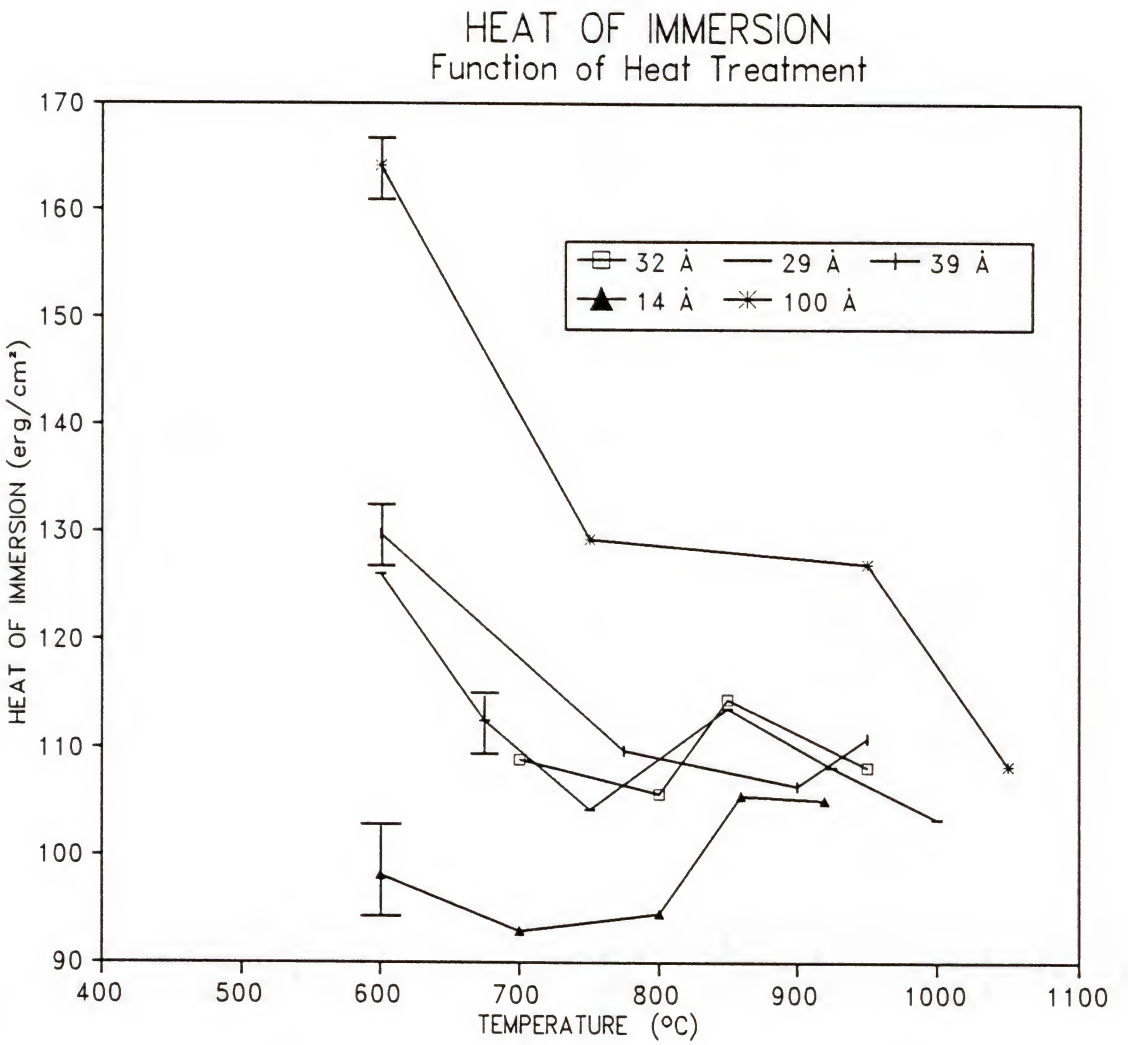

Figure 4.2 The measured heat of immersion with water versus the maximum thermal treatment temperature for a series of different average pore size silica gels.

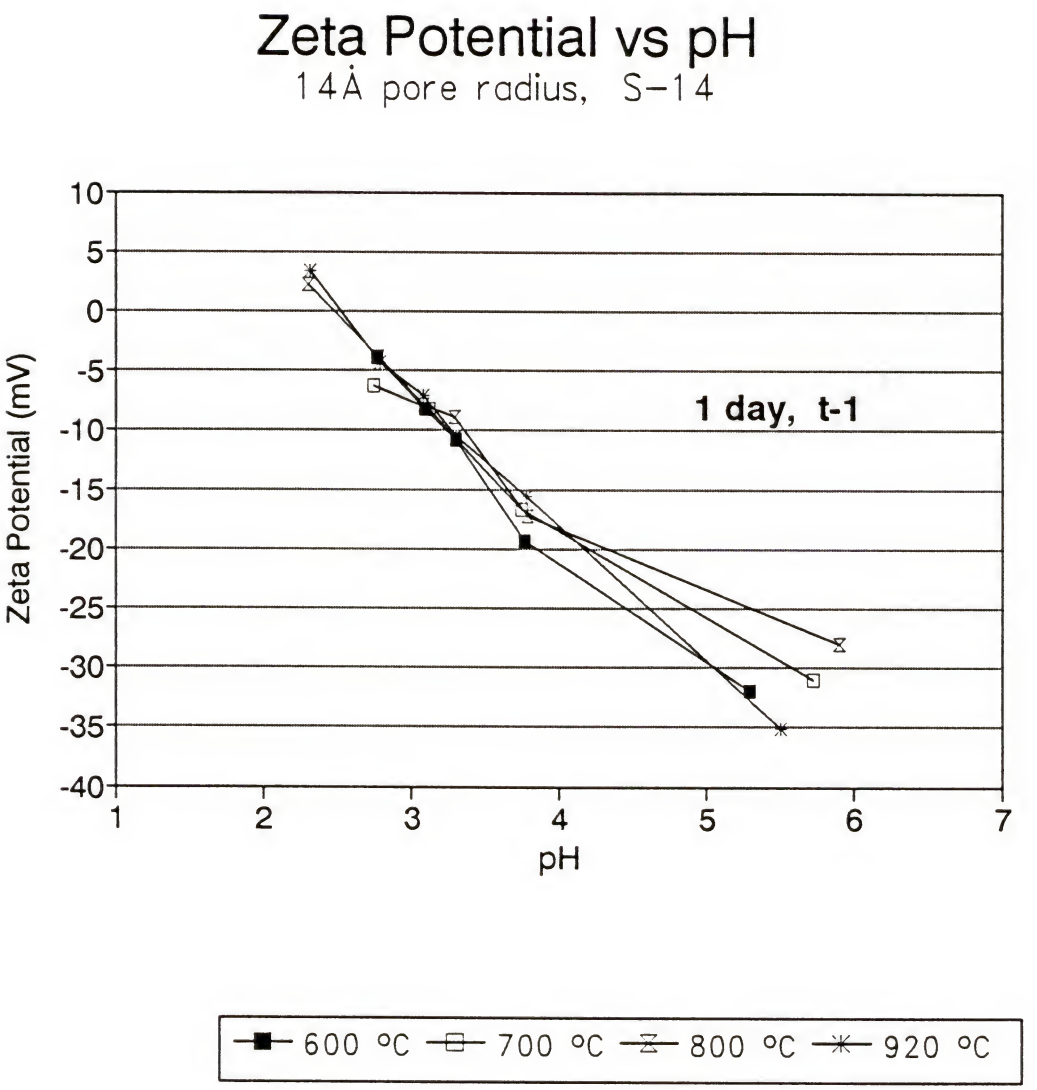

Figure 4.3 The measured zeta potential of aqueous solutions of porous sol-gel silica particles, with an average pore radius of 14 Å, is plotted as a function of solution pH and maximum gel thermal processing temperature. The measurements were taken after aging the solutions 1 day.

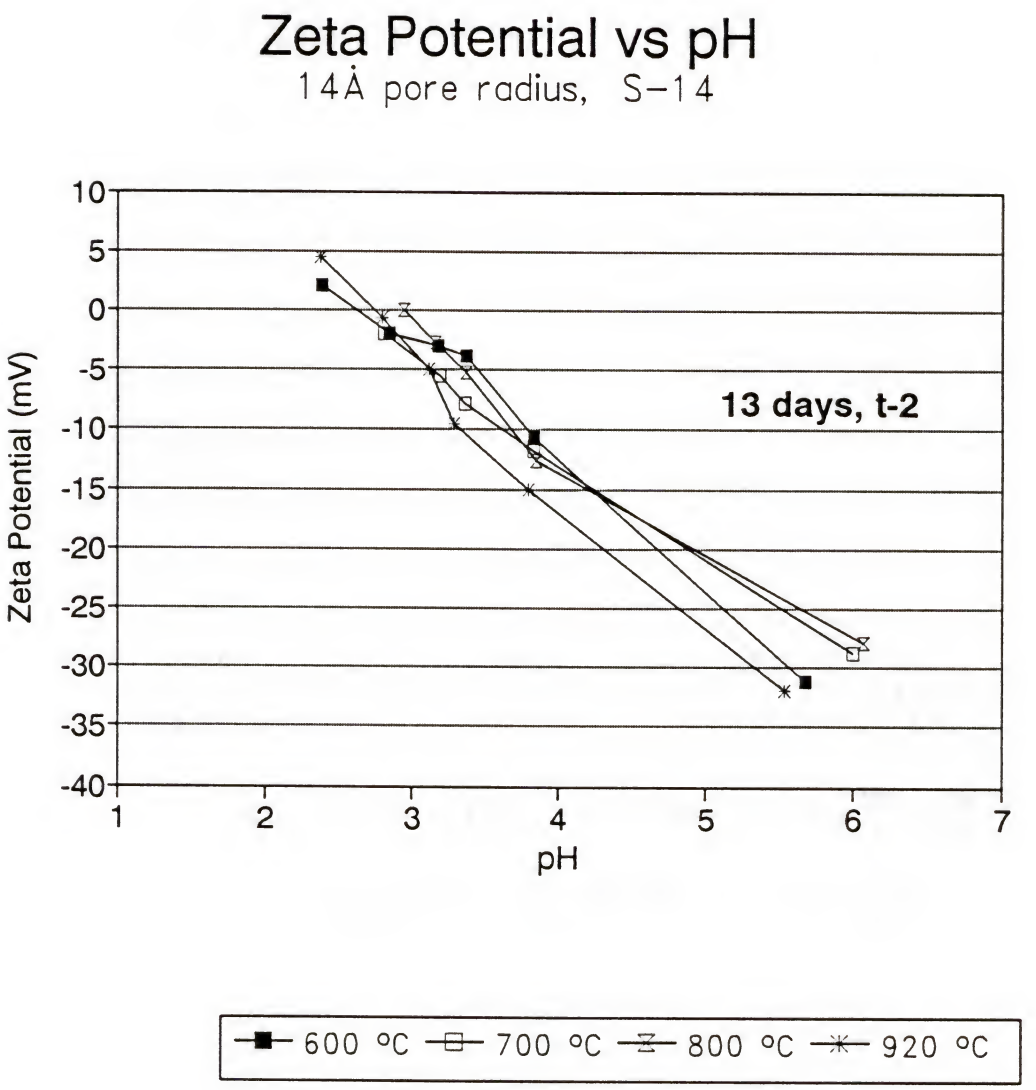

Figure 4.4 The measured zeta potential of aqueous solutions of porous sol-gel silica particles, with an average pore radius of 14 Å, is plotted as a function of solution pH and maximum gel thermal processing temperature. The measurements were taken after aging the solutions 13 days.

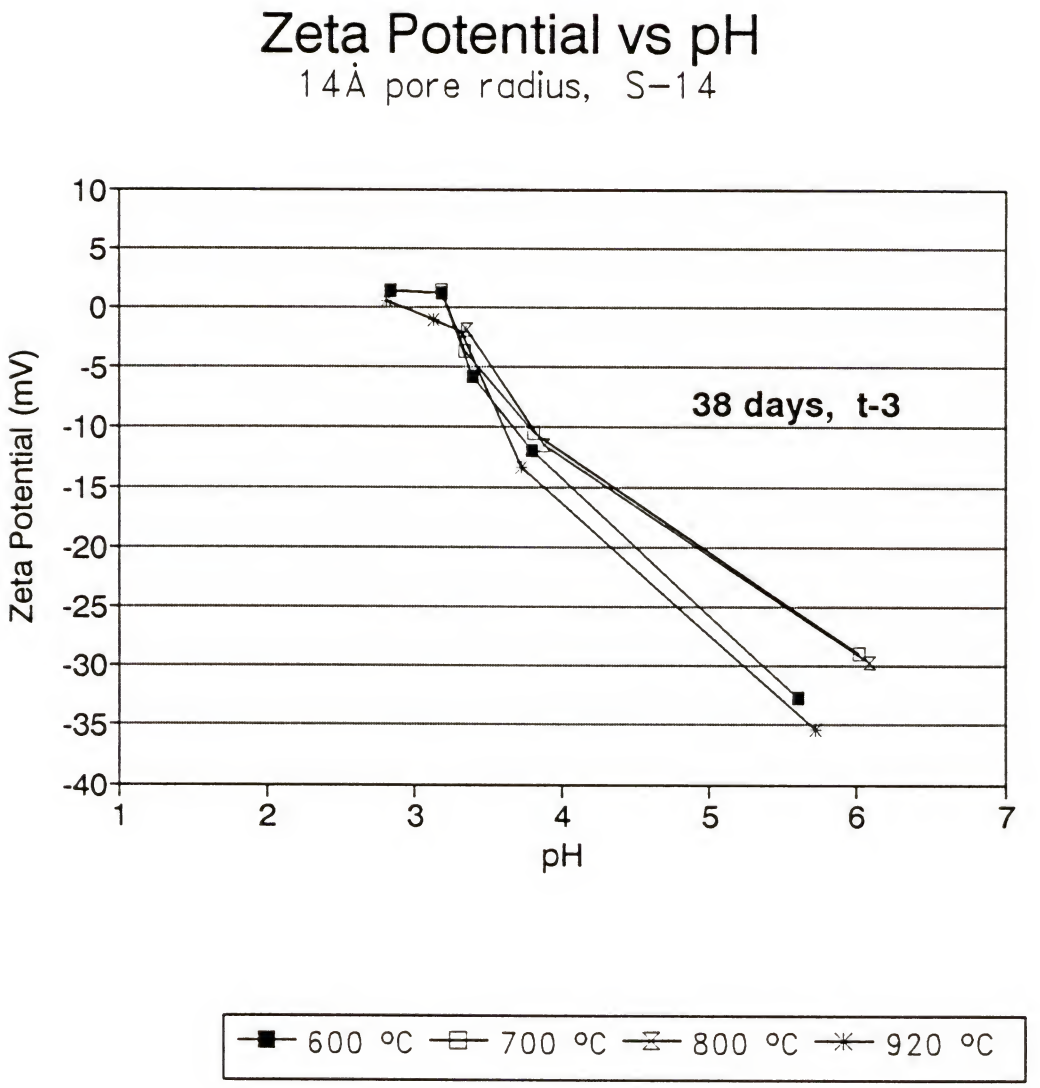

Figure 4.5 The measured zeta potential of aqueous solutions of porous sol-gel silica particles, with an average pore radius of 14 Å, is plotted as a function of solution pH and maximum gel thermal processing temperature. The measurements were taken after aging the solutions 38 days.

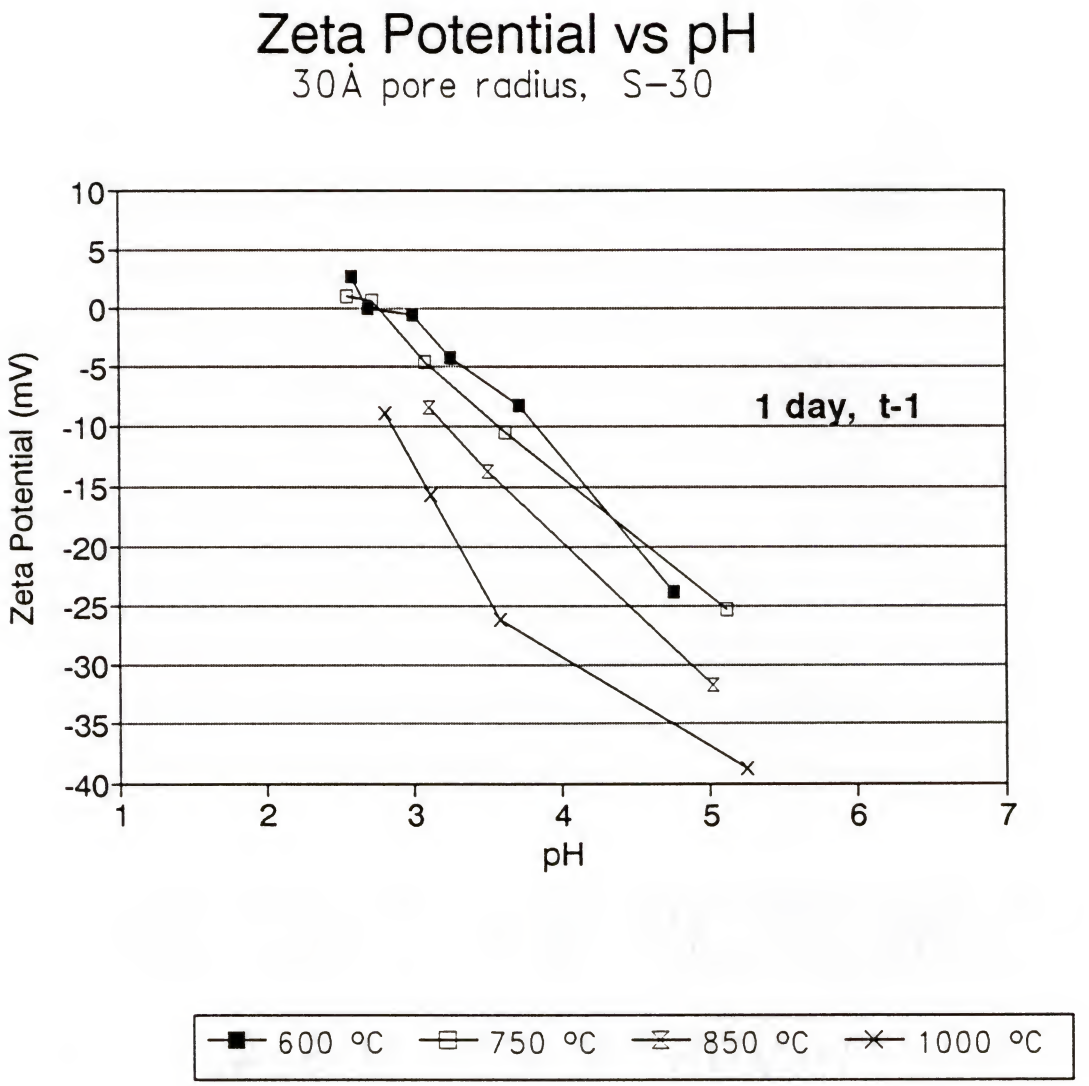

Figure 4.6 The measured zeta potential of aqueous solutions of porous sol-gel silica particles, with an average pore radius of 30 Å, is plotted as a function of solution pH and gel maximum thermal processing temperature. The measurements were taken after aging the solutions 1 day.

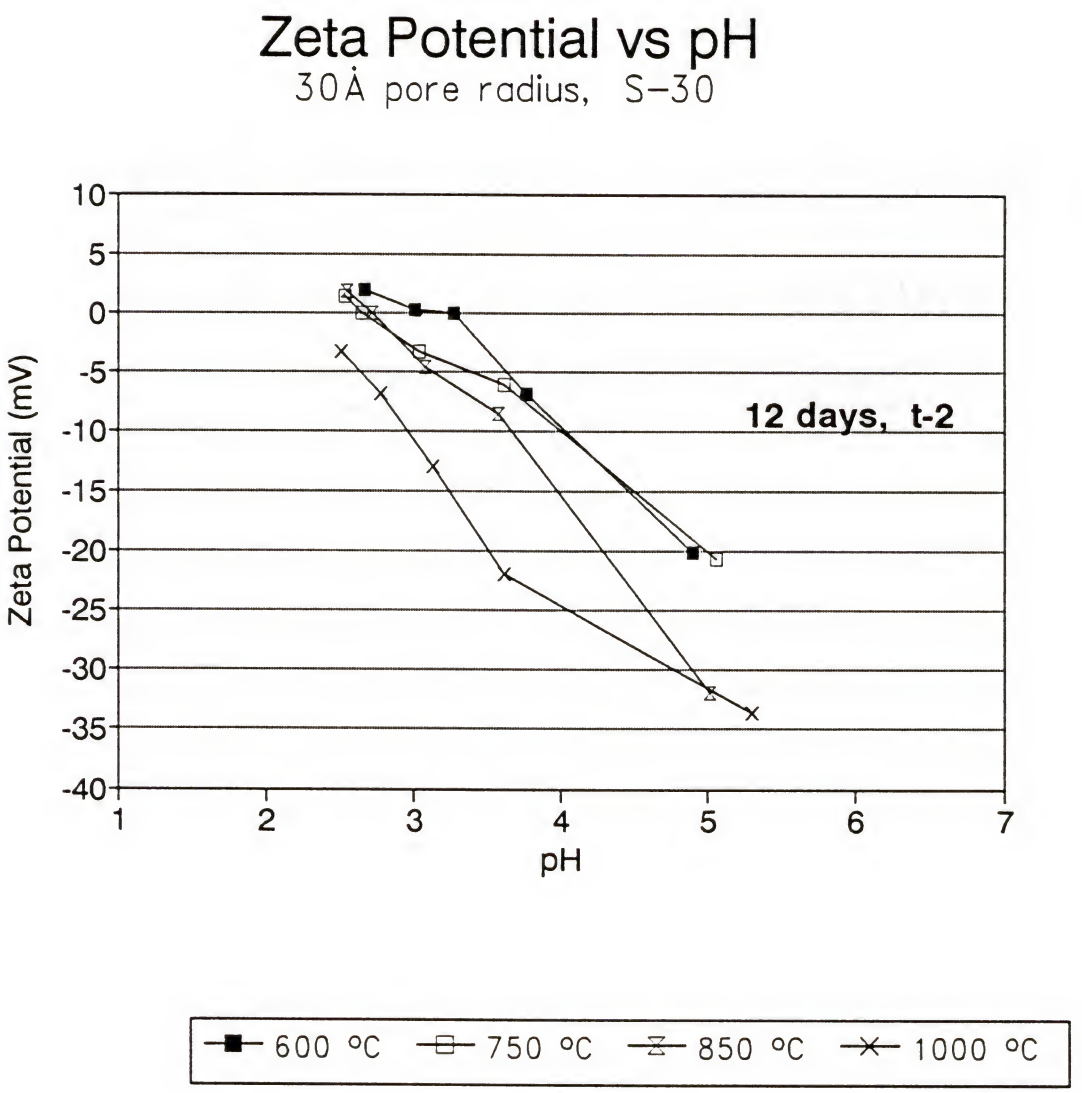

Figure 4.7 The measured zeta potential of aqueous solutions of porous sol-gel silica particles, with an average pore radius of 30 Å, is plotted as a function of solution pH and maximum gel thermal processing temperature. The measurements were taken after aging the solutions 12 days.

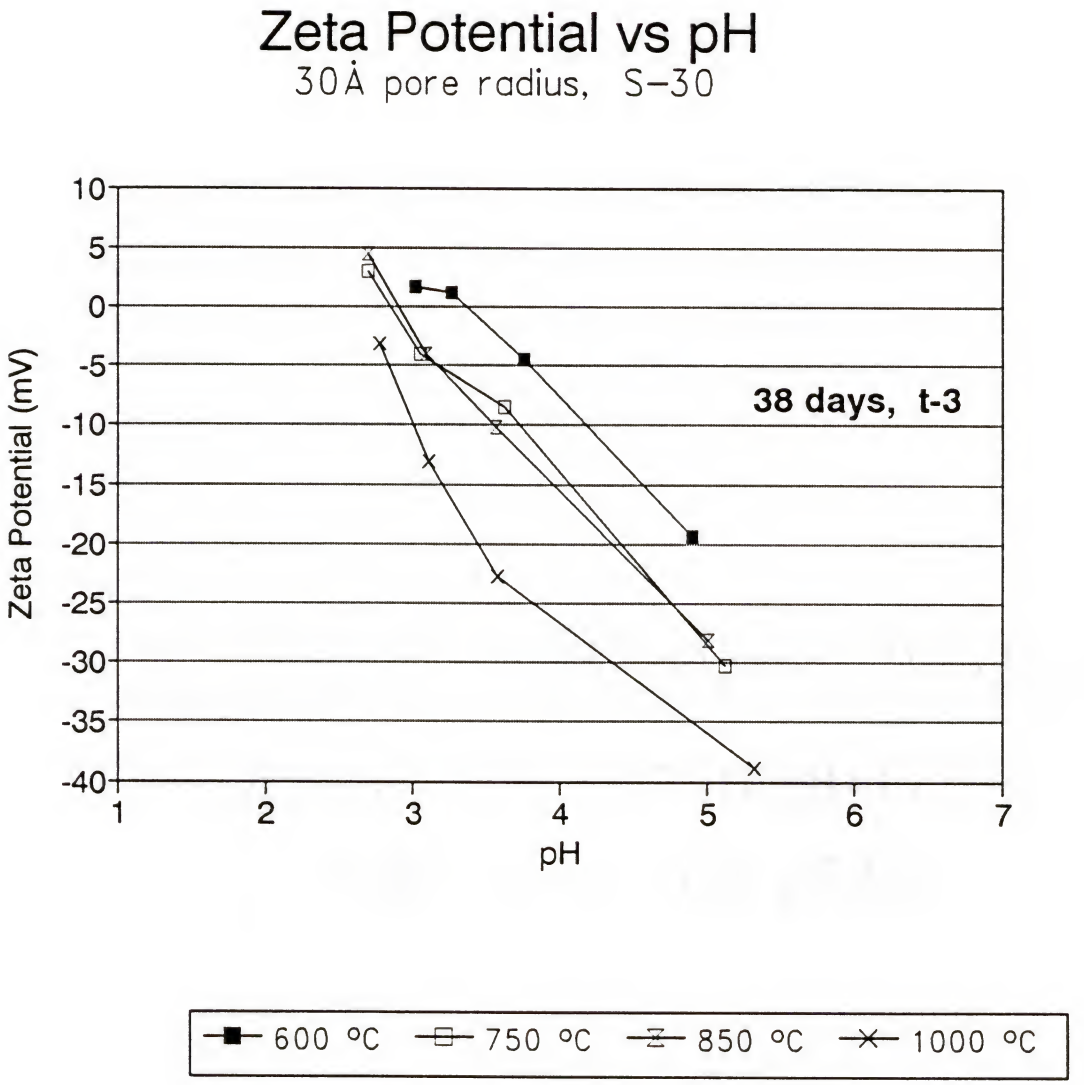

Figure 4.8 The measured zeta potential of aqueous solutions of porous sol-gel silica particles, with an average pore radius of 30 Å, is plotted as a function of solution pH and maximum gel thermal processing temperature. The measurements were taken after aging the solutions 38 days.

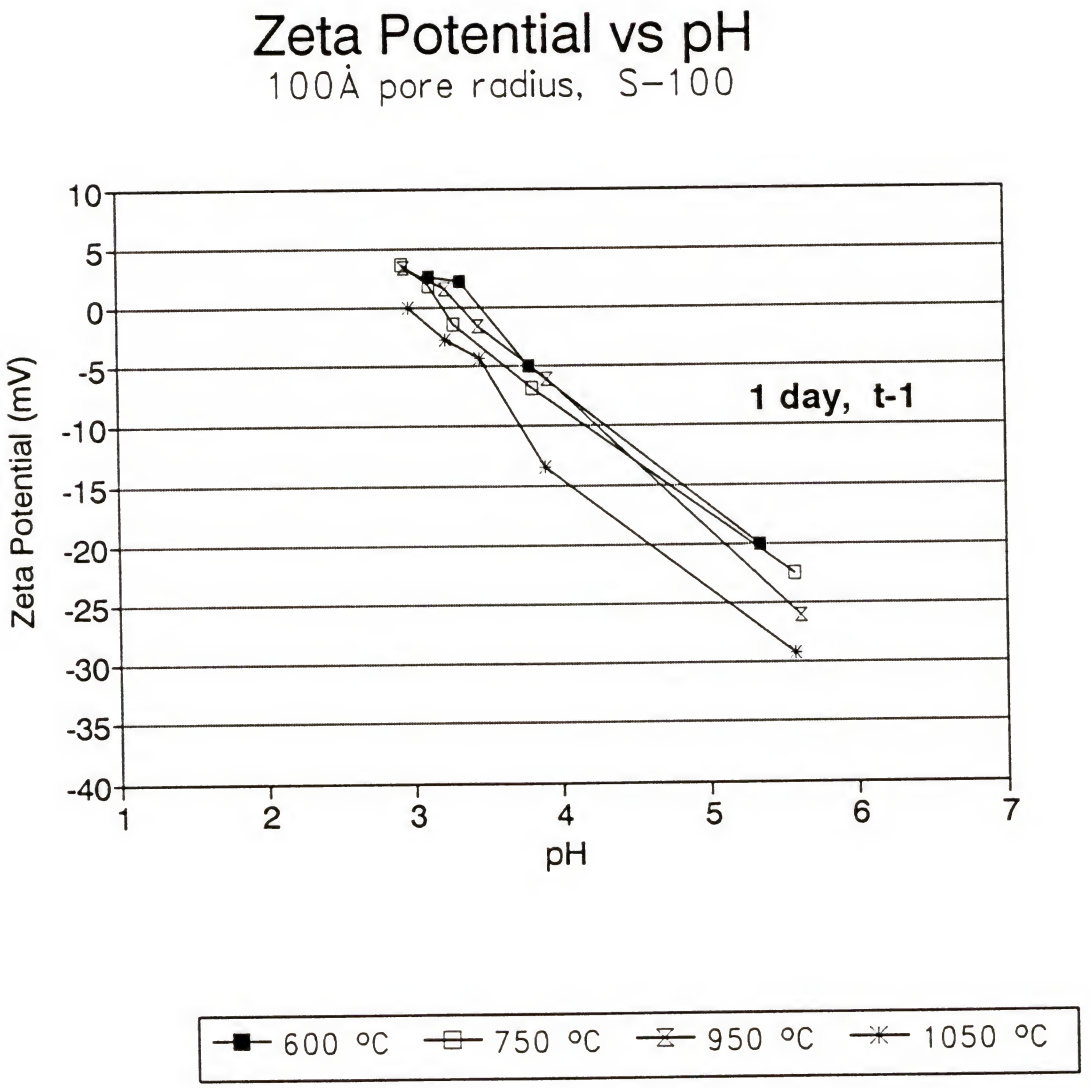

Figure 4.9 The measured zeta potential of aqueous solutions of porous sol-gel silica particles, with an average pore radius of 100 Å, is plotted as a function of solution pH and maximum gel thermal processing temperature. The measurements were taken after aging the solutions 1 day.

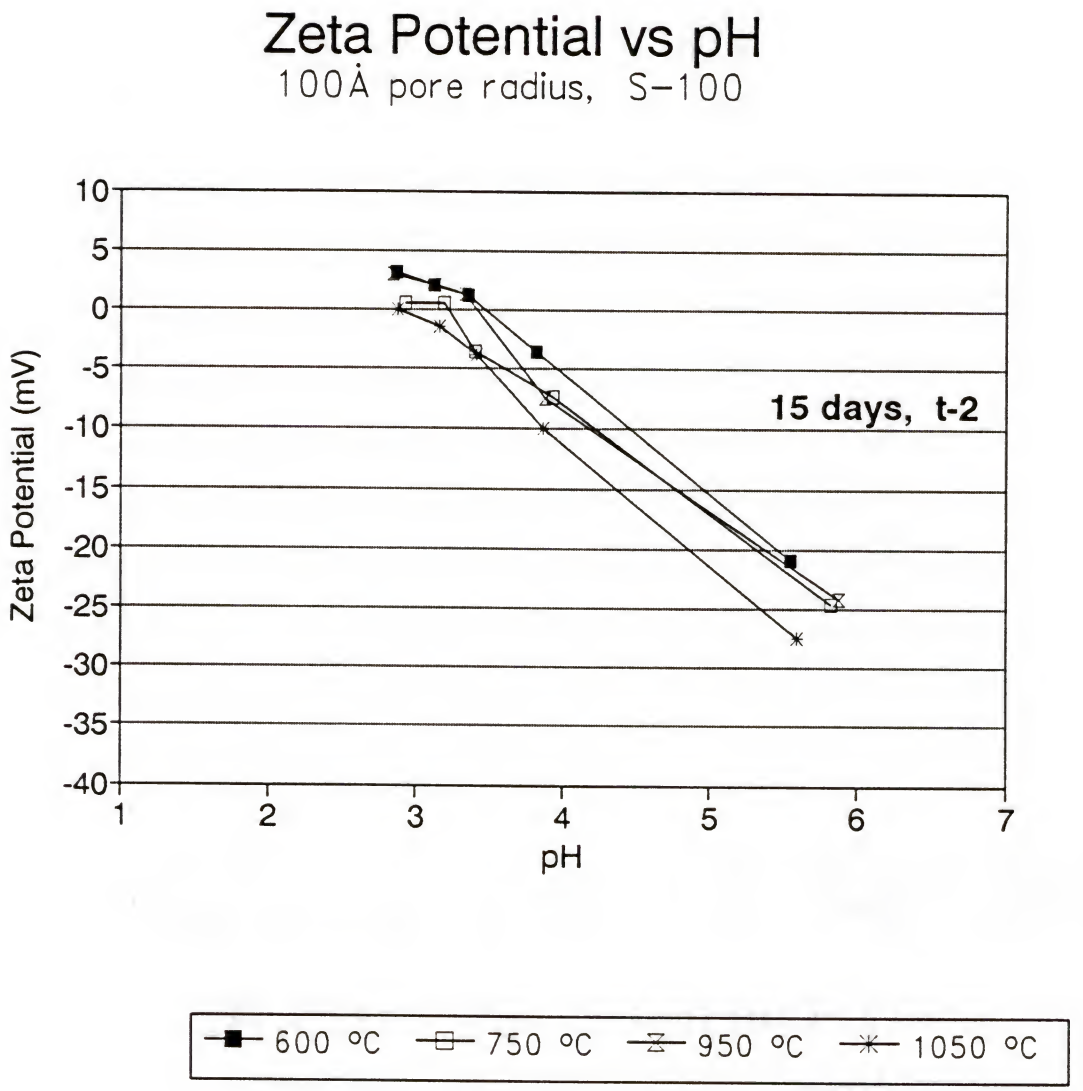

Figure 4.10 The measured zeta potential of aqueous solutions of porous sol-gel silica particles, with an average pore radius of 100 Å, is plotted as a function of solution pH and maximum gel thermal processing temperature. The measurements were taken after aging the solutions 15 days.

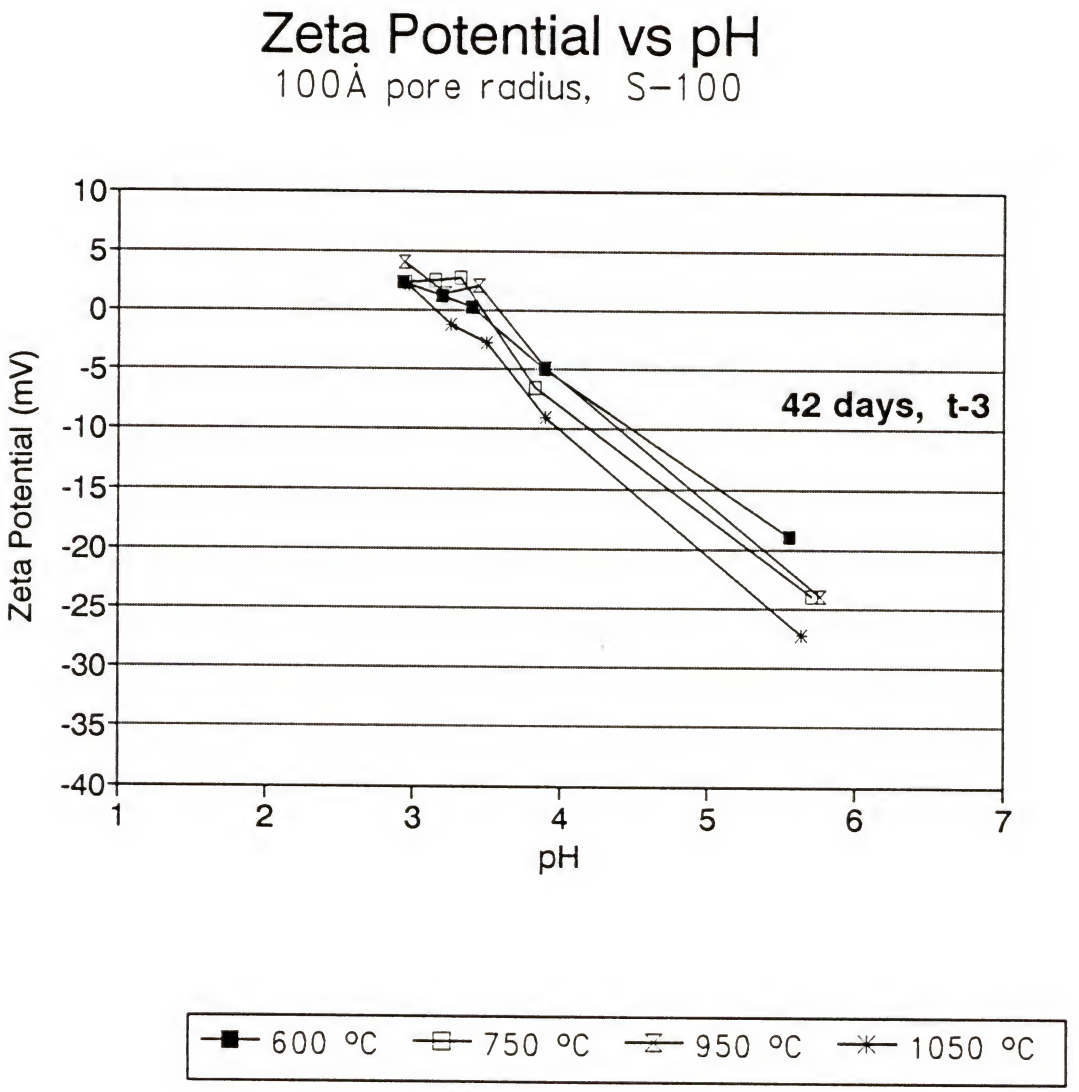

Figure 4.11 The measured zeta potential of aqueous solutions of porous sol-gel silica particles, with an average pore radius of 100 Å, is plotted as a function of solution pH and maximum gel thermal processing temperature. The measurements were taken after aging the solutions 42 days.

4.9-4.11 are for the solutions made with the 100 Å pore radius gels. These will be referred to as solutions S-14, S-30, and S-100, respectively. For each series of three figures the progression from the first to the third figure is the measured zeta potential versus pH as the solution ages. The times are approximately 1-2 days, 15 days, and 40 days, which will be referred to as t-1, t-2, and t-3.

Several trends are evident from comparing the plots at different aging times within a series for a single pore size. First, as the heat treatment temperature of the gel powder in solution is increased the IEP for the solution becomes more acidic. This is most noticeable for solution series S-30 and S-100. The IEP for the 600 °C heat treated gel is 2.9 and the IEP for the 1000 °C gel is 2.4 for aging time t-1. This is same type of trend exhibited by the S-100 and t-1 samples, which show an IEP of 3.4 and 3.0 respectfully for the 600 °C and 1000 °C gels. These trends can be seen more easily by inspecting table 4.5 or figures 4.12-4.14. Table 4.5 is a table indicating the IEP for each heat treated solution as a function of pore size and aging time. Figures 4.12-4.14 represent these same trends graphically for series S-14, S-30, and S-100.

Second, as the solution ages for samples of a given pore size the magnitude of the zeta potential decreases with time for any given pH. This is best illustrated by viewing tables 4.6-4.8. The S-14 series shows slight 2-3 mV changes while the S-100 and S-30 series show 6-7 mV and 12-13 mV changes, respectively. It is also evident from these tables that the magnitudes of the zeta potential are larger the higher the heat treatment temperature of the gels.

Table 4.5. The pH of the isoelectric point of various pore size gels as a function of heat treatment temperature and aging time in water.

Time (days)	14 Å PR Temperature (°C)			
	600	700	800	920
1-2	2.6	2.6	2.5	2.5
11-15	2.7	2.7	3.0	2.8
37-39	3.0	3.1	3.2	3.0

Time (days)	30 Å PR Temperature (°C)			
	600	750	850	1000
1-2	2.9	2.7	2.4	2.4
12-13	3.1	2.8	2.8	2.5
36-40	3.3	2.9	3.0	2.7

Time (days)	100 Å PR Temperature (°C)			
	600	750	950	1000
1-2	3.4	3.2	3.3	3.0
14-16	3.4	3.2	3.4	3.0
37-42	3.4	3.3	3.5	3.2

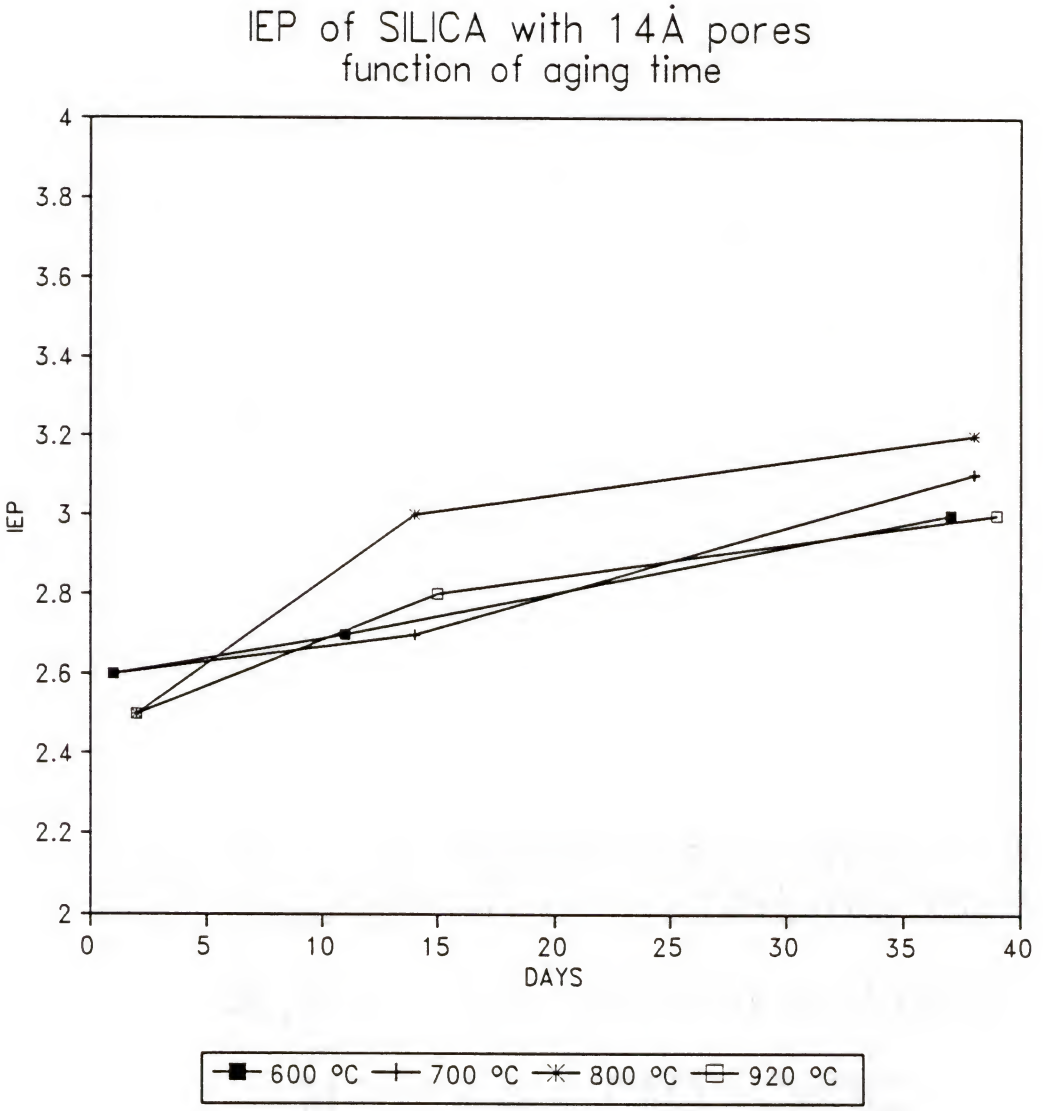

Figure 4.12 The change in IEP of an aqueous dispersion of 14 Å average pore radius sol-gel silica powder as the solution ages. The temperatures are the maximum thermal treatment temperatures for each series of powders.

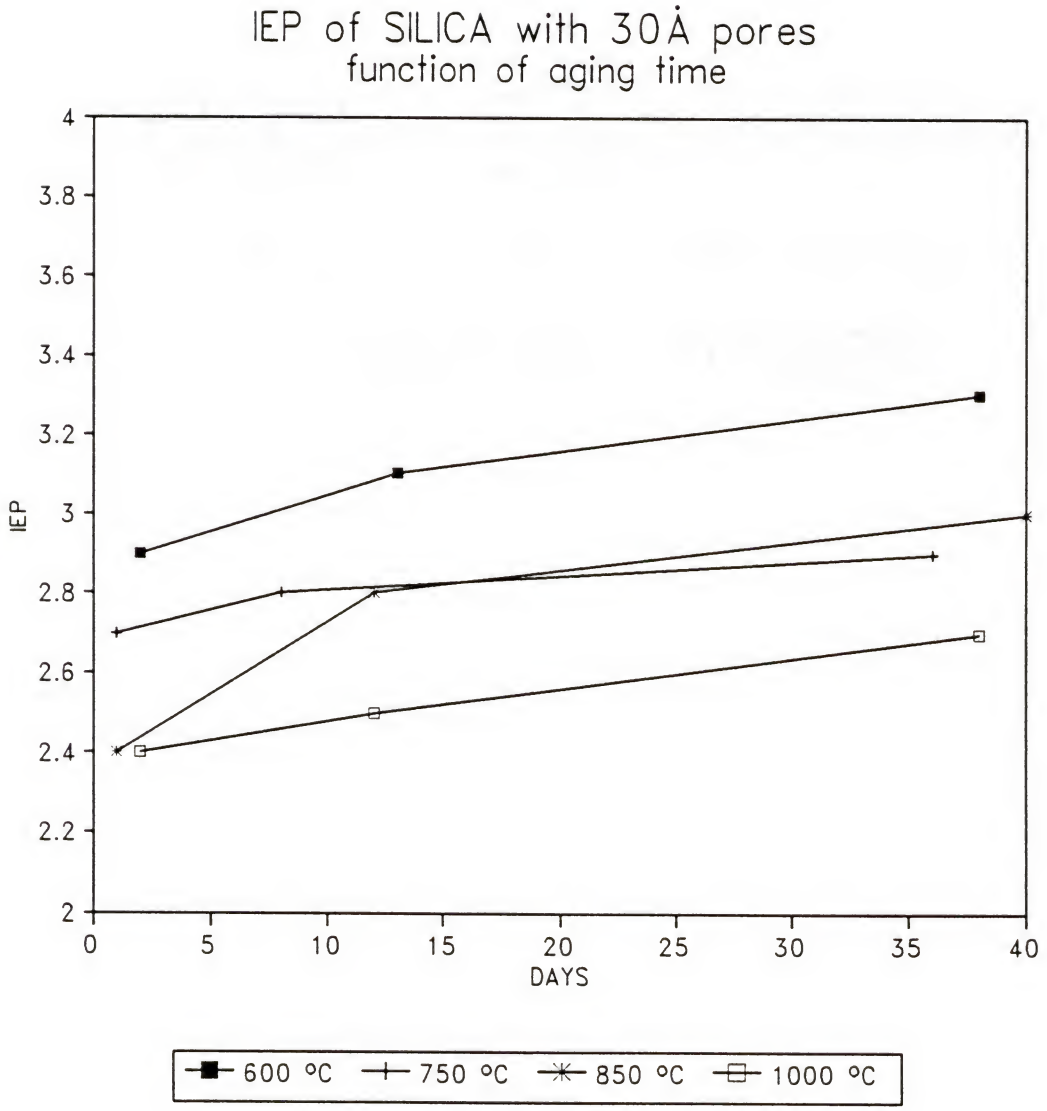

Figure 4.13 The change in IEP of an aqueous dispersion of 30 Å average pore radius sol-gel silica powder as the solution ages. The temperatures are the maximum thermal treatment temperatures for each series of powders.

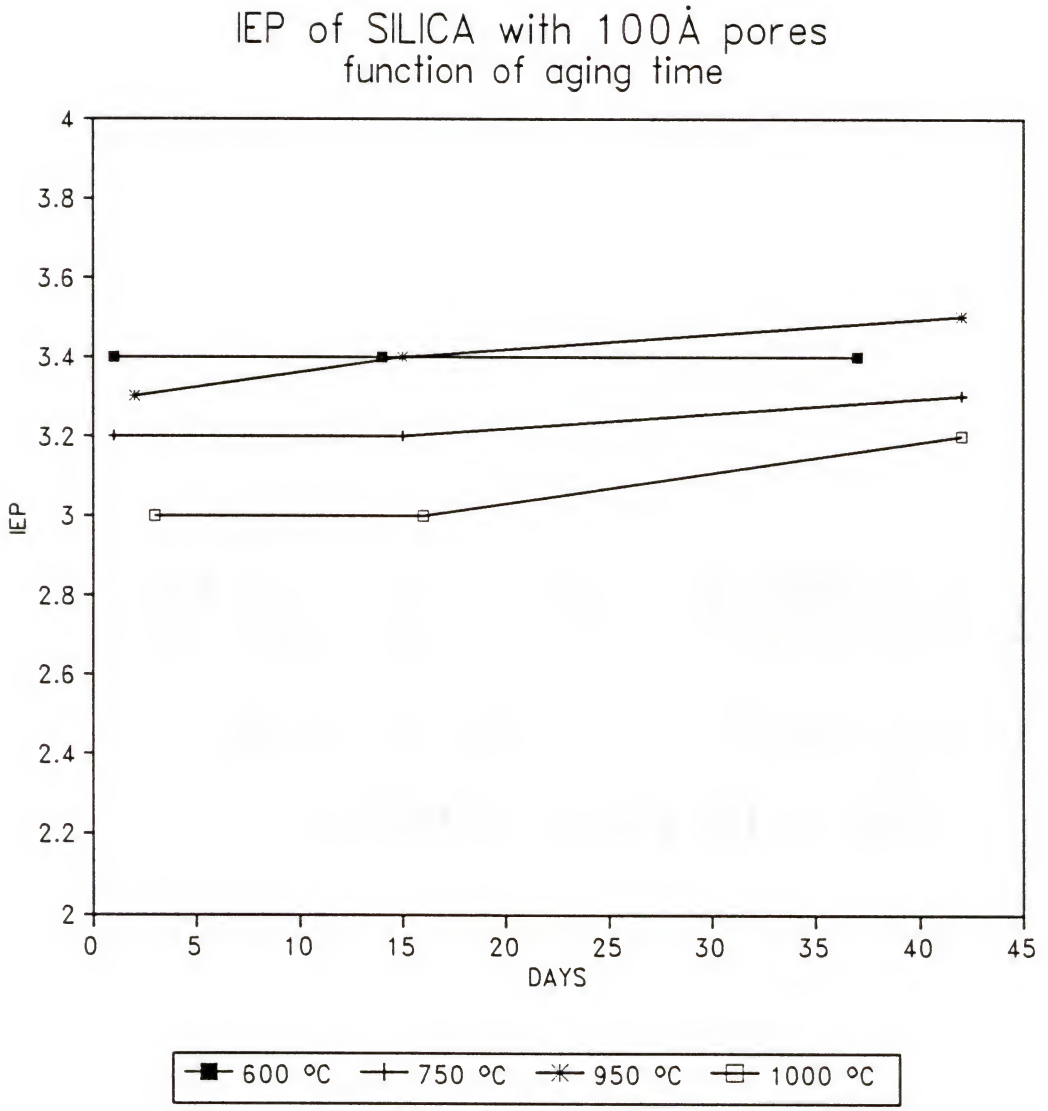

Figure 4.14 The change in IEP of an aqueous dispersion of 100 Å average pore radius sol-gel silica powder as the solution ages. The temperatures are the maximum thermal treatment temperatures for each series of powders.

There are also certain trends in comparing the IEP and the magnitude of the zeta potential between the different series of gels, S-14, S-30, S-100.

First, as the pore radii of the gels increases, the magnitude of the IEP increases at any given heat treatment temperature. This is obvious by inspecting table 4.5 or figures 4.15-4.18. A more direct comparison is made by inspecting figure 4.15 as this is the only sintering temperature in common to all three gels.

Secondly, the magnitude of the zeta potential increases as the heat treatment temperature increases. This difference in general remains constant with aging of the samples. This trend is shown in tables 4.6-4.8. The trends of the heats of immersion and the zeta potentials are discussed in the following section.

4.4.2 Discussion of Results

The heats of immersion data is complicated to interpret because multiple factors can be responsible for the generation of heat as the powders are wet by water. The heat of immersion is a combination of wetting heats (due to the replacement of a higher energy gas-solid interface with a lower energy liquid-solid interface), rehydration heats (formation of silanols), alteration of the adsorbent-adsorbate interaction due to microporosity, roughness of the surface, and the effects of any impurities.

Table 4.6 Zeta potential values(mv) for a series of 14 Å pore size gels, S-14.

# of days	Temperature (°C)	pH 3	pH 4	pH 5
1-2	600	-8	-22	-30
	700	-8	-18	-26
	800	-8	-18	-23
	920	-8	-18	-30
11-13	600	-3	-13	-25
	700	-4	-13	-22
	800	-2	-14	-21
	920	-4	-17	-28
37-39	600	2	-14	-25
	700	2	-12	-20
	800	--	-13	-20
	920	-1	-17	-28

Table 4.7 Zeta potential values (mv) for a series of 30 Å pore size gels, S-30.

# of days	Temperature (°C)	pH 3	pH 4	pH 5
1-2	600	-2	-14	-23
	750	-5	-15	-25
	850	-8	-20	-32
	1000	-15	-29	-38
12-13	600	0	-10	-20
	750	-4	-11	-20
	850	-5	-17	-28
	1000	-12	-25	-32
36-40	600	2	-8	-19
	750	-4	-13	-23
	850	-4	-15	-28
	1000	-11	-27	-37

Table 4.8 Zeta potential values (mv) for a series of 100 Å pore size gels, S-100.

# of days	Temperature (°C)	pH 3	pH 4	pH 5
1-2	600	3	-7	-17
	750	3	-7	-18
	950	3	-8	-19
	1050	0	-14	-24
14-16	600	2	-6	-15
	700	2	-8	-17
	950	1	-8	-17
	1050	-2	-12	-24
37-42	600	2	-6	-14
	700	2	-8	-17
	950	3	-6	-16
	1050	2	-10	-21

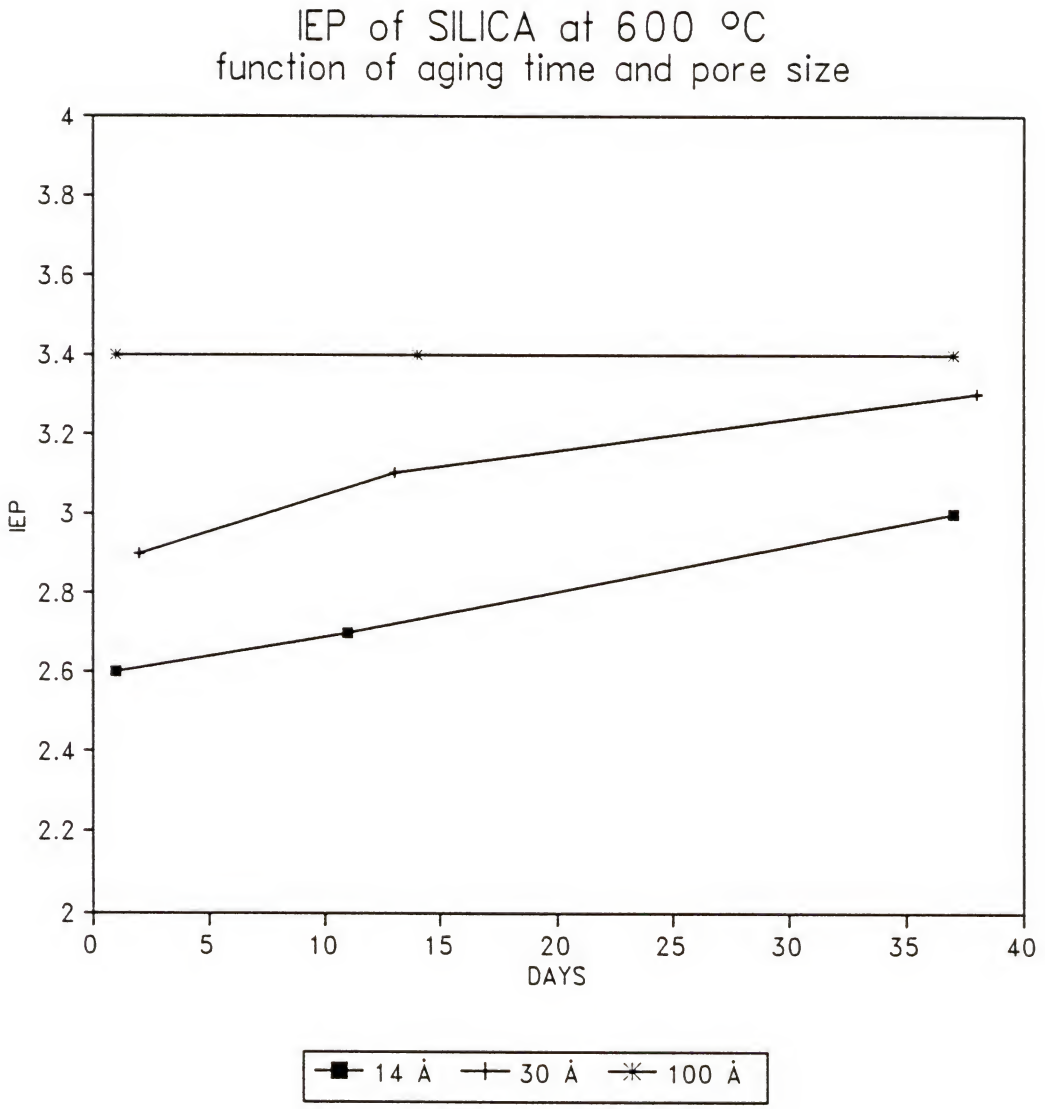

Figure 4.15 This is a plot of the change in isoelectric point of different average pore radius sol-gel silica particles in water as a function of aging time. The gels have been heat-treated in air for 5 hours at the indicated temperature.

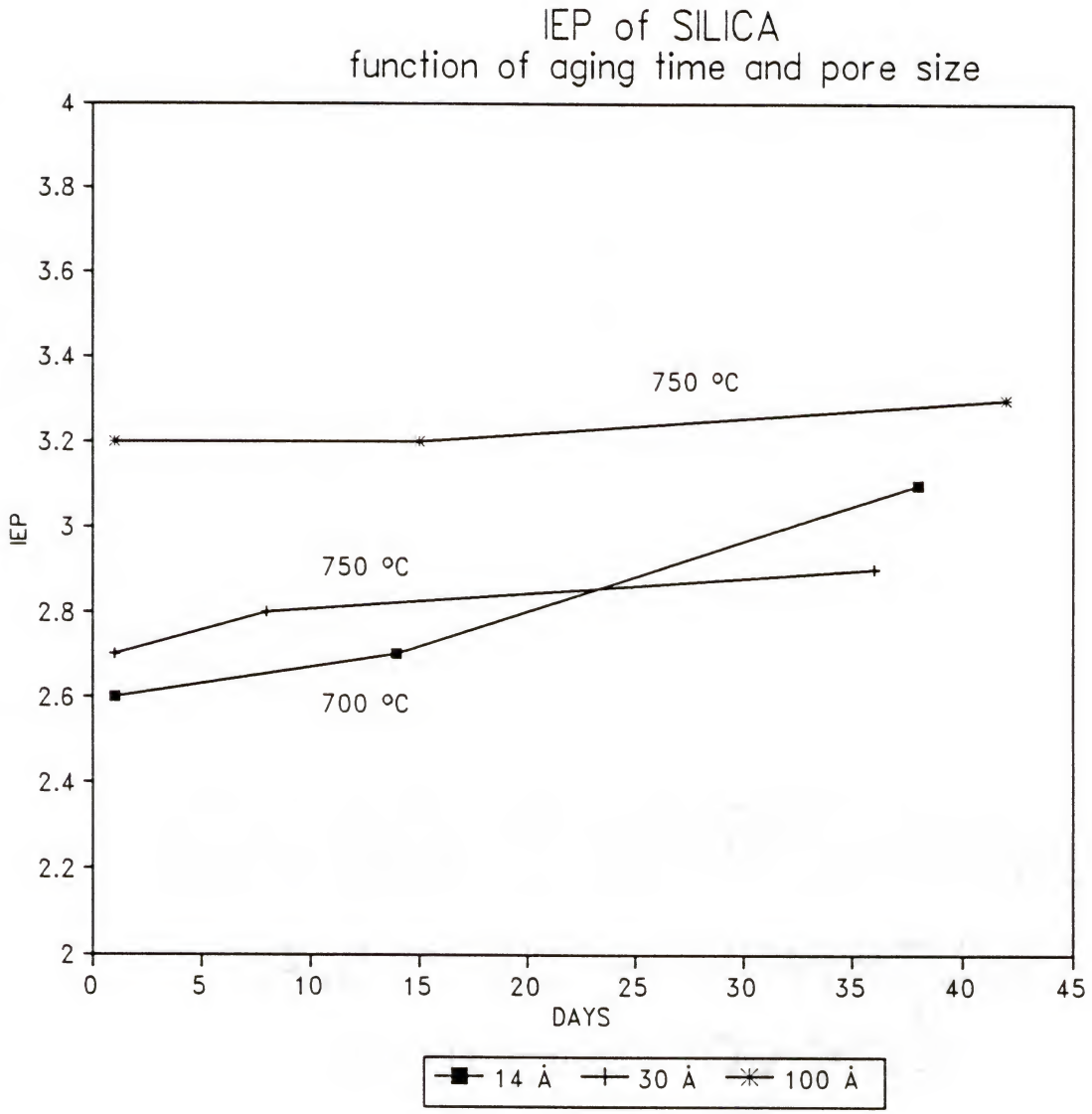

Figure 4.16 This is a plot of the change in isoelectric point of different average pore radius sol-gel silica particles in water as a function of aging time. The gels have been heat-treated in air for 5 hours at the indicated temperature.

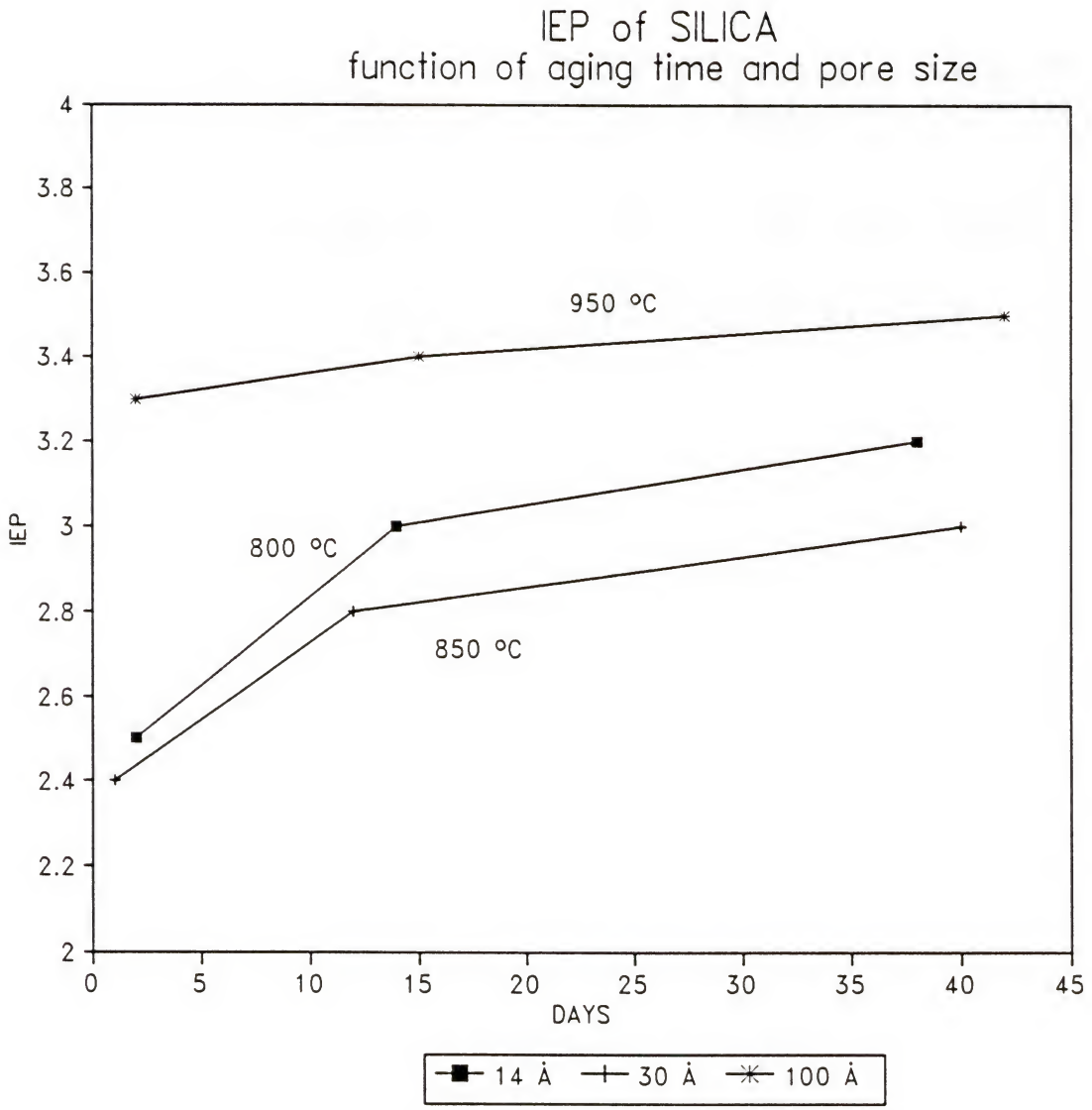

Figure 4.17 This is a plot of the change in isoelectric point of different average pore radius sol-gel silica particles in water as a function of aging time. The gels have been heat-treated in air for 5 hours at the indicated temperature.

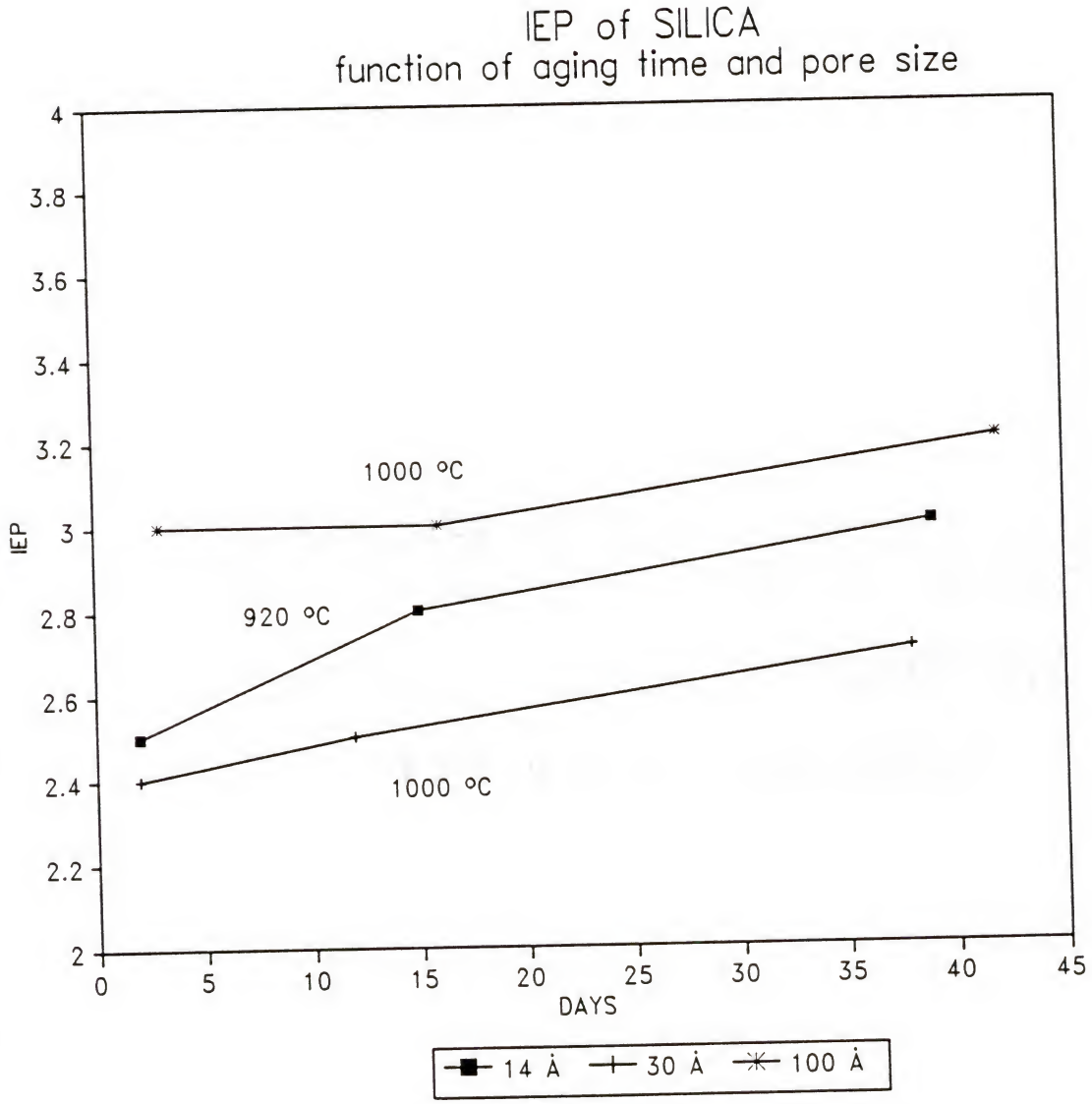

Figure 4.18 This is a plot of the change in isoelectric point of different average pore radius sol-gel silica particles in water as a function of aging time. The gels have been heat-treated in air for 5 hours at the indicated temperature.

4.4.2.1 Wetting

The heat of wetting for a silica surface which is fully hydrated ranges from 190-250 ergs/cm².[92,165,166] The range of heats for the wetting of a siloxane surface are from 50-117 ergs/cm².[92,165,166] The heats generated in this study range from a high of 164 ergs/cm² to a low of 94 ergs/cm². All of the gels except for those with the smallest pore size display heats at least as high as the maximum value from the literature in the wetting of a 100% siloxane surface. If observations are based solely upon the heat generated due to the wetting of surfaces with different silanol concentrations, the largest pore size gels are the most hydrated and the hydration of the surface decreases as the pore size decreases.

The heat of wetting decreases for gels of the same pore size as the processing temperature is raised . This is expected since the silanol concentration [OH] varies as shown in figure 4.19.[167] Relatively small changes in the [OH] concentration take place after approximately 850 °C (0.5 to 0.2 OH/nm²). However, at temperatures of 600 °C much larger [OH] are present on the gels surface (2 OH/nm²) and accordingly there are larger differences in the heats between samples with different pore sizes. This may explain the differences in the heats of immersion between the different pore sizes as the processing temperature increases. The difference between the sample pairs of, 100 Å and 30 Å, and between 30 Å and 14 Å, is approximately 30 ergs/cm² at 600 °C. This difference between the pairs decreases to about 15 ergs/cm² at 800 °C and is almost equivalent for gels heat treated at the highest temperatures.

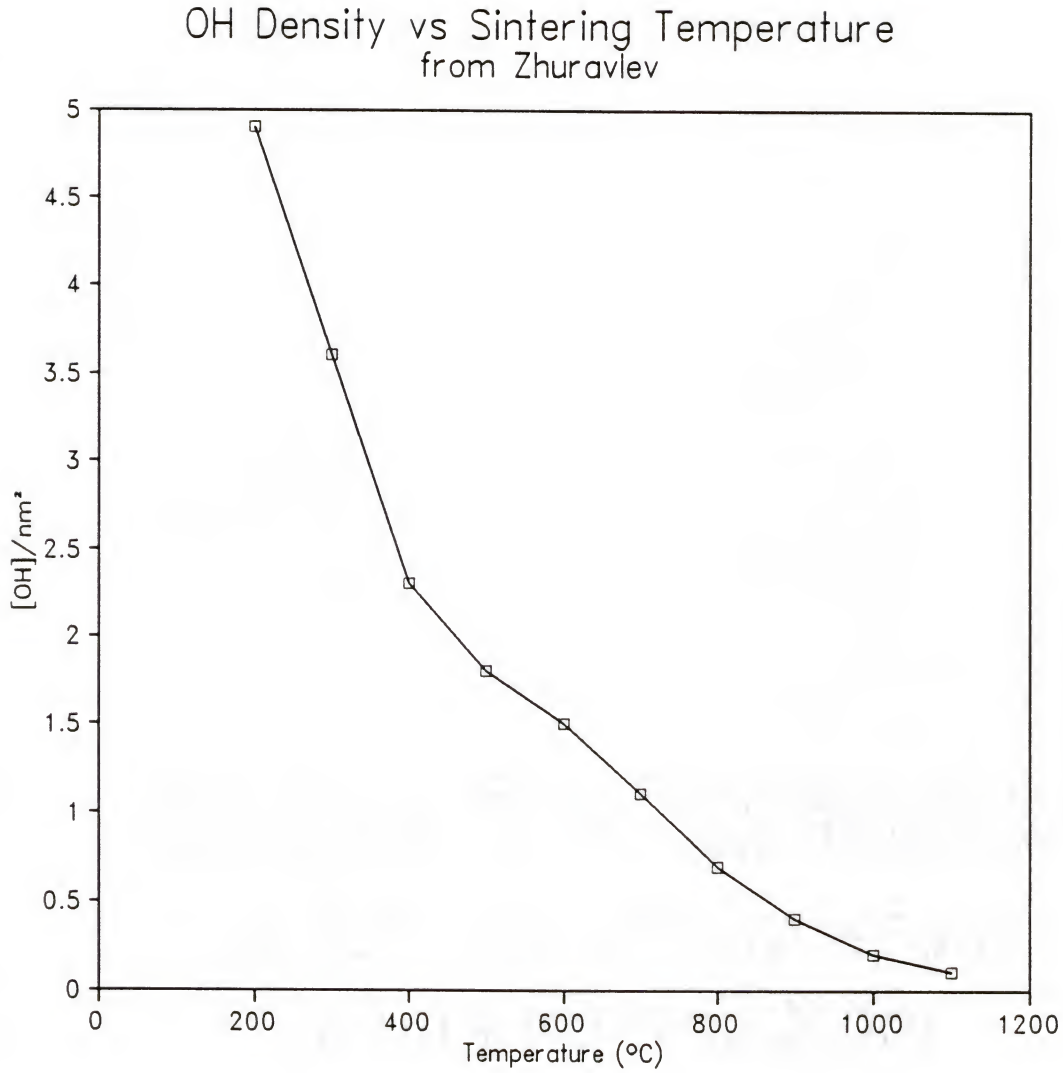

Figure 4.19 Hydroxly concentration per unit area on the surface of a silica gel as a function of the heat treatment temperature. Source: Zhuravlev [167].

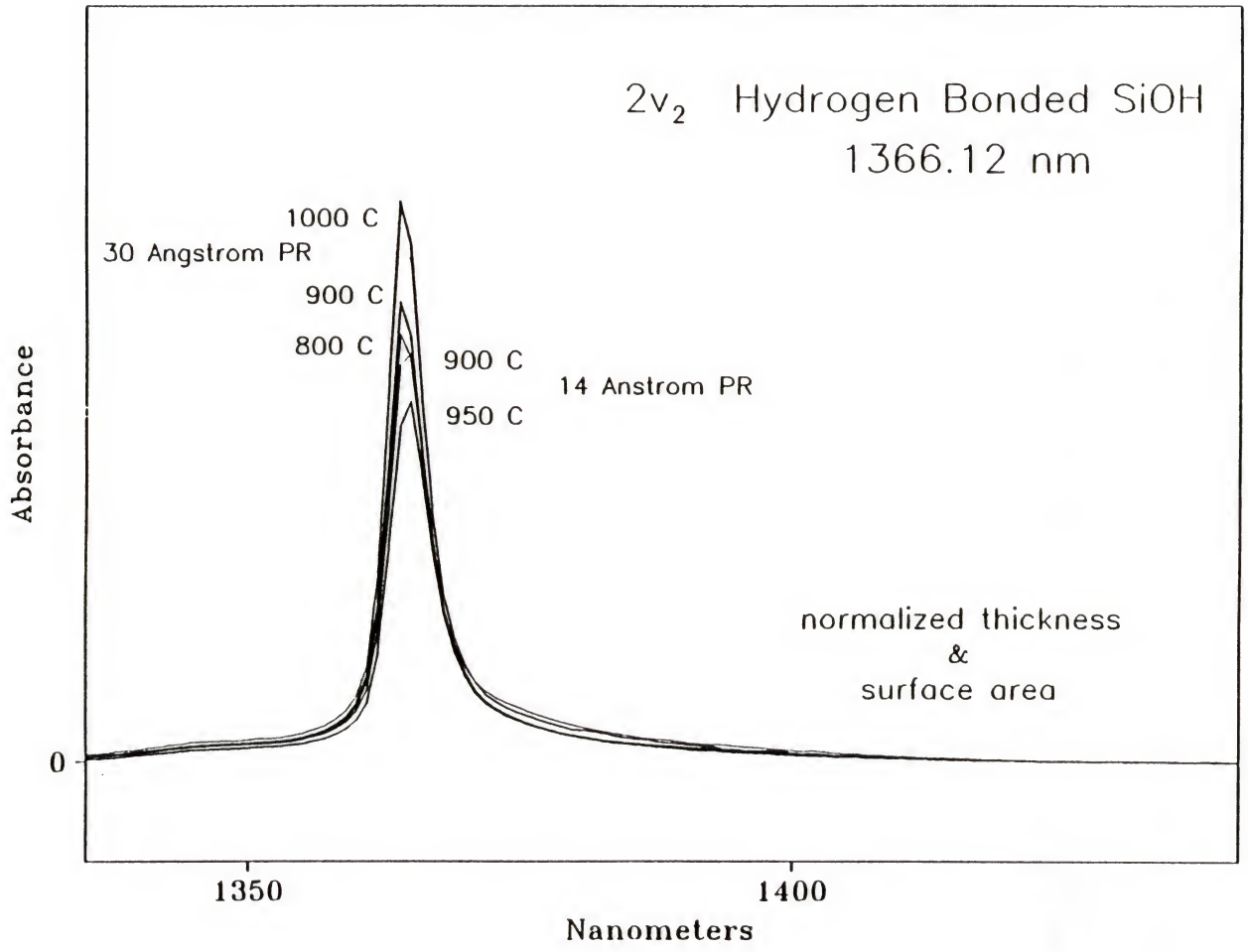

Figure 4.20 The spectra of two different average pore radii gels heat-treated at the indicated temperatures. The 1366.12 nm absorbance peak is for the hydorgen-bonded silanols, $2v_2$. The spectra are for monoliths and have been normalized for sample thickness and surface area.

Figure 4.20 is a plot of the hydrogen bonded silanol concentration on monolithic gels which have been heat treated under the same conditions. The plothas been normalized to the thickness of the gels and surface areas as determined by N_2 BET analysis. The 14 Å PR gel shows a lower hydroxyl concentration over the temperatures investigated than the 30 Å pore radius gel. However, the normalized [OH] concentration as determined from the 1366 nm peak increases with heat treatment for the 30 Å gel. This is an indication that the surfaces have rehydrated upon exposure to the laboratory atmosphere. The larger concentration of [OH] for larger temperatures is consistent with the finding of Wallace[42] who found the 3-membered ring concentration, D_2 defect, to increase linearly with heat treatment temperature. Thus, a larger concentration of 3-membered rings were formed at 1000 °C than at 800 °C and upon exposure to humid air the 3-membered rings rehydrated.[12] This peak corresponds to hydrogen bonded silanols which would be expected to form upon opening of the 3-membered rings. The rate of rehydration of the D_2 defect was already discussed in chapter 2 and is very fast relative to rehydration of a normal vitreous silica surface.

4.4.2.2 Rehydration

The heat in rehydrating a 100 % siloxane surface to a [OH] concentration of approximately 5 has been reported to vary from 130 to 200 ergs/cm².[92] This rehydration heat contributes more than the heat of wetting which varies from 60-100 ergs/cm². Since the D_2 and [OH] concentrations are not known exactly it

makes the interpretation of the heats of immersion difficult. However, the increase in the hydrogen bonded [OH] concentration, as determined in the near-infrared, indicates that the D_2 defects may have largely been eliminated by atmospheric humidity prior to immersion. This may have been enhanced during preparation of the gels as they were ground into powders, as has been shown to increase the hydration of the silica gels.[160] The atmospheric exposure time was minimized during grinding (less than 20 min) but evidently was sufficient to rehydrate the D_2 defects, based upon similar work.[160]

The magnitudes of the heats would be much higher if rehydration of the surface was a significant portion of the total heat generated. The wetting of a 100 % siloxane surface would be between 60 and 100 ergs/cm^2. Add to this the range of hydration heats, 130 to 200 ergs/cm^2, and the total from wetting and rehydrating would be 190 to 230 ergs/cm^2 at a minimum and could approach 300 ergs/cm^2. These heats are substantially higher than the heats reported in this study.

4.4.2.3 Microporosity and surface roughness

Microporosity had been shown to interfere with heat of immersion measurements by modifying the adsorbent-adsorbate interaction.[92] The isotherms and pore size distribution from the BET analysis indicate the presence of micropores for all of the samples but the largest, 100 Å, base aged gel. This gel shows a continual decrease in the heat if immersion with thermal treatment

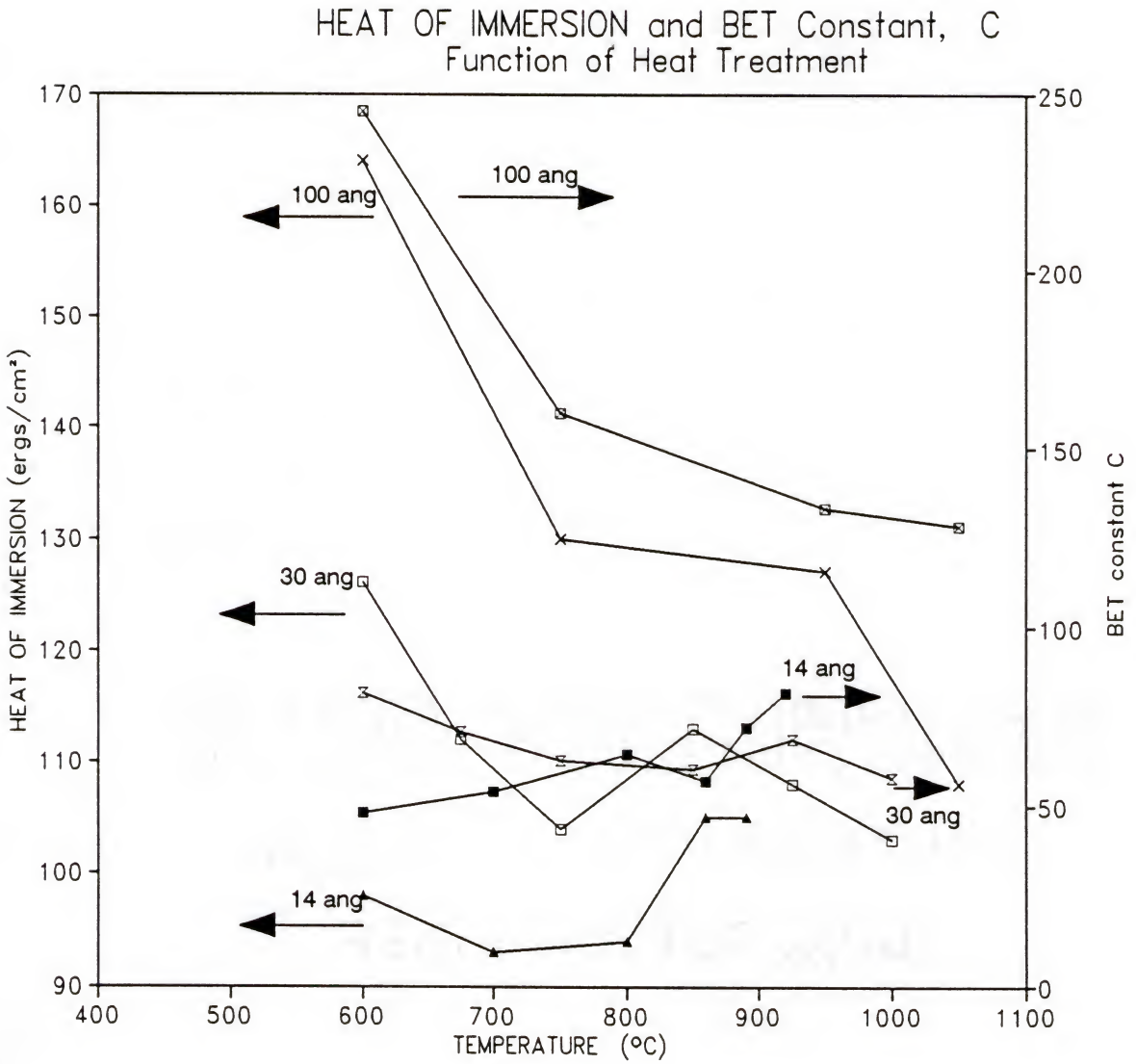

Figure 4.21 The aqueous heats of immersion of porous gel silica powders with the different average pore radius indicated. The BET constant is plotted for the same series of powders as determined from N_2 isotherms.

temperature. The other gels may show more complicated behavior in the heats of immersion after higher temperature temperatures. An error analysis determined that these changes may not be statistically significant. If they are they may be explained by a plot of the BET constant, C, and the heats of immersion, as shown in figure 4.21.

Quantitatively, the change in C correlates with the heats of immersion. This may be expected since C is a parameter in the BET equation which is approximated by $C = \exp(\text{heat of adsorption})$[119] although N_2 is not assumed to interact significantly with the silica surface. Qualitatively, as C increases the adsorbate molecules move more closely into registry with the structure of the surface. Also, the adsorbate cross-sectional area becomes increasing dependent upon the dimensions of the adsorbent. In addition, C increases as the microporosity of the porous material increases due to overlapping wall potentials. The values of C for the 12 and 14 Å pore radius gels increases with the heat treatment temperature. The larger pore size gels have a decreasing value of C with heat treatment temperature.

Thus, the larger pore size gels display progressively lower heats of immersion and a simultaneous decrease in the BET constant for increases in the thermal treatment temperature. The reduction in interaction energy is presumably do to the removal of silanols from the surface although structural changes of the silica could be partly responsible. These heats of immersion are higher than the smaller pore size gels which contain more microporosity and lower values of C as

seen in the pore size distribution curves of figure 3.6 and table 4.1. Along the same line of reasoning, the roughness of the surface will decrease the homogeneity of the surface. If the roughness of the surface is the same order of magnitude as the size of the adsorbate significant reductions in interactions may occur. Brinker[12] discusses the fractal dimension of sol-gel silica. He sites values from the literature of the fractal dimension of the surface, d_s, of gels ranging from 30-50 Å in radius, to be 2.3-2.8. According to Farin[168] the apparent surface area measured by another molecule relative to N_2 is related to the ratio of the cross-sectional diameters and d_s. Water has been shown to have a cross-sectional area, at the surface of a polar adsorbent, of 20-25 Å^2. This is larger than the 16.2 Å^2 cross-sectional area for the N_2 molecule. These values inserted into Farins' equation produce a 25% reduction in the surface area contacted by the water molecule. This indicates that the larger the fractal dimension of the surface the larger will be the difference of the two effective areas seen by each molecule. Thus, during immersion the water might be interacting with a rougher surface for the smaller pore size gel and effectively wetting a smaller surface area. If the surface area determined by the N_2 molecule is used then the normalized heat is too small. One would assume that base aging of the gel has the effect of smoothing out the gel, allowing a stronger interaction of the water with the surface because of the decrease in microporosity and decrease in surface roughness. This could account for 25% of the difference in the heats of immersion between the largest pore size and the samples with microporosity observed in figure 4.2.

4.4.2.4 Impurities

The large difference in the heat of immersion for the base- aged gel could also be due to the residual presence of NH_4OH for the aging process. NH_3 may be present in large enough quantities to alter the heats. It is assumed that since NH_3 is a polar molecule its presence would increase the heat of immersion. However, it seems likely that for heat treatments in excess of 600 °C for 5 hours and some cases 25 hours the ammonia would be removed from the gel. These gels were heat treated in a box furnace which is not as effective as a tube furnace with flowing air in the removal of sintering byproducts. No independent tests for ammonia were conducted, however Orcel's[3] studies on the removal of formamide during sintering of silica gels indicate that ammonia should be cracked and removed by the 600 °C heat treatment.

A discussion now ensues of the measurements of the zeta potential of the same powders. Correlating results between the heats of immersion and the zeta potential are included. The relations will be summarized more formally in the conclusions of this chapter.

4.4.2.5 Zeta potential

Differences in the zeta potential measurements of the gel powders exist with heat treatment temperature, pore size, and aging. These differences are visualized through the IEP or the pH value at zero potential and the absolute magnitude of the zeta potential at pH's other than the IEP. These trends are first discussed for

each of the pore sizes as a function of heat treatment, followed by the differences between the pore sizes, and conclude with the affects of aging.

The IEP was very difficult to obtain for solutions below 2.5 pH or 0.05 M. The values are extrapolated from the curve which is more linear then a zeta potential curve versus pH in the presence of a background electrolyte. The linearity is because the ionic strength and the pH are varying simultaneously. However, the linear shape of the curve makes the extrapolation easier and thus increases the accuracy of the IEP value. Also, by limiting the lower limit upon which the zeta potential was measured these values become more real because of the lower error associated with lower conductivity solutions. The accuracy of the IEP values are at best ± 0.2 pH units. The large number of samples analyzed at each pH created an average value of IEP with a more meaningful statistical significance.

The solutions of the 14 Å pore radius gel powders, S-14, at short times, t-1, exhibit small changes between the heat treatment temperature and the IEP (see table 4.5 or figure 4.3). This is the same trend regardless of the aging time. The series of 30 Å gels, S-30, displays a much larger difference between the IEP and the heat treatment temperature. The IEP in table 4.5 for the 600 °C gel powder is 2.9 and for the 1000 °C it is 2.4. The series of 100 Å pore size gels, S-100, also displays the same behavior; the 600 °C heat treated gel gives an IEP of 3.4 and

1000 °C heat treated gel gives a value of 3.0. This is expected, as in related studies,[160] treatments which dehydrate the gels shift the IEP towards more acidic values.

In the discussion of the heats of immersion it was assumed that the gels heat treated at higher temperatures had a lower [OH] concentration. This is confirmed by the initial value of the IEP for the three series of gels. The IEP for the S-14 series is initially 2.5-2.6, the lowest value of the IEP measured. Conversely, the heats of immersion are the lowest for this series of gels. One would expect the heats of immersion to be approximately constant with heat treatment temperature for this series of gels if the IEP values are an indication of the surface hydration. The heats of immersion are essentially constant from 600 to 800 °C but then increase upon further heat treatment. As discussed in the prior section, the increase in the heat of immersion at higher densification temperatures may be explained by a decrease in surface roughness and therefore not related to the [OH] concentration.

The IEP pH's for the S-30 and S-100 gels as a function of thermal treatment are consistent with the heats of immersion data. The 600 °C stabilized gels for both series produce the largest heats of immersion, and the largest IEP values. The 1000 °C sintered gels which show the lowest heats of immersion, show the lowest IEP value. Also, the heats of the S-100 series, which has the largest value

of the IEP, produced the most heat upon immersion in water. Accordingly, the S-30 series produced intermediate heats between the largest, S-100, and smallest, S-14, pore sized gels.

Studies by Healy and Fuerstenau[169] related the zero point of charge and the heat of immersion for different oxides to the electrostatic field strength of each of the oxides. A linear relation was derived between the heat of immersion and the zero point of charge. A later study[170] found a similar linear correlation between the heats of immersion and the zero point of charge for a series of MnO_2 particles. Even though the same relationship is found in this study the electrostatic field strength cannot be correlated to the heats of immersion and IEP in this study because of the uncertainty of the amount of hydration and the microporosity present in the porous silica gels. The previous studies were conducted on solid particles.

The relative magnitude of the zeta potential values at pH's other than the IEP, indicate a change with heat treatment temperature for the S-14, S-30, and S-100 series. The trend is an increase in the electrophoretic mobility of the S-30 and S-100 series as the heat treatments temperatures are increased, or as the volume fraction of pores is decreased. The values of the zeta potential for the three series of gels, at pH's of 3, 4, and 5, are given in tables 4.6-4.8 as a function of heat treatment temperature. Differences of 7-8 mV exist between the highest and lowest heat treated gels for the S-100 series, while differences of 12-13 mV exist between the highest and lowest heat treated gels for the S-30 series. The values of the zeta

potential for the S-14 series, as a function of heat treatment temperature remain essentially constant. It appears that for a pH of 5 the zeta potential values decrease from -30 mV at 600 °C to -26 and -23 mV as the heat treatment temperature is increased to intermediate temperatures and then back to a value of -30 mV at the highest heat treatment temperature of 920 °C. However, the differences between the zeta potential values at the other two pH's, 3 and 4, as a function of heat treatment temperature do not show any significant difference. The differences between the high and low zeta potential values at pH's, 3 and 4, for the S-30 and S-100 series are consistent with the differences at pH 5. A plot of volume fraction or heat treatment temperature versus the zeta potential for any given pH should produce the same slope.

Figures 4.22-4.30 plot the zeta potential versus the volume fraction of pores, at the three different pH's, 3, 4, and 5, for the three different series of gels. It is indeed evident that the slope remains constant for the S-30 and S-100 series as the pH changes, figures 4.25-4.30. The slope of the plot of the S-14 gels, figures 4.22-4.24, is not constant. Figure 4.24, at pH 5, displays a maximum in the zeta potential versus volume fraction plot, as mentioned above. The plots in figures 4.22 and 4.23 indicate constant or linear relationships. The maximum may be related to both the surface area and the volume fraction. Also, it may not be appropriate to compare the S-14 series to the S-30 and S-100 series since most of the zeta potential measurements for the S-30 and S-100 series were made on gels with volume fractions of porosity 2 to 3 times that of the S-14 gels. The

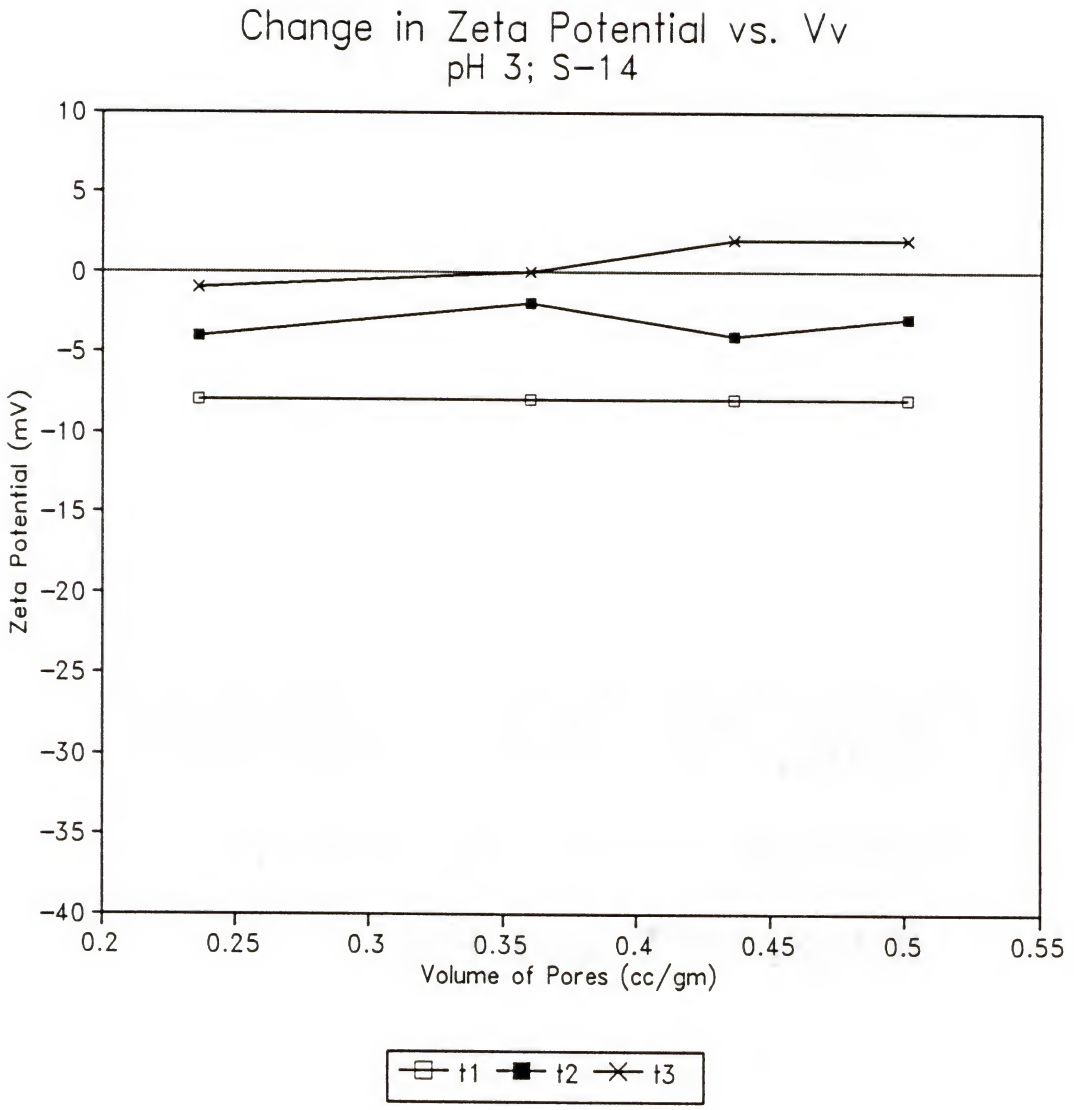

Figure 4.22 The change in the zeta potential as a function of pore volume, for the S-14 series of porous gel powders at pH 3. The variables t-1, t-2, and t-3, represent the different aging times in solution from tables 4.2 - 4.4.

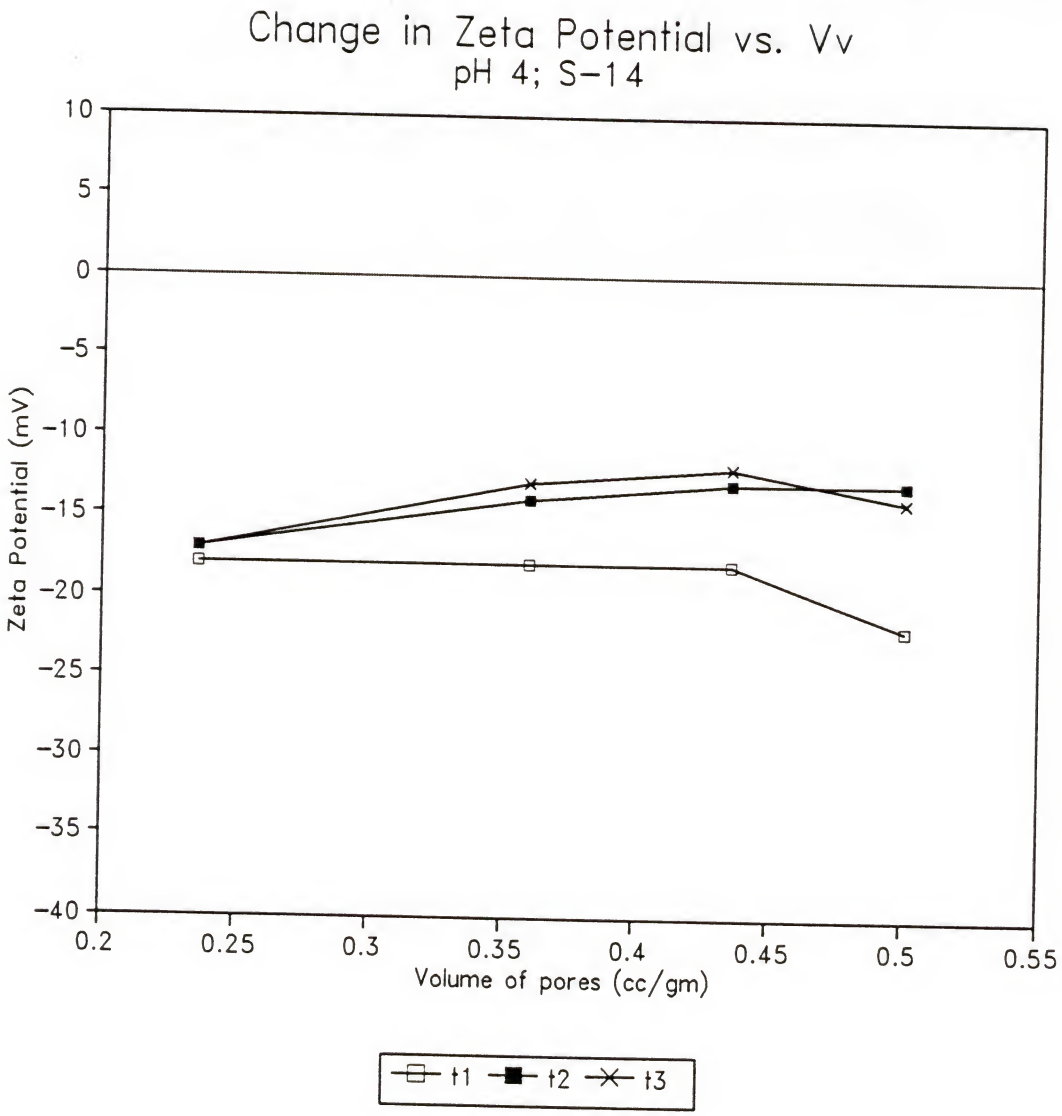

Figure 4.23 The change in the zeta potential as a function of pore volume, for the S-14 series of porous gel powders at pH 4. The variables t-1, t-2, and t-3, represent the different aging times in solution from tables 4.2 - 4.4.

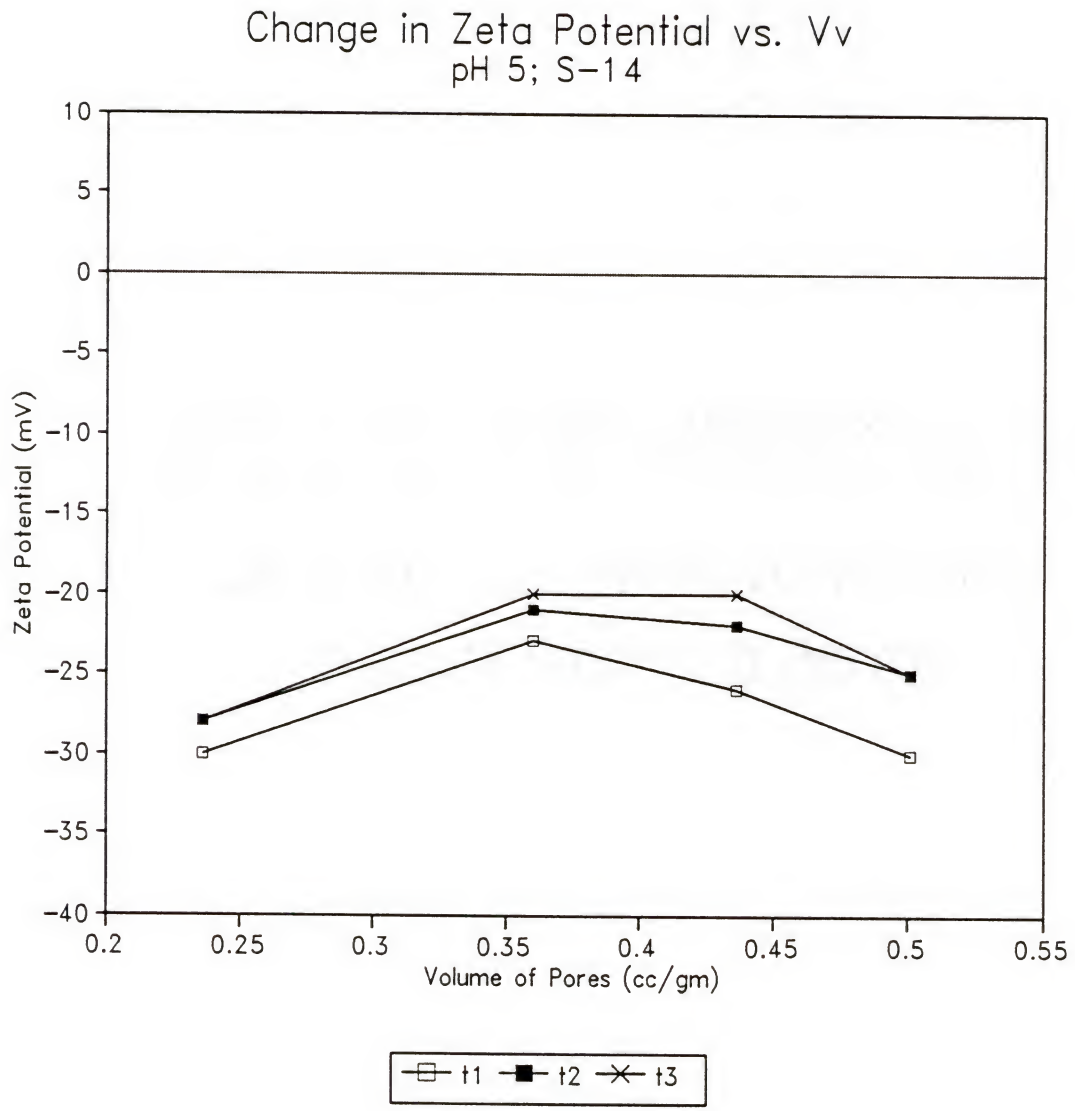

Figure 4.24 The change in the zeta potential as a function of pore volume, for the S-14 series of porous gel powders at pH 5. The variables t-1, t-2, and t-3, represent the different aging times in solution from tables 4.2 - 4.4.

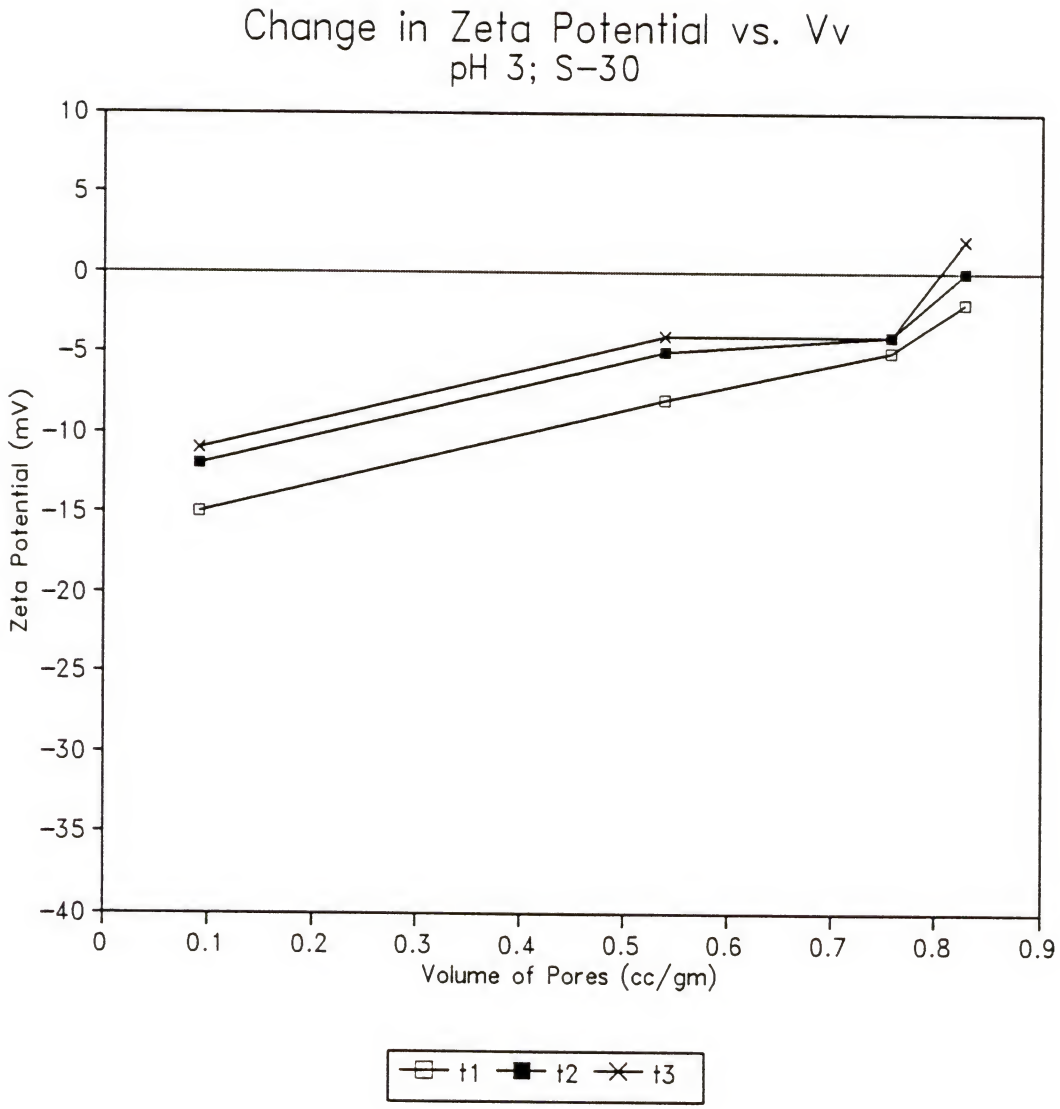

Figure 4.25 The change in the zeta potential as a function of pore volume, for the S-30 series of porous gel powders at pH 3. The variables t-1, t-2, and t-3, represent the different aging times in solution from tables 4.2 - 4.4.

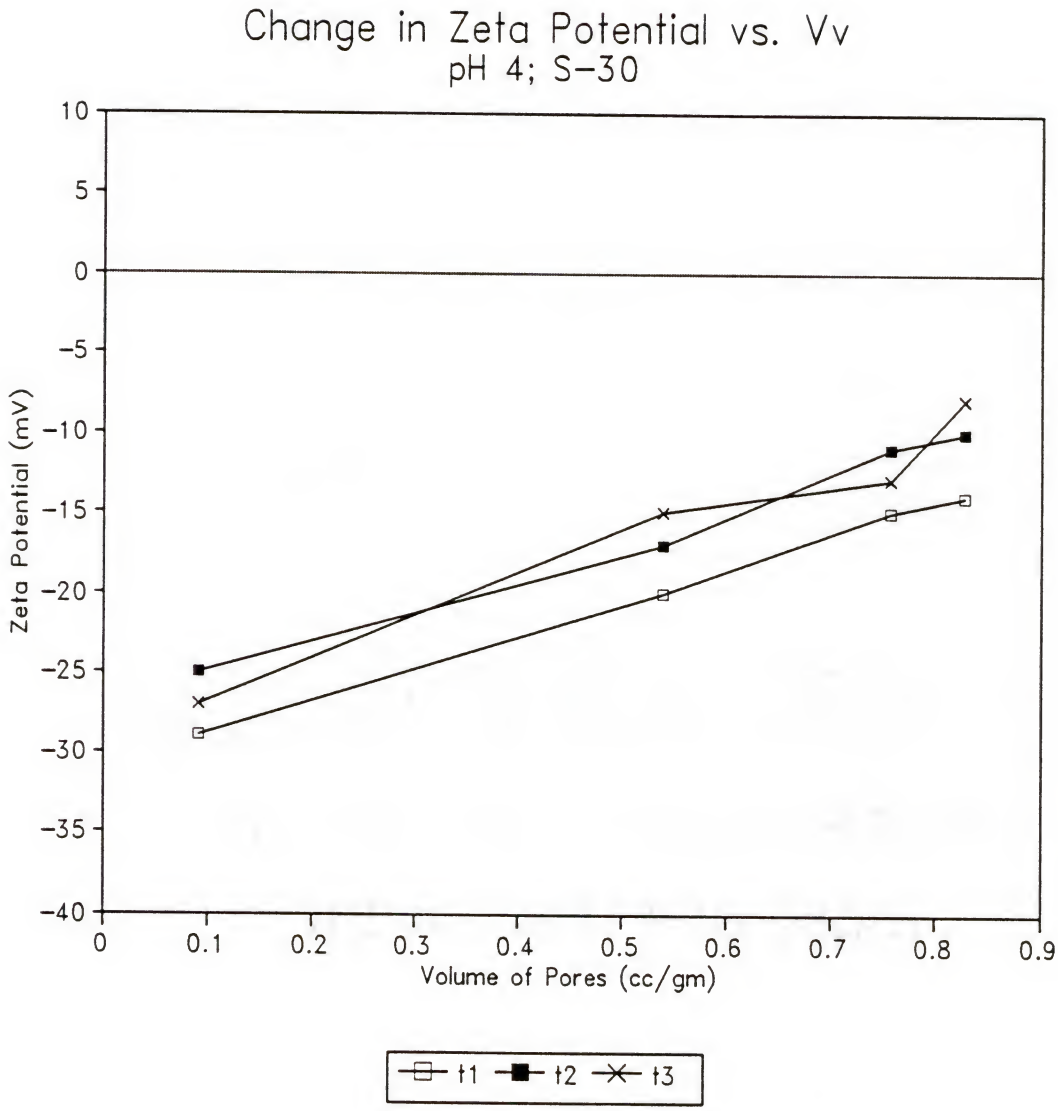

Figure 4.26 The change in the zeta potential as a function of pore volume, for the S-30 series of porous gel powders at pH 4. The variables t-1, t-2, and t-3, represent the different aging times in solution from tables 4.2 - 4.4.

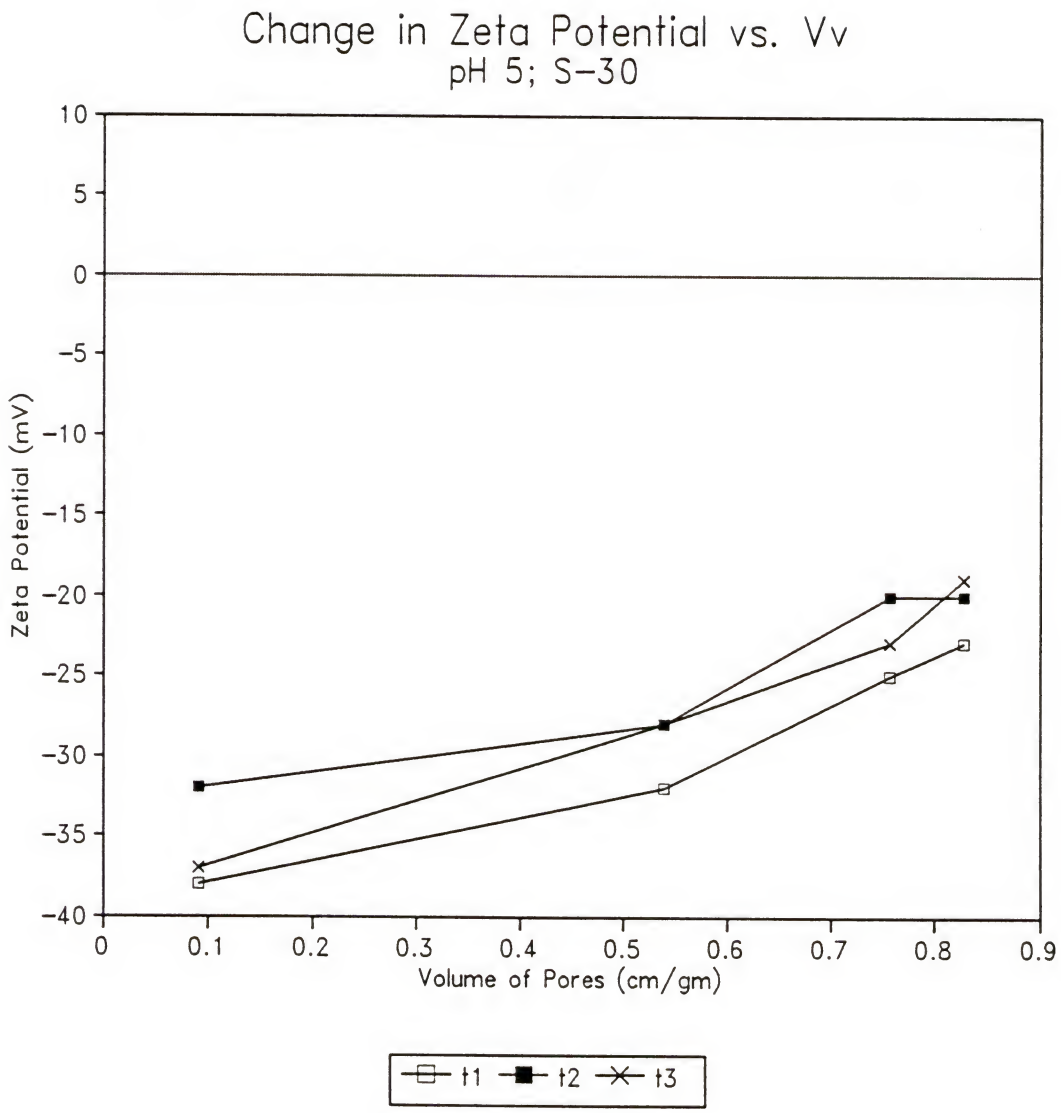

Figure 4.27 The change in the zeta potential as a function of pore volume, for the S-30 series of porous gel powders at pH 5. The variables t-1, t-2, and t-3, represent the different aging times in solution from tables 4.2 - 4.4.

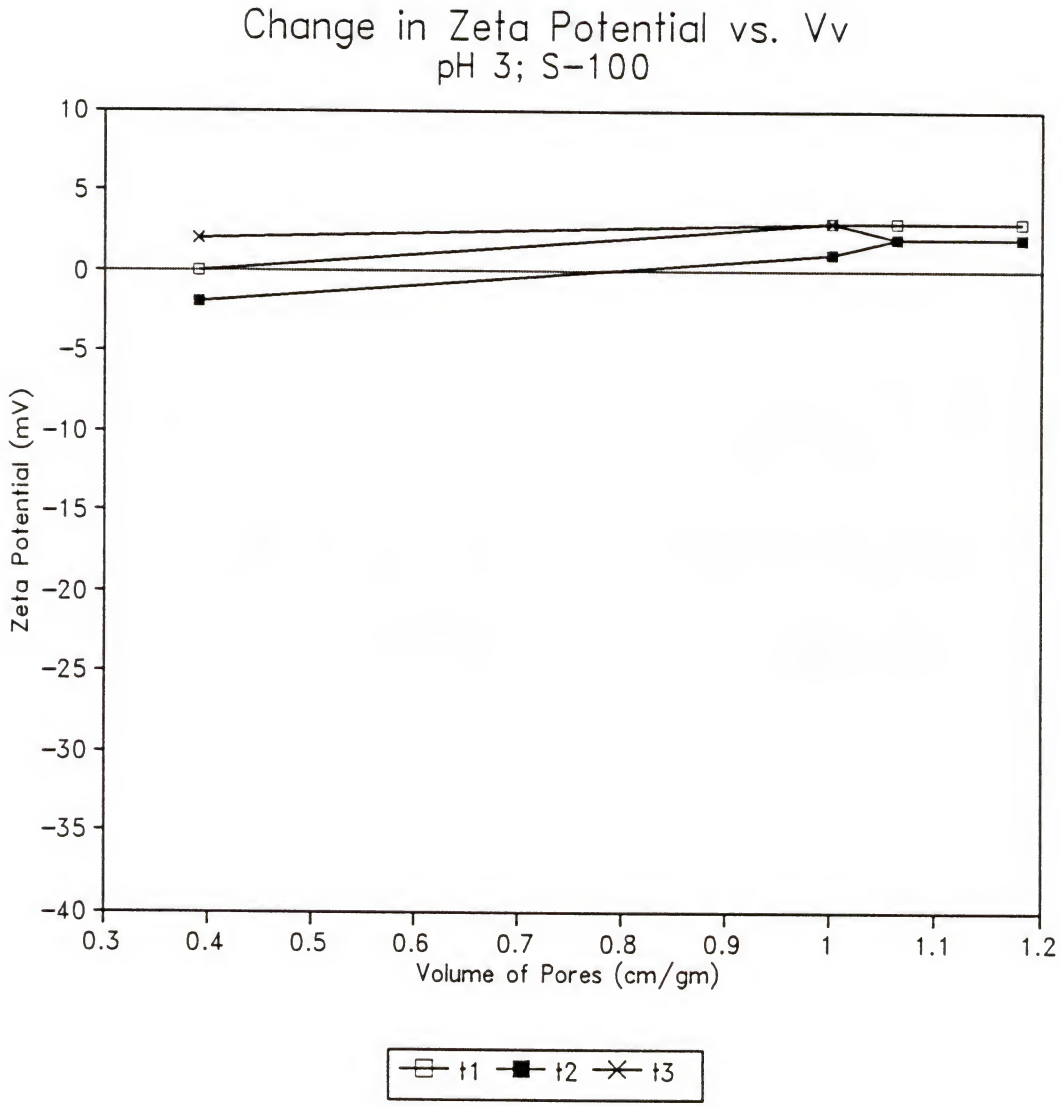

Figure 4.28 The change in the zeta potential as a function of pore volume, for the S-100 series of porous gel powders at pH 3. The variables t-1, t-2, and t-3, represent the different aging times in solution from tables 4.2 - 4.4.

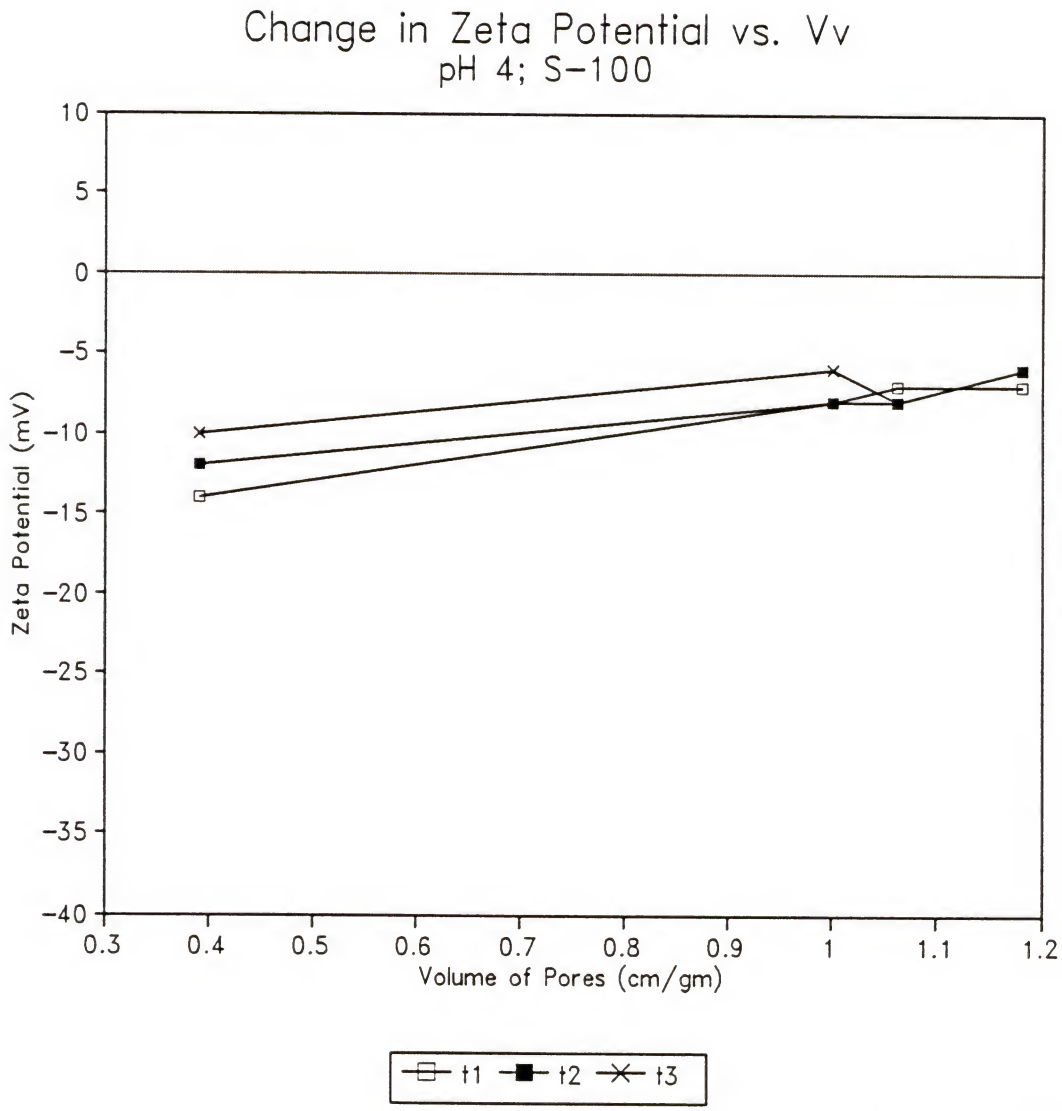

Figure 4.29 The change in the zeta potential as a function of pore volume, for the S-100 series of porous gel powders at pH 4. The variables t-1, t-2, and t-3, represent the different aging times in solution from tables 4.2 - 4.4.

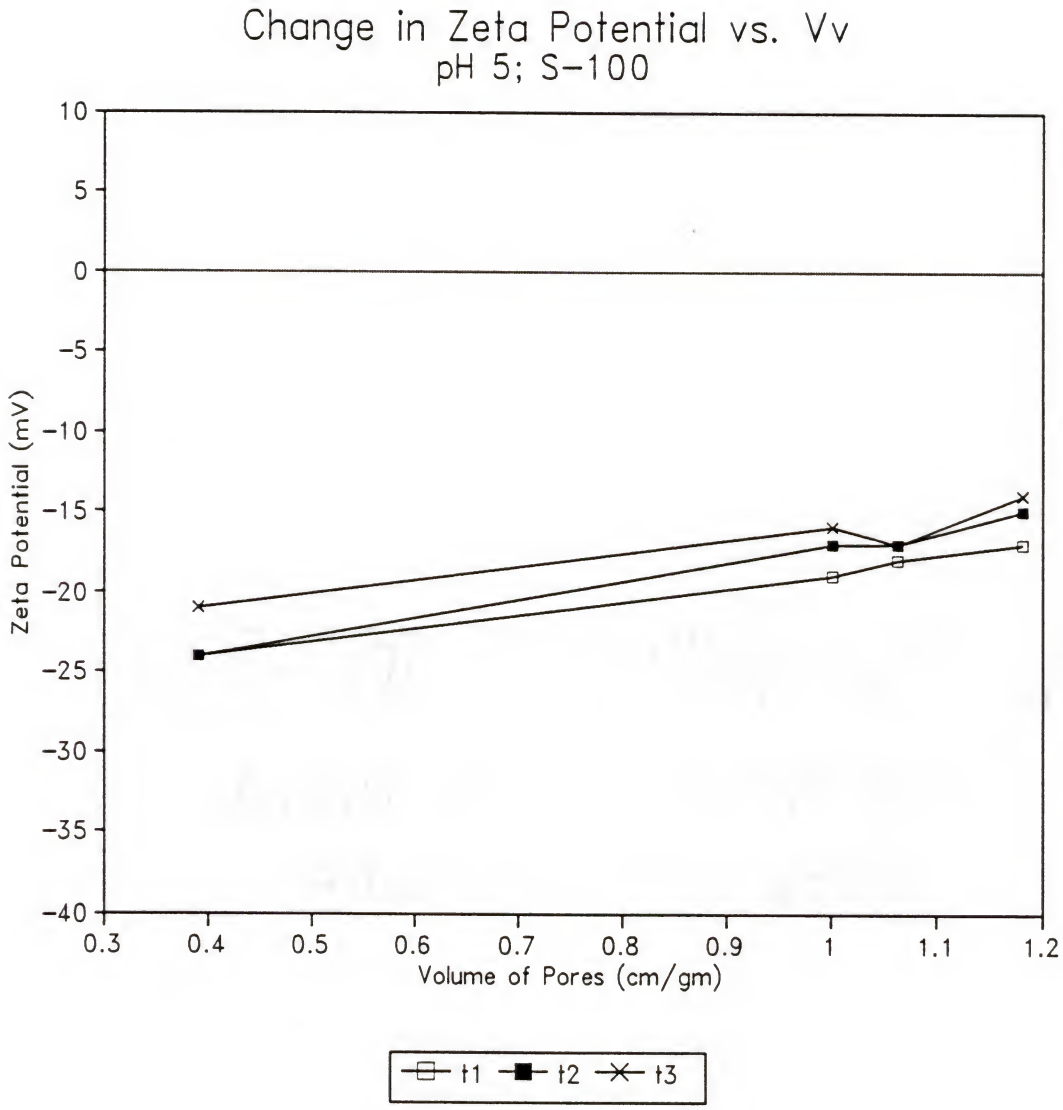

Figure 4.30 The change in the zeta potential as a function of pore volume, for the S-100 series of porous gel powders at pH 5. The variables t-1, t-2, and t-3, represent the different aging times in solution from tables 4.2 - 4.4.

maximum increase of the zeta potential versus volume fraction of pores is observed, for the S-14 series, from volume fractions of 0.5 to 0.25. No measurements in this volume fraction range were made on the zeta potential for the other series of gels.

The differences between the magnitude of the zeta potential value from the lowest and highest heat treated gel for the three series may be explained in terms of the total change in porosity. The largest change in zeta potential values, 12-13 mV, which occurs for different heat treatment temperatures is for the S-30-600 and the S-30-1000 (600 and 1000 °C). There is also an associated change in pore volume from 0.828 cc/gm to 0.092 cc/gm (see table 4.1). This pore volume change is quite large, nearly an order of magnitude difference. The S-100-600 and S-100-1000 zeta potential values at any pH change by 6-7 mV, while the porosity changes from 1.182 to 0.39 cc/gm. Also, the S-14-600 and S-14-920 zeta potential values change by 2-3 mV while the porosity changes from 0.501 to 0.236 cc/gm.

If one assumes a structural density of 2.2 gm/cc for the silica gels these pore volumes can be converted to volume fraction. The differences in volume fraction of pores for the heat treatment extremes within a pore size is 52% to 34%, 65% to 17%, and 72% to 46%, for the S-14, S-30, and S-100, respectively. Thus the differences in the change in volume fraction of pores directly correlates with the changes in the zeta potential. For S-14-600:S-14-920, an 18% change in porosity

produced a 2-3 mV change in zeta potential. For S-100-600:S-100-1000, a 26% change in porosity produced a 6-7 mV change in zeta potential, and for S-30-600:S-30-1000, a 48% change in porosity produced a 12-13 mV change.

Theoretical equations derived by Miller, Berg and O' Brien[171,172] indicate that there is a relationship between the electrophoretic mobility of porous aggregates and the volume fraction of particles. The equation describes both an increase in mobility due to an electroosmotic effect at large κr_p, and a decrease in mobility from a reduction in the applied field as a result of a normal component for small κr_p. The crossover point was predicted to occur at a κr_p value of approximately 7. Scanning electron microscope photographs of the particles used in this study indicate an average particle diameter of 1.5 μm for all three series of gels. Thus, the κr_p values from this study change from approximately 8 to 80 as the pH varies from 5 to 3. According to the theoretical derivation by Miller et al. there should be an increase in the electrophoretic mobility for porous particles studied at these κr_p values. Since their equation was never applied to a porous system the equation may need additional terms or it may only apply to aggregates with much larger pore sizes.

This last segment discusses the changes occurring to the zeta potential as a function of aging time to all three series of gels. The initial measurements were taken at 1-2 days (t-1) with subsequent measurements taken at 2 weeks (t-2) and 5 weeks (t-3).

Both the S-14 and S-30 series gels show an increase in the IEP and a decrease in the zeta potential at pH's higher than the IEP as the aging time increased. This is the same effect as translating the zeta potential versus pH curve to the right or to more basic pH values. The S-100 series shows no significant change in the IEP with aging time and a small decrease in the zeta potential values at higher pH's. A shift in IEP to more basic values is consistent with rehydration.[160,173,174]

An oxide surface can become hydrated by three separate mechanisms:[159] 1. Physical adsorption of water molecules including hydrogen bonding to surface oxygens but no dissociation, 2. chemisorption of water which dissociates, resulting in surface OH groups, 3. Reactions resulting in conversion to an oxyhydride or hydroxide.

Both mechanisms 1 and 2 above are likely to hydrate the silica gels in this system. One interpretation of an increase in the IEP is that the surface charge became more positively charged at the pH associated with the former IEP. Thus, as the curve is shifted to more basic values, the IEP is more basic and the zeta potential decreases in magnitude. This occurs with the specific adsorption of various positively charged cations.[159]

Thus it can be concluded that during the aging of gel series S-14 and S-30 either a more positive charge is being generated upon the surface during

rehydration or that the increase in the number of hydroxyls on the surface that occurs during rehydration of the gels has a net effect of decreasing the negative charge. This effect is not seen with the largest pore size gel of this study.

4.5 Conclusions

The results from the heats of immersion and zeta potential experiments provide valuable information which can be used for both the design of porous substrates for environmental sensors and the interpretation of the diffusion behavior of salt solutions within porous gel silica monoliths.

The heats of immersion were shown to increase with pore size. The increase in heats with pore size was attributed to a decrease in microporosity, a decrease in the surface roughness, a larger silanol concentration density on the surface, and a more immediate rehydration of the surface.

The value of the BET constant, C, was shown to correlate with the heats of immersion. A higher C value produced a larger heat of immersion. The C value decreased with an increase in the thermal treatment temperature for gels with 30 Å or larger pore radii. The small pore nitric acid gels show an increase in the BET constant with heat treatment.

The magnitudes of the heats of immersion exhibited a correlation with the IEP values of the different pore size gel series. The largest pore size gel, 100 Å, displayed the most basic IEP, 3.4, and the largest heat of immersion. The smallest

pore size gel, 14 Å, demonstrated the smallest heats of immersion and the most acidic IEP pH, 2.5.

The smallest pore size gel, 14 Å, exhibited very little differences in the IEP and shape of the zeta potential curve with heat treatment temperature. The 30 Å gel series displayed the most significant change in the IEP and shape of the zeta potential curve with thermal treatment temperature.

The change in the shapes of the zeta potential curves for the two largest pore sizes, 30 Å and 100 Å, was attributed to the change in volume fraction of porosity associated with the heat treatments. The larger the volume fraction of porosity the lower the electrophoretic mobility of the particles. This trend was not observed for the 14 Å gel. This may be due to the lower absolute volume fractions or larger surface area to volume ratios for the smaller pore size gels.

During aging of the different series of gels it was found that the IEP became more basic for the 14 Å and 30 Å pore size materials. The IEP of the 100 Å gels remained essentially constant with aging time.

The best choice for an environmental sensor in the gels investigated in this study is a porous monolithic substrate with the largest pore size. The surface displays a faster rate of equilibrium with water and produces very little change with aging in water. The surface appears to be smoother providing a more homogeneous substrate for impregnation of optically active phases. Both of these factors suggest a lower probability of the gel surface interfering with molecules involved in the sensing operation.

CHAPTER 5
THE DIFFUSION OF HEAVY METAL SALT SOLUTIONS INTO POROUS SILICA MONOLITHS

5.1 Introduction

In order to construct improved composite materials, which require second phase doping, one should understand the transport properties of solutions and the degree of interaction between the surface and these solutions. The extremely small physical size of the pores and active chemical state of the surface suggests that solute-surface interactions will play a role in governing the motion of diffusing species.

Chapter 2 reviewed the literature for molecular transport and motion within restricted geometries. Abundant evidence was cited indicating a significant reduction in the movement of molecules within porous media as the pore size approached the size of the molecule. One finding from chapter 3 was that the penetration rate of water into gels of various pore sizes and volume fraction of porosity was regulated by the pore size.

It was the aim of this series of experiments to determine the relationship between the pore structure of porous silica monoliths and the diffusion behavior of the Cr^{3+} ion into porous sol-gel silica monoliths. The Cr^{3+} ion was chosen for the following reasons: (1) The UV/visible spectrum of the hexa-aqua chromium

species is very simple with two well distinguished Gaussian shaped absorption bands in the visible region (see figure 5.1). This enabled easy integration of the area under the peaks. (2) The extinction coefficient, 13.76 liters/mole*cm, is a relatively large value compared to other hydrated ions. This made it possible to study a smaller bulk solution concentration by optical absorption (.01 M to 1.0 M). (3) The $Cr[(H_2O)6]^{3+}$ ion is extremely stable because of the slow exchange rate[175,176] (0.001 substitutions/sec) of water in the inner coordination sphere. (4) Cr^{3+} has the same charge as most of the optically important rare earth cations but is considerably less expensive. Thus, similar electrostatic or charge dependent phenomena may be infered from the study of Cr^{3+}.

The chapter is organized similarly to the preceding chapters. First, the applicable theory of the diffusion of electrolytes and the formal equations used to determine the diffusion coefficients are discussed. Second, a review is provided of related studies which include the diffusion of electrolytes in bulk solution and porous media, ion hydration, ligand exchange kinetics, and adsorption phenomena. Third, the experimental procedures for measuring the diffusion coefficients and the partition coefficients are presented. The experimental methods are followed by the presentation and discussion of the results. The conclusions are presented at the end of the chapter.

5.2 Theory and Related Studies

The modern theory of liquid structure is a disordered solid in which short-range order persists even though the long-range order characteristic of the solid

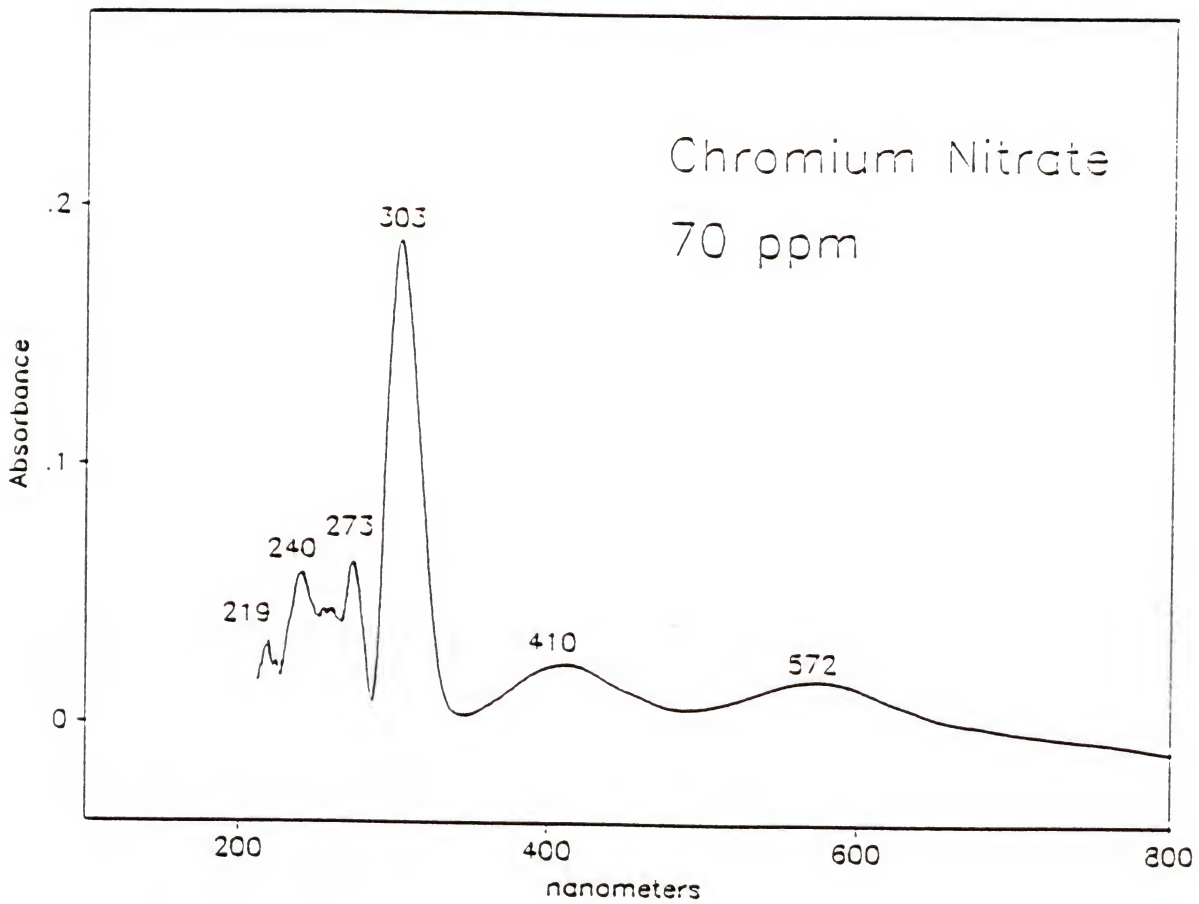

Figure 5.1 The UV/visible spectrum of a dillute chromium nitrate salt solution. The peaks located at 572, 410, 273, 240, and 219 nm are for the transitions of the hexa-aqua chromium ion. The 303 nm peak is a transition for the nitrate anion.

state is lost due to thermal agitation. Morgan and Warren[177] examined the structure of liquid water by x-ray analysis. The maximums in the radial distribution function at 2.90 Å (O-O internuclear distance) and 4.5 Å (second nearest-neighbors) indicate that water is a tetrahedrally coordinated, loosely packed structure held together by electrostatic forces arising from the shape and charge distribution of the water molecule. The structure of water is important from the standpoint that it is the solvent which enables the electrolytes to display their physical and chemical characteristics or peculiarities.

The ion-ion separation in water is a function of the concentration. For a 1:1 electrolyte, the separation distance varies according to $9.4*c^{-1/3}$ Å.[178] The average separation distance between ions varies from 44 Å to 9.4 Å for concentrations of 0.01 M and 1.0 M, respectively. The distinction between dilute and concentrated solutions occurs at 0.1 M which is the concentration at which the number of successive water layers around each ion drops below three upon an increase in the concentration.[178]

Several effects become important as the diffusion theory is advanced from dilute to concentrated solutions. The solvent molecules move in the opposite direction of the solute and the viscous forces may be considerably modified by the presence of a large number of ions. Hartley and Crank[179] developed an expression for the diffusion of a concentrated electrolyte which included the diffusion coefficient of the solvent and a relative viscosity term. It is clear from the review of restricted geometries from chapter 2 that water has a reduced molecular

motion in finite sized geometries. This may be one contribution to the reduction in the diffusion of cations within porous sol-gel silica.

The cause of viscosity increase of electrolyte solutions within porous materials is not clear. However, it is clear that the electrical forces between ions in adjacent layers of an electrolyte solution will increase the viscosity. The mathematical treatment of this effect was given by Falkenhagen.[180] The equation includes two coefficients which account for the interionic electrostatic forces and the ion-solvent interaction. The contribution from the interionic effects is usually small compared to the hydration of the ion effect. Viscosity coefficients for Cr^{3+} could not be found in the literature. However, from a list of other similar ions,[181] the viscosity increase from a dilute solution to 0.1 M is less than 10% at 25 °C.

The variation of the diffusion coefficient for eight uni-valent electrolytes was determined as a function of concentration by Stokes.[182] Over the range of concentrations from .01 M to 1.0 M, the diffusion coefficient is a minimum between 0.1 M and 0.3 M. However, the values differ by less than 5%.

The larger the hydration energy of the metal ions the more stable the complex.[183] The $Cr[(H_2O)_6]^{3+}$ ion exchanges its inner-coordinated water at a rate of 10^{-3} times per second while typical values for hydrated ions such as: Al^{3+}, Fe^{3+}, Ni^{2+}, Co^{2+}, and Nd^{3+} are 10, 10^2, 10^4, 10^5, and 10^7 times per second, respectively.[176] Because Cr^{3+} holds its water so tightly it was assumed that the diffusing entity is the $Cr[(H_2O)_6]^{3+}$.

Diffusion is one of the most fundamental irreversible processes. From a molecular kinetic viewpoint, no individual ions show a preference for motion in any direction, but a definite fraction of the particles in a given volume may be considered to be moving in one direction due to a concentration gradient. Nothing essential is lost by treating or confining the three-dimensional diffusion process to a one-dimensional study. Most methods by which diffusion is studied deliberately restrict the motion to one-dimension flow.[184] One-dimensional diffusion was studied in this investigation in the following manner.

The flux of matter, J, is defined as the amount of material crossing unit area of a plane perpendicular to the direction of flow in unit time. The concentration gradient is the partial of concentration by the partial of distance, and is the rate of increase of concentration with distance measured in the direction of flow. Fick's first and second laws describe this phenomena in terms of a diffusion coefficient, D, for the steady-state and unsteady-state conditions by equations 5.1 and 5.2, respectively.[185]

$$J = - D(\frac{\partial c}{\partial x}) \qquad (5.1)$$

$$\frac{\partial c}{\partial t} = \frac{\partial}{\partial x}(D\frac{\partial c}{\partial x}) \qquad (5.2)$$

The partial of c in equation 5.1 is required because c is dependent upon time and distance but the concentration gradient is constant and does not vary with time. The unsteady-state equation, 5.2, relates c, x, and t for which the concentration

gradient changes with time. Practical experiments are usually defined such that D is a constant. D frequently varies with concentration. This study measures D from the flux at the interface between the porous gel and the solution.

The diffusion into a semi-infinite medium, $x>0$, where the boundary is kept at a constant concentration, C_o, at $x=0$ and the initial concentration throughout the medium is zero requires the solution of eq. 5.2. The solution for the above boundary conditions was found by applying a Laplace transformation.[185] The solution is,

$$C = C_o \, erfc \frac{x}{2\sqrt{(Dt)}} \qquad (5.3)$$

where, t is time in seconds, x is distance in cm, D is the diffusion coefficient in cm^2/sec, C_o is the bulk solution concentration in moles/liter, C is the concentration at x for a given time, and erfc is the error function complement, erfc Z = 1-erf Z. One result of practical importance is the integration of eq. 5.3 to obtain the total amount taken up by the medium for the special case of zero surface concentration. The result is given by Crank,[185]

$$\left(D\frac{\partial C}{\partial x}\right)_{x=0} = \frac{DC_o}{2\sqrt{(Dt)}} \qquad (5.4)$$

which is integrated with respect to time to give the total amount, M_t, which has entered the medium at time t,

$$M_t = 2C_o\left(\frac{Dt}{\pi}\right)^{1/2} \qquad (5.5)$$

Equation 5.5 was used to determine the diffusion coefficient in this study with the following assumptions. The geometry of the porous gel is a plate which was treated as a semi-infinite medium for short times. The sample dimensions are approximately 20 mm square and 2-5 mm thick. The diffusion plane was at the solution-gel interface. The area of measurement was constant as defined by the spot size of the spectrophotometer (5 mm x 5 mm). The side diffusion from the edges was considered to be negligible over the time frame of the experiment. The diffusion coefficients in this study are average values due to the uncertainty of the change in D with the concentration of the solution.

The adsorption of metal ions to the surface of silica has been studied in detail.[186-191] A general relationship from inspection of these studies is evident. Ion adsorption density increases with solution pH. For each metal ion there is a critical pH range, usually less than 1 pH unit wide, over which adsorption increases from 0 to 100%.[189] Adsorption below this critical range is close to zero. The adsorption isotherm of Cr^{3+} has been determined as a function of pH by James and Healy.[189] A majority of the chromium adsorbs between pH 4 and 6. This appears to qualitatively coincide with a pH of 4 for the hydrolysis of the Cr^{3+} ion.[192] All of the experiments with chromium in this investigation were performed with solution pH's below 3.

The diffusion coefficient of NaCl was measured in a wet tetramethoxysilane gel as a function of the TMOS volume ratio.[193] The diffusion coefficient decreased linearly with increasing TMOS volume and had a value 2 times lower than the bulk value at 20% TMOS.

Several studies have shown relationships between the topology of the pore network and transport properties.[194,195] A pulsed gradient spin-echo NMR study[194] showed good agreement between pore hopping theory and the assumption that diffusion within the pore was much faster than between the pores for a random loose pack of polystyrene spheres. This is an important concept for diffusion in materials which contain microporosity like silica gels. The diffusion process may be limited by the microporosity or throats which connect the porous channels.

The second study presented a dynamic Monte Carlo model which indicated that substantial differences exist in the transport of molecules through pore structures of different interconnectivity.[195] The interconnected pores displayed smaller diffusion coefficients than a parallel bundle model. The decrease in diffusion coefficients for an increase in interconnectivity is probably because of the increase in pore length from the added tortuosity or path length.

The diffusion of NaCl has been studied in two substantially different types of porous media. The first study[196] measured the diffusion coefficient of NaCl in silica-alumina catalyst beads with 32 Å diameter pores and the second[197] in a column of 0.2 mm sand particles with a 29% volume fraction of porosity. Both

studies calculated a value of 4.6×10^{-6} cm^2/sec for the diffusion coefficient of Na^+. This was a decrease of 3.5 times from the bulk solution value.

The experimental methods, the operating principle of the NIR/visible/UV spectrophotometer, and the data analysis of the diffusion results are described in the ensuing portion of this chapter.

5.3 Experimental Methods

5.3.1 Materials

Water for these experiments was obtained from a Milli-Q 4-cartridge ion exchange system-18MΩ·cm resistivity. A Fischer® certified $Cr(NO_3)_3 \cdot 9H_2O$ salt was used as received to mix the diffusion solutions. Fisher certified Inductively Coupled Plasma standards (HNO_3 acidified) were used to create various concentrations of standards for the calculation of the molar extinction coefficient for Cr^{3+} at the two visible absorption bands, 407 nm and 575 nm. The molar extinction coefficient was calculated by using the Bouguer-Lambert-Beer Law (equation 5.6),

$$A = \epsilon_\lambda dC \qquad (5.6)$$

where A is the absorbance at the peak maximum, ϵ_λ is the molar extinction coefficient at the peak maximum in liters/mole*cm, d is the path length in cm, and C is the concentration in moles/liter.

After sintering at different temperatures, the gel-plates were sectioned into two pieces, one section was ground into a powder for the N_2 adsorption characterization. The bulk density of the remaining plate was measured three

times using Hg pycnometry. The plate was then immersed overnight in a solution of DI H_2O+HNO_3 which was adjusted to match the pH of the chromium salt solution which later diffused into the gel. The next day, three measurements were made with water utilizing the Archimedes principle to calculate the bulk density. The pore characteristics were determined from the N_2 adsorption isotherms as discussed in chapter 3. The pore characteristics are given in table 5.1.

Solutions ranging from 0.01 M to 1.0 M in chromium were mixed and further acidified with nitric acid so as to insure the formation of the $Cr(H_2O)_6^{3+}$ species. The pH of the solution was varied form 0.5 to 2.74.

5.3.2 Procedures

The flux of the chromium ions into the sample was measured by monitoring the increase in absorbance in the visible portion of the electromagnetic spectrum using a Perkin Elmer Lambda 9-3 UV/VIS/NIR dual beam spectrophotometer. A series of standard concentrations covering the range from 10000 ppm to 100 ppm of Cr^{3+} solution was used to calibrate peak areas and peak maximums with concentration. The 575 nm peak was curve-fitted, integrated under the curve, and then plotted versus concentration and cell thickness (1 cm). The peak maximums were plotted in the same manner. The slope of the plot was equal to the molar extinction coefficient. No significant differences existed between the values of the molar extinction coefficient calculated from the peak areas and the peak maximums. The peak maximums were used to reduce the diffusion data to make the analysis easier. Values of 16.3 liter/mole*cm and 13.8 liter/mole*cm were

Table 5.1 A table of the measured effective diffusion coefficients for various cations at different solution conditions and for different sol-gel pore characteristics.

Pore Radius (Å)	Species	V_v of Pores	Concentration (mole/L)	pH	D_{eff} (cm^2/sec)
14.2	Cr^{3+}	0.36	0.1	1.70	3 E-7
15.0	Cr^{3+}	0.40	0.1	1.70	5 E-7
14.3	Cr^{3+}	0.30	0.5	0.98	2 E-7
14.8	Cr^{3+}	0.38	0.5	0.98	2.1 E-7
27.0	Cr^{3+}	0.48	0.1	1.01	1.8 E-6
26.2	Cr^{3+}	0.44	0.1	1.73	1.3 E-6
26.8	Cr^{3+}	0.43	0.5	0.98	1.1 E-6
97	Cr^{3+}	0.70	0.1	1.01	3.0 E-6
92	Cr^{3+}	0.69	0.1	1.73	2.8 E-6
89	Cr^{3+}	0.66	0.5	0.98	3.1 E-6
16.1	Ni^{2+}	0.32	0.7	1.0	1.2 E-7
16.8	Ni^{2+}	0.37	0.7	3.8	1.6 E-6
25.1	Ni^{2+}	0.38	0.7	2.8	2.8 E-6
16.2	Co^{2+}	0.34	0.7	2.2	3.5 E-7
38.2	Co^{2+}	0.54	0.7	2.2	1.9 E-6
95	Co^{2+}	0.68	0.7	2.2	3.3 E-6
16.1	Nd^{3+}	0.29	0.7	1.0	1.0 E-7
15.8	Nd^{3+}	0.33	0.7	1.0	1.4 E-7

determined from the regression analysis for the 407 nm and 575 nm peaks, respectively. The concentration vs absorbance remained linear over this range. The calibration curve is shown in figure 5.2. The time dependent absorbance files from the diffusion experiments are collected by the same computer program which calculated the extinction coefficients.

The porous gel silica plates were polished with 600 grit SiC sandpaper to ensure near flatness and outgassed overnight at 150 °C in a vacuum oven. Nitric acid was used to lower the pH of the water to a value which matched the pH of the chromium solutions which diffused into the plate. This acid was chosen to keep the counter anion the same in both the water absorbed into the pores and the diffusing nitrate salt solution. Visible absorption bands for the diffusing Cr^{3+} ions occur at 407 and 575 nm, which creates a purple-blue color within the glass. The Lambda-9 spectrophotometer was used to measure the time dependent absorbance by scanning the 1000-185 nm region. Operating via a remote terminal allows an ASCII file of the absorbance spectra to be recorded for later data reduction. Prior to soaking the gel plates in the chromium solution, a baseline spectrum was collected for each sample which was later subtracted from the real time spectrum. During each data interval the plate was withdrawn from the solution, wiped dry, inserted into the sample cell, and a spectrum collected.

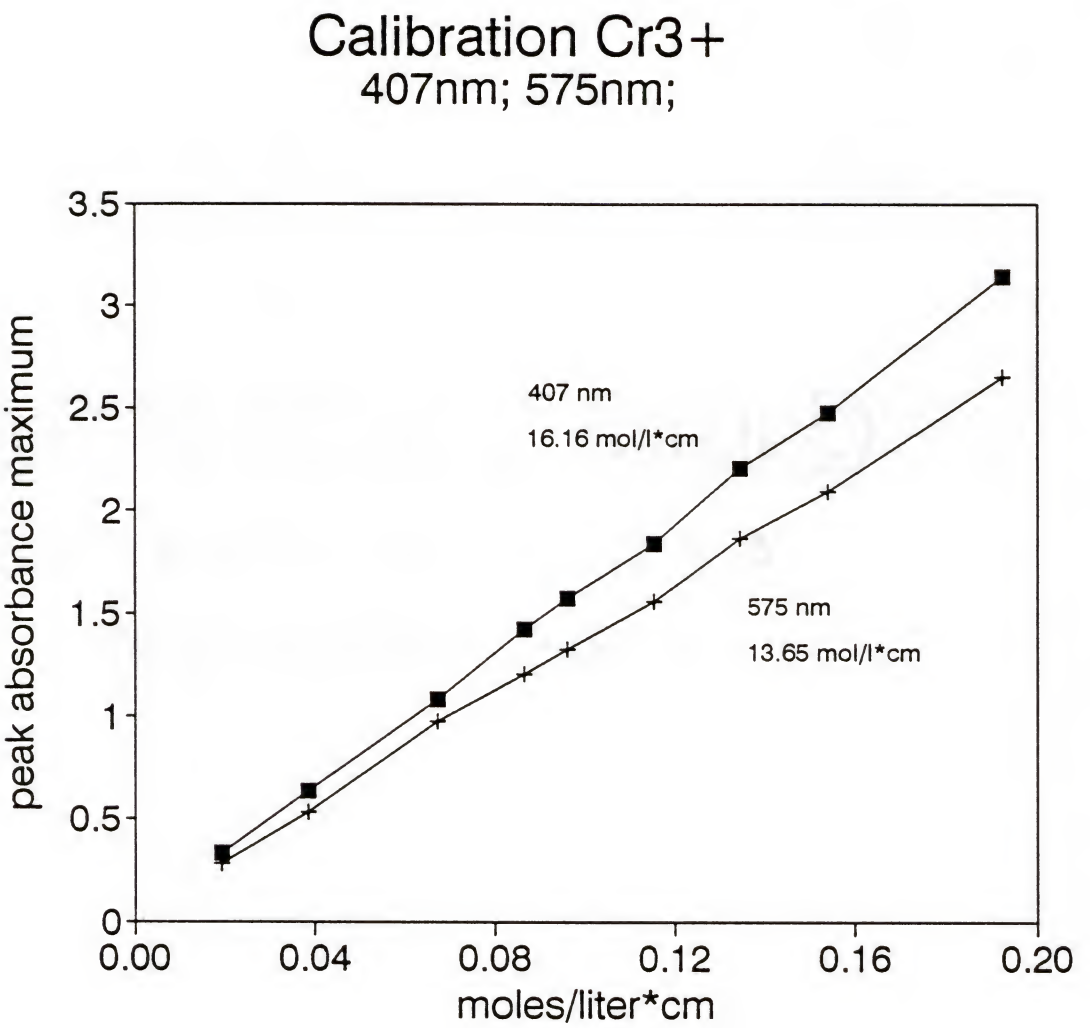

Figure 5.2 Two standard calibration curves of the electronic transitions in the visible region for the hexa-aqua chromium ion.

5.3.3 Analysis

The diffusion coefficient for the hexa-aqua chromium ion in water, $[Cr(H_2O)_6]^{3+}$, was measured as a function of average pore radius and volume fraction of porosity. The following procedures were used to interpret the spectra.

First, an offset was performed to match the time dependent absorbance with the baseline absorbance at 800 nm which does not overlap with the two absorbing bands or change with time. This baseline spectrum was then subtracted from the spectra for each elapsed time, Δt. Figures 5.3 and 5.4 show the spectra before and after correction. Of the two absorbing bands in the visible, the peak positioned at 575 nm was used to calculate the influx of chromium ions into the pore network. The absorbance maximum was determined from the spectra. This is the total number of ions which have entered the two faces of the plate. The peak maximum intensity was divided by the extinction coefficient to obtain the total amount of chromium that has crossed the interface at that time. This total amount, M_t, was then normalized for the area fraction of pores at the surface using the volume fraction of pores found from BET. It was this reduced surface area which was the area available for mass transfer since no solid-state diffusion exists at these temperatures. This normalization allows a comparison to be made between the different pore size samples which possess different volume fractions of porosity.

The solution for the diffusion coefficient was determined by treating this system as a semi-infinite slab with uniform diffusion along the x-axis as described

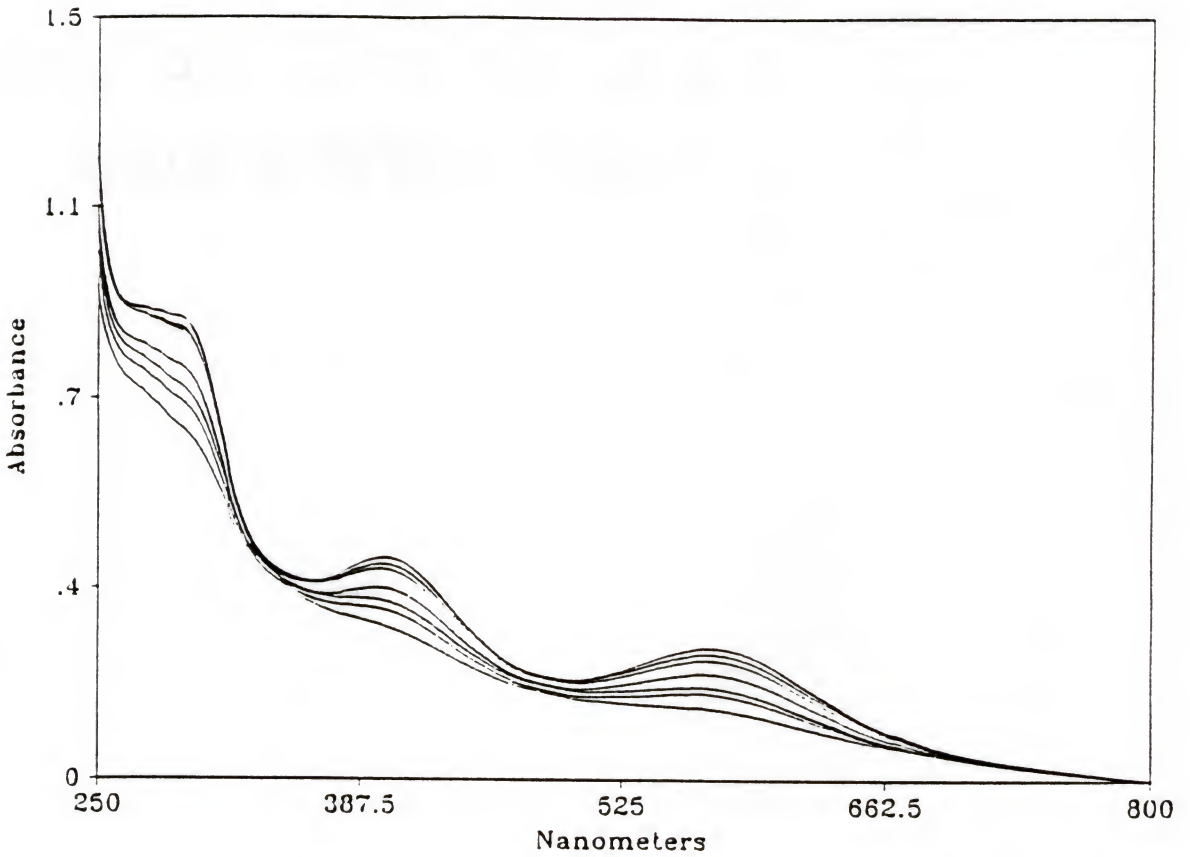

Figure 5.3 The time-dependent visible spectrum for the diffusion of $Cr[(H_2O)_6]^{3+}$ into a porous silica gel monolith.

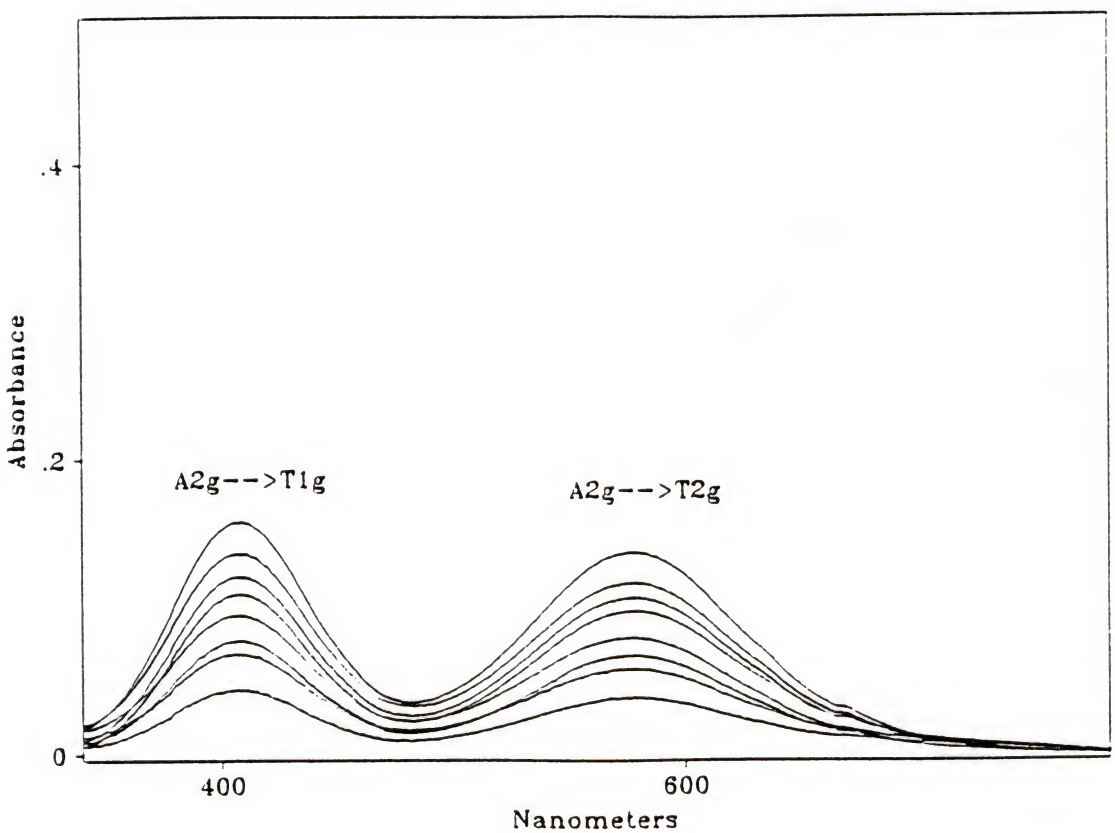

Figure 5.4 The time-dependent visible spectrum for the diffusion of $Cr[(H_2O)_6]^{3+}$ into a porous silica gel monolith which has had the absorption due to the water-filled silica gel monolith subtracted.

in the theory section. Implicit in the semi-infinite model is that the y and z dimensions are much larger than the x direction. In addition, the experimental diffusion times from which the diffusion coefficients were calculated are small. Measurements were taken over a period of a 45 minutes for the larger pore sizes and for up to 4 hours for the smallest pore size. The problem for the semi-infinite plate whose surface is maintained at a constant concentration was described in section 5.2. The diffusion coefficient can be determined from equation 5.5 for small times. The data for a typical run is plotted in figure 5.5. The slope of the plot is the diffusion coefficient which was determined from a linear regression analysis.

5.4 Results and Discussion

5.4.1 Presentation of Results

5.4.1.1 Diffusion coefficients

The effective diffusion coefficients measured in this study are listed in tables 5.1 and 5.2. The species investigated were the nitrate salts of Cr^{3+}, Co^{2+}, Ni^{2+}, and Nd^{3+}. The solution pH, solution concentration, and the pore characteristics are tabulated for each ionic species in table 5.1. The diffusion of Cr^{3+} has been studied more thoroughly than the other metal ions. Table 5.2 lists the pore characteristics, the values of the effective diffusion coefficients and the calculated and normalized tortuosities for the Cr^{3+} ion.

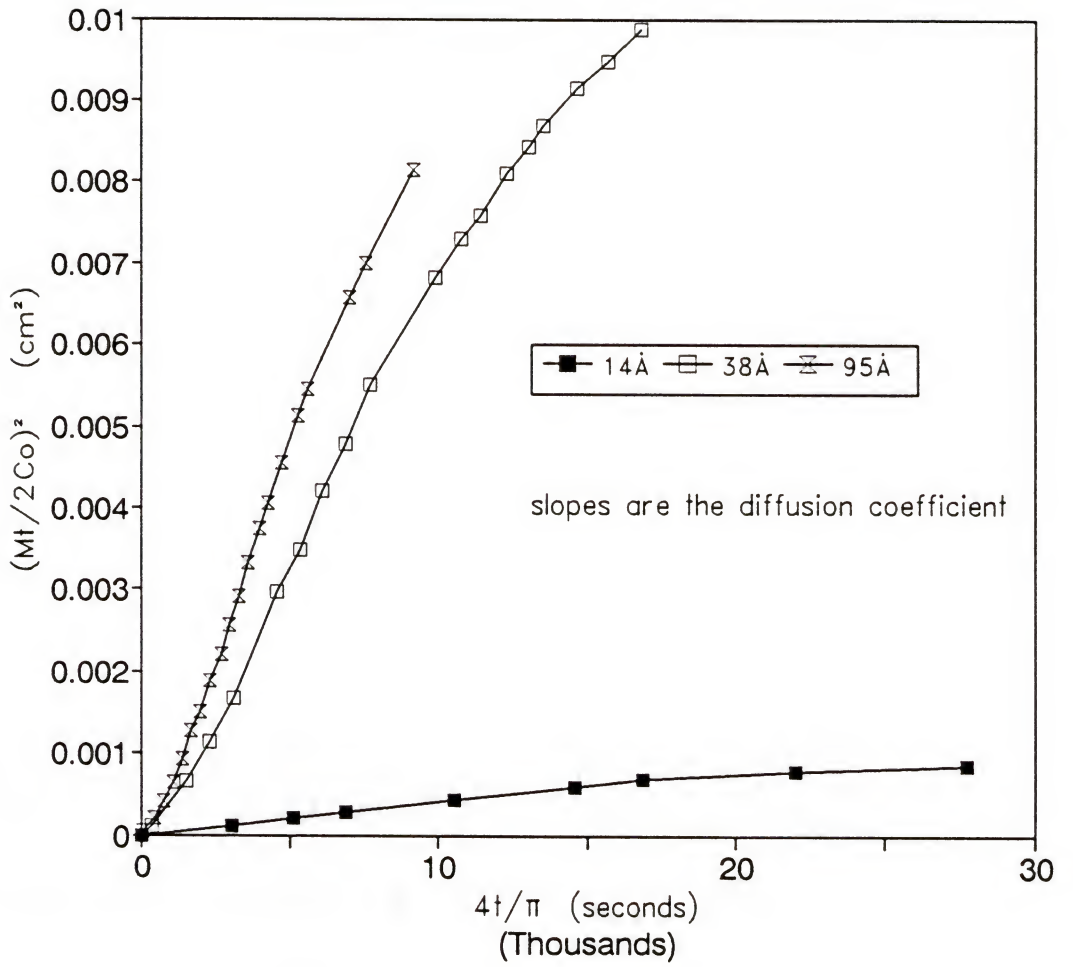

Figure 5.5 The graphical solution of the flux equation used to determine the diffusion coefficient of the $Cr[(H_2O)_6]^{3+}$ into porous monoliths of different average pore radii. The slope is the diffusion coefficient.

Table 5.2 A table of the measured effective diffusion coefficient and calculated tortuosities for the hexa-aqua Cr^{3+} ion.

Pore Radius (Å)	V_v of Pores	D_{eff} (cm^2/sec)	D_{eff}/D_{bulk}	τ	τ_n
14.2	0.40	2.2 E-7	0.044	9.1	4.2
13.6	0.38	2.0 E-7	0.040	9.5	2.6
13.8	0.35	1.3 E-7	0.026	13.5	3.1
13.1	0.35	1.2 E-7	0.024	14.6	4.4
12.5	0.31	1.3 E-7	0.026	11.9	5.5
13.0	0.30	9.8 E-8	0.02	15.3	4.3
12.2	0.27	9.4 E-8	0.019	14.4	3.9
13.2	0.27	1.0 E-7	0.020	13.5	4.1
15.8	0.42	5.2 E-7	0.104	4.0	1.8
16.1	0.38	7.1 E-7	0.142	2.7	1.2
16.2	0.32	4.1 E-7	0.082	3.9	1.5
16.5	0.30	2.9 E-7	0.058	5.2	2.0
28.0	0.60	2.0 E-6	0.40	1.5	0.9
27.8	0.61	1.7 E-6	0.34	1.8	1.0
25.0	0.54	1.1 E-6	0.22	2.5	1.6
24.6	0.51	1.9 E-6	0.38	1.3	0.7
20.0	0.38	1.4 E-6	0.28	1.4	1.0
100.0	0.68	2.8 E-6	0.56	1.2	1.0
95.0	0.64	3.1 E-6	0.62	1.0	0.9
84.0	0.53	2.5 E-6	0.50	1.1	0.9

Figure 5.6 is a plot of the effective diffusion coefficient for the Cr^{3+} ion as a function of pore radius and volume fraction of pores. The solution pH was 1.0 for all of the measured values. Figure 5.7 is the same plot as figure 5.6 except that the values of the effective diffusion coefficient for the other ionic species have been added. The added values are identified by the atomic symbols of each ion.

The tortuosity is defined by Smith[198] to be $\tau = (D_b * Vv)/D_{eff}$ where Vv is the volume fraction of pores. The calculated values for the Cr^{3+} system are listed in table 5.2. Figure 5.8 plots D_{eff} versus tortuosity. The tortuosity increases in a non-linear manner as D_{eff} decreases. Figure 5.9 plots the tortuosity versus the pore radius. The tortuosity decreases as the pore size increases. A large jump in tortuosity, from ≈5 to ≈15, was found between the 16 Å and 13 Å pore radius gels. The volume fraction of pores is included in the tortuosity versus pore size plot and is displayed in figure 5.10. The gels with the highest tortuosity values are those with the smallest pore size and the lowest volume fraction.

5.4.1.2 Partition coefficients

A plot of the partition coefficient, $\Phi = C_p/C_b$, versus pH for different chromium concentrations is graphed in figure 5.11. Two evident trends from the inspection of figure 5.11 are that as the pore size increased, Φ increased and as the concentration was decreased, Φ increased. Figure 5.12 is a plot of Φ versus pH for the other metal ions in the study. Although the trends are less well defined, the general trends for the other ions are similar to those for the chromium ion.

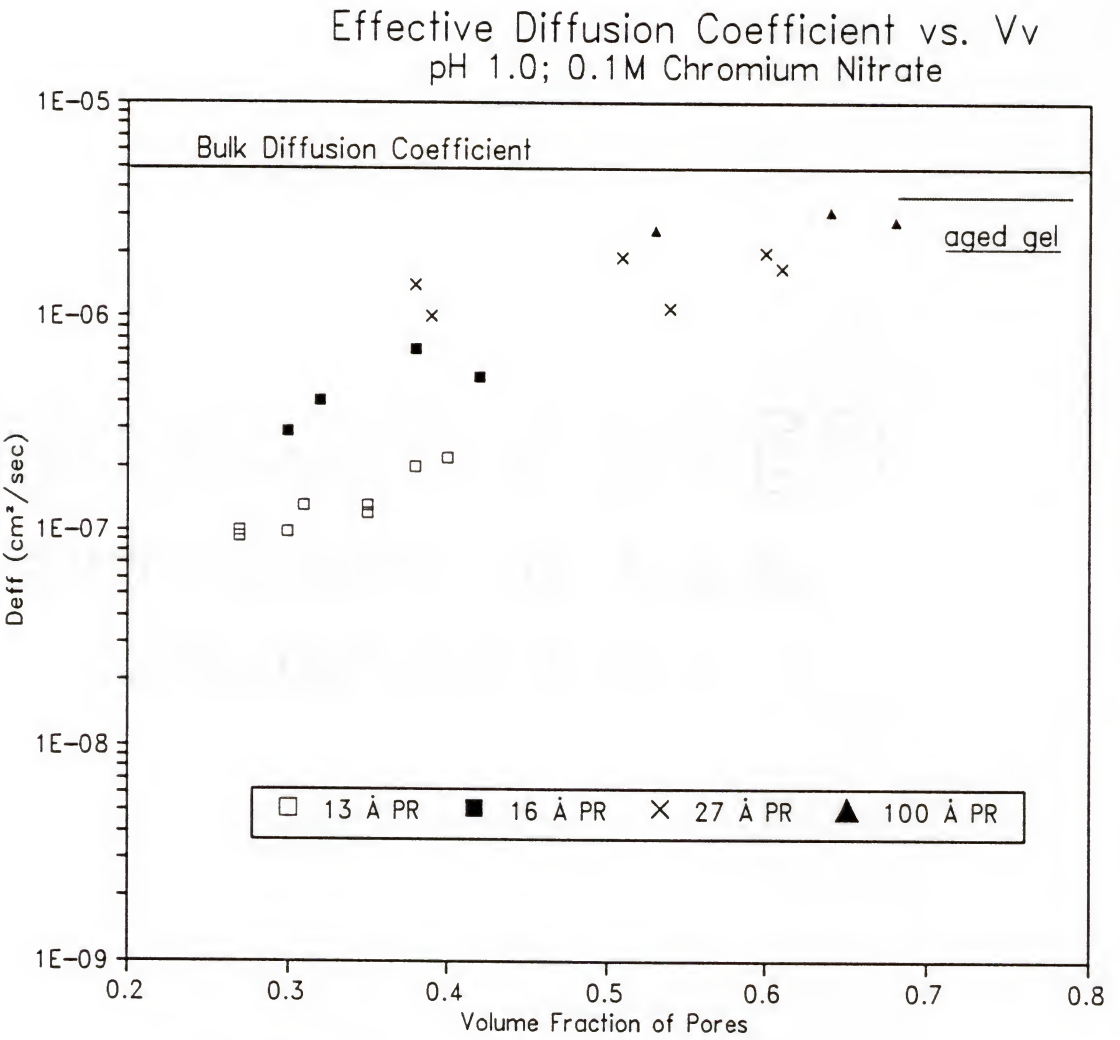

Figure 5.6 The effective diffusion coefficient for the $Cr[(H_2O)_6]^{3+}$ species plotted versus the pore volume fraction for a series of different average pore radius silica gel monoliths.

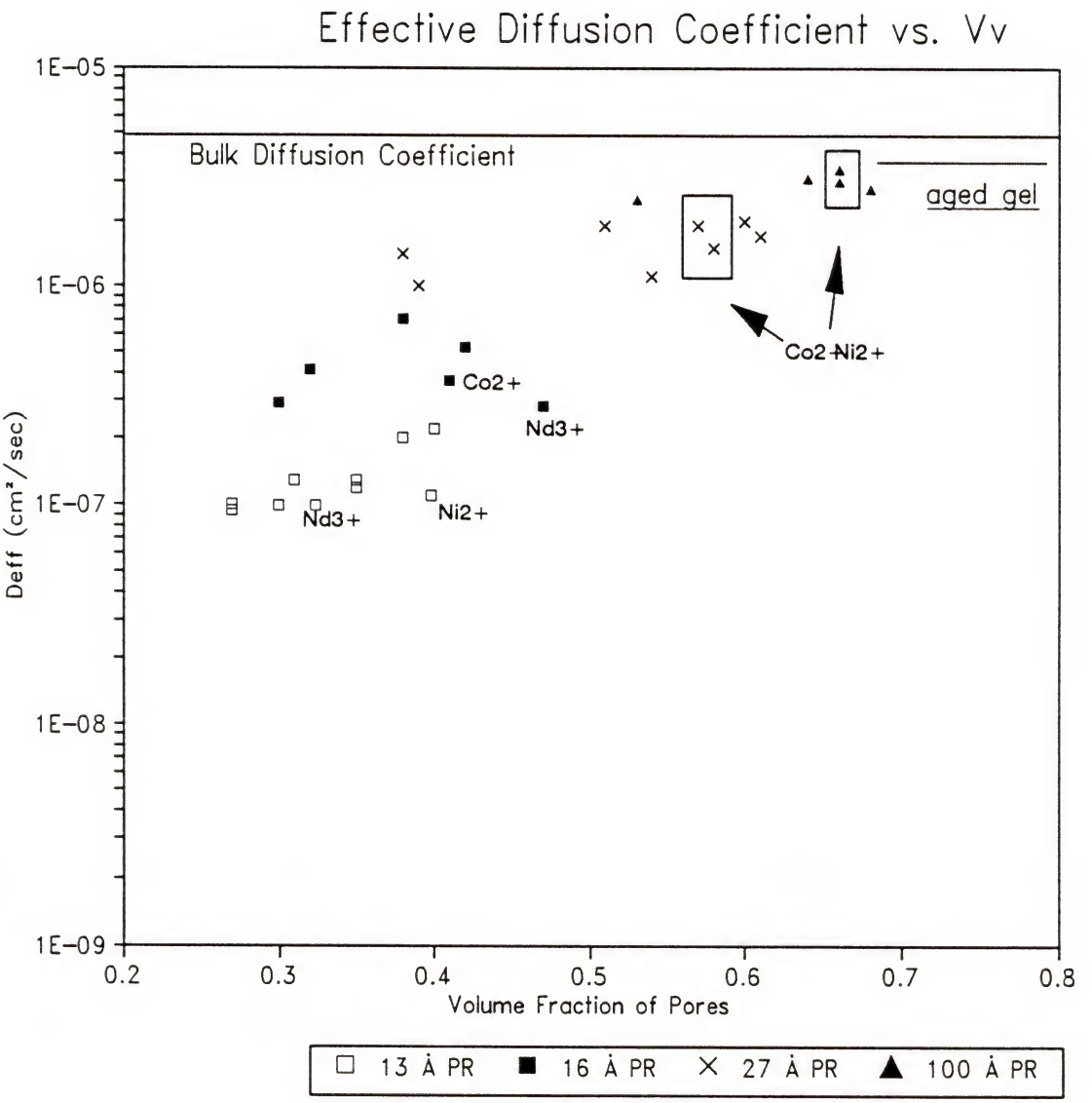

Figure 5.7 A plot of the effective diffusion coefficient for $Cr[(H_20)_6]^{3+}$ species and the other indicated hydrated ions listed in the figure is plotted versus the volume fraction of pores for a series of silica gel monoliths with different average pore radii.

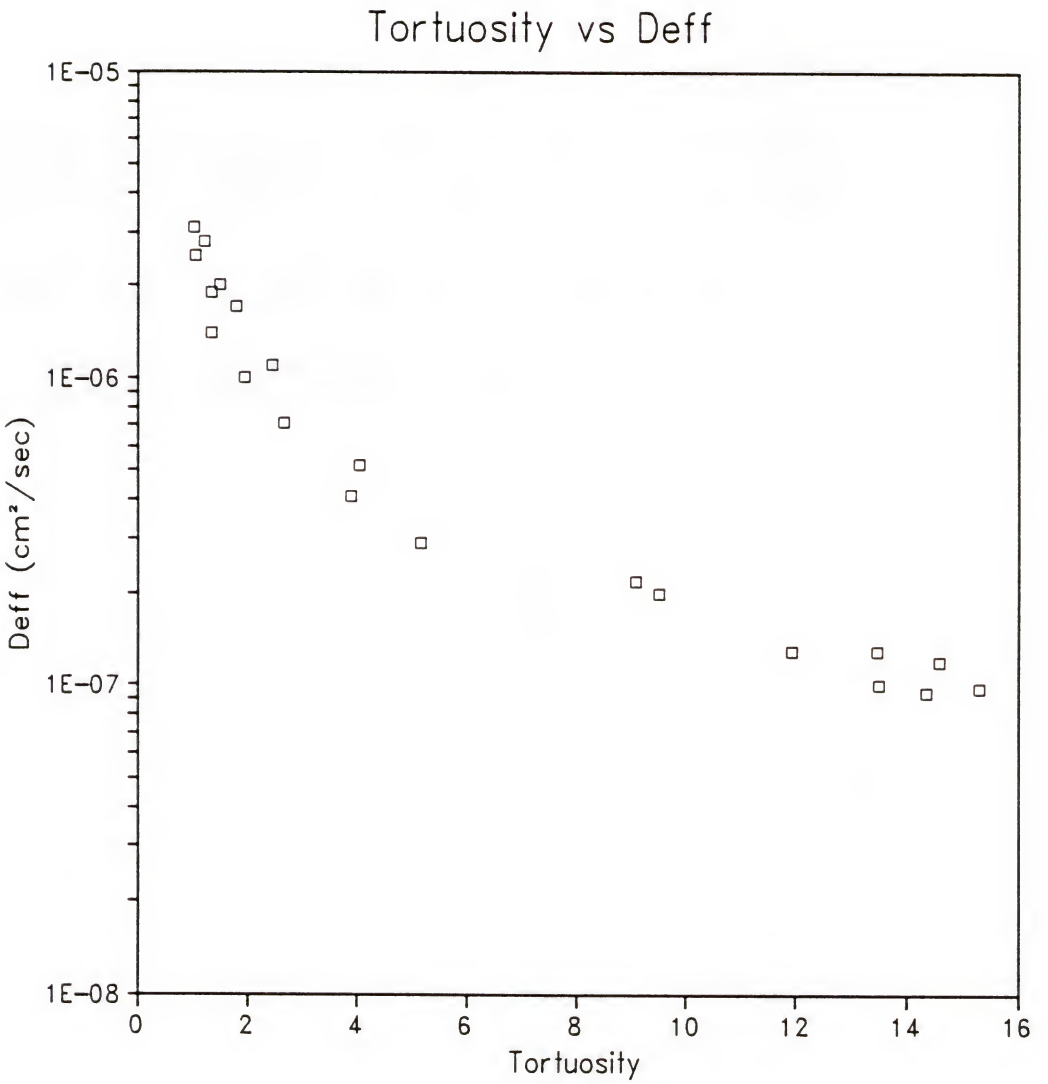

Figure 5.8 A plot of the effective diffusion coefficient for the $Cr[(H_2O)_6]^{3+}$ determined for a range of average pore sizes and volume fractions plotted versus the tortuosity.

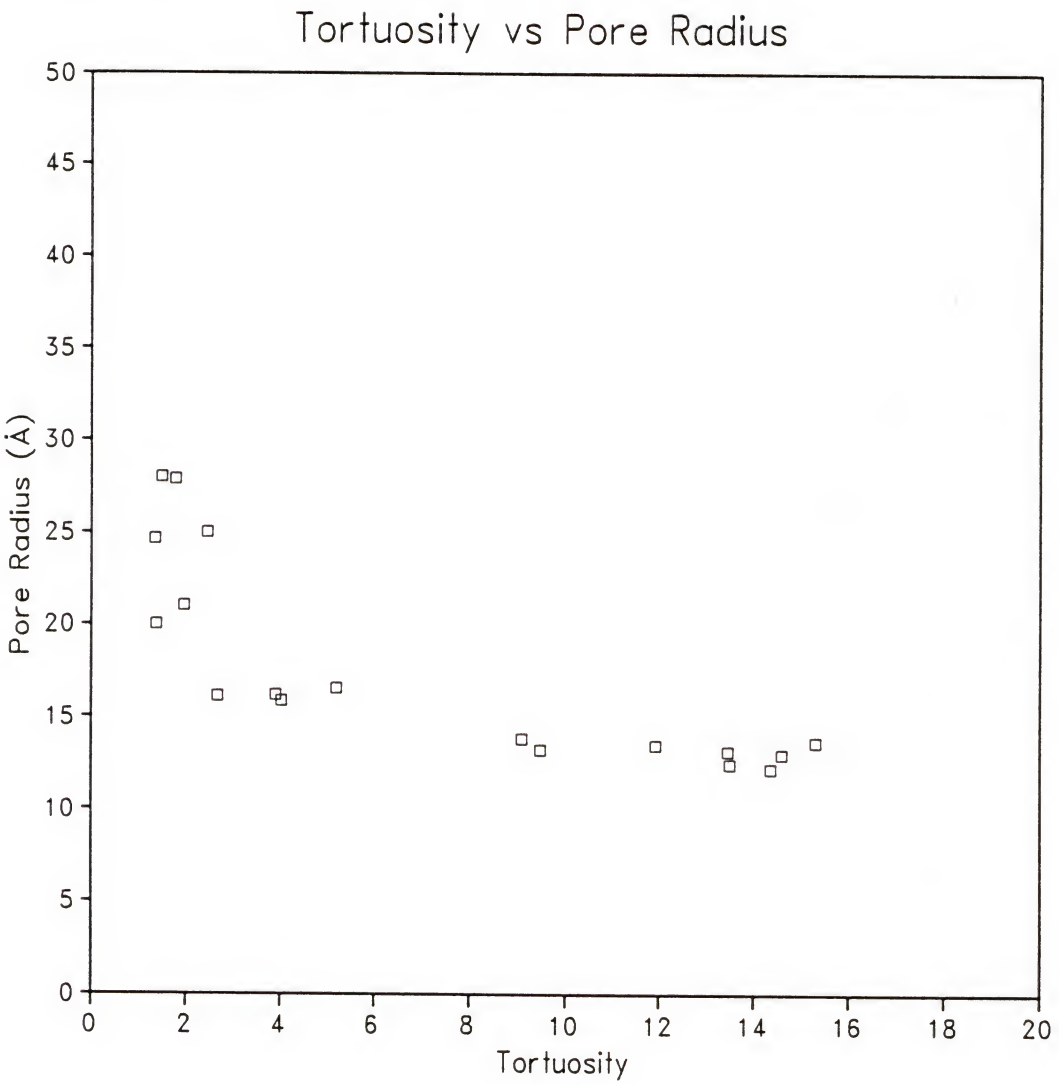

Figure 5.9 A plot of the calculated tortuosity of different silica gel monoliths versus the average pore radius of the gel.

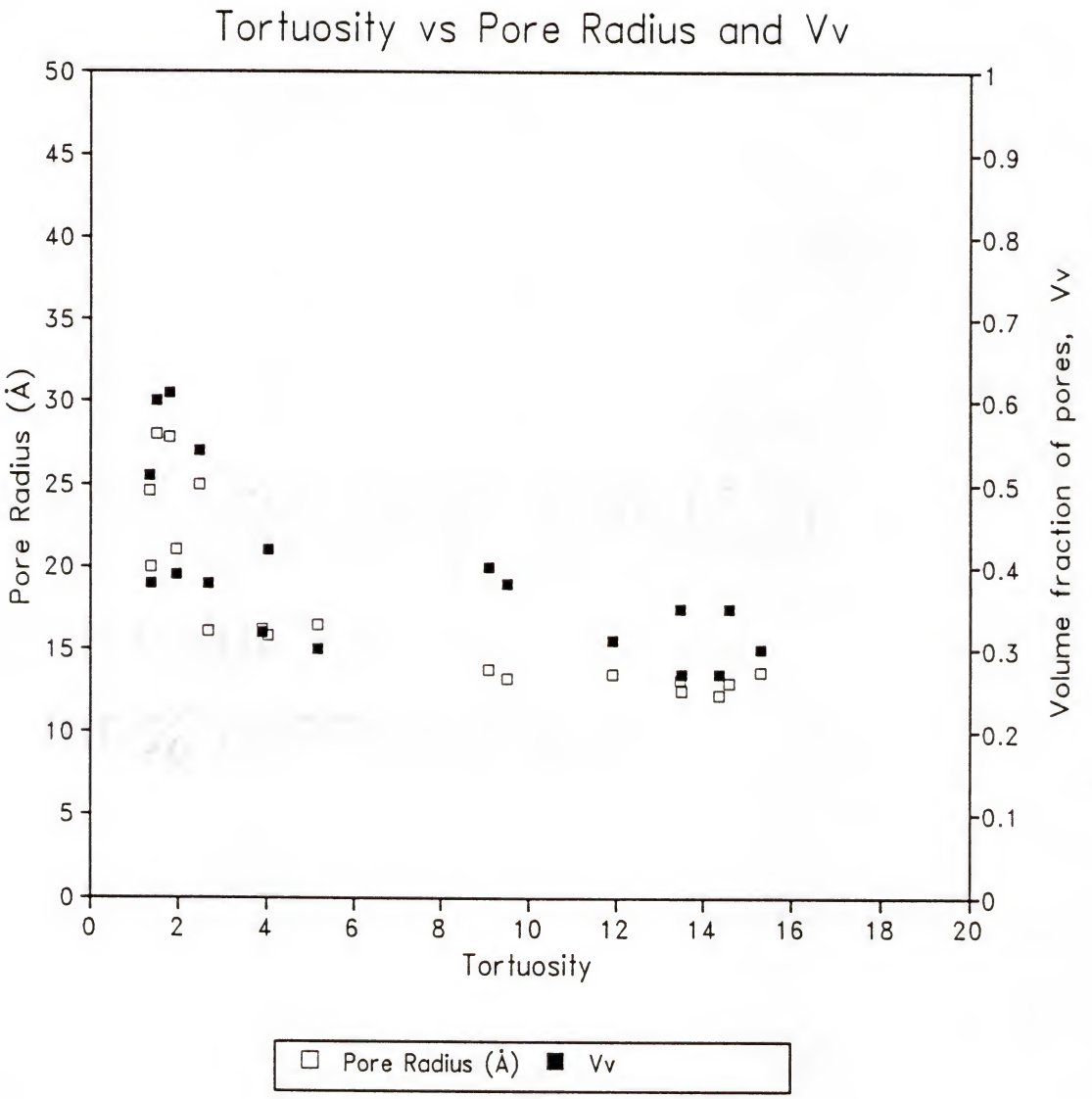

Figure 5.10 A plot of the calculated tortuosity of different silica gel monoliths versus their average pore radii and the volume fraction of pores.

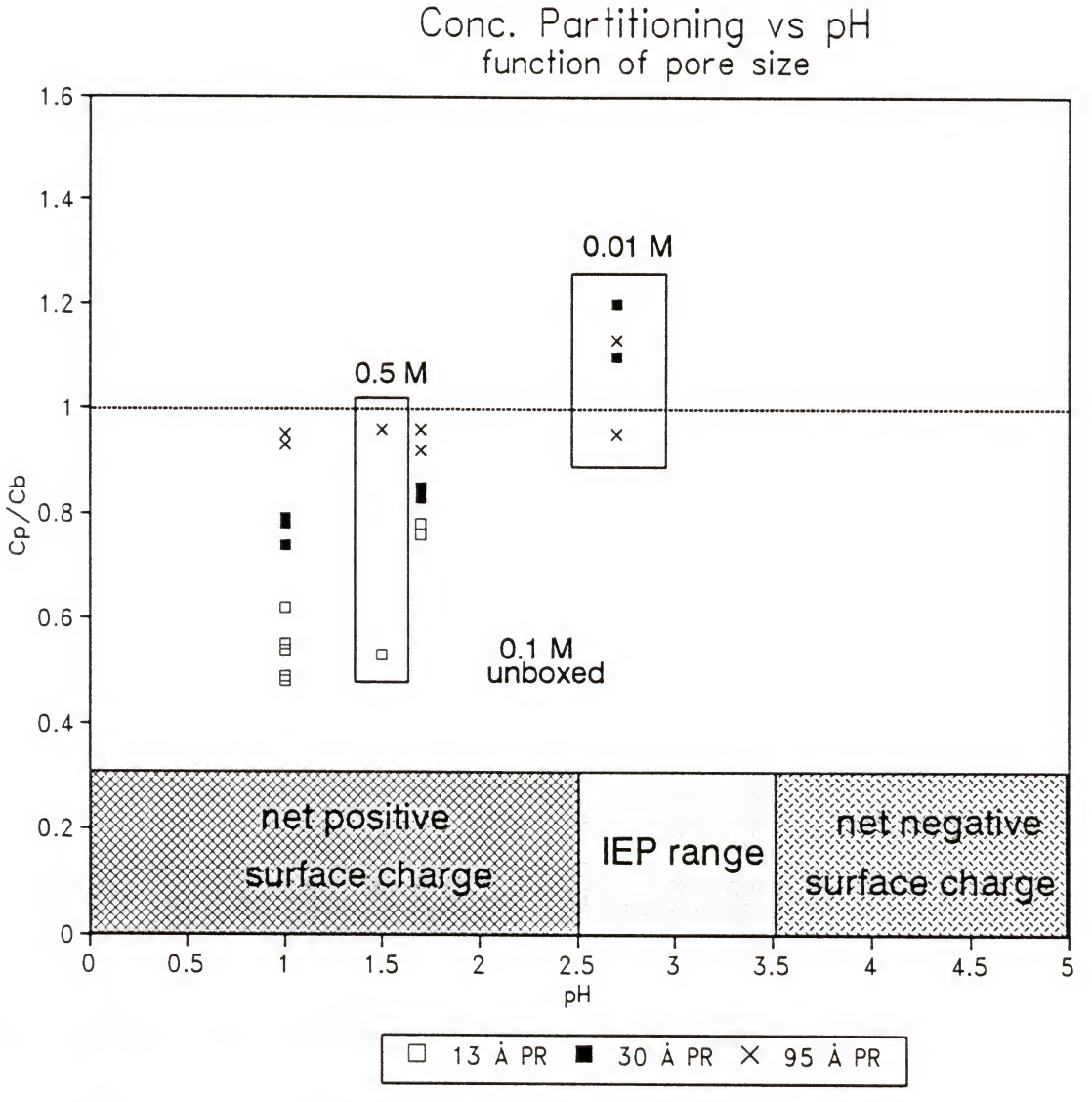

Figure 5.11 A plot of the partition coefficient for the $Cr[(H_2O)_6]^{3+}$ ion versus pH for different solution concentrations and average pore radii.

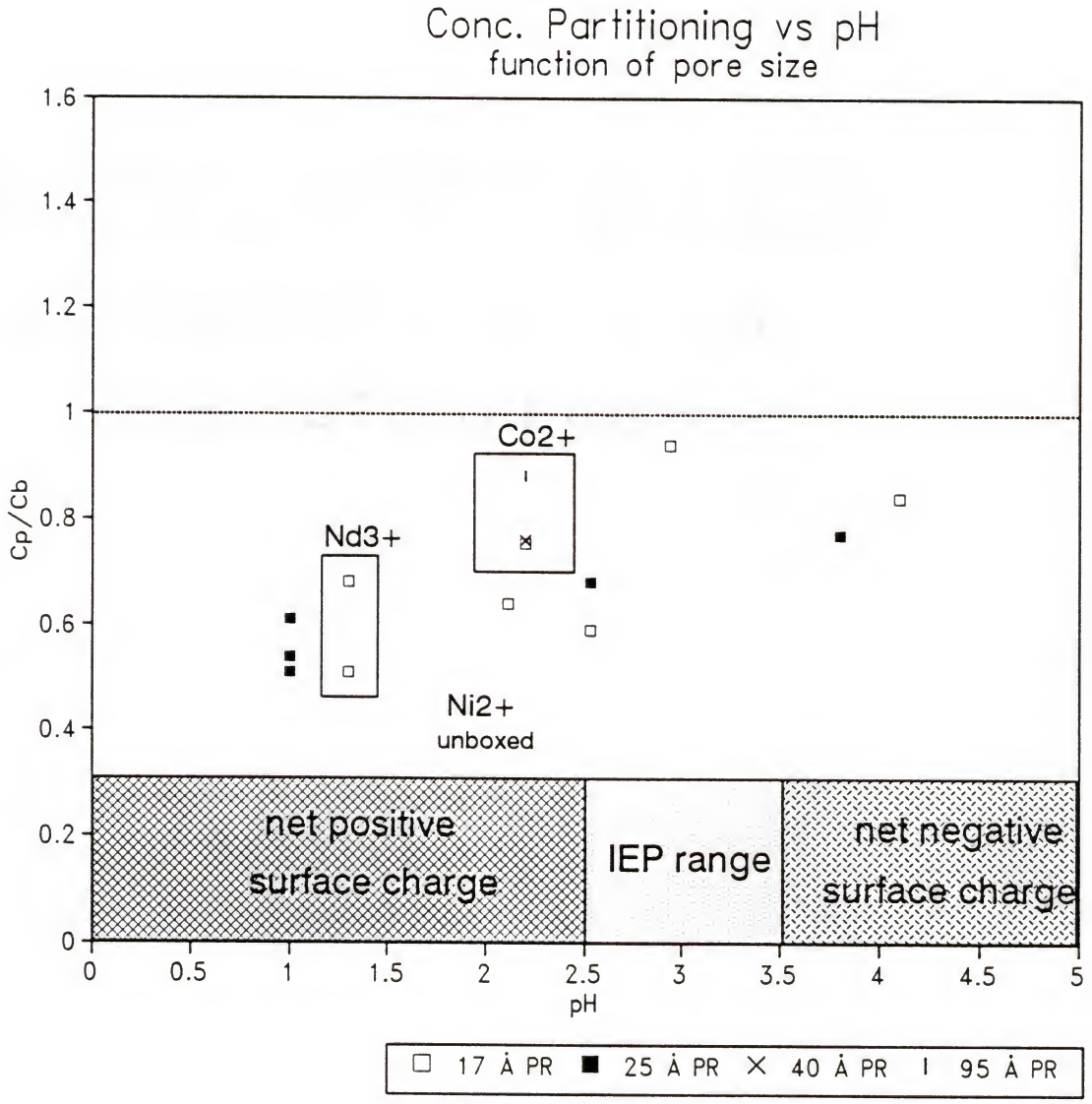

Figure 5.12 A plot of the partition coefficient for the hydrated Ni^{2+}, Nd^{3+}, and Co^{2+} ions as a function of solution pH and average pore radius of the silica gel monoliths.

Figure 5.13 displays a graph of the partition coefficient for the Cr^{3+} ion as a function of concentration for two pore volume fractions of gels. As the concentration was decreased, the partition coefficient increased and as the volume of pores was increased, the partition coefficient increased slightly.

The diffusion coefficients determined from the bulk solution concentration were recalculated with the equilibrium partition concentration as the driving force. This normalized effective diffusion coefficient, $D_{eff,n}$ is graphed versus the pore radius in figure 5.14. The values of $D_{eff,n}$ increase with pore size. The tortuosity was recalculated from the $D_{eff,n}$ and is plotted in figure 5.15 versus the pore radius. A smaller range of tortuosity values were calculated but the tortuosity still increase as the pore size decrease.

The partition coefficient is graphed as a function of Henry's Law constant in figure 5.16 for several values of the hydrated radius of the $Cr[(H_2O)_6]^{3+}$ species. The graph displays almost a one-to-one relationship of Φ with Henry's Law constant. The slope from the regression analysis increased as the hydrated radius increased.

The diffusivity ratio is plotted versus λ, for a hydrated Cr^{3+} radius of 4.5 Å. The trend revealed from figure 5.17 is that a decrease in pore size to approximately three times the hydrated Cr^{3+} ion radius significantly reduces the diffusivity ratio.

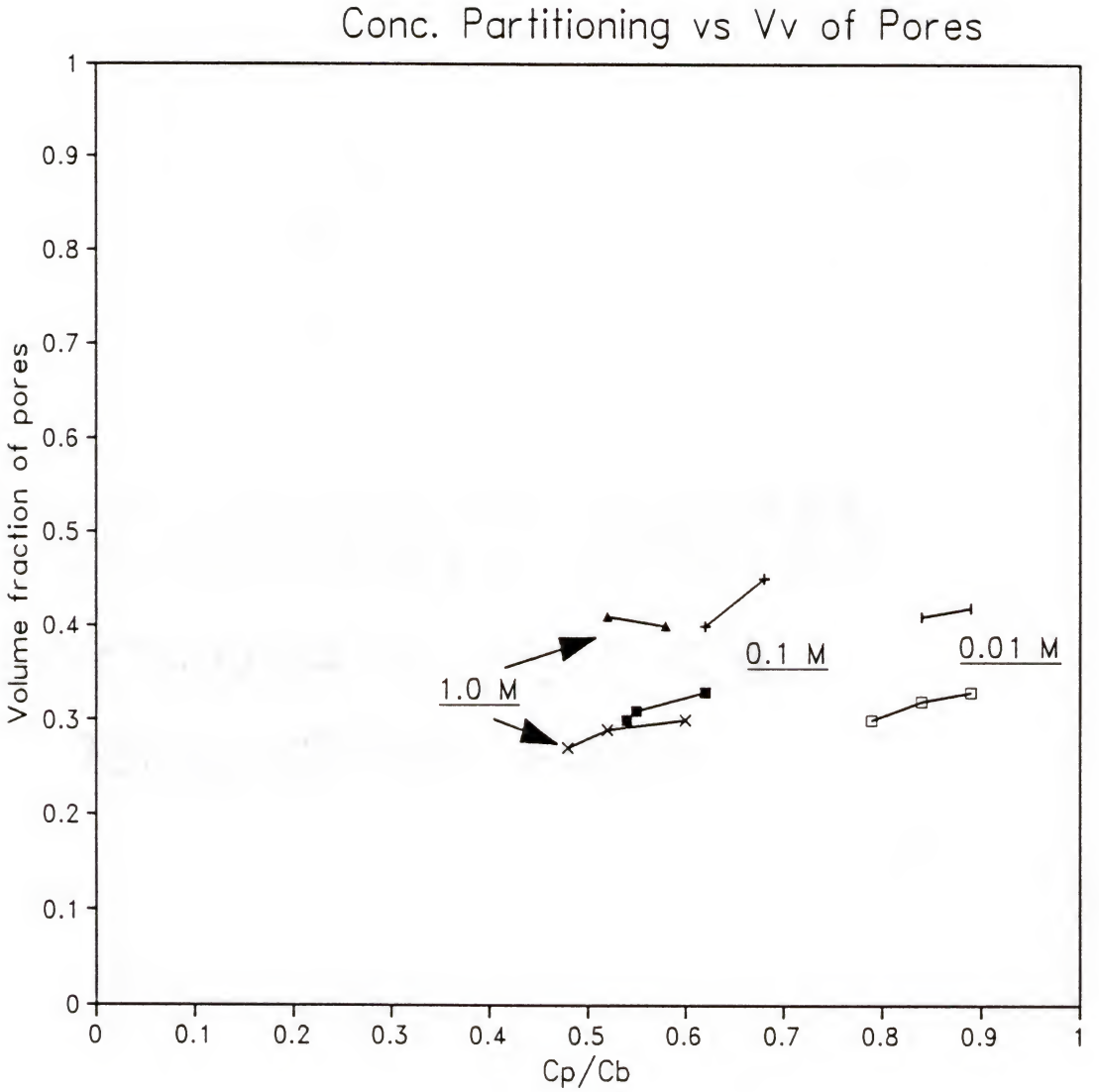

Figure 5.13 A plot of the partition coefficient for the $Cr[(H_2O)_6]^{3+}$ ion as a function of solution concentration at two different volume fractions of porosity.

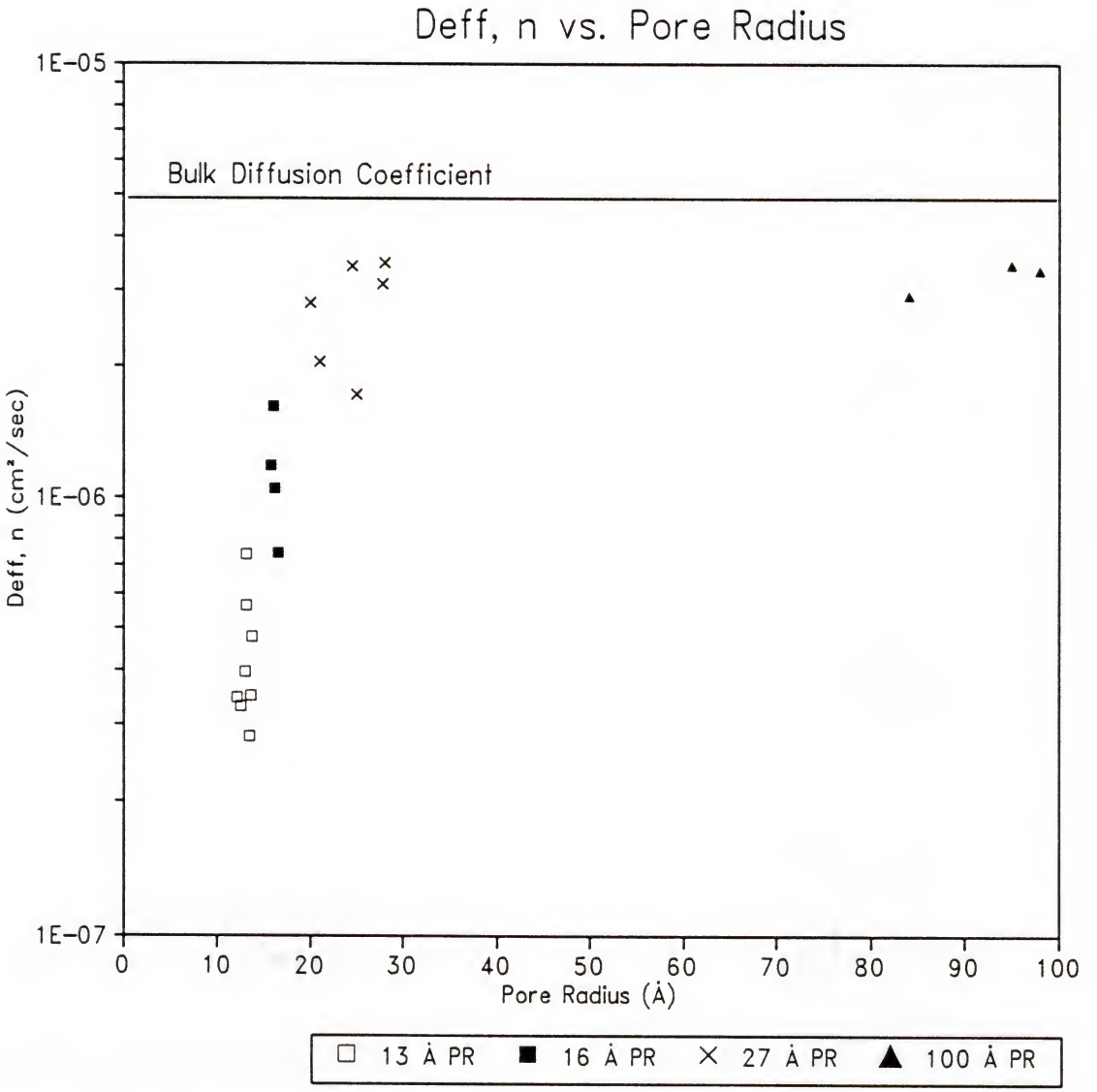

Figure 5.14 A plot of the normalized effective diffusion coefficient versus average pore radius of the silica gel monoliths.

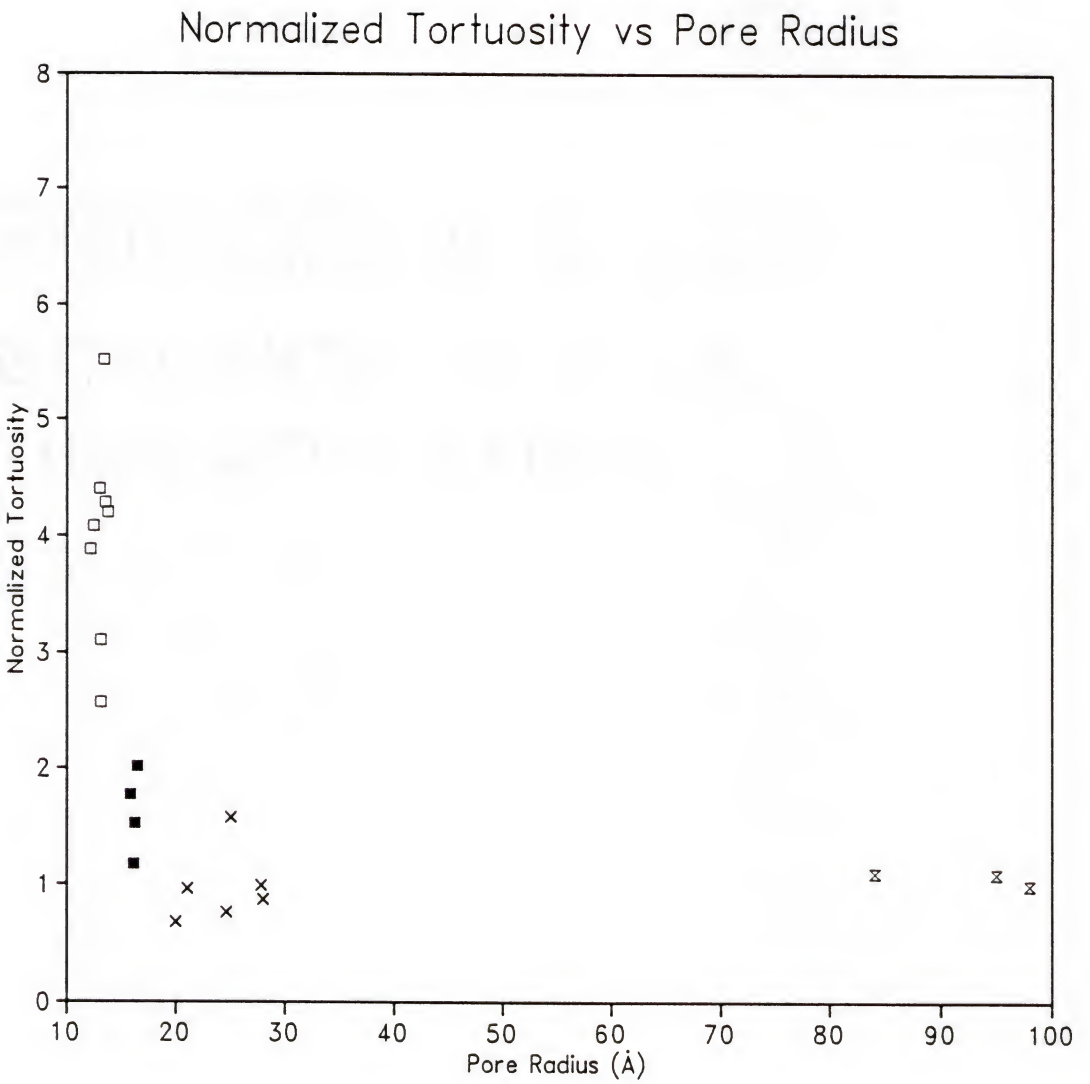

Figure 5.15 A plot of the tortuosity versus the average pore radius of the silica gel monolith.

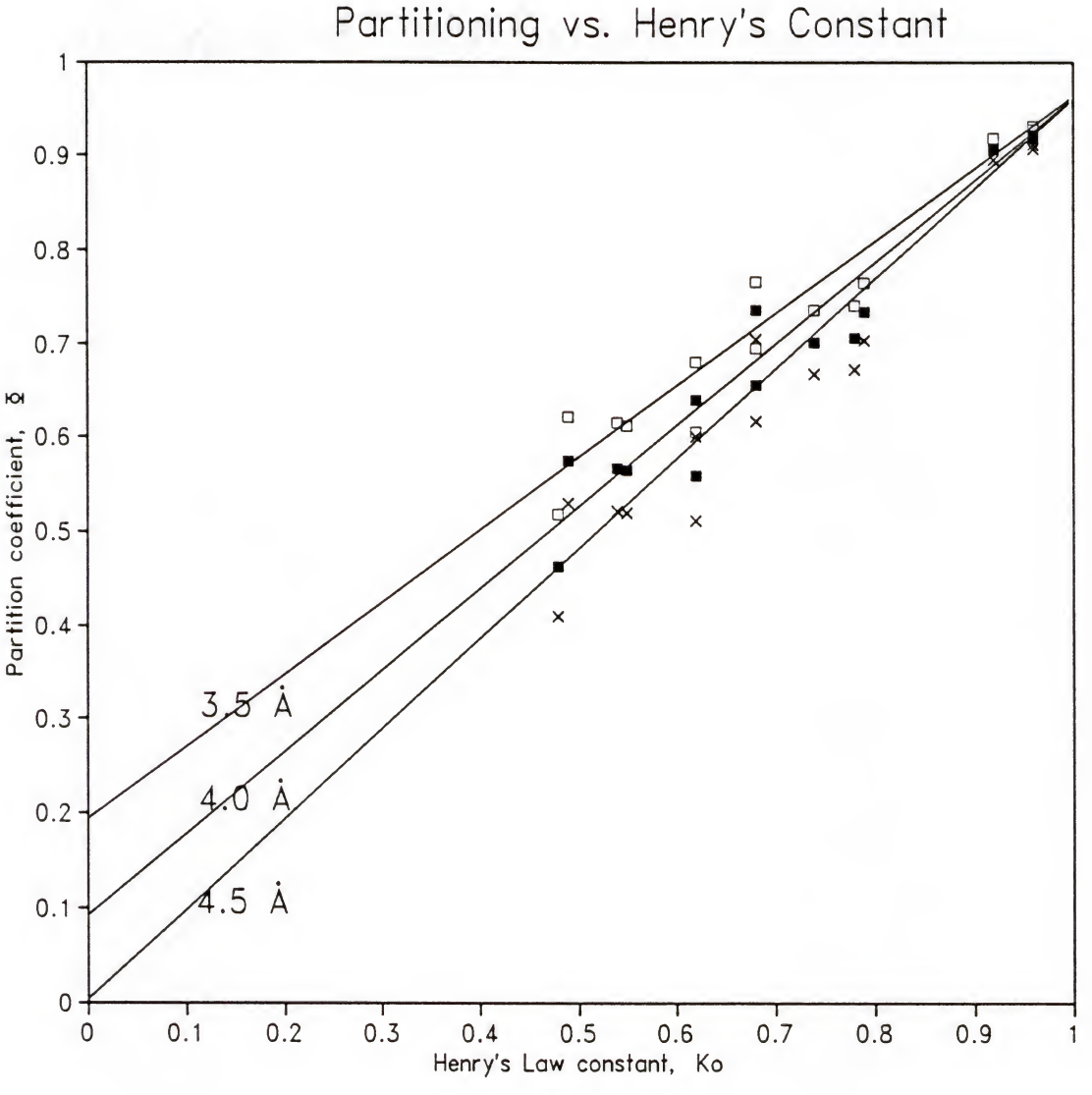

Figure 5.16 A plot of the partition coefficient versus the Henry's law constant. The Henry's Law constant values have been calculated for three different radii (3.5, 4.0, and 4.5 Å) of the hydrated chromium ions.

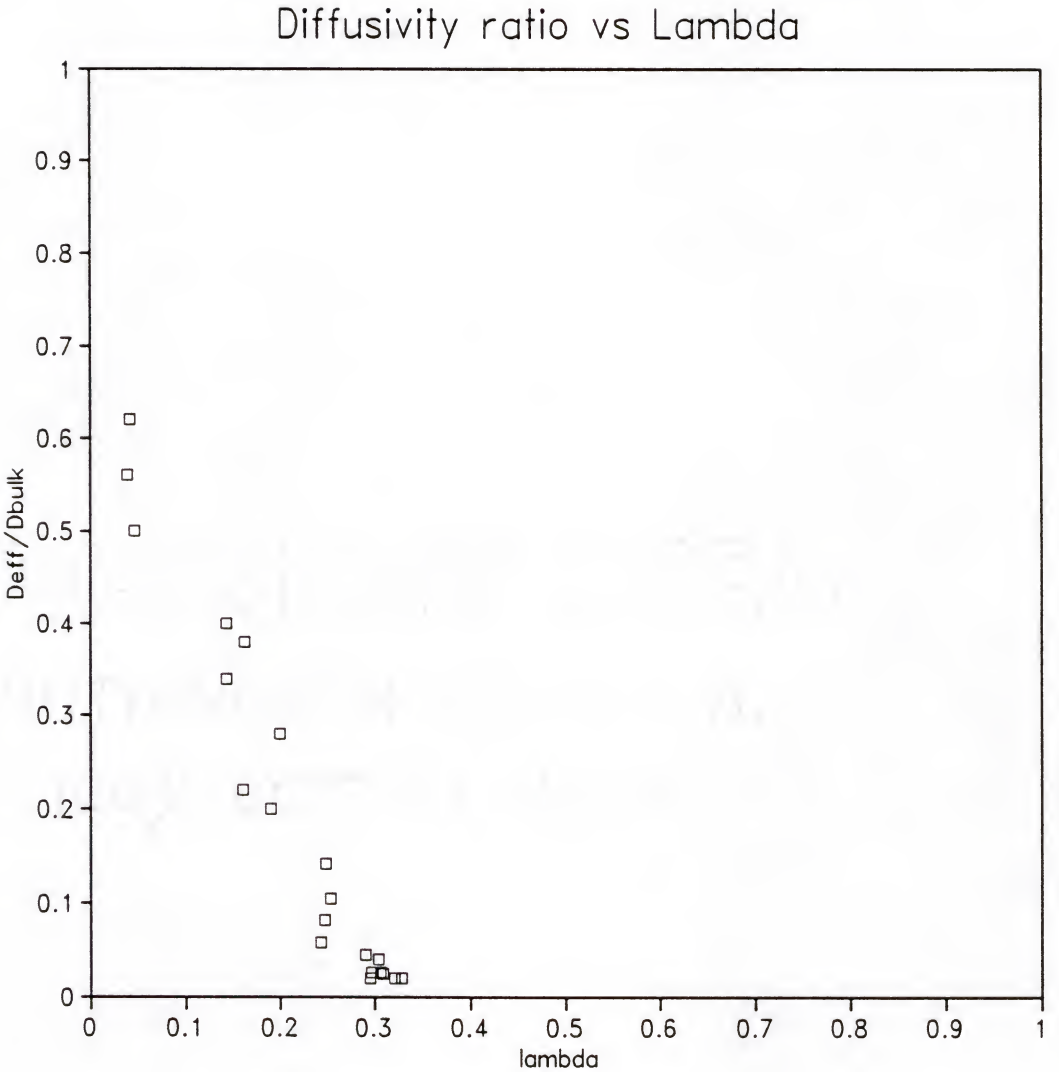

Figure 5.17 A plot of the ratio of the effective diffusion coefficient to the bulk diffusion coefficient versus lambda, the ratio of the hydrated ion radius to the average pore radius.

5.4.2 Discussion of the Results

The most apparent relationship found from the diffusion study was a decrease in the normalized diffusion coefficient as the pore size was decreased. Figure 5.6 indicates the diffusion constants for the largest pore sizes of the study, 100 Å and 27 Å, are only two to three times slower than the bulk diffusion value. These larger pore gels are similar to the diffusion behavior of the aged gels. The effective diffusion coefficient for the 13 Å gels are as much as 50 times slower than the bulk value.

The other metal ions in the study produced similar diffusion values to the Cr^{3+} ion. A detailed analysis of the trends for these ions was not given since they were studied less thoroughly than the Cr^{3+} ion. However, it is significant that the relative values for the effective diffusion coefficient and the partition coefficients of these metal ions are similar to the chromium ion. These are shown in figure 5.7 for comparison to the Cr^{3+} system.

Tortuosity values of materials studied for catalyst supports indicate that most materials have tortuosity values ranging from below unity to 6.[198] However, Krasuk and Smith[199] measured tortuosity values as high as 100 for sintered pellets with pore interconnections greatly reduced. The tortuosity values calculated from the effective diffusion coefficient, shown in figure 5.9, are larger than the normal range (1-6) of values. There may be several explanations for the reduction in the measured effective diffusion coefficient and subsequent increase in the calculated tortuosity.

The effective diffusion coefficients were measured from the flux into the gel. The time in between measurements varied from 3 minutes to 20 minutes depending upon the diffusion rate. Measurements were taken more frequently for the larger pore size gels. The solutions were not stirred during the diffusion runs to prevent the complication of an additional convection term. However, the diffusion coefficient was measured for one sample in an orbital stirrer (75 rpm). No significant differences were found in the fluxes between stirred and unstirred gels. If a stagnant layer developed at the interface of the gel and bulk solution, a decrease in the flux would result from a reduction in the driving force. The solutions were constantly agitated by the frequency of the measurements. Thus, it was assumed that the solutions remained uniform in the bulk and a stagnant layer did not form at the interface.

A build up of positive charge at the interface would also reduce the flux of chromium ions into the gel. It was assumed that the Cr^{3+} ion was not specifically adsorbed onto the surface in this pH range and that the charge on the gel surface was only due to the potential determining ions.

The explaination for the large reduction in the effective diffusion coefficient becomes evident from the analysis of the equilibrium partition coefficients, the second major finding in this chapter. The equilibrium partition coefficient, Φ, was calculated from the visible absorbance after diffusion into the gel has ceased. The path length was determined by measuring the thickness of the gel and multiplying this by the volume fraction of pores. The concentration in the porous gel was then

calculated by dividing the absorbance by the product of the reduced path length and the molar extinction coefficient. The values of the pore concentrations for the Cr^{3+} ion are listed in table 5.3.

The partition coefficient increased with pore radius. This is shown in figures 5.11 and 5.12. The concentration of the Cr^{3+} ion in the 13 Å pore radius gel is 50% of the bulk solution concentration. The concentration in the 95 Å pore radius gel is 95% of the bulk solution concentration.

Figure 5.13 may indicate that the partition coefficient is slightly dependent upon the solution concentration from 0.1 M to 1.0 M. This may not be a significant trend since the combination of errors form the pore volume, gel thickness and absorbance plot measurements could produce errors as large as ±15%. However, the partition coefficient for the 0.01 M solution is substantially larger. As seen in figure 5.11, the values of Φ for 0.01 M are very close to or larger than one. The solution pH is 2.74 for the 0.01 M solution. A direct comparison of the concentration effects between the partition coefficients at 0.01 M and the higher concentrations can not be made since the other solutions are at pH's of 1 and 1.76. However, this plot reveals that there is direct evidence for the increase in partition coefficient as a function of pH.

The measured IEP values from the electrophoresis study of chapter 4 indicate that the pH range for a net zero surface charge on these porous gels is from 2.5 to 3.5. The partition coefficient increased above unity at a chromium solution pH of 2.74. This coincides with the IEP range.

Table 5.3 Partitioning of the heavy metal salt solutions.

Pore Radius (Å)	Species	C_{Bulk} (mol/L)	C_{Pore} (mol/L)	C_p/C_b	pH
14.2	Cr^{3+}	1.0	0.52	0.52	1.0
13.6	Cr^{3+}	1.0	0.58	0.58	1.0
13.8	Cr^{3+}	1.0	0.48	0.48	1.0
13.1	Cr^{3+}	1.0	0.52	0.52	1.0
12.5	Cr^{3+}	1.0	0.60	0.60	1.0
13.0	Cr^{3+}	0.1	0.068	0.68	1.0
12.2	Cr^{3+}	0.1	0.062	0.62	1.0
12.2	Cr^{3+}	0.1	0.062	0.62	1.0
14.1	Cr^{3+}	0.1	0.055	0.55	1.0
12.6	Cr^{3+}	0.1	0.054	0.54	1.0
14.8	Cr^{3+}	0.01	0.0089	0.89	1.0
15.0	Cr^{3+}	0.01	0.0085	0.85	1.0
13.2	Cr^{3+}	0.01	0.0089	0.89	1.0
14.1	Cr^{3+}	0.01	0.0079	0.79	1.0
12.8	Cr^{3+}	0.01	0.0079	0.79	1.0
13.8	Cr^{3+}	0.1	0.078	0.78	1.7
13.0	Cr^{3+}	0.1	0.076	0.76	1.7
13.9	Cr^{3+}	0.01	0.011	1.10	2.7
28.0	Cr^{3+}	0.1	0.146	1.46	2.7
27.8	Cr^{3+}	0.1	0.079	0.79	1.0
25.0	Cr^{3+}	0.1	0.078	0.78	1.0
29.6	Cr^{3+}	0.1	0.085	0.85	1.7
20.0	Cr^{3+}	0.1	0.083	0.83	1.7
21.0	Cr^{3+}	0.1	0.074	0.74	1.0
95	Cr^{3+}	0.1	0.093	0.93	1.0

Table 5.3 Continued

94	Cr^{3+}	0.1	0.094	0.94	1.0
100	Cr^{3+}	0.1	0.095	0.95	1.0
93	Cr^{3+}	0.1	0.096	0.96	1.7
98	Cr^{3+}	0.1	0.092	0.92	1.7
26.2	Ni^{2+}	0.7	0.35	0.50	1.0
24.3	Ni^{2+}	0.7	0.385	0.55	1.0
22.0	Ni^{2+}	0.7	0.434	0.62	1.0
16.1	Ni^{2+}	0.7	0.448	0.64	2.2
15.8	Ni^{2+}	0.7	0.385	0.55	2.5
27.1	Ni^{2+}	0.7	0.476	0.68	2.5
16.1	Ni^{2+}	0.7	0.623	0.89	3.0
26.1	Ni^{2+}	0.7	0.532	0.76	3.8
16.7	Ni^{2+}	0.7	0.567	0.81	4.2
17.1	Co^{2+}	0.7	0.504	0.73	2.2
38.3	Co^{2+}	0.7	0.511	0.72	2.2
95.1	Co^{2+}	0.7	0.602	0.86	2.2
16.2	Nd^{3+}	0.7	0.476	0.68	1.3
16.1	Nd^{3+}	0.7	0.350	0.50	1.3

The Healy and James[189] study of Cr^{3+} ion adsorption behavior on the solution pH indicated that a majority of the Cr^{3+} adsorbed between pH's 4 and 6. The adsorption isotherm indicated that a small percentage of chromium adsorbed at lower pH's. Their study was conducted at a solution concentration of 0.001 M. As the concentration is increased the ion adsorption density is increased.[200] Therefore, ion adsorption would be larger at any given pH and a larger percentage of the Cr^{3+} may be adsorbed at a pH of 2.74.

As the pH is increased the net positive charge decreases on the surface of the gel. The electrostatic repulsion between the surface and the Cr^{3+} would also decrease. This would allow closer interaction of the cations with the walls and increase the concentration within the pore. The adsorption of the Cr^{3+} ion onto the surface will increase the volume available in the pores for Cr^{3+} ions. This should increase the concentration within the pore.

The partitioning effects should be the largest for the smallest pore sizes. The hydrated Cr^{3+} ion radius has been reported to vary from 3.5 to 4.61 Å. Therefore, the number of hydrated Cr^{3+} ions which can fit across the dimensions of the average pores measured in this study, from purely geometrical considerations, are 2-3 ions for the 13 Å pore radius gel and 21-27 ions across the 95 Å pore radius gel. If additional electrostatic constraints are added the number of ions across the pore decreases. Only integral numbers of ions are possible across the dimensions of the pores. Small changes in the electrostatic repulsion due to a change in solution pH may be enough to allow an additional ion across

the diameter of the pore. The percent increase of hydrated chromium ions across the pores for the 13 Å pore radius is much larger than the percent increase for the 95 Å pore radius gel. This could account for the differences between the change in partition coefficients with pH for the different pore size gels.

The reduced concentration within the pore can be substituted for the bulk solution concentration as the driving force for the diffusion. The normalized effective diffusion coefficients, $D_{eff,n}$, calculated from the reduced pore concentration and the recalculated tortuosities, τ_n, are plotted as a function of pore radius in figures 5.14 and 5.15, respectively.

The slowest value of $D_{eff,n}$ is now only 15 times slower than the bulk diffusion and the range of tortuosities vary from 5.5 to 0.7. These values of tortuosities now fall within the expected range of less than unity to 6.

The major contribution to the partition coefficient is the Henry's law constant,[201] $K_o = (1-\lambda)^2$. This term is essentially the ratio of the volume accessible to the center of the solute to the total measured pore volume. The equation is valid for low concentrations where the solute-solute interactions are unimportant. Values of 3.5 Å, 4.0 Å, and 4.5 Å were chosen as the hydrated Cr^{3+} ion radius to calculate K_o. Figure 5.16 displays the different calculated values of K_o plotted against the measured partition coefficients for the different pore size gels in this study.

The R^2 values are nearly identical from the regression, 0.924, 0.928, and 0.930, since the same data points were used with different numerical values of the

hydrated radius. The best fit should produce a slope of 1 and a y-axis constant of 0. The slopes of the lines and the y-constants for the 3.5 Å, 4.0 Å and 4.5 Å hydrated radii are, 0.76 and 0.191, 0.85 and 0.095, and 0.93 and 0.002, respectively. The 4.5 Å hydrated radius of the chromium ion provides the best fit. This is only an approximation since the gels contain a distribution of pore sizes, ionic interactions might be occurring, and specific interactions may be occurring between the ions and the surface. However, it agrees with the value of 4.61 Å measured by Nightingale.[202]

The ratio of the effective diffusion coefficient to the bulk solution diffusion coefficient is plotted versus lambda. The value of lambda is calculated using 4.5 Å as the Cr^{3+} ion radius in figure 5.17. A significant reduction in the effective diffusion coefficient occurs as the pore size approaches three times the radius of the gel. Similar results for the reduction in the diffusion coefficient for other systems has been found at $\lambda = 0.33$.

The diffusion of chromium ions into the porous gels is sometimes associated with the maximum in the absorbance shifting to longer wavelengths. The magnitude of the shift can vary from 3-5 nm to 25 nm and is a function of solution pH and concentration.

The peak shifting initially occurred while the chromium solutions were diffusing out of the porous gels. The solution conditions were a 0.1 M solution of chromium nitrate at pH 1.7. The gel was saturated with the solution and displayed a peak maximum at 575 nm. It was then placed in a water and nitric acid solution

of pH 1.7. The peak maximum remained at 575 nm until very little chromium was left in the gel. The peak maximum then began shifting to longer wavelengths. It was difficult to assign a definite peak maximum to the shifted peak because the concentrations were near the sensitivity limit of the spectrophotometer. However, the peak shift was approximately 15-20 nm. This indicated that the peak shifting was a function of concentration or that the last ions within the gel were in a different environment than the rest of the solution.

During the initial diffusion of a 0.01 M Cr^{3+} solution, at 2.74 pH, the peak maximum is at 575 nm. As the diffusion proceeded the peak maximum began to shift to higher wavelengths. A spectrum of the peak shifting phenomena is shown in figure 5.18. Since this solution was at a higher pH it is possible that the shifting was due to the pH of the solution. Figure 5.19 is a plot of the $Cr[(H_2O)]^{3+}$ solutions from a range of approximately 0.005 M to 1.0 M. The pH varies from 0.5 to 3.0 for the different concentrations, respectively. As can be seen very little if any peak shifting occurs for the change in these solution variables. The peak shifting must be due to an interaction of the hydrated ion with the surface of the gel silica.

A thermodynamic model of the adsorption of hydrolyzable metal ions was presented by James and Healy.[191] Their conclusion, based upon previous work,[189,190] is that the adsorbed species are separated from the surface by at least one water molecule. This indicates that the ions are not required to lose their inner or primary hydration sheaths. An additional EPR line broadening study by Cornet

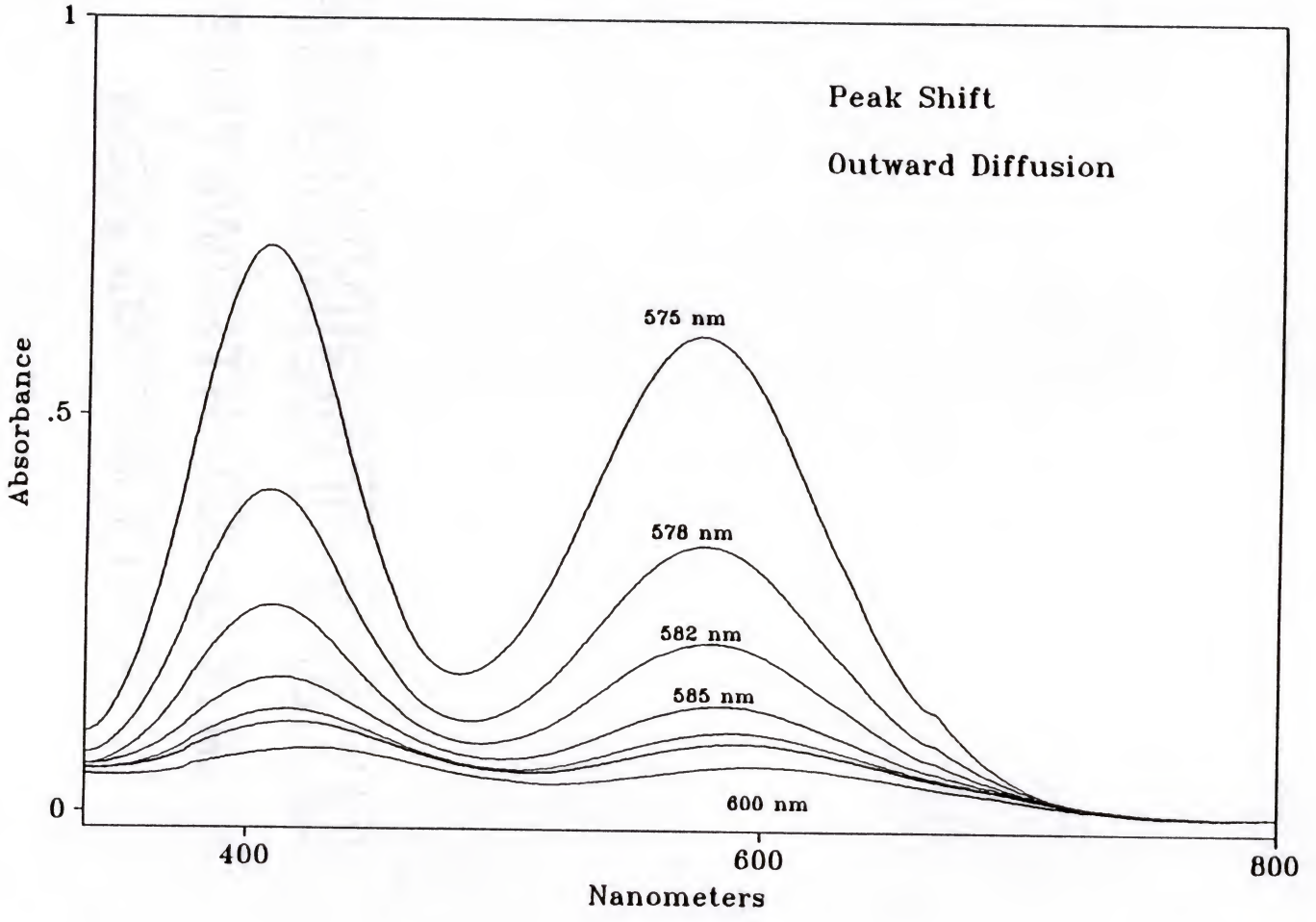

Figure 5.18 A time dependent plot of the visible spectrum of a silica gel monolith as a chromium salt solution diffuses out. The numbers on the plot indicate the wavelengths of the peak maxima.

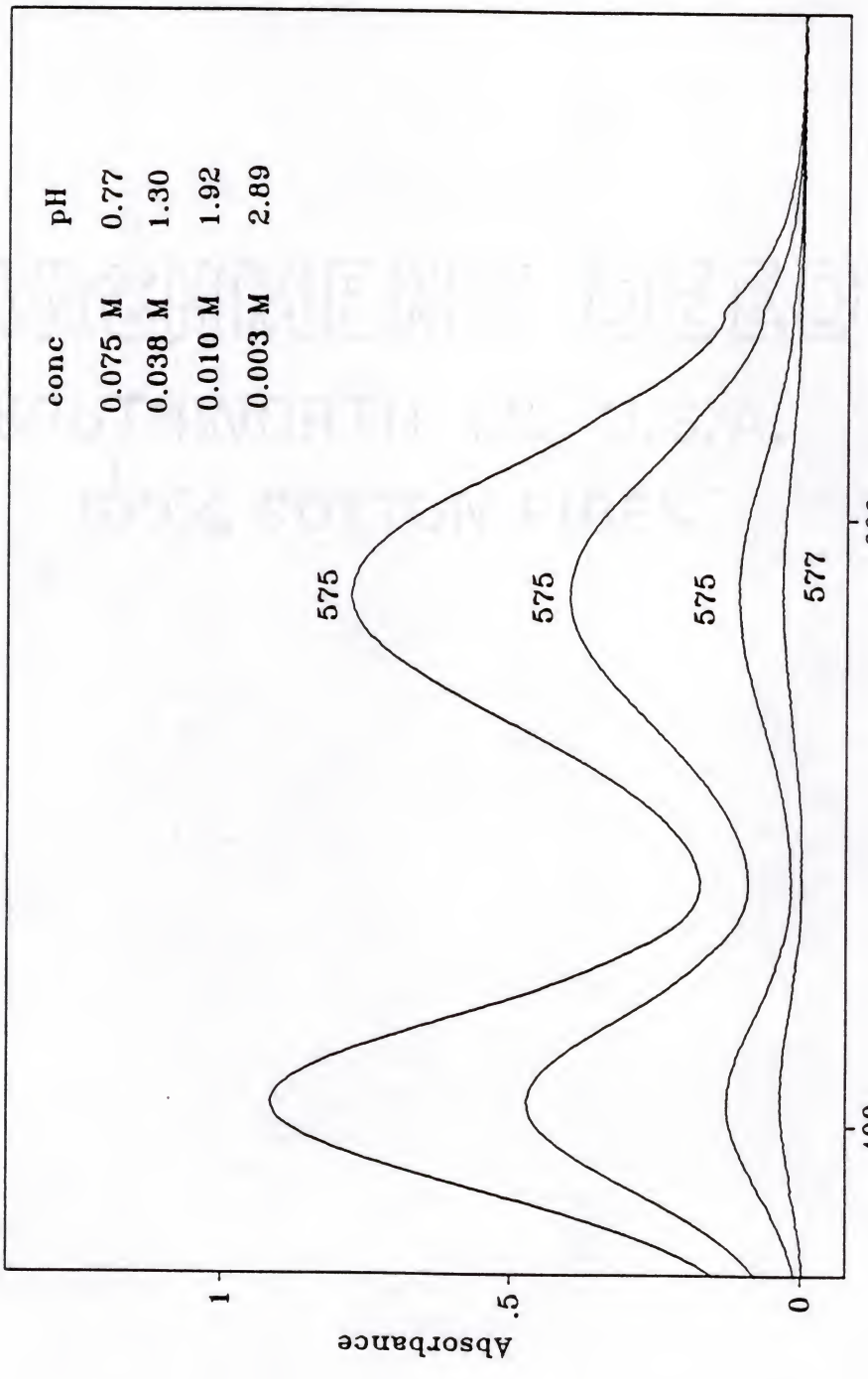

Figure 5.19 A plot of standard chromium nitrate salt solutions at the concentrations and pH's indicated.

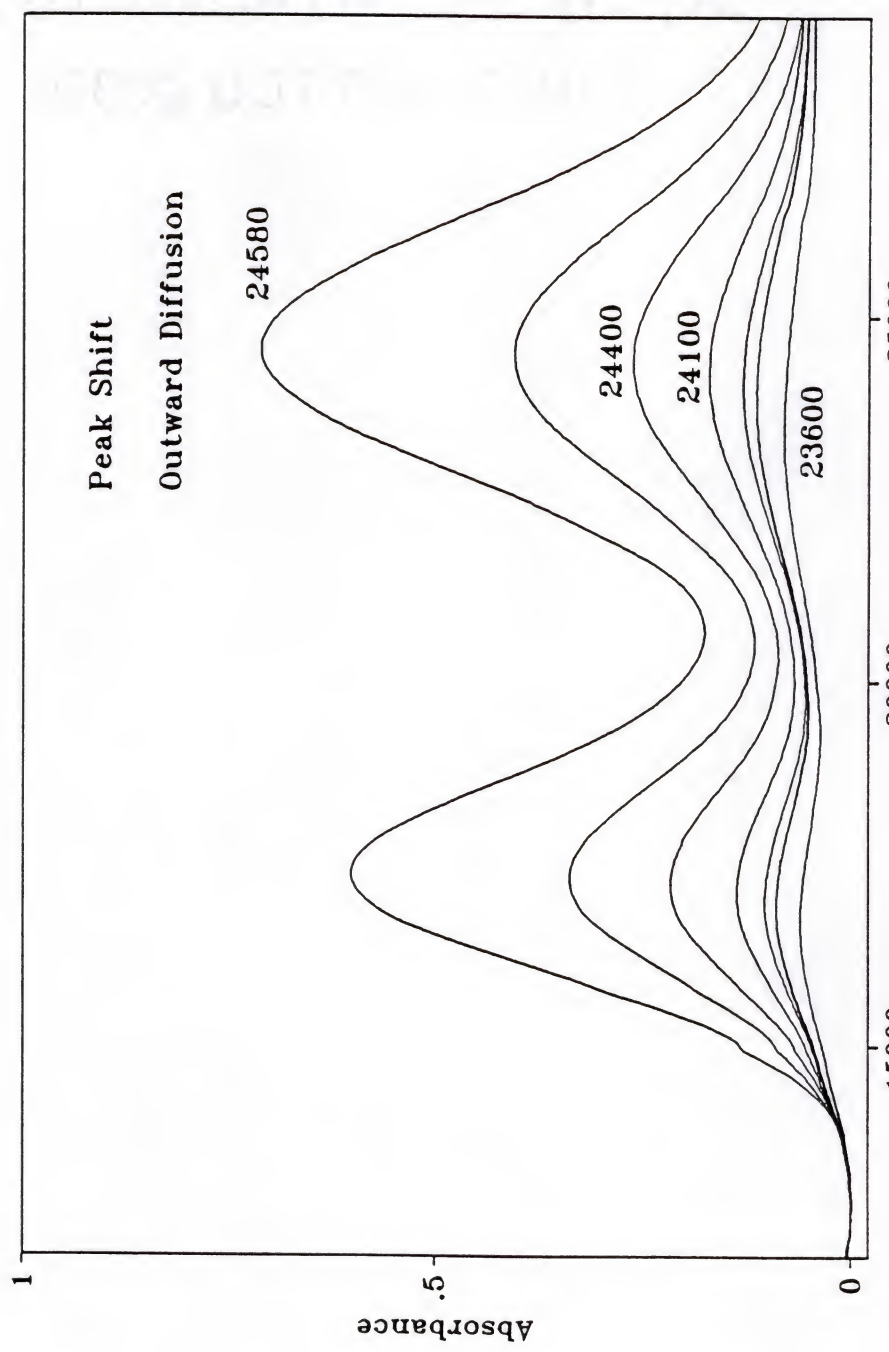

Figure 5.20 A time dependent plot of the visible spectrum of a silica gel monolith as a chromium salt solution diffuses out. The numbers on the plot indicate the wavenumbers of the peak maxima.

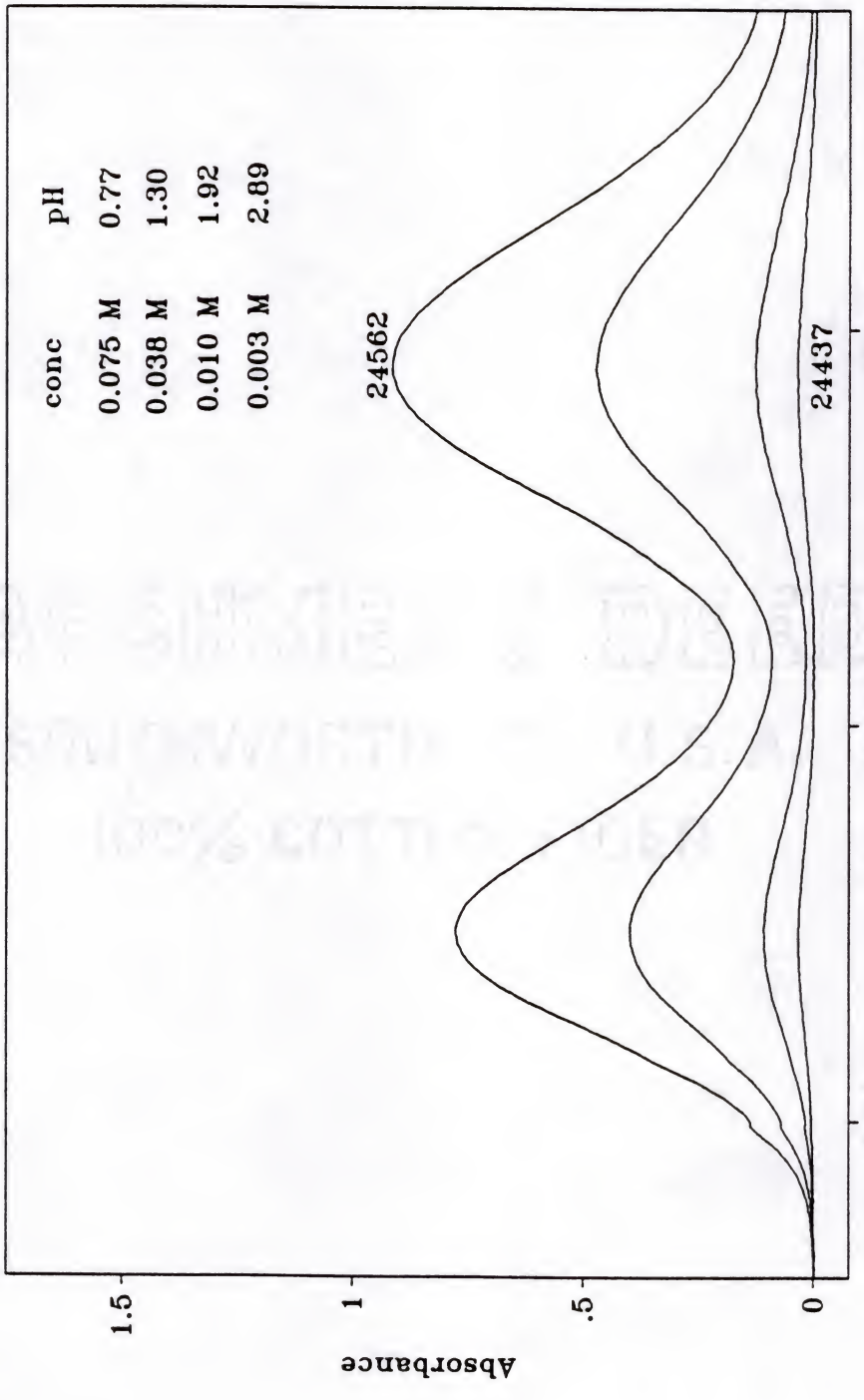

Figure 5.21 A plot of standard chromium nitrate salt solutions at the concentrations and pH's indicated.

and Burwell[203] indicated that the environment of the Cr^{3+} ion is in the same environment in the pores of silica gel as in bulk solution.

It appears from these studies that the influence of the surface modifies the primary hydration sphere which influences the energy of the electronic transition. In order to understand the peak shifting phenomena more thoroughly, semi-empirical molecular orbital calculations were performed. These results are given in chapter 6.

5.5 Conclusions

The objective of this chapter was to study the effect of the sol-gel processing parameters upon the diffusion and partitioning of chromium salt solutions within silica gel porous monoliths. Conclusions drawn from this analysis are as follows.

The partitioning of the chromium was a strong function of the solution pH and the pore size of the porous monoliths. The smallest pore size investigated produced partition coefficients of 0.48 to 0.64 for the most concentrated solution of 1.0 M. These partition values shifted to 0.78 to 0.89 as the concentration was decreased from 1.0 M to 0.01 M. As the pore size increased the partition coefficients increased from ≈0.5 to ≈0.95 for a constant concentration and solution pH. The partition coefficients approached the limit of 1 as the pH was increased towards the IEP of the silica monoliths. At a pH of 2.74 the partitioning was greater than 1. The value of the partition coefficients for a solution pH of 2.74

ranged from 0.95 to 1.18 for the three pore sizes investigated. There was no apparent trend with pore size at this pH.

The diffusion coefficient for the hexa-aqua chromium ion, as determined from the bulk solution driving force, is one and a half orders of magnitude smaller than the diffusion in bulk solution for the smallest pore size measured. The largest pore size showed a decrease of one-half the diffusion coefficient from the bulk value. The diffusion into unconsolidated aged samples produced diffusion coefficients approximately equivalent to the values for the largest pore size heat treated gels. The tortuosities calculated from these effective diffusion coefficients ranged from 15.3 to 1.4.

The diffusion coefficient was recalculated by using the equilibrium partition concentration within the pore as the driving force for diffusion. The effect was largest on the smallest pore size increasing the diffusion coefficient by an order of magnitude. The recalculated tortuosities ranged from 5.5 to 0.7.

The effective diffusion coefficient decreased the most as the ratio of the hydrated chromium radius to pore radius approached 0.3. This may indicate that pores smaller than the average pore size might be controlling the diffusion of chromium into the porous gel network or that additional forces, due to the smaller size of the pores, are contributing to the reduction of the ion's movement.

A shifting of the peak maximum of the d-d transitions for the hexa-aqua Cr^{3+} ion occurred during the diffusion into the pores. The shifting is most prominent at

higher pH's. The peak shifting is due to interaction of the ion with the pore wall during a change in surface charge of the silica.

CHAPTER 6
INVESTIGATION OF THE BINDING OF Cr^{3+} TO POLYSILOXANE STRUCTURES WITH A SEMI-EMPIRICAL MOLECULAR ORBITAL MODEL

6.1 Introduction

ZINDO[204] (Zerners Intermediate Neglect of Differential Overlap) is a semi-empirical molecular orbital package which utilizes the Hartree-Fock, Self-Consistent Field method to calculate atomic and molecular structures. This method has been applied to the investigation of the $Cr^{3+}/H_2O/SiO_2$ system. Experimental evidence indicates peak shifting for the $^4A_{2g} \rightarrow {}^4T_{2g}$ and $^4A_{2g} \rightarrow {}^4T_{1g}$ transitions of the $[Cr(H_2O)_6]^{3+}$ species within porous sol-gel silica monoliths. This shift indicates a change in the local or immediate environment surrounding the Cr^{3+} ion. ZINDO has been used to obtain optimized molecular structures from which the electronic spectra have been computed using the INDO/S[205] model hamiltonian. Combining the theoretical results with the experimental data various dopant/silica interactions are proposed which may be responsible for the red-shifting of these transitions.

6.2 Molecular Orbital Modeling

The theoretical study of molecules is usually classified into two separate methods. The classical approach of molecular mechanics[206] (MM) and the quantum chemical approach of ab initio and semi-empirical models. The

distinguishing difference is that classical methods model the motion of atomic nuclei and quantum chemistry models the structure of the electrons of the atoms with respect to a temporarily fixed position of nuclei.

The Born-Oppenheimer approximation applied to the nonrelativistic, time-independent Schrödinger equation (the Hamiltonian operator is composed of kinetic and potential terms for both the electrons and the nuclei and is the basis of molecular modeling) states that the equation for molecules can be separated into two parts, one describing the motion of the nuclei and the other the electrons. Thus, the separated hamiltonian for the nuclei part is used to solve the vibrational part of the problem and the remaining electronic hamiltonian is used to solve the electronic equation. The electronic equation is composed of the kinetic and potential terms for the electrons and the potential term between the electrons and the nuclei. It is from the electronic portion of the equation that one can ultimately determine the fundamental chemical properties of the molecule (i.e. from the electron distribution).

Molecular mechanics calculations employ empirically derived sets of equations for the Born-Oppenheimer surface whose mathematical form is familiar in classical mechanics (i.e. harmonic oscillator). This set of potential functions or force field, contains adjustable parameters that are optimized to obtain the best fit between the experimental and calculated values of geometries, conformational energies, heats of formations, or other properties. It is assumed that the parameters and force constants are transferrable from one molecule to another.

This method, which studies the motion of the nuclei around which electrons are assumed to find an optimum distribution, is not amenable to the study of the $Cr^{3+}/H_2O/SiO_2$ system. The changes which occur in the visible spectrum of the Cr^{3+} ion are due to a rearrangement or change in the molecular or electronic orbitals. MM can not calculate the electronic state of a molecular configuration.

At the other end of the theoretical spectrum from MM, are the ab initio methods. All the integrals describing the elctrons are exactly evaluated in ab initio theory. Reviews of the available theory[207-209] as applied to ab initio modeling clearly indicate the complexity and time involved in such calculations. Large basis set (roughly the number of atomic orbitals used to describe the molecule) ab initio calculations, which include electron correlations, are capable of producing accurate results comparable to experiments. However, the computational time for a quantum chemical calculation is proportional to the size of the basis set. Ab initio calculations scale as N^4, semi-empirical as N^3, where N is the size of the basis set, and MM as N^2 (N is the number of atoms).[210] These time dependencies indicate that the total number of atoms which can be treated by each method decrease by a factor of ten as the level of theory increases. The limiting reality of the calculational time/number of atom relationship, combined with the requirement that years of experience are necessary to be able to compute at this level of sophistication, advises the use of semi-empirical theory to describe the $Cr^{3+}/H_2O/SiO_2$ interactions.

Quantum mechanical in nature, semi-empirical methods lie between the MM and ab initio methods. As mentioned above, the large number of approximations in semi-empirical methods decreases the number of terms to be evaluated and significantly reduces calculational time. However, semi-empirical methods are only as good as the parameter set from which they are based. Various degrees of differential overlap of electron wave functions exist in commonly available semi-empirical methods. Three- and four-center integrals are completely ignored and the one- and two-center integrals are approximated using functions from molecular data and formal theory. In general, the more wavefunction overlap the more parameters are required. Several methods are available and should be utilized according to what information is being sought and which system the molecular chemist (or materials scientist) is modeling. CNDO/1,[211,212] CNDO/2,[213] Pariser-Parr-Pople,[214] INDO,[215] INDO/S,[204,216] NDDO,[211] MINDO/3,[217] MNDO,[218] AM1,[219] and PM3,[220,221] are among the methods which use the self-consistent field as the one-electron hamiltonian and all valence orbitals as the basis set. These methods are reviewed with respect to the difference between the calculated property and the experimentally determined value, referred to as the error.[210,222] The errors vary significantly depending upon the type of molecular system being studied.[210,222]

The basic idea of molecular orbital theory is to solve the electronic Schrödinger equation such that the geometries and the properties calculated from the energy of the molecule and its charge density are as close as possible to experimental results. This permits one to study unknown molecules more

assuredly. Each semi-empirical method has its own set of parameters which predicts different levels of accuracy in properties for different types of molecules (it predicts the best properties for molecules similar to those included in the parameterization).

The basic idea of the Hartree-Fock self-consistent field method is the same for all of the more recent semi-empirical methods. The concept is to determine an approximate electronic wavefunction which describes all n-electrons in a molecule. The eigenvalue of the wavefunction is its energy while the wavefunction multiplied by its complex conjugate gives the electron distribution or probability of finding an electron in space. One initial approximation for this wavefunction is the product of n-molecular orbitals or wavefunctions. The molecular orbitals are described in terms of atomic orbitals since molecules are composed of atoms. These atomic orbitals are "best" represented by Slater-type orbitals. However, these orbitals are computationally difficult to handle and can be approximated nicely by varying numbers of Gaussian type orbitals (usually 3-6 Gaussians per Slater) which are easier to handle. Included with each atomic orbital is a coefficient which allows varying proportions of the different atomic orbitals to make up the molecular orbitals. These coefficients are determined from the Schrödinger equation semi-empirically. The beautiful part of molecular orbital theory is that the electrons are delocalized and in theory all the molecular orbitals conceivably have a component from all the atomic orbitals of the molecule.

Now that the hamiltonian for all n-electrons has been formed a further approximation enables it to be represented by the sum of n-one-electron effective hamiltonians, whose eigenfunctions are the molecular orbitals. The energy of these molecular orbitals is approximately equivalent to the ionization potential. The operator of this effective hamiltonian is a function of the occupied orbitals and this dependency is why the reduced eigenfunction must be solved self-consistently. Therefore an initial guess for the molecular orbitals is made producing a second value as the next input (hopefully improved functions are generated) until the change is within a certain tolerance. The molecular structure is self-consistent.

6.2.1 ZINDO

ZINDO was developed at the University of Florida Quantum Theory Project.[204] ZINDO provides two different valence-electron only semi-empirical procedures: a method for computing spectroscopic properties and a method for computing molecular geometries (conformations and structures). This model is a valence-electron-only program; it cannot calculate properties which depend upon the inner-shell electrons.

ZINDO uses the theoretically-based INDO parametrization which include parameters for d-orbitals for many of the transition elements, including Cr. ZINDO also has an alternative parameterization (INDO/S) for electronic (UV/visible) spectra which produces good results. In general, the INDO/S reproduces the ezcitation energies of transitions below 40,000 cm^{-1} within 2,000 cm^{-1} at the CIS level.[210] Occasionally charge transfer bands have greater errors, but $d \rightarrow d^*$

excitations are particularly well reproduced. Also, the model will not reproduce spectra within about 2 eV of the first ionization potential of a system, for it does not contain Rydberg orbitals.[210]

6.3 Experimental

6.3.1 Peak Shifting Phenomena

Silica monoliths were prepared by hydrolysis and polycondensation of tetramethyl orthosilicate (TMOS), $Si(OCH_3)_4$, under acidic conditions as presented in chapter 3 of this dissertation. Initially the two absorption maxima (λ_{max}) for the d-d Cr^{3+} transitions occur at 408 nm and 575 nm. The magnitude of the red shift varies depending upon the pH and concentration of the solution. The peak shifting has been described in chapter 5. It is the nature or origin of this shifting which is examined theoretically here.

6.3.2 Experimental Discussion

The peak shifting which occurs within the gel with time may be explained by invoking one or more of the following mechanisms:

a. Hydrogen-bonding of the hexa-aqua Cr^{3+} species to the surface of the glass. The state of the water immediately adjacent to the surface has been proposed to have a higher viscosity[223] due to its attraction to the surface. This interaction rearranges the electron density in this polarizable molecule. If this water molecule is incorporated into the inner hydration sphere of the Cr^{3+} ion a

modification to the equilibrium geometry would occur changing the frequency of the absorption.

b. Substitution of another ligand into the inner coordination sphere of the Cr^{3+}. The only free ions available for substitution into the inner coordination sphere are OH^- and NO_3^- anions. These substitutions would lower the electric field strength around the central ion and consequently produce shifts in the spectra. However, both anions are weaker than water in the spectrochemical series. The electrostatic effect of an extremely confined environment, as produced by very small pore gels, may also induce some spectral shift.

c. Chemisorption at the surface. A hydroxyl on the glass surface or a deprotonated hydroxyl, $\equiv SiO^-$, may substitute for one or more of the coordinated waters. This would distort the octahedral symmetry of the Cr^{3+} ion changing the metal to ligand distances which again would affect the transition frequency.

d. Elimination or ring opening catalysis of the D_1 defect. The D_1 defect or four-member siloxane ring has been shown to rehydrate slowly[12] ($\approx$ 100x slower than the D_2 defect) upon exposure to a humid environment. This ring opening could be catalysised by the presence of the hexa-aqua ion or the ring may be opening following an unaltered kinetic path incorporating the Cr^{3+} ion onto the resulting chain end. Both effects would alter the frequency of the transition.

e. Proton abstraction from a water molecule within the inner coordination sphere of Cr^{3+}. Surface species of the glass may abstract a proton from one of

the six water ligands. This result would produce $[Cr(H_2O)_5OH]^{2+}$ altering the absorption frequency of the d-d transitions and acidifying the surface.

6.4 Theoretical Modeling

6.4.1 Theoretical Method

The INDO/1[215] method has been used to optimize molecular geometries and INDO/S was used to generate electronic spectra of these optimized species. The theory is based on a self-consistent field method to acquire geometries and a configuration interaction singles (CIS) to obtain the electronic spectra. The electronic spectra were generated using only configuration interaction single excitations with a typical CI involving 7 occupied and 7 virtual molecular orbitals.

6.4.2 Parameterization

Anderson et al.[224] have calculated the spectra of the hydrated ions of the first transition series and reproduced the experimental spectra accurately. Their calculation for the $[Cr(H_2O)_6]^{3+}$ species involved a longer metal to oxygen distance ($\approx$2.15 Å) than found from crystallographic or gas phase data (1.75-1.99 Å).[225-227] The present calculations reproduce a more reasonable Cr-O distance while accurately reproducing the electronic spectra. This was done by modification of the empirical parameter, β, which includes the resonance integrals. INDO/1 parameters were first adjusted to reproduce the characteristic bond lengths and angles of various silicon/oxygen systems.[228] Further optimization of the INDO/S terms enabled the matching of the experimental and theoretical spectra for the

hydrated species as a calibration before exploring the other model species considered herein.

6.4.3 Structures

Various plausible molecular structures were constructed to simulate the different environments of the Cr^{3+} ion within the porous network, see Figures 1-3. The structure of the clusters was optimized using the INDO/1 model hamiltonian, ensuring that the gradient (residual forces on the atoms in the molecules) was typically <5E-4. A range of possible spin multiplicities were considered in the optimization in order to determine the ground state. The quartet was found to be the lowest energy state for all the structures investigated which is in accord with ligand field theory. Once a stable geometry was determined a CIS calculation was then executed. The results of the geometry optimization and configuration interaction calculations are presented in the following section.

6.4.4 Theoretical Results

Figures 1-3 include schematic representations of the seven molecular models investigated. Each structure is accompanied by a table describing its geometry. The results of the configuration interaction calculation are presented in Table 6.1 in an abridged format. Each molecular species is represented in the first column and its calculated electronic states and oscillator strengths in the second and third column respectively. Only the first three or four electronic states are listed for each molecular cluster. Many more states were calculated (as many as 280 configurations) but are not listed because we are attempting to follow the

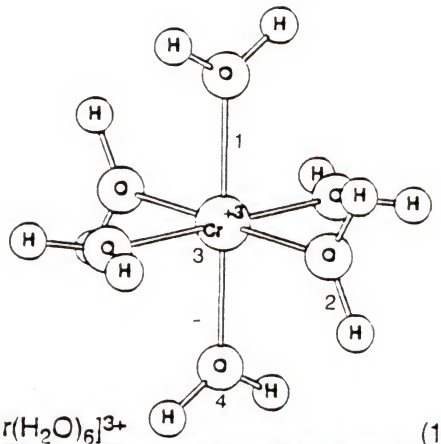

$[Cr(H_2O)_6]^{3+}$ (1a)

Label	Bonding Atoms	Value
1	Cr-O	1.97 Å
2	O-H	0.95 Å
3	Mulliken q	3.95 e⁻
4	Mulliken q	6.67 e⁻

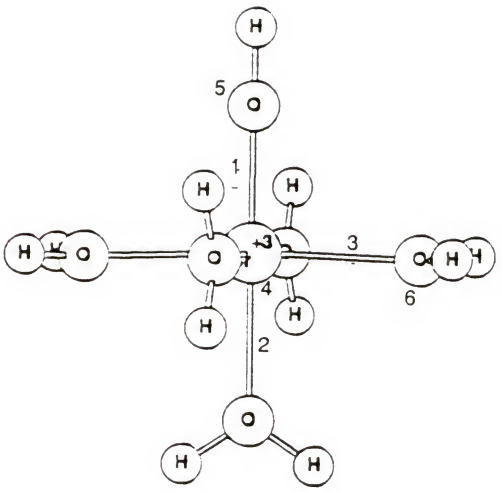

$[Cr(H_2O)_5OH]^{2+}$ (1b)

Label	Bonding Atoms	Value
1	Cr-OH	1.74 Å
2	Cr-O	2.00 Å
3	Cr-O	1.99 Å
4	Mulliken q	4.04 e⁻
5	Mulliken q	6.92 e⁻
6	Mulliken q	6.66 e⁻

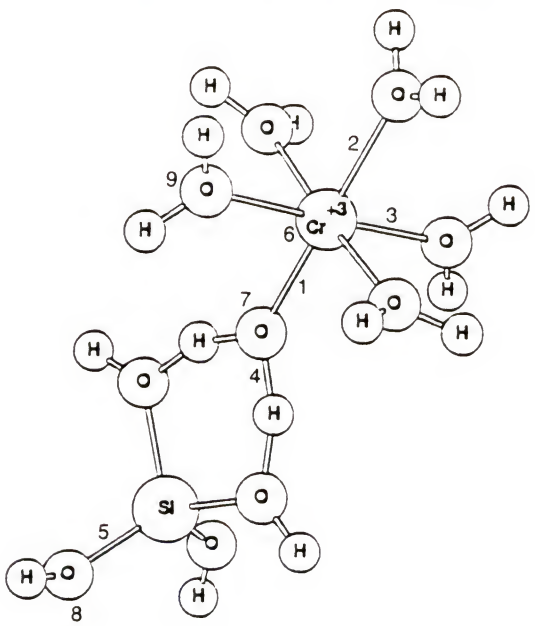

$Si(OH)_4[Cr(H_2O)_6]^{3+}$ (1c)

Label	Bonding Atoms	Value
1	Cr-O	1.85 Å
2	Cr-O	1.98 Å
3	Cr-O	2.00 Å
4	O-H	1.08 Å
5	Si-O	1.63 Å
6	Mulliken q	4.02 e⁻
7	Mulliken q	6.87 e⁻
8	Mulliken q	2.48 e⁻
9	Mulliken q	6.67 e⁻

Figure 6.1 (a) Chromium hexa-aqua structure, (b) Chromium hexa-aqua structure with an OH ion substituted for a water ligand, (c) Chromium hexa-aqua structure hydrogen-bonded to a silicic acid molecule.

$[Si(OH)_4Cr(H_2O)_5]^{3+}$ (2a)

Label	Bonding Atoms	Value
1	Cr-O	1.98 Å
2	Cr-O	1.97 Å
3	Cr-O	1.95 Å
4	Si-O	1.63 Å
5	Mulliken q	3.95 e⁻
6	Mulliken q	6.72 e⁻
7	Mulliken q	2.50 e⁻
8	Mulliken q	6.70 e⁻
9	Mulliken q	6.67 e⁻

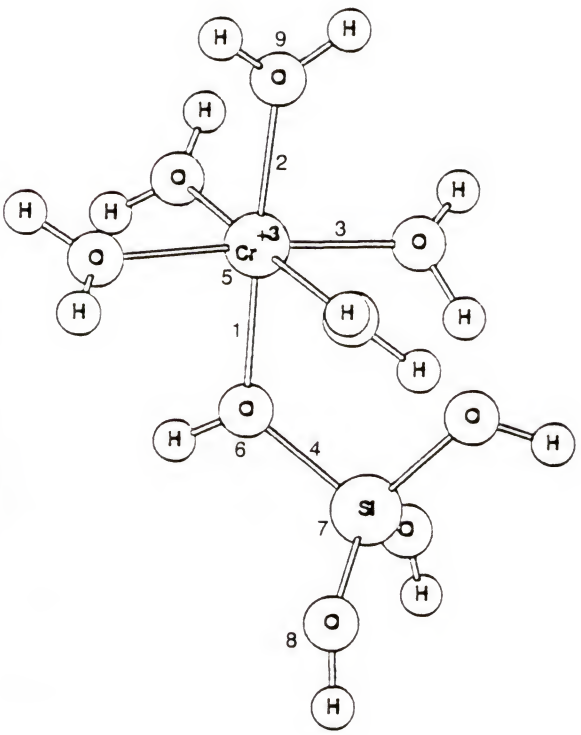

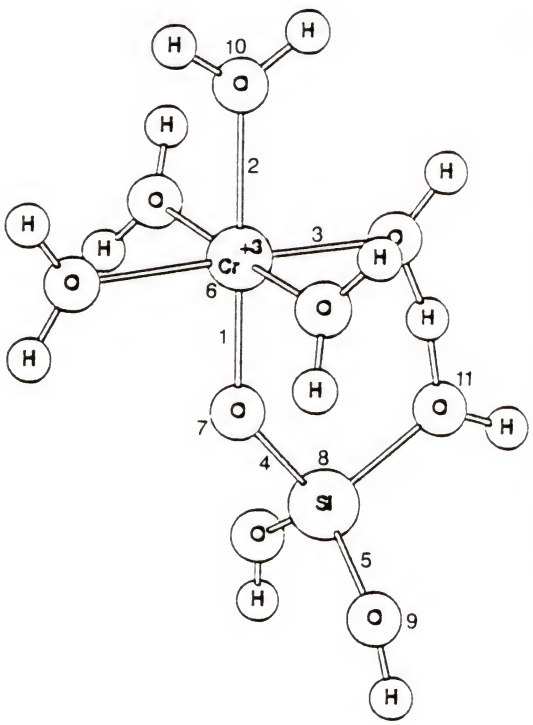

$[Si(OH)_3O\text{-}Cr(H_2O)_5]^{2+}$ (2b)

Label	Bonding Atoms	Value
1	Cr-O	1.79 Å
2	Cr-O	1.93 Å
3	Cr-O	2.00 Å
4	Si-O	1.71 Å
5	Si-OH	1.64 Å
6	Mulliken q	4.04 e⁻
7	Mulliken q	6.87 e⁻
8	Mulliken q	2.58 e⁻
9	Mulliken q	6.70 e⁻
10	Mulliken q	6.67 e⁻
11	Mulliken q	6.78 e⁻

Figure 6.2.(a), (b) Chromium hexa-aqua structure with a neutral silicic acid molecule and a silicic acid anion substituted for a ligand water respectively.

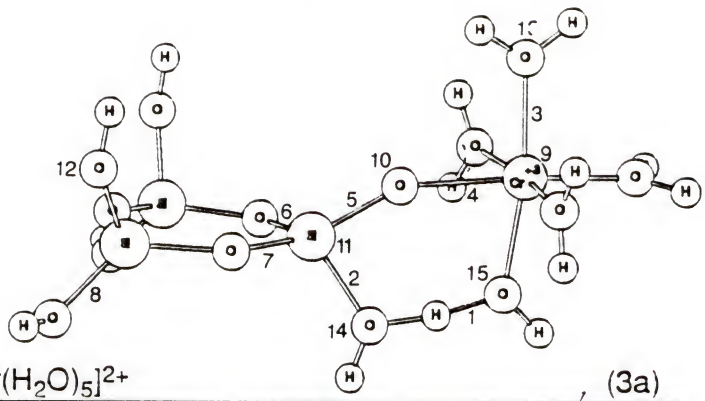

$[(SiO)_3(OH)_5O\text{-}Cr(H_2O)_5]^{2+}$, (3a)

Label	Bonding Atoms	Bond Distance	Label	Mulliken q
1	O-H	1.13 Å	9	4.06 e⁻
2	Si-OH_2O	1.73 Å	10	6.91 e⁻
3	Cr-OH_2	1.96 Å	11	2.56 e⁻
4	Cr-OSi	2.01 Å	12	6.70 e⁻
5	Si-OCr	1.72 Å	13	6.66 e⁻
6	O-SiOCr	1.68 Å	14	6.66 e⁻
7	O-SiOCr	1.69 Å	15	6.77 e⁻
8	Si-OH	1.65 Å		

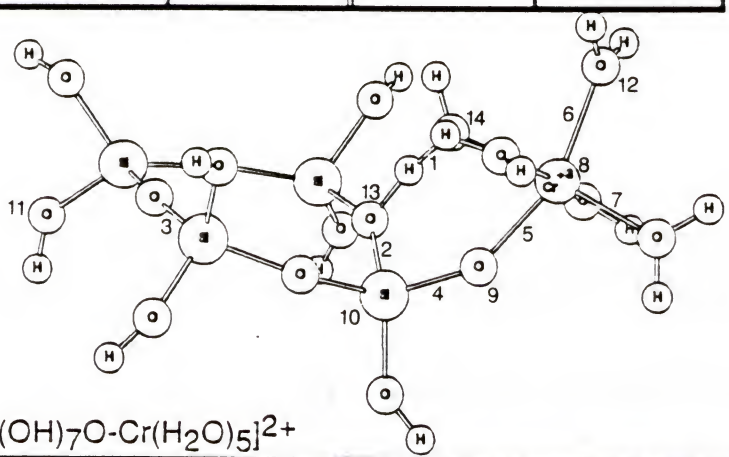

$[(SiO)_4(OH)_7O\text{-}Cr(H_2O)_5]^{2+}$ (3b)

Label	Bonding Atoms	Bond Distance	Label	Mulliken q
1	O-H	1.08 Å	8	4.06 e⁻
2	Si-OSi	1.72 Å	9	6.92 e⁻
3	Si-OSi	1.65 Å	10	2.46 e⁻
4	Si-OCr	1.69 Å	11	6.70 e⁻
5	Cr-OSi	1.86 Å	12	6.66 e⁻
6	Cr-OH_2	2.06 Å	13	6.73 e⁻
7	Cr-OH_2	1.93 Å	14	6.78 e⁻

Figure 6.3 (a), (b) A hydrated Chromium 3+ structure bonded to 3-and 4-membered siloxane ring anion species respectively.

Table 6.1. Calculated electronic states of various Cr and Cr/SiO model complexes.

Molecular Structure	Electronic Spectrum (nm)		
$[Cr(H_2O)_6]^{3+}$ #,*	575 (0) $^4T_{2g}$	420 (0) $^4T_{1g}$ (F)	267 (0) $^4T_{1g}$ (P)
$[Cr(H_2O)_5OH]^{2+}$	599 (0), 599 (0), 590 (0)	389 (0), 387 (0)	--
$[Si(OH)_4Cr(H_2O)_6]^{3+}$	593 (0), 576 (0), 568 (0)	449 (.0033), 431 (.0022)	--
$[Si(OH)_4Cr(H_2O)_5]^{3+}$	546 (0), 534 (0), 511 (0)	425 (0), 402 (0)	--
$[Si(OH)_3O^-Cr(H_2O)_5]^{2+}$	604 (0), 526 (0), 472 (0)	455 (0), 388 (0)	--
[3 Ring$O^-Cr(H_2O)_5]^{2+}$	663 (.0006), 559 (.0002)	475 (.0010), 470 (0)	--
[4 Ring$O^-Cr(H_2O)_5]^{2+}$	629 (0), 594 (0), 583 (0)	455 (.0015), 450 (0)	--

Literature values of 575, 407, 265 nm from A. Lever, "Inorganic Electronic Spectroscopy", Elsevier Science Publishing, NY, NY, p. 419, 1984.

* Experimental Values of 575, 408, 275 nm.

Oscillator Strengths are in parenthesis following the electronic state. 0 represents an electric-dipole forbidden transition.

experimental shifting of the $^4A_{2g} \rightarrow {}^4T_{2g}$ transition. An interpretation of the calculated geometries and electronic states is presented in the following section.

6.5 Discussion

The first cluster investigated was the Cr^{3+} hexa-aqua species shown in Figure 6.1a. Calibration or optimization of its spectrum and geometry is a requirement to validate a platform from which observations can be drawn about the model clusters. As mentioned earlier, the bonding parameter, β, for the silicon and oxygen atoms, in the INDO/1 method had been previously obtained to reproduce the proper Si-O distance and O-Si-O bond angle in various siloxane structures[228]. The first three computed transitions turn out to be electric-dipole forbidden with zero oscillator strength. Vibronic interactions cause the transitions to be observed in experiment. The ß for oxygen in the INDO/S method was adjusted to reproduce the first three electronic states of the $[Cr(H_2O)_6]^{3+}$. Inspection of Table 6.1 reveals the calculated electronic states to be in excellent agreement with the experimental values. With this optimization completed we proceed by investigating the geometry and electronic states of the $[Cr(H_2O)_6]^{3+}$ interacting with silicon/oxygen clusters.

The next logical step from the calibration calculation was to introduce a hydroxyl ion into the inner coordination sphere. This cluster, $[Cr(H_2O)_5OH]^{2+}$, is displayed in Figure 6.1b. The Cr-O bond length between the OH^- and the Cr^{3+} ion is predicted to be 1.74 Å as compared to the longer Cr-OH_2 distance. This results in a lowering of the symmetry of this species resulting in loss of degeneracy of the

t_{2g} orbitals. Table 6.1 shows the results of the CIS which predicts red shifting of the triply degenerate band to 599, 599, and 590 nm. This hydroxyl substitution is not likely to occur since the gels were soaked in a 1.5 pH solution prior to the diffusion of the salt solution. However, if the equilibration between the gel and acid solution was slow or incomplete or if finite-size effects alter normal bulk solution equilibrium this hydroxyl substitution could be responsible for the spectral shifts. This structure is more likely to be created by the abstraction of a proton from one of its coordinated waters. A basic site such as SiO^- on the glass surface would be apt to abstract a hydrogen.

The last cluster, Figure 6.1c is the hexa-aqua species and a neutral silicic acid molecule representing a hexa-coordinated Cr^{3+} ion hydrogen-bonded to the surface of the porous glass. The calculation predicts a Cr-O bond length of 1.85 Å for the water ligand associating with the silicic acid hydroxyls. In this case one also observes an increase in the metal-oxygen distance of the other five waters, $\approx$2.00 Å. The Mulliken charge on the oxygen correlates with the change in the Cr-O length in the three structures. A decrease of the charge on the oxygen bonded to the chromium results in longer bond lengths and vice-versa from electrostatic arguments. The modification of geometry by the silicic acid bears out the observed spectral shift. As shown in Table 6.1 two states are red-shifted and one slightly blue shifted. The H-bonded $[Cr(H_2O)_6]^{3+}$ structure may be in disagreement with EPR line broadening studies of Cornet and Burwell,[203] which indicate that the aqueous Cr^{3+} exists in the same environment within the pores

as in bulk solution. It is possible that this structure was not present at the time of their measurement or the difference between the two structures is not large enough to be resolved in a line-broadening measurement.

Another proposed mechanism is the substitution of a hydroxyl from the silica surface into the inner coordination sphere of the metal ion. These models for binding are presented in Figure 6.2. The structure seen in Figure 6.2a substitutes a neutral silicic acid molecule for one of the waters and Figure 6.2b has substituted a deprotonated or charged silicic acid molecule. The gradual change in the structures presented in Figure 6.1 to 6.3 involves the successive increase in size of the substituted species for the ligand water. The effect can be seen in both the calculated bond lengths and electronic states. The $[Si(OH)_4Cr(H_2O)_5]^{3+}$ structure has calculated transitions which are considerably blue-shifted from the 575 nm absorption. The same is true of the $[Si(OH)_3O^-Cr(H_2O)_5]^{2+}$ structure with the exception of one state being red-shifted. The red-shift for this cluster is a result of the hydrogen-bonding of a water ligand with a hydroxyl of the silicic acid, and a consequent increase in the Cr-O bond length for the remaining water ligands. Shorter bond lengths produce higher energy transitions.

The final two structures are the interaction of the hydrated Cr^{3+} with three and four membered siloxane ring structures (see Figure 6.3). The electronic states for these clusters are listed in Table 6.1 but are difficult to interpret due to a near continuum of states predicted by the CIS calculation. However, an interesting effect with the ring geometries is seen. The presence of the Cr/H_2O species

adjacent to the rings increases the Si-O bond lengths in the ring. Bonds 6 and 7, in the three membered-ring and bond 2 in the 4 membered ring are calculated to be 1.68 Å, 1.69 Å, and 1.72 Å respectively. This is an increase from 1.65 Å for a non-bridging oxygen and 1.67 Å for a bridging oxygen away from the adsorption site. The straining of Si-O bonds by water is a recognized mechanism for fracture.[229] The possibility exists that the already strained 3 and 4 membered siloxane rings are further strained due to the adsorption of the Cr^{3+} species. In addition, the Cr^{3+} species may be incorporated onto the glass surface by this ring-opening and may be one of the factors influencing the environment of the Cr^{3+} ion. Further analysis of these more involved siloxane structures is required. This analysis and these calculations are a beginning in modeling this type of system.

6.6 Conclusions

The electronic spectra for the Cr^{3+} hexa-aqua species was accurately reproduced with an improved geometry over previous calculations. The calculations based on geometrical arguments and electronic states indicate that hydrogen-bonding, the deprotonation of a coordinated water ligand, and/or the substitution of a charged hydroxyl for a ligated water molecule are plausible mechanisms to explain the red-shifting of the visible absorptions seen experimentally. In addition, it has been demonstrated that semi-empirical modeling methods are capable of elucidating interactions occurring between the surfaces of porous sol-gel matrices and impregnated species. Certainly, additional calculations

and experiments are required before a full understanding of the local environment of the Cr^{3+} within the porous gel matrix can be fully achieved

CHAPTER 7
CONCLUSIONS AND SUGGESTIONS FOR FUTURE WORK

The objectives of this research were to study the evolution of the porous network during the processing of silica gel monoliths and to provide new knowledge about the relationships between the chemical behavior of heavy metal salt solutions and the pore structure of the porous monoliths. The main conclusions of this research are summarized as follows:

1) Characterization of the porous gels by different methods indicates that the pore morphologies of the gels can be successfully altered at various steps in the process. Different pore-size gels can be created from the sol by varying the type and amount of catalyst. Aging of the gels at higher pH's produce gel pores nearly ten times larger than unaged samples. Heat treatment of the gels is an effective method for creating constant pore size gels with varying amounts of volume fraction and surface areas.

2) Immersion of the gels in water revealed a trend indicating the minimum bulk density required for the gels to withstand rehydration pressures. The minimum bulk density is a function of the pore size, the volume fraction of porosity, and the surface defects generated on the surface during mechanical processing. This minimum bulk density is a useful indicator for preparing porous monoliths for use in environmental sensing.

3) The penetration rate of water was theoretically as well as empirically fit to two different equations. It was determined that the average pore size and not the number of interconnections of the pores which control the permeation rate. A topological model was used to calculate the number of branches for the different pore size gels. It was shown that the penetration rate of water was controlled by the average pore size and not the number of branches of pores.

4) The results from the heats of immersion from different pore structure gels indicate that heats of immersion increase with pore size. The increase in heats of immersion with pore size were attributed to a decrease in microporosity, a decrease in the surface roughness, a larger silanol concentration density on the surface, and a more immediate rehydration of the surface. The value of the BET constant, C, was shown to correlate with the heats of immersion. A higher C value produced a larger heat of immersion. The C value decreased with an increase in the thermal treatment temperature for gels with 30 Å or larger pore radii. The small-pore nitric acid gels showed an increase in the C with heat treatment.

5) The zeta potential measurements indicated differences in the electrophoretic mobility for the different pore size gels. The IEP of the porous powders increased from 2.5 to 3.5 as the pore size increased. The change in the shapes of the zeta potential curves for the two largest pore sizes, 30 Å and 100 Å, was attributed to the change in volume fraction of porosity associated with the heat treatments. The larger the volume fraction of porosity the lower the electrophoretic mobility of the particles. This trend was not observed for the 14 Å

gel. During aging of the different series of gels it was found that the IEP became more basic for the 14 Å and 30 Å pore size materials. The IEP of the 100 Å gels remained essentially constant with aging time.

6) The smallest pore size gel, 14 Å, exhibited small differences in the IEP and shape of the zeta potential curve with heat treatment temperature. The 30 Å gel series displayed the most significant change in the IEP and shape of the zeta potential curve with thermal treatment temperature. The best choice for an environmental sensor in the gels investigated in this study is a porous monolithic substrate with the largest pore size. The surface displays a faster rate of equilibrium with water and produces very little change with aging in water. The surface appears to be smoother providing a more homogeneous substrate for impregnation of optically active phases. Both of these factors suggest a lower probability of the gel surface interfering with molecules involved in the sensing operation.

7) The partitioning of the chromium ion was a strong function of the solution pH and the pore size of the porous monoliths. As the pore size increased the partition coefficients increased from ≈ 0.5 to ≈ 0.95 for a constant concentration and solution pH. At a pH of 2.74 the partitioning was greater than 1.

8) The diffusion coefficient for the hexa-aqua chromium ion, as determined from the bulk solution driving force, is one and a half orders of magnitude smaller than the diffusion in bulk solution for the smallest pore size measured. The largest pore size showed a decrease of one-half the diffusion coefficient from the bulk

value. The diffusion into unconsolidated aged samples produced diffusion coefficients approximately equivalent to the values for the largest pore size heat treated gels. The tortuosities calculated from these effective diffusion coefficients ranged from 15.3 to 1.4. The diffusion coefficient was recalculated by using the equilibrium partition concentration within the pore as the driving force for diffusion. The effect was largest on the smallest pore size. The recalculated tortuosities ranged from 5.5 to 0.7.

10) A shifting of the peak maximum of the d-d transitions for the hexa-aqua Cr^{3+} ion occurred during the diffusion into the pores. The shifting is most prominent at higher pH's and coincides with the pH for which the partition coefficient exceeds unity. The peak shifting is most likely a result of the interaction of the ion with the change in surface charge of the silica.

Some useful avenues for future research might include:

1) The level of understanding of restricted diffusion processes increases dramatically with a better definition of the shape and size of the porosity. The sol-gel process may be able to produce pores of distinct shapes, sizes, and surfaces. These pores could be designed to match the molecular shape and activity of second phases, significantly increasing the molecular design capabilities of these materials.

2) The chemical modification of the sol-gel silica surface has been investigated to a level of sophistication which is capable of producing varying degrees of surface energies. It would be effective to combine the studies of

surface modification with the different pore structures of these glasses to more completely separate the geometrical effects from the chemical interactions of molecules in restricted geometries.

3) The measurement of the electrophoretic mobilities of porous particles has wide ranging implications to such diverse fields as: mineral processing, medicine, and materials science. It is obvious that porous particles do not behave like solid particles. The cause and effect of these differences is not known and has not been reported on. Any studies of porous particles along these lines may have a significant impact on this new research area.

4) The restricted behavior of actual environmental contaminates within these glasses is a valuable area of science to investigate. These glasses may one day not only be able to sense these contaminates but remove them from the environment. A study which may facilitate the removal of environmental hazards from this earth benefits everyone.

REFERENCE LIST

1. L. Hench and J. West, Chemical Reviews, 90, 1990, pp. 33-72.

2. L. Hench and D. Ulrich, eds., "Ultrastructure Processing of Ceramics Glasses and Composites", Wiley, New York, 1984.

3. L. Hench and D. Ulrich, eds., "Science of Ceramic Chemical Processing", Wiley, New York, 1986.

4. J. Mackenzie and D. Ulrich, eds. "Ultrastructure Processing of Advanced Ceramics", Wiley, New York, 1988.

5. D. Uhlmann, M. Weinberg, and D. Ulrich, eds. "Ultrastructure Processing IV", Wiley, New York, 1989.

6. C. Brinker, D. Clark, and D. Ulrich, eds. "Better Ceramics Through Chemistry", Vol. 32, Elsevier, New York, 1984.

7. C. Brinker, D. Clark, and D. Ulrich, eds., "Better Ceramics Through Chemistry II", Vol. 73, Materials Research Society, Pittsburgh, Pennsylvania, 1986.

8. C. Brinker, D. Clark, and D. Ulrich, eds. "Better Ceramics Through Chemistry III", Vol. 121, Materials Research Society: Pittsburgh, Pennsylvania, 1988.

9. L. Hench and J. West, eds., "Chemical Processing of Advanced Materials", John Wiley, New York, 1992.

10. L. Klein, ed., "Sol-Gel Technology for Thin Films, Fibers, Preforms, Electronics, and Specialty Shapes", Noyes, Princeton, NJ, 1988.

11. L. Klein, ed., "Sol-Gel Optics, Processing and Applications", Klumer Academic, Boston, 1994.

12. C. Brinker and G. Scherer, "Sol-Gel Science", Academic Press: Boston, 1990.

13. L. Hench and J. Nougues, in "Sol-Gel Optics, Processing and Applications", Klumer Academic, Boston, 1994, 59.

14. "List of Hazardous Constituents for Ground Water Monitoring", Federal Register, 40 CFR parts 264 and 270, 52, (131) 25492, 1987.

15. J. Lu and W. Barcikowski, eds., Proceedings of the National Conference on Hazardous Waste and Hazardous Materials, Atlanta, GA, March 1986.

16. J. Oxenford, Proceedings from SPIE "Chemical, Biochemical, and Environmental Sensors", vol. 1172, 1989, 108.

17. R. Niessner, W. Roberts, and A. Krupp, Proceedings from SPIE "Chemical, Biochemical, and Environmental Sensors", vol. 1172, 1989, 145.

18. W. Chudyk, K. Pohlig, L. Wolf, and R. Fordiani, Proceedings from SPIE "Chemical, Biochemical, and Environmental Sensors", vol. 1172, 1989, 123.

19. B. Mac Graith, G. O'Keeffe, C. McDonagh, and A. McEvoy, Electronic Letters, 30, 11, 1994, 888.

20. R. Reisfeld, and C. Jorgenson, eds., "Chemistry, Spectroscopy, and Applications of Sol-Gel Glasses", Springer-Verlag, Berlin, 1992.

21. J. Klafter and J. Drake, eds., "Molecular Dynamics in Restricted Geometries", John-Wiley, New York, 1989.

22. B. Derjaguin, N. Churaev, and V. Muller, "Surface Forces", Consultants Bureau, New York, 1987.

23. W. Hardy, Proc. Roy. Soc. London, A86, 1912, 610.

24. A. Reychler, Kolloid Zeits., 12, 1913, 277.

25. J. Henniker, Reviews of Modern Physics, 21, 2, 1949, 322.

26. B. Derjaguin, I. Abricosova, and E. Lifshitz, Quart. Rev., 10, 1956, 295.

27. J. Kitchener, and A. Prosser, Proc. Roy. Soc., A 242, 1957, 403.

28. W. Black, J. de Jongh, J. Overbeek, and M. Sparnaay, Trans. Faraday Soc., 56, 1960, 1597.

29. B. Derjaguin, Pure and Applied Chemistry, Vol. 10, 1965, 375.

30. N. Zakhavayeva, B. Derjaguin, A. Khomutov, and S. Andreyev, "In Research in the Field of Surface Forces", Vol II, p. 173., USSR Academy of Science Press, Moscow, 1964.

31. J. Bikerman, Proceedings of the Symposium on Adhesion and Cohesion, p.14, Amsterdam, 1961.

32. L. Kurbatov, Zh. Fiz. Khim., 24, 1950, 899.

33. J. Warnock, D. Awschalom, M. Shafer, Phys. Rev. B, 34, 1986, 475.

34. L. Nikiel, T. Zerda, and L. Hench, Ceramic Trans., 19, 1991, 189.

35. A. Brodka and T. Zerda, J. Chem. Phys., 95, 1991, 3710.

36. J. Watson and T. Zerda, Appl. Spectroscopy, 45, 8, 1991, 1360.

37. G. Peschel and K. Adlfinger, J. of Colloid and Interface Science, 34, 4, 1970, 505.

38. B. Derjaguin and N. Krylov, Akad. Nauk SSSR Otd. Tekhn. Nauk Inst. Mashinoved. Soveshch. Vyazkosti Zhidkostei Kolloidn. Rastvorov, 2, 1944, 52.

39. V. Morariu and R. Mills, Zeitschrift fur Physikalische Chemie Neue Folge, 79, 1972, 1.

40. M. Dunn, J. Dore, and P. Chieux, J. Crystal Growth, 92, 1988, 233.

41. J. Li, D. Ross, and M. Benham, J. Appl. Cryst., 24, 1991, 794.

42. S. Wallace, Porous Silica Gel Monoliths: Structural Evolution and Interactions With Water, Ph. D. Dissertation, University of Florida, Gainesville, 1991.

43. F. D'Orazio, S. Bhattacharja, W. Halperin, K. Eguchi, and T. Mizusaki, Phys. Rev. B, 42, 16, 1990, 9810.

44. C. Braun and W. Drost-Hansen, in "Colloid and Interface Science", M. Kerker ed., Vol. III, Academic Press, New York, 1976, 533.

45. R. Watts-Tobin, Philos. Mag., 6, 1961, 133.

46. F. Etzler, J. Colloid and Interface Science, 92, 1, 1983, 43.

47. G. Stey, The Structrure of Water at Metal-Oxide Interfaces, Ph. D. Dissertation, University of Pittsburgh, 1967.

48. J. Bernal and R. Fowler, J. Chem. Phys., 1, 1933, 515.

49. A. Luzar, S. Svetina, and B. Zeks, J. Chem. Phys., 82, 11, 1985, 5146.

50. J. Israelachvili, J. of Colloid and Interface Science, 110, 1, 1986, 263.

51. J. Israelchvili, Chemica Scripta, 25, 1984, 7.

52. J. Giddings, E. Kucera, C. Russell, and M Meyers, J. Phys. Chem., 72, 1968, 4397.

53. E. Glandt, AICHE Journal, 27, 1, 1981, 51.

54. E. Glandt, J. of Colloid and Interface Science, 77, 2, 1980, 512.

55. A. Post and E. Glandt, J. of Colloid and Interface Science, 108, 1, 1985, 31.

56. C. Cotton, C. Satterfield, and C. Lai, AICHE J., 21, 2, 1975, 289.

57. J. Wong and J. Quinn, in "Colloid and Interface Science", vol. V, ed. M Kerker, Academic Press, New York, 1976, 169.

58. M. Davidson, U. Suter, and W. Deen, Macromolecules, 20, 1987, 1141.

59. F. Smith and W. Deen, J. Colloid and Interface Science, 78, 1980, 444.

60. F. Smith and W. Deen, J. Colloid and Interface Science, 91, 2, 1983, 571.

61. E. Verwey and J. Overbeek, "Theory of the Stability of Lyophobic Colloids", Elsevier, Amsterdam, 1948.

62. P. Wiggins, Biophysical Journal, 13, 1973, 385.

63. A. Einstein, "Investigations on the Theory of the Browmian Movement", R. Furth, ed., Dover, New York, 1956.

64. B. Uzelac and E. Cussler, J. Colloid and Interface Sci., 32, 3, 1970, 487.

65. R. Robinson and R. Stokes, "Electrolyte Solutions", 2nd ed., Butterworth, London, 1959.

66. J. Pappenheimer, E. Renkin, and L. Borrero, Am. J. Physiol., 167, 1957, 13.

67. A. Solomon, J. Gen. Physiol., 51, 1968, 335s.

68. A. Kernstein, Phys. Rev. B 31, 4, 1985, 1612.

69. A. Kernstein, Phys. Rev. B 32, 5, 1985, 3361.

70. D. Price, and A. Varma, in "Diffusion and Convection in Porous Catalyst", AICHE Symposium, no. 266, Vol. 84, 1987, 88.

71. R. Barrer, "Surface and Volume Flow in Porous Media", E. Flood ed., Marcel Dekker, New York, 1967, 551.

72. S. Bhatia, AIChE Journal, 34, 7, 1988, 1094.

73. L. Riekert, AIChE Journal, 31, 5, 1985, 863.

74. R. Fleischer, H. Alter, S. Furman, P. Price, and R. Walker, Science, 178, 1972, 255.

75. W. Deen, AIChE Journal, 33, 9, 1987, 1409.

76. C. Bean, The Physics of Porous Membranes-Neutral Pores in "Membranes", G. Eisenman, ed., Dekker, New York, 1, 1972, 1.

77. J. Anderson and J. Quinn, J. Chem. Soc. Faraday Trans. I, 68, 1972, 744.

78. R. Beck, and J. Schultz, Biochim. Biophysi. Acta, 255, 1972, 273.

79. D. Malone and J. Anderson, Chemical Engineering Science, 33, 1978, 1429.

80. H. Brenner and L Gaydos, J of Colloid and Interface Science, 58, 2, 1977, 312.

81. N. Garnier and N. Ostrowsky, J. Phys. II France, 1, 1991, 1221.

82. M. Davidson and W. Deen, J. of Membrane Science, 35, 1988, 167.

83. J. Anderson, I. Kathawalla, and J. Lindsey, in "Diffusion and Convection in Porous Catalyst", AIChE Symposium Series, no. 266, vol. 84, 1987.

84. W. Deen and F. Smith, III, J. of Membrane Science, 12, 1982, 217.

85. M. Bishop, K. Langley, and F. Karasz, Physical Review Letters, 14, 57, 1986, 1741.

86. W. Deen, M. Bohrer, and N. Epstein, AIChE Journal, 6, 27, 1981, 952.

87. W. Dozier, J. Drake, and J. Klafter, Physical Review Letters, 2, 56, 1986, 197.

88. T. Zerda, A. Brodka, and J. Coffer, J. Non-Crystalline Solids, 1993.

89. W. Koh and J. Anderson, J. of Colloid and Interface Science, 1, 64, 1978, 57.

90. M. Ebelmen, Ann. Chimie Phys., 1846, 16, 129.

91. R. Roy, J. Am. Ceram. Soc., 1956, 39, 145.

92. R. K. Iler, The Chemistry of Silica, Wiley: New York, 1955.

93. M. Yamane, S. Aso, and T. Sakiino, J. Mater. Sci., 13, 1978, 865.

94. M. Yamane, S. Aso, S Okano, and T. Sakaino, J. Mater. Sci., 14, 1979, 607.

95. J. Pouxviel, J. Boilet, J. Beloeil, and J. Lallemand, J. Non-Crystalline Solids, 89, (1987), 345.

96. R.T. Morrison and R.N. Boyd, "Organic Chemistry", Allyn & Bacon: Boston, 1976.

97. I. Artaki, T. Zerda, and J.Jonas, J. Non-Crystalline Solids, 81, (1986), 381.

98. C. Plank, and L. Drake, J. Colloid Science, 2, 1947, 339.

99. G. Orcel, L. Hench, I. Artaki, J. Jones, and T. Zerda, J. Non-Crystalline Solids, 105, 1988, 223.

100. M.G. Voronkov, V.P. Mileshkevich, and Y. Yuzhelevski, The Siloxane Bond, Consultants Bureau, New York, 1978.

101. J. C. Pouxviel, J.P. Boilet, J.C. Beloeil, and J.Y. Lallemand, J. Non-Crystalline Solids, 89, 1987, 345.

102. R. Aelion, A. Loebel, and F. Eirich, J. Am. Chem. Soc., 72, 1950, 5705.

103. E. Pope and D. Mackenzie, J. Non-Crystalline Solids, 87, 1986, 185.

104. S. Liu, Control of the Texture of Gel-Silica by Aging, Ph. D. Disseration, University of Florida, 1991.

105. Y. Klimentova, L. Kirichenko, and Z. Vysotskii, Ukr. Khim. Zh., 36, 1970, 56-58.

106. G. Scherer, J. Non-Crystalline Solids, 87, 1986, 199-225.

107. G. Scherer, J. Non-Crystalline Solids, 108, 1989, 28-36.

108. R. Dwivedi, J. Mater. Sci. Lett., 1986, 5, 373.

109. T. Kawaguchi, J. Jura, N. Taneda, H. Hishikura, and Y. Kokubo, J. Non-Crystalline Solids, 1986, 82, 50.

110. M. Wilson, Drying Kinetics of Pure Silica Xerogels, M.S. Thesis, University of Florida, Gainesville, 1989.

111. C. Brinker, G. Scherer, and E. Roth, J. Non-Crystalline Solids, 72, 1985, 345-368.

112. G. Scherer, "Relaxation in Glasses and Composites", Wiley, New York, 1986.

113. M. Hair, "Infrared Spectroscopy in Surface Chemistry", Dekker, New York, 1967.

114. G. Young, J. Colloid Interface Sci., 13, 1958, 67.

115. J. Peri and A. Hensley, J. Phys. Chem., 72, 1968, 2926.

116. B. Bunker, D. Haaland, T. Michalske, and W. Smith, Surf. Sci., 222, 1989, 95-118.

117. B. Morrow and I. Cody, J. Phys. Chem., 80, 1976, 1995.

118. B. Morrow and I. Cody, J. Phys. Chem., 80, 1976, 1998.

119. S. Gregg and K. Sing, Adsorption, Surface area and Porosity, Academic Press, London, 2nd ed., 1982.

120. J. Walsh and W. Brace, J. of Geophysical Research, 89, no. B11, 1984, 9425.

121. A. Katz and A. Thompson, Physical Review B, 34[11], 1986, 2179.

122. P. Wong, J. Koplik, and J. Tomanic, Physical Review B, 30[11], 1984, 6606.

123. S. Lukasiewicz and J. Reed, J. Am. Ceram. Soc., 71[11], 1988, 1008.

124. P. Debye and R. Cleland, J. Appl. Phys., 30[6], 1959, 843.

125. W. Wade, Soc. of Petroleum Engineers Journal, April, 1974, 139.

126. J. Bouaziz, T. Woignier, D. Bourret, and R. Sempere, J. Non-Crystalline Solids, 82, 1986, 225-231.

127. M. Yanuka, F Dullien, and D. Elrick, J. Colloid and Inter. Sci., 112[1], 1986, 24.

128. M. Yanuka, J. Colloid and Inter. Sci., 127[1], 1989, 35-47.
M. Yanuka, J. Colloid and Inter. Sci., 127[1], 1989, 48-58.

129. F. Dunllien, "Porous Media: Fluid Transport and Pore Structure", Academic Press, New York, 1979.

130. K. Kendall, Physics and Chemistry of Porous Media, AIP Conference Proceedings, number 107, eds. D. Johnson and P. Sen, 1984, 78.

131. E. Rideal, Phil. Mag., 44, 1922, 1152.

132. E. Washburn, Phys. Rev., 17, 1921, 374.

133. W. Vasconcelos, Topological Analysis of Densification of Silica Gels, Ph. D. Dissertation, University of Florida, Gainesville, FL, 1989.

134. A. Adamson, "Physical Chemistry of Surfaces", 4th ed., John Wiley, New York, 1982.

135. A. Scheidegger, "The Physics of Flow Through Porous Media", 3rd ed., University of Toronto Press, Canada, 1974.

136. T. Healy and D. Fuerstneau, J. Colloid Sci., 20, 1965, 376.

137. A. Zettlemoyer, J. Colloid and Interface Science, 28, 1968, 343.

138. O. Mellgren, R. Gochin, H. Shergold, and J. Kitchener, Proceedings 10th International Mineral Processing Congress, London, 1973, 451.

139. D. Griffths, The Effect of pH and Temperature on the Heat of Immersion of Alumnia, M.S. Thesis, University of California, Berkleley, 1973.

140. A. Zettlemoyer, Ind. Eng. Chem., 57, 1968, 27.

141. G. Young and T. Bursh, J. of Colloid Sci., 15, 1960, 361.

142. J. Taylor and J. Hockey, The Journal of Physical Chemistry, 70, 7, 1966.

143. A. Agzamkhodzhaev, L. Zhuravlev, A. Kiselev, and K. Shengeliya, Colloid Journal of the USSR, 36, 1974, 1036.

144. W. Wade, R. Every, and N. Hackerman, J. of Phys. Chem., 64, 1960, 355.

145. M. Egorov, K. Krasil'nikov, and E. Sysoev, Doklady Akad. Nauk. SSSR, 108, 1956, 103.

146. G. Young, J. of Colloid Science, 13, 1958, 67.

147. J. Taylor and J. Hockey, The Journal of Physical Chemistry, 70, 7, 1966, 453.

148. J. Whalen, J. Phys. Chem., 71, 6, 1967, 1557.

149. A. Tyler, J. Taylor, B. Pethica and J. Hockey, Trans. Faraday Soc., 67, 2, 1971, 483.

150. D. Meyer and N. Hackerman, J. Phys. Chem., 70, 7, 2077, 1966.

151. L. Gouy, J. Phys., 4, 1910, 457.

152. P. Chapman, Philos. Mag., 6, 1913, 475.

153. B. Derjaguin and L. Landau, Acta Physicochim., USSR, 14, 1941, 633.

154. E. Verwey and J. Overbeek, "Theory of the Stability of Lyophobic Colloids", Elsevier, Amsterdam, 1948.

155. H. Hamaker, Physica, 4, 1937, 1058.

156. O. Stern, and Z. Elektro., 30, 1924, 508.

157. R. Hunter, "Foundations of Colloid Science", vol. 1, Clarendon Press, Oxford, 1987.

158. R. Hunter, "Zeta Potential in Colloid Science", Academic Press, London, 1981.

159. G. Parks, Chem. Rev., 65, 1965, 177.

160. J. Horn, Electrokinetic Properties of Silica, Aluminia, and Montmorillonite, Dissertation for the Ph. D., University of Florida, Gainesville, 1978.

161. J. Jednacak, V. Pravdic, and W. Haller, J. of Colloid and Interface Science, 49, 1, 1974, 16.

162. J. Perram, R. Hunter, and H. Wright, Chemical Physics Letters, 23, 2, 1973, 265.

163. D. Yates and T. Healy, J. Colloid and Interface Science, 55, 1976, 9.

164. H. Yotsumoto and R. Yoon, J. of Colloid and Interface Science, 157, 1993, 434.

165. J. Taylor, J. Hockey, and B. Pethica, Proc. Brit, Ceram. Soc., 5, 1965, 236.

166. V. Kiselev, Russian Journal of Physical Chemistry, 34, 3, 1960, 332.

167. L.T. Zhuravlev, Langmuir, 3, 1987, 316-318.

168. D. Farin and D. Avnir, J. Chromatog., 406, 317, 1987.

169. T. Healy and D. Fuerstenau, J. of Colloid Science, 20 1965, 376.

170. T. Healy, A. Herring, and D. Fuerstenau, J. of Colloid and Interface Science, 21, 1966, 435.

171. N. Miller, J. Berg, and R. O'Brien, J. of Colloid and Interface Science, 153, 1, 1992, 237.

172. N. Miller, J. Berg, and R. O'Brien, J. of Colloid and Interface Science, 159, 1993, 253.

173. P. Johansen and A. Buchanan, Australian J. of Chem., 10, 1957, 398.

174. M. Robinson, J. Pask, and D. Fuerstenau, J. American Ceramic Soc., 47, 1964, 516.

175. J. Hunt and H. Taube, J. Chem. Phys., 19, 5, 1951, 602.

176. S. Petrucci, "Ionic Interactions", Academic Press, New York, 1971.

177. J. Morgan and B. Warren, J. Chem. Phys., 6, 1938, 666.

178. R. Robinson and R. Stokes, in "Electrolyte Solutions", Butterworths, London, 1959, 15.

179. G. Hartley and J. Crank, J. Trans. Faraday Soc., 45, 1949, 801.

180. H. Falkenhagen and M. Dole, Phys. Z., 30, 1929, 611.

181. E. Nightingale, Jr., in "Chemical Physics of Solutions", B. Conway and R. Barradas, eds., John Wiley, New York, 1964, 87.

182. R. Stokes, J. Phys. Chem., 72, 1950, 2244.

183. G. Pass, in "Ions in Solution", Clarendon Press, Oxford, 1974, 67.

184. E. Cussler, "Diffusion, Mass Transfer in Fluid Systems", Cambridge University Press, Cambridge, 1984.

185. J. Crank, "The Mathematics of Diffusion", 2nd ed., Clarendon Press, Oxford, 1975.

186. R. Burwell, R. Pearson, G. Haller, P. Tjok, and S. Chock, Inorganic Chemistry, 4, 8, 1965, 1123.

187. A. Kozawa, J. of Inorganic Nuclear Chemistry, 21, 1966, 315.

188. P. Schindler, B. Furst, R. Dick, P. Wolf, J. of Colloid and Interface Science, 55, 2, 1976, 469.

189. R. James and T. Healy, J. of Colloid and Interface Science, 40, 1, 1972, 42.

190. R. James and T. Healy, J. of Colloid and Interface Science, 40, 1, 1972, 53.

191. R. James and T. Healy, J. of Colloid and Interface Science, 40, 1, 1972, 65.

192. C. Baes and R. Mesmer, "The Hydrolysis of Cations", Robert E. Krieger Publishing Company, Malabar, Florida, 1986.

193. S. Gits-Leon, F. Lefaucheux, and M. Robert, J. of Crystal Growth, 84, 1987, 155.

194. P. Callaghan, A. Coy, T. Halpin, D. MacGowan, K. Packer, and F. Zelaya, J. Chem. Phys., 97, 1, 1992, 651.

195. M. Sahimi and V. Jue, in "Diffusion and Convection in Porous Media", AIChE Symposium Series, 84, 226, 40.

196. C. Satterfield, C. Colton, and W. Pitcher, AIChE J., 19, 3, 1973, 628.

197. R. Stoessell and J. Hanor, J. of Geophysical Research, 80, 36, 1975, 4979.

198. J. Smith, "Chemical Engineering Kinetics", 3rd. ed., McGraw-Hill, New York, 1981.

199. J. Karusk and J. Smith, AIChE J., 18, 1972, 506.

200. P. Schindler, in "Adsorption of Inorganics at Solid-Liquid Interfaces", eds., M. Anderson and A. Rubin, Ann Arbor Science, Ann Arbor, MI, 1981.

201. E. Glandt, AIChE J., 1981, 27, 1, 1981, 51.

202. E. Nightingale, Jr., J. Chem. Phys., 63, 1959, 1381.

203. D. Cornet and R. Burwell, J. American Ceramic Soc., 90, 1968, 2489.

204. A. Bacon and M. Zerner, Theor. Chim. Acta, 53, 1979, 21.

205. M. Zerner, G. Loew, R. Kirchner, and U. Mueller-Westerhoff, J. Am. Chem. Soc., 102, 1980, 589.

206. U. Burkert and N. Allinger, "Molecular Mechanics", American Chemical Society, Washington D. C. , 1982.

207. R. Bartlett and J. Stanton, in "Reviews in Computational Chemistry", eds. K. Lipkowitz and D. Boyd, VCH Publishers, New York, 1990.

208. C. Dykstra, J. D. Augspurger, B. Kirtman, and D. Malik, in "Reviews in Computational Chemistry", eds. K. Lipkowitz and D. Boyd, VCH Publishers, New York, 1990, 83.

209. D. Boyd, in "Reviews in Computational Chemistry", eds. K. Lipkowitz and D. Boyd, VCH Publishers, New York, 1990, 321.

210. M. Zerner, in "Reviews in Computational Chemistry", eds. K. Lipkowitz and D. Boyd, VCH Publishers, New York, 1990, 313.

211. J. Pople, D. Santry, and G. Segal, J. Chem. Phys., 43, 1965, S129.

212. J. Pople and G. Segal, J. Chem. Phys., 43, 1965, S136.

213. J. Pople and D. Beveridge, "Approximate Molecular Orbital Theory", McGraw-Hill, New York, 1970.

214. J. Murrell, "The Theory of Electronic Spectra of Organic Molecules", Methuen and Wiley, New York, 1964.

215. J. Pople, D. Beveridge, and P. Dobosh, J. Chem. Phys., 47, 1967, 2026.

216. J. Ridley and M. Zerner, Theor. Chim. Acta, 53, 1979, 21.

217. R. Bingham, M. Dewar, D. Lo, J. Am. Chem. Soc., 92, 1970, 1285.

218. M. Dewar and W. Thiel, J. Am. Chem. Soc., 99, 1977, 4899.

219. M. Dewar, E. Zoebisch, E. Healy, and J. Stewart, J. Am. Chem. Soc., 107, 1985, 3902.

220. J. Stewart, J. Comput. Chem., 10, 1989, 209.

221. J. Stewart, J. Comput. Chem., 10, 1989, 221.

222. J. Stewart, in "Reviews in Computational Chemistry", eds. K. Lipkowitz and D. Boyd, VCH Publishers, New York, 1990, 45.

223. S. Wallace and L. Hench, J. of Sol-Gel Science and Technology, 1, 1994, 153.

224. W. Anderson, W. Edwards, and M. Zerner, Inorg. Chem., 25, 1986, 2728.

225. J. Stephens and D. Cruickshank, Acta Cryst., B26, 1970, 222.

226. A. Bystrom and K. Wilhelmi, Acta Chemica Scandinavica, 4, 1950, 1131.

227. K. Wilhelmi, Acta Chemica Scandinavica, 19, 1965, 165.

228. R. Bendale and L. Hench, under preparation.

229. T. Michalske and B. Bunker, J. Appl. Phys., 56, 10, 1984, 2686.

BIOGRAPHICAL SKETCH

James Michael Kunetz was born January 10, 1962, in Frankfurt, West Germany. Mr. Kunetz moved to Laurel, Maryland, in 1965 where he attended local schools and graduated from Pallotti High School in the spring of 1980. In the fall of 1980, Mr. Kunetz enrolled at the University of Maryland, College Park, to study chemical engineering. During his undergraduate studies Mr. Kunetz was employed in the ceramics division at the Naval Research Laboratory. He graduated from the University of Maryland in the fall of 1985 with a Bachelor of Science in chemical engineering under the co-operative education program.

In the fall of 1986 he entered the graduate school of the University of Florida, from which he received his Master of Science in 1989. Since then he has pursued work toward the degree of Doctor of Philosophy in materials science and engineering.

I certify that I have read this study and that in my opinion it conforms to acceptable standards of scholarly presentation and is fully adequate, in scope and quality, as a dissertation for the degree of Doctor of Philosophy.

Larry L. Hench, Chairman
Garduate Research Professor
of Materials Science
and Engineering

I certify that I have read this study and that in my opinion it conforms to acceptable standards of scholarly presentation and is fully adequate, in scope and quality, as a dissertation for the degree of Doctor of Philosophy.

Joseph H. Simmons
Professor of Materials Science
and Engineering

I certify that I have read this study and that in my opinion it conforms to acceptable standards of scholarly presentation and is fully adequate, in scope and quality, as a dissertation for the degree of Doctor of Philosophy.

E. Dow Whitney
Professor of Materials Science
and Engineering

I certify that I have read this study and that in my opinion it conforms to acceptable standards of scholarly presentation and is fully adequate, in scope and quality, as a dissertation for the degree of Doctor of Philosophy.

Robert T. DeHoff
Professor of Materials Science
and Engineering

I certify that I have read this study and that in my opinion it conforms to acceptable standards of scholarly presentation and is fully adequate, in scope and quality, as a dissertation for the degree of Doctor of Philosophy.

James M. Boncella
Associate Professor
of Chemistry

This dissertation was submitted to the Graduate Faculty of the College of Engineering and to the Graduate School and was accepted as partial fulfillment of the requirements for the degree of Doctor of Philosophy.

August, 1995

Winfred M. Phillips
Dean, College of Engineering

Karen A. Holbrook
Dean, Graduate School